A FINITE ELEMENT FRAMEWORK FOR MULTISCALE/MULTIPHYSICS ANALYSIS OF STRUCTURES WITH COMPLEX MICROSTRUCTURES

A Dissertation

by

JULIAN VARGHESE

Submitted to the Office of Graduate Studies of
Texas A&M University
in partial fulfillment of the requirements for the degree of

DOCTOR OF PHILOSOPHY

August 2009

Major Subject: Aerospace Engineering

A FINITE ELEMENT FRAMEWORK FOR MULTISCALE/MULTIPHYSICS ANALYSIS OF STRUCTURES WITH COMPLEX MICROSTRUCTURES

A Dissertation

by

JULIAN VARGHESE

Submitted to the Office of Graduate Studies of
Texas A&M University
in partial fulfillment of the requirements for the degree of

DOCTOR OF PHILOSOPHY

Approved by:

Chair of Committee, John D. Whitcomb
Committee Members, Dimitris Lagoudas
Zoubeida Ounaies
Xin-Lin Gao
Head of Department, Dimitris Lagoudas

August 2009

Major Subject: Aerospace Engineering

ABSTRACT

A Finite Element Framework for Multiscale/Multiphysics Analysis of Structures with Complex Microstructures. (August 2009)

Julian Varghese, B.Tech., University of Kerala, India;

M.S., Texas A&M University

Chair of Advisory Committee: Dr. John D. Whitcomb

This research work has contributed in various ways to help develop a better understanding of textile composites and materials with complex microstructures in general. An instrumental part of this work was the development of an object-oriented framework that made it convenient to perform multiscale/multiphysics analyses of advanced materials with complex microstructures such as textile composites. In addition to the studies conducted in this work, this framework lays the groundwork for continued research of these materials.

This framework enabled a detailed multiscale stress analysis of a woven DCB specimen that revealed the effect of the complex microstructure on the stress and strain energy release rate distribution along the crack front. In addition to implementing an oxidation model, the framework was also used to implement strategies that expedited the simulation of oxidation in textile composites so that it would take only a few hours. The simulation showed that the tow architecture played a significant role in the oxidation behavior in textile composites. Finally, a coupled diffusion/oxidation and damage progression analysis was implemented that was used to study the mechanical behavior of textile composites under mechanical loading as well as oxidation. A parametric study was performed to determine the effect of material properties and the number of plies in the laminate on its mechanical behavior. The analyses indicated a significant effect of the tow architecture and other parameters on the damage progression in the laminates.

DEDICATION

To my parents

ACKNOWLEDGEMENTS

I would like to express my deep sense of gratitude to my advisor, Dr. John D. Whitcomb, for supporting me financially, morally and academically. Without his patience and constant guidance, this work would have never been complete. The care and genuine regard for the well being of his students is something that can be found in very few people. I also wish to thank him and his lovely family for all the wonderful get-togethers we've had over the years.

I would like to express my gratitude to Dr. Dimitris Lagoudas, Dr. Zoubeida Ounaies and Dr. Xin-Lin Gao for serving on my advisory committee and for providing the valuable time from their busy schedules. I also want to thank Dr. Thomas Strganac for readily offering to take Dr. Ounaies' place during my dissertation defense.

My sincere thanks also go to Aerospace Engineering Department staff, especially Ms. Karen Knabe, Pam McConal and Miriam Aldrete, who are among the sweetest people I have met in my life, for their kind help during my graduate studies here at Texas A&M.

A whole bunch of thanks goes to my teammates, both present and previous – Xiaodong, Jae, Deepak, Jong-il, Bhavya, Brian, Ross, Kevin and others. It was great being part of such a lively and friendly group of people. I am also thankful to all of my friends, especially Sandeep, Loka, Brandis, Aditya, Pratheesh, Kirti and many others for their support. I am thankful to all the people who have directly or indirectly helped me accomplish whatever I have.

Finally, I wish to express my sincere appreciation to my father, mother and sister for their never-ending support, love, prayers and sacrifices. Without them, I would not have been able to pursue graduate studies here at Texas A&M University.

This work is based on research supported by the Texas Institute for Intelligent Bio-Nano Materials and Structures for Aerospace Vehicles, funded by NASA Cooperative Agreement No. NCC-1-02038, and the US Air Force Office of Scientific Research (AFOSR), funded by Contract Ref No. FA9550-07-1-0207. Any opinions, findings and conclusions or recommendations expressed in this material do not necessarily reflect the

views of the National Aeronautics and Space Administration or the AFOSR. I also wish to acknowledge the helpful discussions with Dr. K. Pochiraju, Dr. G. Tandon and Dr. G. Schoeppner.

TABLE OF CONTENTS

Page

Page

LIST OF FIGURES

Page

Page

Page

Page

Page

Page

LIST OF TABLES

1. INTRODUCTION

Advanced materials are being used increasingly in a variety of fields such as aerospace, automobile, defense, medical and sports. Many of these materials have complex microstructures which increases the challenges involved with designing these materials as well as predicting the behavior of these materials. Figure 1.1 shows a schematic of a few examples. Two of the examples involve nanotubes. The void in the center of the tube adds geometric complexity. The clustering of nanotubes creates what looks like 'macro' fibers that add an additional microstructural scale. In addition, the irregular distribution of 'macro' fibers adds complexity. The laminate is described by multiple length scales: fiber/matrix, lamina and laminate. The lamina also has distributed cracks. The last figure is a micrograph of a polyurethane foam. The geometric complexity is obvious.

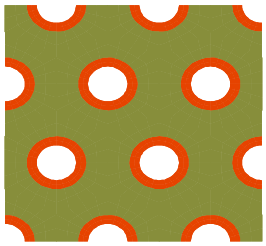

Carbon Nanotubes in Matrix

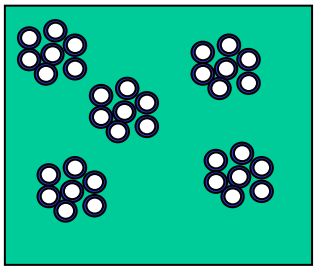

SWNT Bundles in Matrix

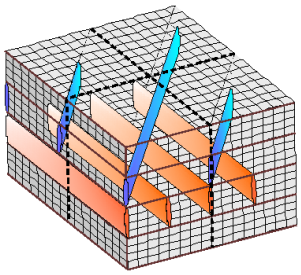

Laminate with Transverse Matrix Cracks

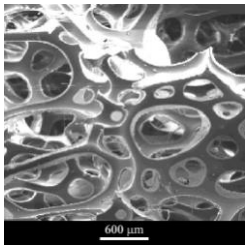

Micrograph of polyurethane foam [1]

Figure 1.1: Materials with complex microstructure

This dissertation follows the style of *Journal of Composite Materials.*

A typical engineering problem deals with a configuration that is at a length scale at least a few orders of magnitude larger than the size of the microstructure. Some examples include a structure made out of composite containing carbon nanotubes or a stringer stiffened panel that is made of composite material (where the fibers in the tows are as small as a few microns thick). The problem becomes impractical to solve if the entire configuration is to be modeled at the same length scale as its complex microstructure. This work focuses on the behavior of textile composites, which have different levels of microstructure. Multiscale analyses are required to capture the detailed behavior of these materials.

The use of these advanced materials in different applications requires a thorough understanding of the effect of the operating environment on these materials. The operating environment for these materials could vary from freezing and wet conditions in marine applications to high temperature and oxidizing environments in aerospace applications. Determining the effect of these environments on the material is a very challenging problem. This requires a thorough understanding of the underlying mechanisms and the physics involved with the different processes. The needs for simulations that try to predict the behavior of composites under a variety of environmental conditions underscore the requirement for the ability to perform multi-physics analyses conveniently. This work attempts to approach this problem and set a framework in place that makes it convenient for a user to perform such analyses. This section first gives a brief introduction to textile composites followed by definition of the different geometric parameters in textile modeling. The section concludes with a statement of objectives.

1.1 Introduction to Textile Composites

Over the last three decades, a wide variety of industries have been using composite materials because of its high specific strength and stiffness compared to conventional meals/alloys [2]. Textile composites can provide a unique combination of properties that cannot be obtained from conventional tape laminates. Technology from the centuries-old textile industry could be potentially used in the manufacturing of these composites.

Techniques for high-speed textile perform manufacturing make these types of composites appealing. Another advantage of these composites is the increased damage tolerance dues to the tow interlacing [2]. These composites can be mass-produces and tend to be more cost-effective than conventional tape laminates. They can also be used to create complex performs thereby potentially reducing the part count substantially. These composites are being used in applications ranging from prostheses for amputees to turbine blades for wind energy farms as shown in Figures 1.2 and 1.3.

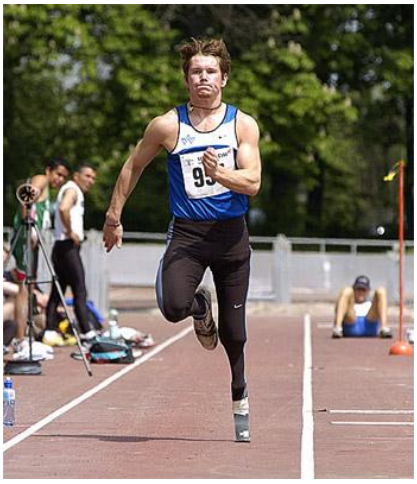

Figure 1.2: Composite prostheses [3]

Figure 1.3: Wind turbine blades [4]

Textile performs can be manufactured using a variety of techniques. The most common forms of textile manufacturing techniques can be broadly classified into braiding, weaving and knitting. All the techniques are similar in that they have interlaced tows creating a preform which is then impregnated with resin to create the composite. Figure 1.4 shows a few of the idealized weave architectures. All the analyses in this work focus on plain weave composites. Therefore, to facilitate discussion in the following sections, the next section defines some of the geometric parameters that are used to describe a plain weave idealization.

1.2 Definition of Geometric Parameters in Plain Weave Composites

Although in reality, textile composites do not have a perfectly periodic microstructure, it is typical to assume a periodic microstructure in order to make analysis feasible. The microstructure of textile composites is characterized by tow undulation and interlacing. The tows are made up of thousands of fibers. A simplified description of the manufacture of these composites is as follows. The tows are interlaced with each other using one of many techniques mentioned in the previous section to obtain a mat. The mats are stacked on the top of each other in various orientations to achieve the desired thickness. The mats are then impregnated with the matrix and cured to make the textile composite. There are different specific processes to obtain the final product but the basic idea behind the manufacture is the same as described above.

The idealized microstructure of woven composites is characterized by the orthogonal interlacing of two sets of tows called the warp and the fill tows. The fill tows run perpendicular to the direction of the warp tows. Figure 1.4 shows the common forms of the woven architectures such as Plain weave, twill weave, 4-harness satin, 5-harness satin, 8-harness satin and basket weave. The figure shows that in all the architectures except for the plain weave, the tows have both the undulated and straight regions. In the case of the plain weave, the tows are assumed to have a lenticular cross-section and the

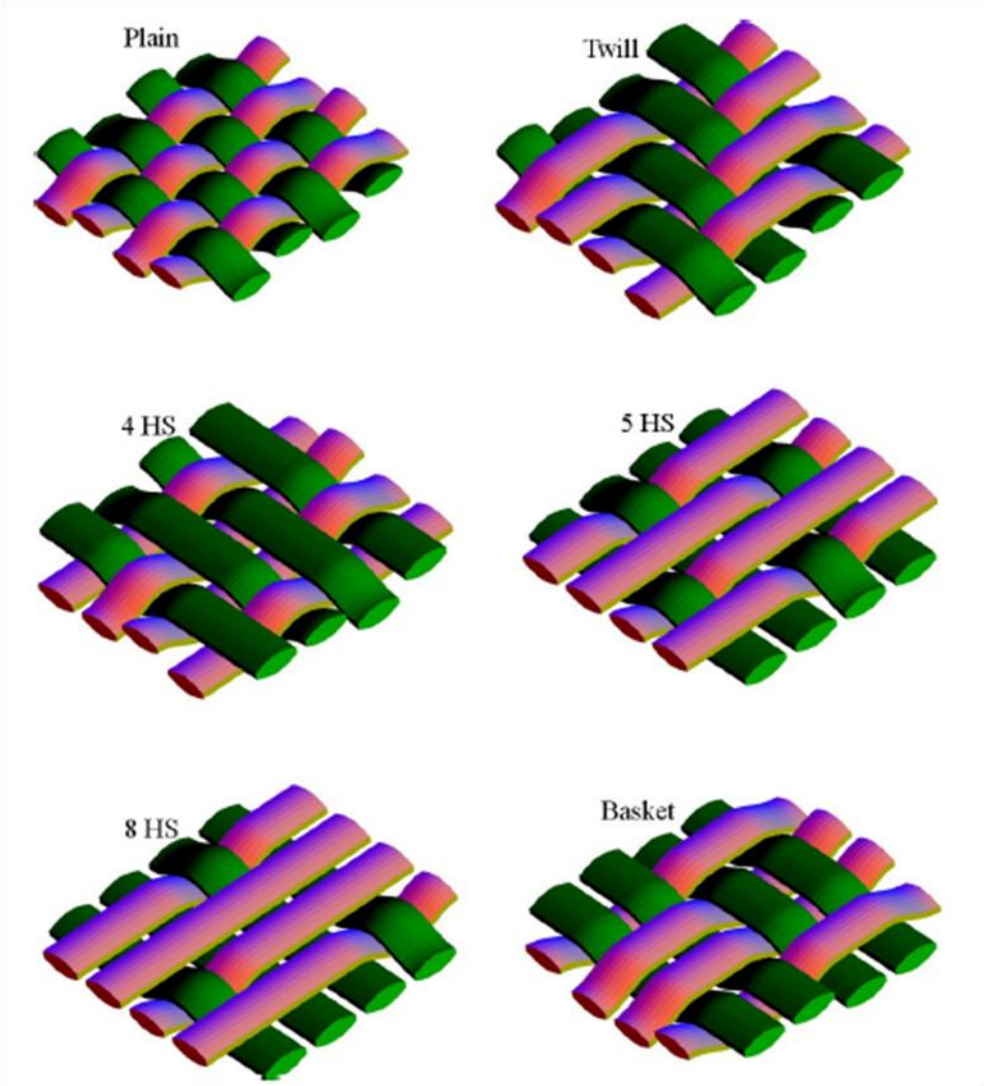

Figure 1.4: Idealized schematics of woven preforms without matrix pockets
(HS means Harness Satin) [5]

entire length of both fill and warp tows is undulated. In this work, the focus is on the plain weave composite. The rest of this section will define the different parameters used to describe an idealized plain weave microstructure.

The periodic nature of the plain weave microstructure is exploited to perform micromechanical analyses. The unit cell of a periodic microstructure is defined as the smallest region that can reproduce the whole microstructure by using spatial translation of its copies alone and not using rotation or reflection. Figure 1.6 shows a typical tow taken out a plain weave microstructure shown in Figure 1.5. Note that xyz are the local directions for the tow and XYZ are the global directions for the unit cell. In Figure 1.6, h is the mat thickness and λ is the wavelength of the wavy region. The waviness ratio is defined herein as h/λ. The cross-section of the tow can vary from lenticular to flattened to elliptical. In this work, the tow cross-section shape perpendicular to the horizontal plane is assumed to be lenticular. Moreover this tow cross-section is assumed to stay the same along the towpath. Therefore, it also means that the cross section shape on the plane perpendicular to the tow path does not remain the same along the tow path. The tow that would be running across the one in Figure 1.6 would follow the same undulation except with a phase difference of half the wavelength. The curved surface of a warp tow is in full contact with the corresponding curved region of the fill tow that is traversing under or over it as shown in Figure 1.5. Therefore, the tow path that defines the undulation would be related to the shape of the tow cross-section. The curved portion of the cross-section can be defined by a simple sinusoidal function of the form

$$z = \frac{h}{4}\cos\left(\frac{2\pi(s+s_0)}{\lambda}\right) + z_0 \tag{1.1}$$

where s = x or y, s_0 and z_0 are offsets, h is the mat thickness, and λ is the wavelength of the wavy region as shown in Figure 1.5.

The tow volume fraction (V_T) in the model and fiber volume fraction (V_f) in the tow determine the overall fiber volume fraction (V_{fo}) as follows:

$$V_{fo} = V_T \times V_f \tag{1.2}$$

The effect of heterogeneity was analyzed by Whitcomb et al. in ref. [6] and it was shown that the behavior can be reasonably predicted by average parameters. The manner in

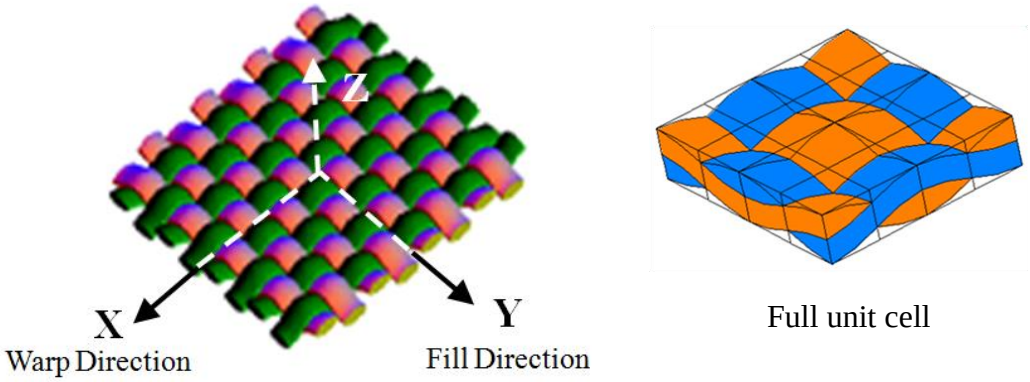

Figure 1.5: Plain weave microstructure and its unit cell

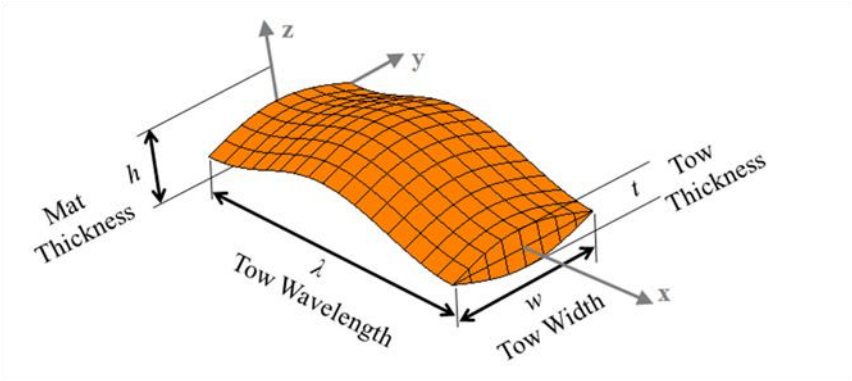

Figure 1.6: Geometry of typical tow

which the mats are stacked is called the stacking sequence. There are virtually countless possible stacking sequences. Typically, two idealized stacking sequences are considered when analyzing these materials. If the mats are spatially translated in a direction perpendicular to the plane of the mat, and stacked on top of each other, the sequence is called a simple stacking. In such a case, the undulation of the tows is in phase for all the mats. If consecutive mats are mirror images of each other at the mat interface, or in other words, symmetric about the mat interface, then the resulting sequence is called a

symmetric stacking. Figure 1.7 gives a schematic of simple and symmetric stacking of mats. Additional stacking sequences can be generated from various combinations of the simple and symmetric stacking sequences.

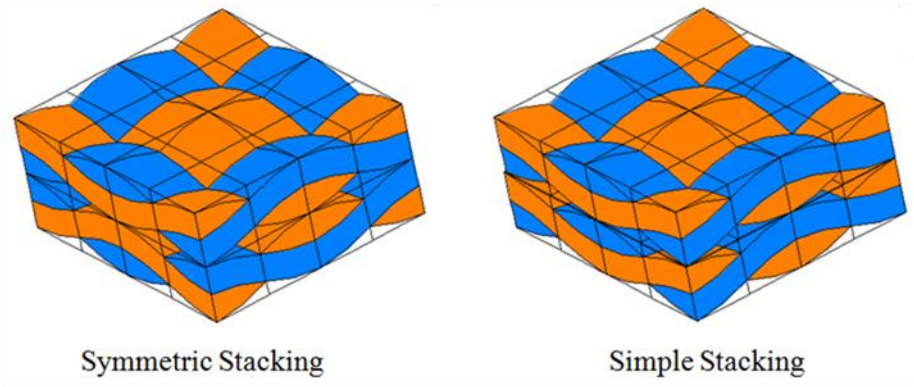

Figure 1.7: Simple and symmetric stacking sequences

1.3 Statement of Objectives

Although textile composites have many advantages and are used in a wide variety of industries, optimal characterization and design of these materials through experimental testing is not practical because of the range of textile architectures and numerous design parameters. The goal of this work is to develop a finite element analysis framework to predict the behavior of advanced materials with complex microstructures such as textile composites under extreme operating environments. To reach this goal, the work will involve performing multiscale/multiphysics analyses of textile composite configurations. The objectives of this work can be classified as follows

1) Develop a robust object-oriented finite element analysis framework that allows for convenient implementation of new analysis methods that could include standard elasticity models as well as models for other types of physical phenomena. This also includes implementing a framework that can handle analysis of multiple models concurrently and streamline data flow among models. It should be a flexible analysis tool that the user can maintain and extend with ease.

2) Use the framework to perform a global/local analysis of a woven DCB specimen. The framework uses a hierarchical model to automatically combine the discrete local model with the global model. Discretely modeling the tow architecture in the local model will give a much more detailed variation of the strain energy release rate at the crack front than possible with homogenized properties.

3) Simulate the oxidation behavior in textile composites. This involves:

a) Implementing and validating an oxidation model based on the work by Pochiraju et al [7-9].

b) Develop a strategy to determine and validate homogenized oxidation properties for the tow.

c) Develop strategies to expedite the simulation of oxidation since these models are computation intensive.

4) Develop a coupled analysis model to predict the effect of oxidation on the damage initiation and progression in textile composites. This will include developing a constitutive model to capture the effect of oxidation on the mechanical properties of the material in the textile composite. The coupled multiphysics model will be used to predict the mechanical behavior of a plain weave graphite/PMR-15 composite that is under mechanical load as well as undergoes oxidation for 200 hours.

2. REVIEW OF STATE OF KNOWLEDGE

The following subsections will summarize the state of the art in the development of finite element tools and the analysis of textile composites as it pertains to this work. It starts off by talking about the origins of the finite element method. This is followed by a discussion of the finite element programs available and the development of finite element analysis packages. An important part of a finite element program is the equation solver. A brief discussion of the various solvers used for solving large models is provided next. Then, the multiscale challenges inherent in predicting the behavior of textile composites will be discussed. This includes a review of the analytical methods for describing the behavior of textile composites. The advantages and limitations of the various methods will also be discussed. Global/local analysis methods were used for at least part of the analyses in this work. Hence, global/local methods will be discussed next. The next section reviews the advances made in progressive failure analysis of textile composites. This is followed by a review of damage in textile composites due to environmental conditions such as moisture, high temperature and oxidation. Particular attention is paid to the effects of oxidation on composites and the advances made in trying to simulate the oxidation behavior in composites. The section concludes by discussing the scope of this research work.

2.1 Introduction

Depending on its complexity, analysis of a scientific problem can be very cumbersome and time-consuming. Even if the governing equations are determined, it is usually not possible to arrive at a closed form solution of the problem. An alternative is to use numerical techniques to solve the equations involved. This might not give you an exact solution, but depending on how you solve the equations, it is possible to get a practical solution for the problem.

The drawback of numerical solving of problems is that it is a tedious process and becomes hard to manage with increase of complexity. For this reason, it is not practical to solve large problems numerically by hand. With the advent of computers, the time

required to analyze large problems has been considerably reduced. In addition to the advantage of a much higher processing speed, the computer takes care of the 'book-keeping'. The finite element method, which is basically a numerical technique to solve partial differential equations, gained popularity with the development of computers. Richard Courant, a German mathematician is generally acknowledged the originator of the FEM. His technique which relied heavily on the works of Lord Raleigh, Boris Galerkin, and Walter Ritz was used in 1943 to solve torsion of a cylinder [10]. Shortly thereafter, the finite element method was reinvented in a series of papers by Argyris and Kelsey (1960) [11] and Turner, Clough, Martin and Topp (1956) [12] who were engineers working on airplane structures design. With this method, it became easy to analyze structural components with complex shapes. Although, it was initially used to analyze structural problems, the finite element method is currently used in many fields of science as well as business and finance engineering [13].

Gone are the times when one needed a supercomputer to analyze a finite element model. With the explosive growth of the computer industry, it is now possible to run a fairly large model on a desktop PC. Although, an increase in computer processing speed reduces the time taken for solving a set of equations, there are other bottlenecks that hold up the time required for an analysis. Ironically, with the availability of very fast computers, some of the major bottlenecks involved in analyzing a problem from start to finish are those processes that require human involvement.

There are many factors that govern how quickly one can perform an analysis of a structural configuration. When using finite elements, the steps typically consist of defining a solid model, converting the solid model into a finite element mesh, preparing the non-geometric data input (such as material properties and boundary conditions), using a finite element solver to solve the equations and provide the solution in terms of displacements, stresses, etc., and most importantly interpret the results. Each of these steps can be quite time consuming in terms of computing power and human involvement. The aim of this work is to develop a framework that allow the user to

expedite these steps when analyzing structures with complex microstructures and thereby reduce the overall analysis time.

2.1.1 Finite Element Analysis Programs

There are many kinds of finite element packages that are available to the finite element method user community. These include a number of large finite element packages that came out of the early work done in the industry and research organizations, such as NASTRAN that came out of NASA Langley [14] and ANSYS that came out of the nuclear industry [15-16]. These and other commercial packages like ABAQUS[17] have evolved over time to become powerful finite element packages that are used by many in industry as well as researchers for a wide range of problems. The finite element community including the world of researchers can be broadly divided into two groups. One groups consists of users or analysts of the finite element method who require codes that are highly robust, well-documented and fully verified. They need software that come with good technical support. They need software that can solve their problem but they are not necessarily interested in knowing all the details regarding how the computations are actually carried out. Large commercial finite element packages like ANSYS and ABAQUS and packages made for specialized problems are exactly what fit the needs of this first group. The other group of people, consisting of researchers and developers of the finite element method, prefer to have access to a reliable, established source code which can then be used as a foundation and building blocks for the development of new strategies or methods for solving problems that haven't been solved before. While a considerable amount of research is done using commercial finite element packages such as ANSYS and ABAQUS, these packages do not fully satisfy the needs of every individual in this second group very well. These packages do however, offer some features for allowing the analysis of new problems. For instance, ANSYS has the USERMAT feature which allows user-defined materials and user-defined subroutines and similarly ABAQUS has the UMAT feature. The material called Nitinol exhibits a very different stress-strain curve for loading and unloading that cannot be modeled with existing material model in ANSYS. Barret and Fridline [18] were able to implement a

user-defined material model in ANSYS that simulated the Nitinol superelastic behavior. The atomic-scale finite element method (AFEM) is a multiscale computation method proposed by Huang et al [19] that aims to be as accurate as molecular mechanics simulations while be much faster than the commonly used order-N^2 conjugate gradient method. This new method was implemented by Huang et al in ABAQUS using the USER-ELEMENT feature. These are just a couple of examples of new methods/models that been implemented by researchers using commercial finite element packages. The major commercial finite element software developers strive to provide features that serve the requirements of analysts across many industries, and while they are successful to some extent in that regard, it is virtually impossible to satisfy the requirements of every researcher without letting the user obtain control of the inner workings of the program. Such a situation would not only be impractical from a business point of view but it would make the task of maintaining and enriching the software a nightmare. By maintaining control over the software, the commercial developers are able to provide a quality-assured, robust and reliable finite element package with technical support that is able to satisfy a fairly large consumer base. Therefore, the group in the finite element method users community that wants to have more access to the core of the finite element program than the commercial software developer is willing to provide, has to resort to either writing their own finite element code or use one of the many open-source finite element packages freely available as a foundation for their research work.

Prior to the 1990's, most finite element programs were written using functional programming languages such as FORTRAN-77, which was considered the language of choice for numerical and scientific applications. The in-house codes, written by developers for their specific application needs, in these functional languages tend to be monolithic and difficult to maintain and extend even though some of them have very good functionality. With the growing popularity of the object oriented programming paradigm in the 90's, a number of finite element packages were developed in object oriented programming languages such as C++. The object oriented design philosophy provides features such as encapsulation, data abstraction, inheritance and polymorphism.

Encapsulation is the ability to store data and function in a single unit, known as a *class* in object oriented terminology. *Abstraction* allows representing essential features without including the background details or explanations. Classes use the concept of abstraction and are defined as a list of abstract attributes. *Inheritance* allows a class to have the same behavior as another class and extend or tailor that behavior to provide special action for specific needs. Simply stated, *polymorphism* is the ability to use a general interface to manipulate things of various specialized types. These features make it possible to build software using software components that correspond to real-world high level entities. A paper by Jun Lu et al [20] details the advantages of using an object oriented design for finite element programs. Following a good object oriented design philosophy makes the code much simpler, flexible and allows for extensibility, reusability and reliability.

There are still many in-house codes and free finite element packages that are built using the functional programming languages. Z88 [21] is one such example of a finite element package written in ANSI-C. It is a fast, powerful and compact finite element analysis program that can run on a variety of platforms. Z88 features 20 finite element types and comes with a mesh generator and plot programs. It has a limited number of options in terms of solvers. It is released under a GNU GPL Freeware license and therefore users have access to the entire source code but due to its underlying design it is not very convenient in terms of extensibility. It is more appropriate for analysis using the already available features in the problem and slight modifications. Ref. [22] gives a fairly large list of free finite element packages that are relatively sophisticated. These include packages that object oriented as well as those that are not.

Deal.II [23] is an object-oriented finite element library written in C++ by Wolfgang Bangerth and Guido Kanschat. It is targeted at adaptive finite elements and error estimation. It comes with a complete stand alone linear algebra library that also interfaces with other packages such as PETSc and METIS. It supports a variety of computer platforms and is also optimized for multiprocessor machines. It supports a variety of elements and its object-oriented design allows for new elements to be

implemented conveniently. It comes with considerable documentation and is widely used in many areas of academia. The library is intended as a foundation for building finite element programs thereby freeing the programmer from aspects like mesh handling and refinement, handling of degrees of freedom, input and output of data and such. The application developer has to provide other aspects of the final application such as mesh generation and other specific application needs.

Getfem++ [24] is another C++ library for finite element programs. It focuses on elementary computations and allows creation of custom element matrices, with arbitrary dimensions, degrees of freedom, and several integration methods. It offers a complete separation between integration methods (exact or approximated), geometric transformations (linear or not) and finite element methods of arbitrary degrees. It offers a wide range of element types including Hermite elements, XFem, multigrid methods to name a few and the addition of a new finite element method is convenient. The library also includes the usual tools for finite elements such as assembly procedures for classical PDEs, interpolation methods, computation of norms, mesh operations (including automatic refinement), boundary conditions and post-processing tools such as extraction of slices from a mesh. Getfem++ can be used as a foundation to build very general finite elements codes, where the finite elements, integration methods, dimension of the meshes, are just some parameters that can be changed very easily, thus allowing a large spectrum of experimentations. Like Deal.II, Getfem++ has no meshing capabilities and therefore the application developer has to account for mesh generation. Although it does not have meshing capabilities, once it is provided a mesh, the program can refine the mesh automatically. It allows for importing meshes in formats such as GiD , GmSH and emc2.

Both Deal.II and Getfem++ are very good options as building blocks for a finite element framework but on their own they do not provide the additional functionality needed for the analysis of special materials like textile composites, which is the focus of this work. One possibility would be to use some of the features provided by these libraries in the proposed framework.

Zebulon [25] is a fairly sophisticated object-oriented finite element package with advanced non-linear solution capabilities. The package was initially developed as a research and teaching tool and progressed to build a wide commercial user base. It was originally written in FORTRAN and in 1992, the entire program was re-written in the object oriented programming language C++. The authors [26] wrote a few papers that detailed the aspects of object oriented finite element design which became relevant as the project size increases. This drives home the point that good object oriented design is a lot easier to maintain, manage and extend when compared to functional languages such as FORTRAN-77. Even if it boils down to speed issues, FOTRAN-77 does not offer any significant advantages in execution times. Object oriented C++ programs are being using in real-time mission critical applications such as the Mars rover and in marine diesel engines and cell phones [27]. While Zebulon does not contend to be a state of the art meshing or solid modeling tool, it provides interfaces to other packages that are already excellent in that field. Zebulon boasts of a wide range of material models such as hyper-elastic incompressible materials, generalized Maxwell visco-elasticity and composite materials, including anisotropic viscoplasticity with damage to name a few. Zebulon can also run a diverse range of finite element problems such as fluid-structure interfaces, fracture mechanics techniques and diffusion with moving Stefan boundaries. It is also capable of using multiple processors for solving finite element models. It also allows the user to add custom material models, element formulations, boundary conditions, output routines, and virtually all other operations of the calculation using C++ source code or a special pre-processing modeling language (called ZebFront) that comes with the package. No alteration is required to the standard code in order to make this possible, therefore the base application is safe from user errors. The interface is also seamless making the user additions look just like the standard options of the program.

OOF2 [28] is a package specifically for the finite element analysis of microstructures. It is designed to help materials scientists calculate macroscopic properties from images of real or simulated microstructures. It reads an image, assigns material properties to features in the image, and conducts virtual experiments to determine the macroscopic

properties of the microstructure. This is an open–source software that is developed by the Center for Theoretical and Computational Materials Science, which is part of the National Institute of Standards and Technology (NIST). They are working on the next version of the program that will be able to handle 3D micrographs. OOF2 can potentially handle any problem of the form "Flux = Modulus times gradient of Field" and "divergence of Flux = Applied Force". It can solve the heat transfer equation, mechanical force and the coulomb equation. It includes material properties for linear elasticity, thermal conductivity, dielectric permittivity and piezoelectricity to name a few. The program is based on the C++ finite element classes and tied together in a Python infrastructure, which is another easy to use, high-level object-oriented scripting language. New fields and fluxes can be added to the program by simply adding a few lines of Python or C++ code. It can export mesh geometry directly to ABAQUS if one chooses to use that package for further analysis. OOF2 is completely scriptable in Python and can also be run interactively from a graphical user interface. Although OOF2 is currently threaded, it is not possible to use multiple processors to solve a finite element model. They are working on a version that will include a parallel solver.

Comsol MultiPhysics (formerly known as FEMLAB) [29] started out as an add-on for MATLAB called PDE Toolbox. Since then, it has evolved into a powerful and interactive stand-alone environment for modeling and solving scientific and engineering problems based on partial differential equations. It is cross-platform and provides an extensive interface to MATLAB and its toolboxes. Comsol is known for its ease in setting up multi-physics models. Models can be built by simply specifying the relevant physical quantities. Other ways to set up the model is by specifying the governing equations in Comsol or by even specifying the weak-form equation. Comsol then applies and runs the finite element method in conjunction with adaptive meshing and error control with an option of several solvers. The latest version of the package also allows the user to import CAD files as well as a new material library with a wide range of different materials. Comsol is used in the industry as well as academia and research for almost all engineering and science related fields. Since Comsol is commercial software,

it does not allow access to its source code. While Comsol is ideal for many multiphysics finite element modeling, there are several limitations as well. For example, Comsol supports Lagrange and Hermite interpolation but it is not possible to introduce new types of interpolations such as B-Splines. Comsol is an easy to use tool for already implemented types of models or user-defined models with complicated governing equations as long as it is conforms to Comsol's requirements. On the other hand, it is not a very convenient tool for the analysis of textile composites which involves considerable data management and postprocessing. Implementing something like a progressive damage analysis of textile composites in Comsol would take a considerable amount of work, if possible at all.

2.1.2 Solvers

During a finite element analysis, the most time-consuming step is usually the actual solving of the equations. With the advances in computer technologies such as memory and processor speeds, it is possible to analyze larger finite element models and solve them faster than ever before. There are in general two types of solvers – direct solvers and iterative solvers. For relatively small problems, direct solvers are usually quicker than iterative solvers, but as the matrix size increases, direct solvers become more computationally and memory intensive than iterative solvers. For this reason, beyond a certain problem size, it is usually more advantageous to choose iterative solvers over direct solvers.

In order to run a very large finite element model, one usually has to use supercomputers that have multiple processors. Depending on the system architecture, the supercomputer could have a memory design such as shared memory [30], distributed memory, distributed shared memory or Non-Uniform Memory Access (NUMA). Solvers were implemented that could make use of multiple processors to solve the finite element model simultaneously. With newer and faster PCs coming out every year, the average size of models that can be solved on the PC kept growing. Now we are at the point where the speed of a single processor has more or less stagnated and the latest class of PCs coming out in the market use processors with multiple 'processing units' or 'cores'.

These new PCs fall under a class of systems called Symmetric multiprocessing (SMP) systems [31]. This is a multiprocessor computer architecture where two or more identical processors are connected to a single shared main memory. In order to take full advantage of these new processors, one needs to use parallel solvers that can coordinate computational tasks simultaneously among the different cores in order to solve the finite element model. It is also possible to hook up multiple computers together in what is known as clusters [32] in order to use the collective number of processors simultaneously as in a multi-processor supercomputer.

Different computer vendors used to have their own specifications and instruction set in order to control and coordinate the use of the multiple processors in the computers that they manufacture. This made it very hard to develop portable codes that could be used across different types of machines. In an effort to eliminate this problem, some standard Application Programming Interfaces (APIs) were introduced that all the vendors conformed to. In this way, the programmers used the instructions in the APIs and did not have to worry about how exactly the vendors implemented the task in their computer. As long as their program would be running on a machine that supported the API, the program would work. The performance on different machines could vary because how exactly the vendors implement the API is up to them and could be different for various machines.

Three of the most commonly used APIs are Pthreads, OpenMP and the Message Passing Interface (MPI). Pthreads[33] or POSIX threads is the IEEE POSIX 1003.1c standard that defines the API for creating and manipulating threads. This standard is not as common as the other two for developing parallel programs. The OpenMP which stands for Open Multi-Processing [34] is an API that supports multi-platform shared memory multiprocessing programming in C/C++ and FORTRAN on many architectures, including UNIX and Microsoft Windows platforms. Jointly defined by a group of major computer hardware and software vendors, OpenMP is a portable, scalable model that gives programmers a simple and flexible interface for developing parallel applications for platforms ranging from the desktop to the supercomputer. OpenMP currently only

runs efficiently in shared-memory multiprocessor platforms and scalability is limited by memory architecture. The Message Passing Interface (MPI) [35] is a language-independent communications protocol used to program parallel computers. Although MPI is not sanctioned by any major standards body, it has become the de facto standard for communication among processes that comprise a parallel program running on a distributed memory system. Actual distributed memory supercomputers such as computer clusters often run these programs. MPI's goals are high performance, scalability, and portability. While it is generally considered to have been successful in meeting these goals, it has also been criticized for being too low level and difficult to use, hence sometimes being referred to as the assembly language of parallel programming. It is highly portable because MPI has been implemented for almost every distributed-memory architecture available on the market. It is fast because each implementation is in principle optimized for the hardware on which it runs. It is also supported on shared memory and Non-Uniform Memory Access(NUMA) architectures, which makes it very portable and at the same time provide high performance.

There are a number of parallel solvers available that can make use of multiple processors to concurrently solve a finite element model. One such solver is called the Pardiso [36-38] solver which stands for Parallel Direct Solver. The PARDISO package [39] is a thread-safe, high-performance, robust, memory efficient and easy to use software for solving large sparse symmetric and unsymmetric linear systems of equations on shared memory multiprocessors. The authors of PARDISO who are at the University of Basel in Spain have licensed the library free of charge for non-commercial and non-profit internal research purposes. The package uses the OpenMP API to implement the parallel solver thereby making it very efficient for shared memory systems. For the same reason, it is not efficient for machines with processors that do not share the same memory resources such as distributed memory machines. Intel has licensed the PARDISO solver from the University of Basel to include it in their Math Kernel Library [40], which is optimized for the Intel computer chips. The scalability of the parallel algorithm is nearly independent of the shared-memory multiprocessing architecture, and speed-ups of up to

seven times (on eight processors) have been observed [41]. The efficiency of a direct solver depends greatly on how small the bandwidth of the sparse matrix is. In order to increase the efficiency of the solver, the matrix is usually reordered in such a way that the bandwidth is reduced before the solver actually starts solving the system of equations. The PARDISO package uses a program called METIS [42] for this purpose. The METIS package is developed by George Karypis' group in the University of Minnesota. The group has also developed ParMetis [43] which is an MPI-based parallel library that extends the functionality provided by Metis for parallel computations and large scale numerical simulations. The parallel algorithms [44] implemented in this package have been shown to significantly outperform other popular reordering algorithms.

PETSc [45-47] is a suite of data structures and routines for the parallel solution of scientific applications modeled by partial differential equations. It uses the MPI standard and is scalable. The PETSc library is developed at the Argonne National Laboratory and is available for free with support. PETSc, which is built for use in large-scale application projects, is widely used in the academia and research institutions with applications ranging from nano-simulations to computational fluid dynamics to geosciences. While PETSc is easy to use for beginners, it allows advanced users to have detailed control over the solution process. It includes a large suite of parallel linear and nonlinear equation solvers that are easily used in application codes written in C, C++, FORTRAN and Python. It is portable to both windows and UNIX environments. While PETSc has a number of iterative solvers with a range of preconditioners, it does not provide many direct solvers. On the other hand, it does provide interfaces to a number of external packages that have direct solvers which work in parallel.

One such external package that PETSc interfaces with is called MUMPS [48-50], which stands for MUltifrontal Massively Parallel sparse direct Solver. It is a distributed multifrontal solver written in Fortran-90 and uses the MPI standard. MUMPS is public domain, based on public domain software developed during the Esprit IV European project PARASOL (1996-1999) by CERFACS, ENSEEIHT-IRIT and RAL. The solver

interfaces to FORTRAN, C, C++, Matlab and Scilab. It can solve large linear systems with symmetric positive definite matrices, general symmetric and unsymmetric matrices. While the PARDISO solver is ideal for shared memory processor machines including the new multi core machines because of the OpenMP implementation, the MUMPS solver is ideal for large distributed memory machines including clusters because of its MPI implementation. It also provides several options for the matrix reordering schemes such as approximate minimum degree ordering (AMD, [51]), PORD [52] and METIS [42].

While this review mentions a few of the widely used parallel solvers, it does not cover every parallel solver available for large sparse matrices. N. I. M. Gould, Jennifer Scott and Yifan Hu provide an independent review and detailed comparison of the performance of various sparse direct linear solvers in these reports [53-55].

2.2 Multiscale Analysis of Textile Composites

Textile composites exhibit multiple scales of complexity. The major scales are the fiber/matrix scale, the tow architecture scale, the "laminate scale" (i.e. multi-layered textiles), and the structural scale [56]. These scales are illustrated in Figure 2.1. A lot of work has been done on analysis at the fiber/matrix scale [57-59], but not much has been done for the high temperature oxidizing environment that is part of the focus in this work. The techniques already present in the literature need to be tailored to account for oxygen permeation and the resultant degradation due to oxidation. Accounting for the tow architecture scale presents severe challenges even for highly idealized cases. Compared to modeling of tape laminates [60-64], there has been relatively little effort for textile composites. A common strategy for designers is to use the laminated plate theory with empirical known-down factors for properties. Obviously, this does not lead to fundamental understanding that could guide optimal design of the material. The following will review the wide range of analyses that have been developed.

A majority of the predictive models for textile composites can be categorized as either 1) very simple due to assuming isostrain or isostress or a combination of both, 2) a hybrid

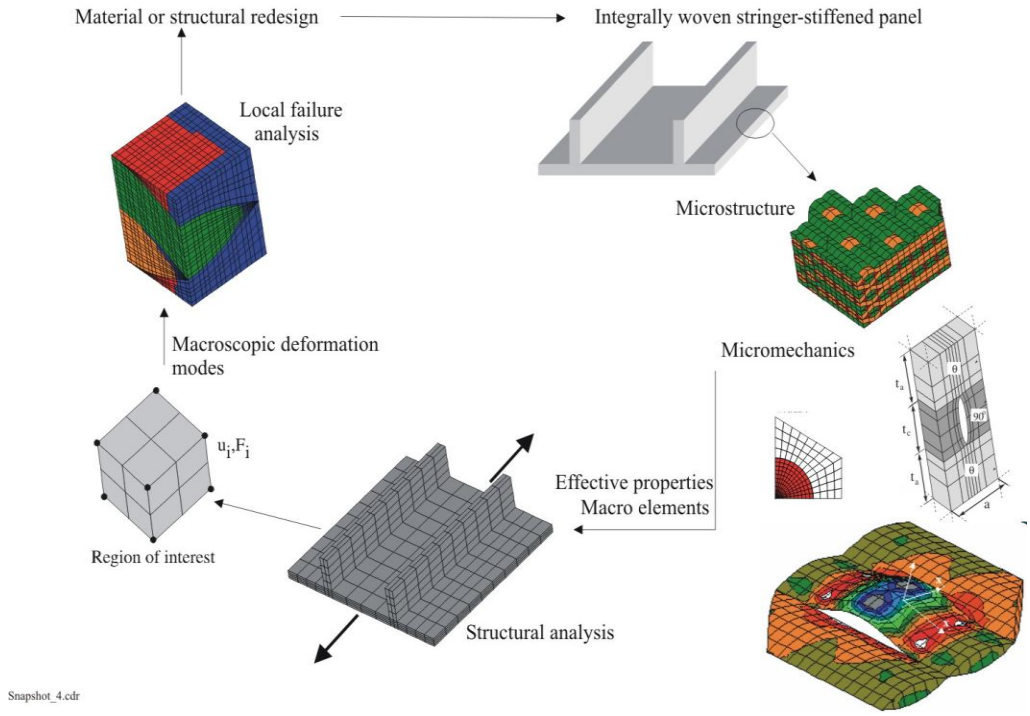

Figure 2.1: Multiscale Analysis (Figure courtesy Dr. John Whitcomb)

of strength of materials and piecewise isostrain or isostress assumptions or, 3) full three dimensional finite element modeling. The first two categories have close ties to laminated plate theory. There are also some hybrid approaches, such as the binary model developed by Cox et al. [65]. For certain engineering moduli, all of these approaches have been shown to give similar trends. For others, either the predictions of the engineering properties differ, or an estimate is not even provided by the simpler analyses. Whitcomb et al. showed that the ability of the "enhanced laminate theory" models to predict in-plane extensional modulus for a plain weave was related to two simplifying assumptions that introduced canceling errors [66].

Simple models involve simplifying assumptions concerning geometric modeling of the tow path and boundary conditions. These models vary in terms of the accuracy of the assumed displacement or stress field. Nevertheless, simple models do offer some significant insights into the behavior of textiles. On the other hand, one cannot get

detailed information like the microscopic stress distribution or the modes of failure. But the insights obtained from full 3D models or the experiments can be utilized to refine and modify simpler models and make them more robust. The following section will talk about the simple models first and then the full 3D models.

2.2.1 Progress in Development of Simple Models

Ishikawa and Chou [67] pioneered the development of simple 1D models based on lamination theory to predict thermo-elastic properties. The 1D crimp model accounted for fiber undulation, but the mosaic model did not [67-69]. The basic strategy of the 1D crimp model was extended to 2D by Naik, Shembekar and Ganesh [70-71].

The translation to 2D was accomplished by volume averaging in each subregion using isostrain or isostress assumptions and then combining the homogenized subregions… again using isostress or isostrain assumptions. They developed what they called the parallel-series model (PS) and the series-parallel model (SP) depending on assembling the elements first in parallel or in series respectively. Hahn and Pandey [72] extended the above 2-D models to a 3-D thermo-elastic model that models the undulation of fibers in both directions along with a sinusoidal cross-section shape of the yarns. The condition of isostrain was applied whose accuracy still remains to be verified through experiments. Verpoest [73] used the principle of minimum total complementary energy to develop a model for predicting the full set of 3D engineering moduli.

One common observation that can be made from these efforts is that if the goal is to just predict engineering moduli of undamaged materials, the existing suite of simple models is probably sufficient. This is because in reality, comparatively flat weaves are used and their moduli are dominated by quite simple physics. Unfortunately, the accuracy of some of the simple models appears to be a result of fortuitous cancellation of errors rather than good approximation of the physics [66]. Whitcomb and Tang [74] showed that all of the 3D engineering moduli can be predicted quite accurately even for very wavy weaves if the behavior of the undulated regions is described adequately. They also showed that some of the most popular approximations appear to have little physical basis.

2.2.2 Progress in Development of Full 3D Finite Element Models

Although moduli can be predicted fairly easily, prediction of the effects of textile design on damage initiation and growth, degradation due to oxidation, and coupling of these phenomena requires a much more detailed description of the textile architecture than the simple models can possibly provide. Fortunately, the rapid increase in easily accessible computational power has made 3D analysis much more practical. Figure 2.2 shows the

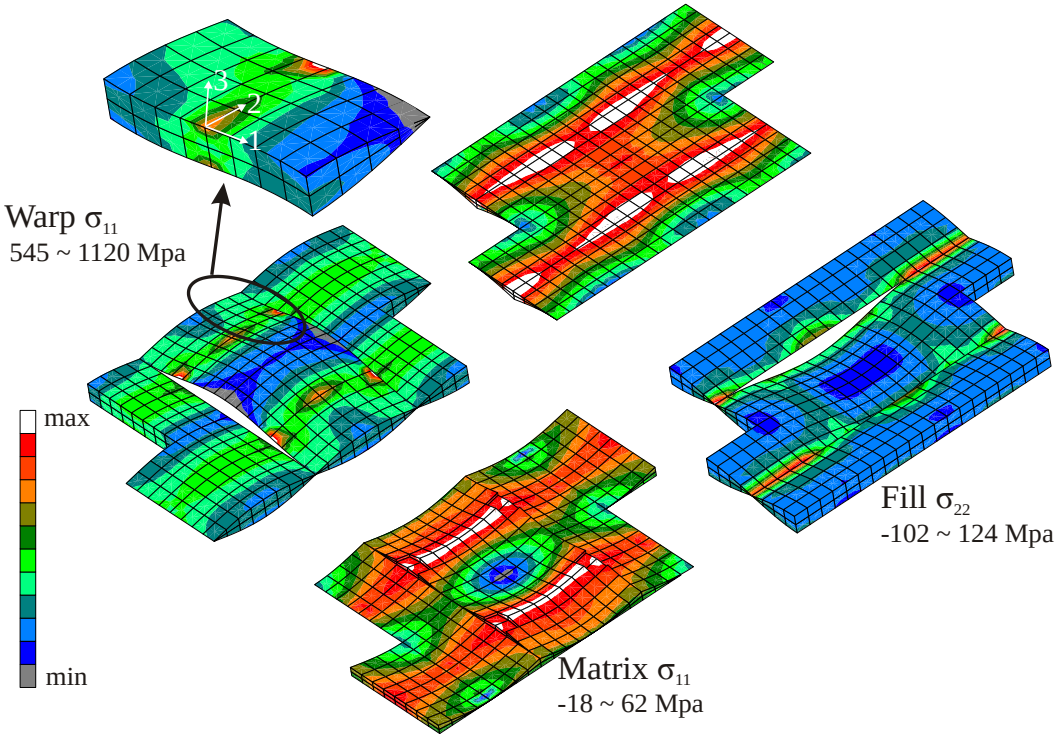

Figure 2.2: Stress contours for 5-harness satin weave

typical stress contours for a 5-harness satin weave composite subjected to a uniaxial load. The stress states are fully three-dimensional and complex even for the simplest loading. The interpretation of these stress states is a difficult job because the stresses can be so localized that the scale is small compared to the size of the fibers in the tow. The real tow architecture has more chaotic geometry than idealized textile geometry that will further increase the complexity of the stress state.

Some of the earliest 3D models of woven composites were developed by Paumelle et al. [75-76] and Whitcomb et al. [66,77-78]. More recently Kuhn et al. [79-80], and Ji and Kim [81] have developed models for woven composites. These efforts predicted not only effective macroscopic moduli, but also local stress concentrations that could lead to premature failure. Geometric and material nonlinearities (including failure) were included in work by Blackketter [82], Whitcomb [83], and Kollegal and Sridharan [84]. Gibson and Guan [85] examined the viscoelastic response of woven composite.

Most of the 3D models in the literature are for plain weave composites. The reason is that it is by far the simplest of the weaves, so mesh generation is relatively simple and the computational requirements are quite small, at least for linear analysis. However, there are exceptions. Whitcomb et al. has also published results for 4, 5, and 8-harness satin weaves, twill weave and 2x2 braids [74,77,78,86]. D'Amato [87] developed a model for triaxial braids. Naik [88] developed models for braids.

Analysis of textile composites can require large finite element models. Fortunately, periodicity within the microstructure can be exploited that reduce the analysis region to just a small unit cell. A unit cell is a region that can produce the whole microstructure by spatially translating its copies. Even then, a model of a single unit cell can be very large depending on the type of analysis. The computational cost can be reduced further by exploiting symmetries in the textile unit cell. Unfortunately, the boundary conditions for partial unit cell models are much more complicated and not intuitive like they are for the full unit cell. For example, Figure 2.3 shows the slave/master face pairs for a 2x2 biaxial braid [86]. Refs [89-90] describe systematic procedures for deriving these complex boundary conditions for partial unit cell models.

Mesh generation is one of the major challenges for the analyst. It is impractical to perform parametric study using 3D models unless the model itself is defined parametrically. That is, there must be a way to vary the characteristics of the tow architecture with the specification of only a few parameters. Tang used this technique very effectively in ref [74], where results were generated for numerous different weave configurations with very little human intervention.

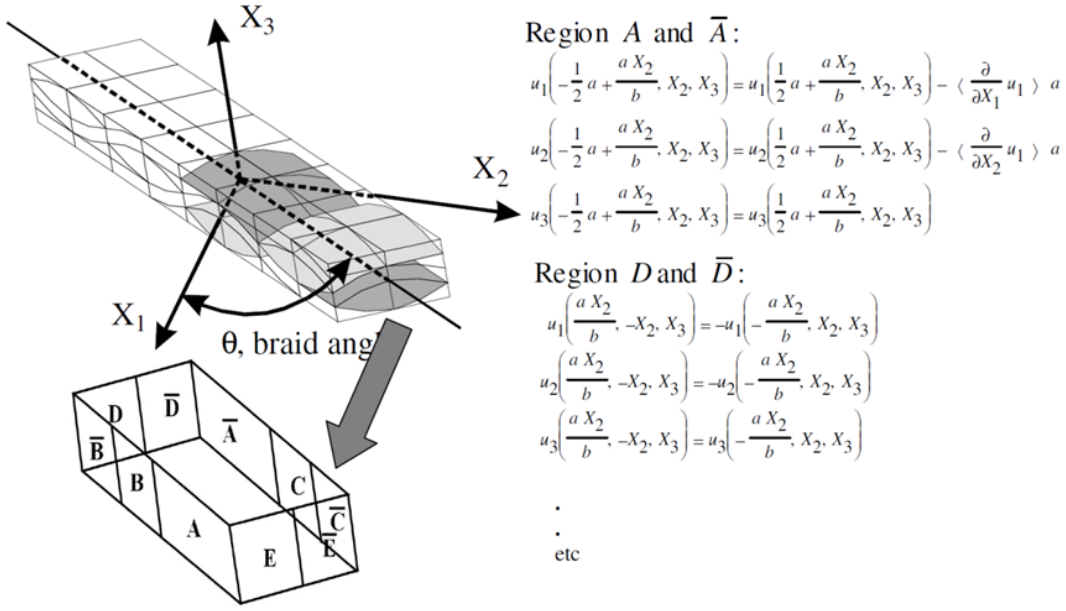

Figure 2.3: Multi-point constraint relations: boundary conditions for braid half-unit cell (Figure courtesy Dr. John Whitcomb)

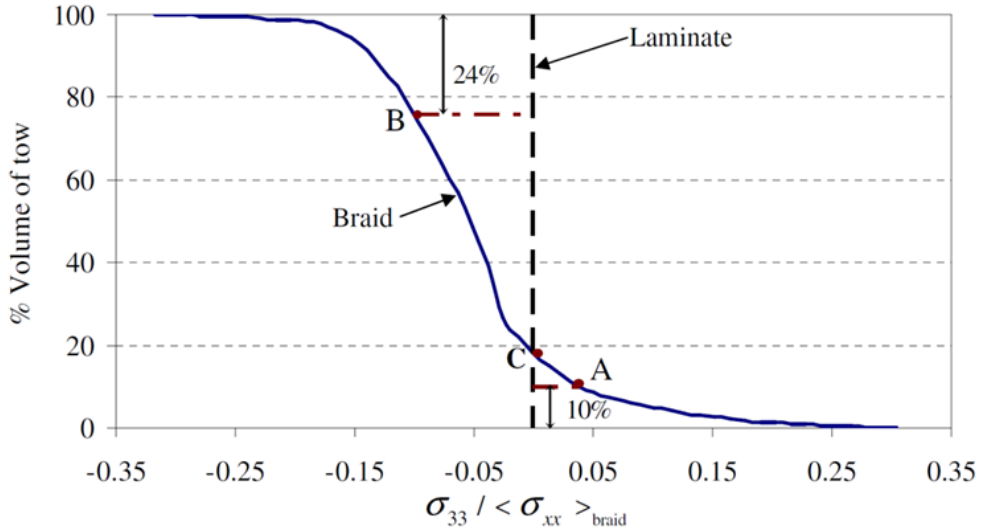

Figure 2.4: Volume distribution of S33 in ±30˚ braid tow with WR=1/3 when $<S_{xx}> = 1$ was applied

Three-dimensional analysis produces a tremendous amount of information. Sometimes it is useful to post-process the details to obtain a "bigger picture" interpretation. For example, Figure 2.4 shows a stress vs. volume plot that reveals just how much volume of a composite is subjected to the highest stresses [91]. Figure 2.5 shows how the axial load in a fiber tow varies along the tow path. Non-standard presentations of results like those just mentioned are quite useful in developing an intuitive understanding of the behavior.

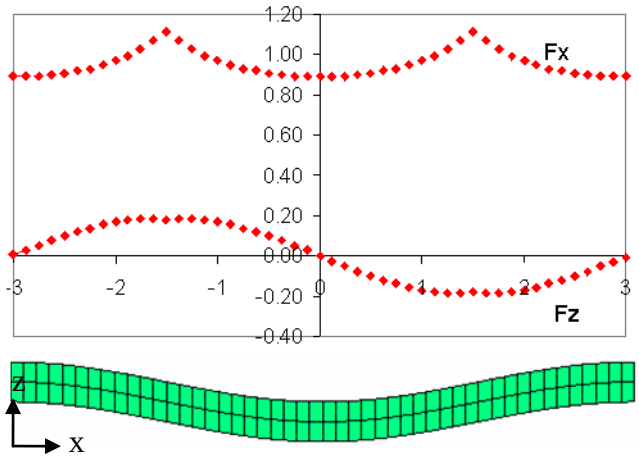

Figure 2.5: Tow stress resultants for plain weave in a linear elastic analysis

Periodic analysis is generally used in the modeling of textile composites because it is practically impossible to model the tow architecture for an entire composite specimen or structure. This is obviously an approximation since in reality there are irregularities due to variations in tow geometric properties such as waviness, cross section shape, and fiber volume fraction. A few researchers have considered variation of the tow architecture in a specimen. Whitcomb et al. [92] considered the effect of variation in braid parameters on the progressive failure behavior of a 2x2 braided composite laminate. A bottom-up multi-scale finite element modeling approach was employed that sequentially considered the fiber/matrix scale, the tow architecture scale and the laminate scale. Full 3D analysis was used to obtain effective 3D moduli for a variety of perturbations from a reference configuration. Then these effective properties were assigned to random locations in a macroscopic model of a uniaxial specimen. Aggarwal predicted the effects of tow

misalignment caused by the manufacturing process or forcing the fabrics to conform to molds [93] (see Figure 2.6). No detailed 3D analysis was developed and only the effects on stiffness were predicted. Lee et al. [94] and Bednarcyk et al. [95] also investigated the effects of irregularity of the microstructure; however, there was no attempt to model the actual wavy shape of the tows.

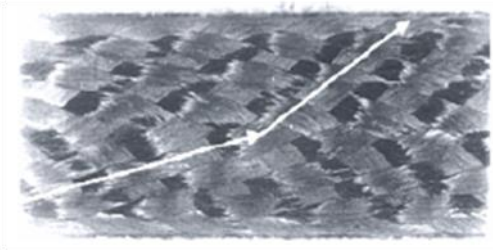

Figure 2.6: Yarn misalignment in flat braided composite [93]

Unintentional variation of architecture is minor in comparison to the large changes that must occur if a specimen is not of constant curvature. Even a braided tube of varying diameter will have significant variations in braid angle. More complex but very practical configurations such as the textile Pi joint (Figure 2.7) [96] or composite pin joints [97] have very large changes in tow architecture. There have been attempts to model such

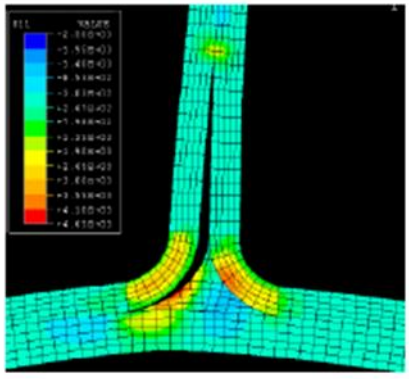

Figure 2.7: Pi Joint with damage [96]

structures, but only homogenized properties have been used (e.g. ref [97]). It is not practical to model the tow architecture throughout such complex configurations, but

global/local strategies, such as that in the next section, can be used to obtain refined information in selected local regions.

2.3 Global / Local Analyses

The term global/local analysis refers to a very broad collection of strategies aimed at including a good approximation of the large scale effects in a detailed analysis of a local region. It is not feasible to use a refined idealization of every detail throughout a structure or even a specimen. On the other hand, the boundary conditions for a detailed local model depend on the surrounding region. Therefore, one cannot ignore the larger scale when performing detailed analysis of a suspected critical region. One could quite fairly argue that global/local analysis methods have been used for as long as people have performed analysis. For example, design of a truss bridge years ago would not include details of the rivets when determining the nominal dimensions of the truss members, but eventually the rivets must have been considered. The focus of this section will be on methods that are particularly suited for expediting finite element analysis of materials with complex microstructure and have the potential for producing very accurate results.

It is convenient to categorize the methods as either uncoupled or coupled. An uncoupled method would perform analysis of the large scale problem using a crude approximation of the microstructure, such as effective moduli determined from homogenization theory. After the crude (global) analysis is completed, displacement and/or force information from the analysis is used to define boundary conditions on a much smaller more refined model [98]. Of course, the different levels of approximation typically results in loss of equilibrium. Whitcomb [99,100] described an iterative procedure to enforce equilibrium between global and local models.

A coupled analysis integrates the crude and refined models into a single model. For example, homogenized properties or macro elements [101,102], might be used for 95% of a model, but in the remaining 5% the microstructure is modeled discretely. Macro elements are special finite elements that allow inhomogeneity within a single element [101,102]. Figure 2.8 shows a $1/4^{th}$ plain weave unit cell which is modeled using a single

20-node macro element. The corresponding conventional mesh uses 64 elements and 381 nodes. Because of the complex spatial variation of material properties, there is significant distortion, even under simple extension. As illustrated by Figure 2.8, a single macro element can reproduce much of the deformation behavior of a traditional model with far more nodes.

Whether the analysis is coupled or uncoupled, one of the fundamental challenges is how to interface the idealizations, since the meshing would typically be incompatible. Whitcomb et al. [103] used multipoint constraints to approximately satisfy compatibility at the interface. The nodal displacements on the more refined side of the interface are slaved to the nodal displacements on the other side using the coarse side interpolation of the displacements. Unfortunately, this method cannot be generally used (other than for

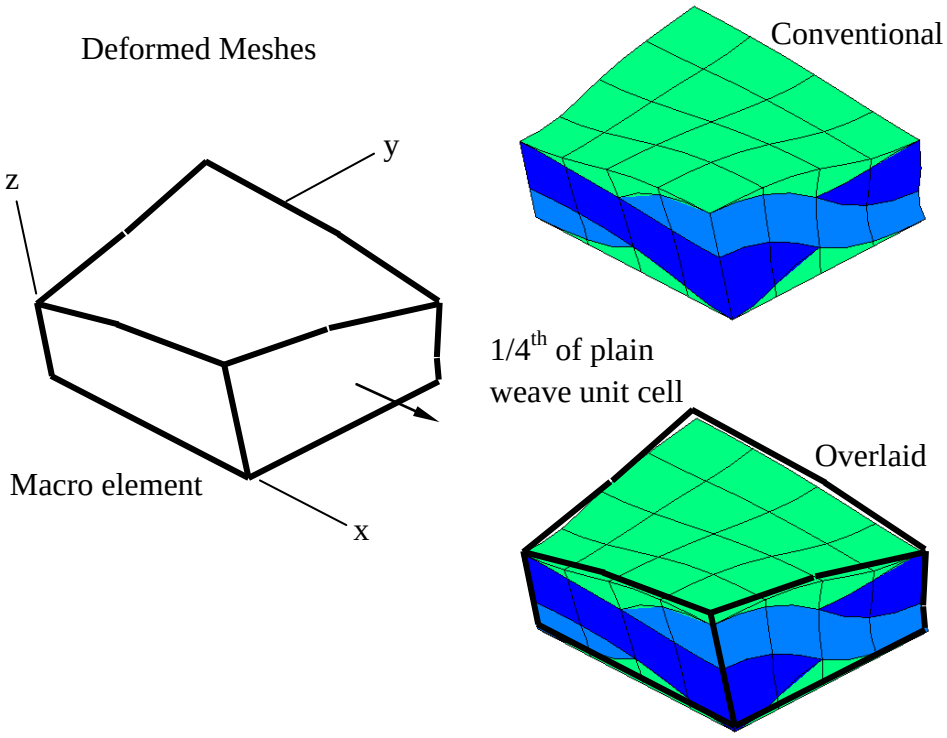

Figure 2.8: Macro element used to model weave microstructure

special configurations) because it does not accurately account for overlaps or for gaps between meshes. This results in the loss of linear consistency in the discrete

representation. Dohrmann et al [104-106] published an important result which describes how two independently meshed regions can be joined correctly and linear consistency can be maintained. They provided two requirements that need to be met in order to recover linear consistency. While these requirements are difficult to implement in practice, there are reliable approximations that can be implemented reasonably. Ransom [107] proposed using a higher order spline fit of the interface displacements from the crude model. A variational framework using Largrange multipliers for interfacing regions with incompatible meshes is described in a series of papers by Housner, Aminpour and Ransom [108-113]. This technology was recast in the form of an element, thereby facilitating the use of the method for more than two subdomains. A layer of interface elements are introduced between the two subdomains and the boundaries on either side of the interface are associated with the interface elements. Although a variety of structural configurations have been studied using this interface technology, the accuracy and efficiency for microstructural analysis has not been determined. The various interface techniques all share a common weakness: it is not trivial to define the boundaries for the regions involved, sort/associate the nodes on opposite sides of the interface, and then impose the selected constraint conditions on the associated nodes. Effective use of global/local methods requires that much of this process be automated.

Some commercial finite element analysis packages provide their users with the ability to assemble large models from different ‘parts’. The trend is to move towards a unified CAD and FEA environment where designers and engineers can conceptualize, design, optimize, validate and simulate their ideas. Ansys has their DesignSpace [114] simulation package while Abaqus has the Unified FEA Product Suite [115]. There are also some software packages developed by government institutions that allow rapid development and simulation of prototype assemblies. SIMBA (Simulation Manager and Builder for Analysts), developed by Sandia Labs [116], also builds FE models from various components. It is used mainly to build and manage complicated finite element models of weapon systems saving analysts large amounts of problem setup time. Using NextGRADE by NASA [117], which stands for Next Generation Rapid Analysis and

Design Environment, you can rapidly build a structure using stock components and then analyze it. NextGRADE uses the interface element technology developed by Aminpour et al [108-113] to assemble different components.

2.4 Progressive Failure Analyses

One higher level challenge is the prediction of non-linearity caused by damage initiation and progression in textile composites. Using 3D finite element analyses, the failure can be predicted two ways for textile composites. One involves a discrete modeling of damage and other involves accounting for damage in a homogenized way in which the modulus or strength properties are degraded whenever some damage is detected. An accurate modeling of geometry, implementation of a reasonable failure criteria and a property degradation model are prerequisites for this type of modeling approach.

There have been a few attempts in discrete modeling of damage [118], but most of efforts have been in homogenized modeling of damage. Various researchers have proposed different damage models. Most of these models are similar in the sense that they degrade the stiffness coefficient or increase the compliance coefficients of the yarns and matrix after failure criteria determines the occurrence of a damage mode. These models differ from each other in various ways. The models basically differ in what degradation factors [118] they use for degrading the properties under a particular failure mode. Secondly, some degrade only the diagonal entries in the compliance or stiffness matrix and some affect the off-diagonal terms also. Another difference between damage models is whether the matrix, which is isotropic initially, is considered anisotropic or not after damage. Some of the models are based on the experimental observations while some have theoretical basis. A comparison of some of the damage models available in the literature will be provided here. The damage model given in ref [82] has been widely used to predict initiation and growth of damage by many researchers [119-120]. Whitcomb and Chapman [121] proposed a property degradation model based on the Blackketter et al's [82] model. This was a combination of the method used by Blackketter et al [82], Stanton and Kipp [122] and Whitcomb and Srirengan [118]. The model involved degradation of engineering moduli of the yarns when a certain failure

mode was detected. Whitcomb and Chapman's [121] model is similar to the model given by Blackketter el al. [82] except for few differences like the degradation factors are different in the two models. Both the models affect only diagonal entries in the compliance matrix. Zako et al. [123] developed an anisotropic damage constitutive equation based on damage mechanics. Different damage modes were considered in the yarns. The degradation factors were calculated from a damage tensor. This model inherently affects the off-diagonal terms also. An anisotropic damage model was considered for yarns, and an isotropic damage model was considered for the matrix. Even though the isotropic damage model for the matrix starts off with an undamaged matrix that is isotropic, as the damage initiates and progresses, the matrix could become anisotropic. Tamma et al. [124] proposed a damage model in which they provided physical explanation of what properties should be degraded under a particular failure mode. They considered the degradation of off-diagonal terms also. Anisotropic damage models were proposed both for the yarns and for the matrix. Recently Sankar et al. [125] developed a direct micromechanics method (DMM), which does not make any assumptions based upon homogenized properties. Failure envelopes for a plain-weave textile composite were developed and any arbitrary loading including the moments can be applied to their detailed 3D finite element model. The method employed was used to develop phenomenological failure criteria for textile composites. A drawback is that their method considers only damage initiation with no regard to damage progression. A more detailed discussion about damage mechanisms in textile composites is given in Section 9.

2.5 Damage Due to Environmental Conditions

Woven composite structures are expected to undergo a range of hygrothermal and oxidizing environmental conditions during their service life. Environmentally induced degradation of textile composites has been examined experimentally. However, the characterization is typically macroscopic. For example, Luan et al. [126] studied the corrosion of a C-SiC composite with SiC coating (SiC-C/SiC) under a low frequency cyclic stress in various gas atmospheres of oxygen, water vapor, and sodium sulfate vapor at temperatures from 1000 to 1300 °C. A model for the cyclic stress corrosion mechanism of the composite was proposed from the experimental study and an equation to predict the lifetime of the composite under cyclic stress conditions was derived from the model. Hale [127] characterized the strength reduction of three GRP composite materials as a function of temperature and testing environment (sea water and crude oil condensate). In neither case was the microscopic damage mechanisms considered.

Haque and Rahman [128] investigated the damage development in woven ceramic matrix composites under tensile and cyclic loading at elevated temperatures. The tensile strength of SiC/SiNC woven composites was found to increase with increased temperatures up to 1000°C. Elevated temperature was found to have a remarkable effect on the fatigue strength. At 700°C, the fatigue strength was approximately 50 percent of the ultimate strength, while at 1000°C it was found to be less than 20 percent of the ultimate strength. They developed rate equations for modulus degradation and life prediction under fatigue loading at room and elevated temperatures which fitted well with the experimental results. In some cases, the success of the application itself depends on the ability of the composite to withstand environmental conditions. For example, cryogenic propellant tanks fabricated using composites need to be able to avoid leakage of the propellant through the micro cracks in the composite material. Peddiraju et al [129] simulated the leakage of gaseous hydrogen through the thickness of a damaged composite laminate and predicted the leakage rate at room and cryogenic temperatures.

Polymer matrix composites absorb moisture during service. This can lead to plasticization of the polymer matrix, alter the stress state and degrade the fiber/matrix

interface [130-132]. Due to this, a good understanding of the moisture absorption and desorption behavior is important for predicting long-term material and structural performance. Some good work has been put in to investigating the thermal conductivity and moisture diffusion behavior of polymer matrix woven composites. Dasgupta and Agarwal [133] studied the thermal conductivity of plain weave composites using a homogenization technique and were able to achieve very good agreement with the experimental results. Roy et al. [134] examined the effect of preexisting matrix-cracks on the moisture diffusion behavior of a 5-harness satin weave composite using a continuum damage mechanics approach based on the theory of irreversible thermodynamics. Li et al. [135] investigated the moisture diffusion behavior in hybrid woven composite laminates using a simple 1D diffusion model to simulate the effect of stacking sequence of woven plies on the diffusion behavior. Tang et al [136] studied the effect of tow architecture on the diffusion behavior in woven composites. This helps in identifying the dominant architectural factors that affect the diffusion behavior of a polymer matrix woven composite. Their analysis consisted of two steps – calculating the effective diffusivity of the fiber tows with matrix and then using these properties to model the tow with the corresponding tow architecture in the woven composite. The effective diffusivity of the tows was calculated using 3D finite element micromechanics [137]. The effect of irregular fiber distribution was taken into account using a finite element based ‘bi-zone’ model [138]. Simulations of moisture diffusion tests for a 3-ply woven hybrid composite were performed and found to be in close agreement with experimental results.

2.5.1 Effect of Oxidation

Oxidation at high temperature has been a concern for a long time. Of course, the definition of high temperature depends on the material system. Carbon fiber-reinforced silicon carbide composites (C–SiC) exhibit excellent mechanical properties at temperatures below 1650°C and have been designed and developed for high-temperature applications such as the high thrust-to-weight ratio turbine engines and reentry thermal protection for spacecraft. However, the mismatch in thermal expansion coefficients

between the carbon fiber and the SiC matrix induce matrix and seal coating microcracking during cooling from the processing temperature [139]. These cracks allow for oxygen to leak in and react with the carbon fibers at temperatures above 400 °C [140-142]. This oxidation in turn will degrade the mechanical properties of the composite. Luan et al [143] examined C-SiC composites being oxidized or corroded in various gas atmospheres and found that oxygen was the major factor degrading the composite under conditions with cyclic stresses. They proposed a model for the cyclic stress corrosion mechanism from the experimental results as well as an equation to predict the lifetime of the composite. Halbig et al [144] studied oxidation tests of C/SiC composites at elevated temperatures and developed a model that simulates the diffusion of oxygen into a matrix crack bridged by carbon fibers.

Carbon-carbon composites are designed for extremely high temperatures, but they must be protected from oxidation. Various researchers have studied the behavior of carbon-carbon and proposed schemes for oxidation protection. Ceramic coatings alone do not provide a comprehensive barrier against oxidation because of the mismatch between the coefficients of thermal expansion. Due to this mismatch, cracks form in the coatings. As an additional form of protection, particulates are added to the matrix [145]. These 'inhibitor' particulate materials are usually boron, boron carbide or silicon carbide. Ochoa and Elliott [146] studied oxidation under isothermal, cyclic thermal, and thermo-mechanical fatigue conditions for inhibited carbon-carbon composites. Mass loss and material property degradation assessment was undertaken with subsequent exploratory nondestructive testing utilizing dynamic mechanical analysis (DMA) and piezoelectric ultrasonic composite oscillator technique (PUCOT) techniques. Degradation in shear and axial moduli were measured as oxidation progressed. Lou et al. [147] examined the effect of additives on the mechanical properties of oxidation-resistant carbon/carbon composites (C/C). The additives used in their test included silicon carbide, silicon nitride, and metal borides. These additives resulted in large increases in flexural modulus and strength. Recently Mazany et al [148] filed a patent on oxidation inhibition of carbon-carbon composites. Their invention involves two steps: (a) contacting the carbon-

carbon composite with an oxidation inhibiting composition composed of phosphoric acid or an acid phosphate salt, at least one aluminum salt, and at least one additional metal salt and (b) heating the carbon-carbon composite at a temperature sufficient to form a deposit from the oxidation inhibiting composition within at least some of the penetrated pores of the carbon-carbon composite.

Schoeppner, Pochiraju and Tandon [7] developed a multidisciplinary approach aimed at predicting the performance of high-temperature polymer matrix composites (HTPMCs). HTPMCs are used in a variety of aerospace applications. Pochiraju et al have performed an extensive review of the state of the art in predicting thermo-oxidative degradation and performance of HTPMCs[9]. Unfortunately, there is still much more research required and all the underlying mechanisms for the predicting the behavior of these materials are yet to be determined. Characterizing the behavior of these materials is not trivial [149-152] and very time-consuming and in some cases, reliable methods to determine certain properties do not yet exist. Pochiraju et al also reviewed the effect of oxidation and aging on the fibers as well as composite behavior. Tandon et al [7] characterized the behavior of neat PMR-15 resin and developed a model to predict the thermo-oxidation of the material. Thermo-oxidative aging was simulated with a diffusion reaction model in which temperature, oxygen concentration and weight loss effects were considered. The model which was implemented using FEM considered diffusion, reaction and oxidation of the resin system. The model developed by Pochiraju et al [7-9] is used as the basis for the oxidation model developed in this work and is discussed in detail in Section 3. They also used the FEM to model the oxidation behavior in a Graphite/PMR-15 composite [9], where they assumed the fiber did not oxidize. The oxidation model developed by Pochiraju et al tends to be very computation-intensive and most of their analyses were performed at the fiber/matrix scale. Pochiraju et al [153] also used the oxidation model to predict the evolution of stresses and deformation in HTPMCs by accounting for thermo-oxidation induced shrinkage. The oxidation model and the non-linear elastic deformation analyses are coupled using information obtained by experimental observation of shrinkage in neat PMR-15 resin under aging in oxygen and argon.

Roy et al [154] developed a multi-scale model based on micromechanics and continuum damage mechanics to simulate the accelerated fiber-matrix debond growth in a unidirectional HTPMC undergoing oxidation. The model was used to predict the mechanical behavior of a laminate in a three-point bending test incorporating the damage caused due to oxidation. Wang and Chen [155] developed a computation micromechanics approach based on irreversible thermodynamics to obtain constitutive properties of HTPMCs while tracking thermo-oxidative reactions, microstructural damage and thermo-mechanical loading. A two-scale homogenization theory is also used to determine macroscopic behavior of these composites. They also stressed the need for many not yet available thermal, chemical, mechanical and interphase properties and microstructural parameters in order to accurately predict the behavior of HTPMCs.

2.6 Scope of Research

The primary objective of this research work is to develop a better understanding of the behavior of textile composites. This will help in optimal design of these materials because experimental testing and characterization of textile composites is a very time-consuming and expensive process. Moreover, the problem is more challenging when trying to determine the effect of the operating environment on the mechanical behavior of the textile composite.

The proposed research is described in four main sections. The first section talks about the development a robust finite element framework that can handle the multiscale/multiphysics analysis of structures with complex microstructure. In this work, all the analyses focus on the behavior of textile composites. Therefore, the framework will be developed keeping that in mind. The second section uses the framework to perform a multiscale analysis of a woven DCB specimen. The next section discusses the development, implementation and validation of a model to simulate the oxidation process in textile composites. This also includes the strategies developed to speed up the oxidation analysis. The last section describes the coupled multiphysics model that is used to predict damage progression in a textile composite that is under mechanical load as well as being oxidized.

2.6.1 Development of Multiscale/Multiphysics Finite Element Framework

There are many commercial and public domain software packages for finite element analysis. However, they are typically not designed for the particular challenges one will face when performing detailed 3D analysis of textile composite structures. Textile composites have multiple microstructural scales – the fiber/matrix scale, the lamina scale, and the laminate scale. This complex microstructure of textile composites makes it necessary to use multiscale analyses in order to obtain detailed information about their behavior. Moreover the proposed work also studies the behavior of textile composites under oxidizing environments. This requires a multiphysics analysis that couples damage progression analyses with oxidation simulations. These sorts of novel analysis methods

are not convenient to implement in commercial FEA packages due to the restrictive nature of these software.

A finite element analysis framework called ‘BETA’ will be developed, which is a successor to the existing in-house finite element code, "ALPHA". Alpha has been used for static linear and nonlinear thermo-mechanical analysis and transient diffusion analysis of textiles. Existing tools will form the foundation of the proposed finite element framework. Although the existing code was designed to be quite modular and extensible, experience has shown that the needs of those performing detailed analysis of textiles is quite severe. The new framework will have several enhancements over the existing in-house code in order to meet the needs of the proposed work. The goal is to design a robust framework that can be enhanced and extended in the years to come by future users and lives beyond the term of this research work. Towards this end, the software will be designed using an object oriented philosophy. This incorporates features such as inheritance, polymorphism, data abstraction and encapsulation. When designed properly, this kind of programming philosophy makes it a lot easier and convenient to maintain, manage, modify, extend and enhance a large software package.

The new framework will make use of the latest hardware improvements such as multi-processor machines which are very common now. The framework will also be portable so that it can be used on both the Windows as well as UNIX/LINUX environments. The developed framework will be used to analyze different configurations including textile composites subjected to a high temperature oxidizing environment. The framework will include tools for geometric description, including spatial variation of material properties, mesh development, finite element solver, and postprocessing. It will also provide better control of output for debugging algorithms and postprocessing of results. A more detailed description of the framework is given in Section 4.

2.6.2 Multiscale Analysis of Woven DCB Specimen

As mentioned in the previous section, textile composites have multiple levels of microstructure. This kind of microstructure can cause a complex load path and complex

three dimensional stress distributions in a laminate even for a simple uniaxial loading. A thorough understanding of why and where these stress concentration occur will give insight into how to better design these material. This will help in getting better performance and life from the material. Better modeling and analysis capability will allow the designer to predict the behavior of realistic composite structures and complement the experimental testing and characterization.

A typical engineering problem deals with a configuration that is at a length scale at least a few orders of magnitude larger than the size of the microstructure. Some examples include a structure made out of composite impregnated with carbon nanotubes or a stringer stiffened panel that is made of composite material (where the fibers in the tows are as small as a few microns thick). The problem becomes impractical to solve if the entire configuration is to be modeled at the same length scale as its complex microstructure.

In order to reduce the computational cost when analyzing such a system, different regions of the model are often modeled at different microstructural scales. The focal configuration investigated in this work is a double cantilever beam (DCB) specimen fabricated with woven fabric. A woven composite DCB specimen has several such microstructural scales. The laminate is described by multiple length scales as shown in Figure 2.9: fiber/matrix in tow, woven composite lamina, and

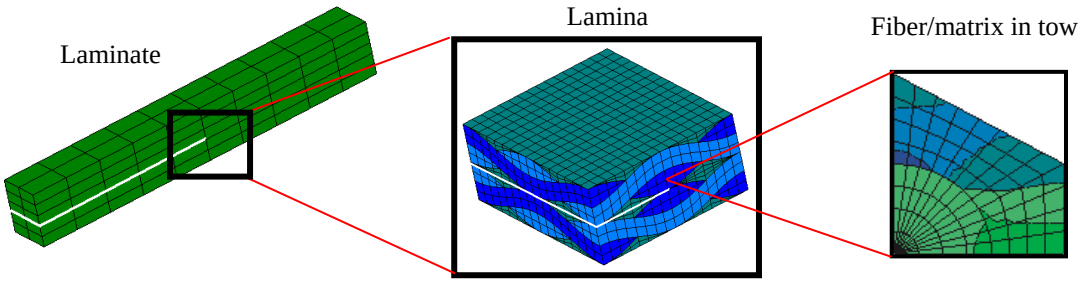

Figure 2.9: Different microstructural scales in a DCB specimen fabricated with woven composites

laminate. When conducting a detailed stress analysis of the DCB specimen, the region

around the crack tip would be modeled discretely at the lamina scale with the tow and matrix or maybe even at a smaller fiber/matrix scale. The region away from the crack tip can be modeled at a larger microstructural scale assuming that the homogenized properties simulate the load transfer to the crack tip region accurately. When there are multiple scales in a single problem, managing the information from each scale can become intractable. The information could include model attributes such as the mesh, material properties, load, and boundary conditions or analysis results like displacements and stresses. The book-keeping and transfer of this information between different scales in a finite element analysis (FEA) takes considerable effort on the part of the analyst. There are many factors that govern how quickly one can perform analysis of a structural configuration. When using finite elements, the steps typically consist of defining a solid model, converting the solid model into a finite element mesh, preparing non-geometric data input (such as material properties and boundary conditions), using a finite element solver to solve the equations and provide the solution in terms of displacements, stresses, etc., and most importantly interpret the results. Each of these steps can be quite time consuming in terms of computing power and human involvement. Certain hierarchical aspects involved in analyzing a problem can be exploited to reduce the analysis time. These hierarchical techniques can be used in the development, organization, and management of finite element models to solve a problem faster and makes it easier for the analyst to manage the models and its results. In an earlier work [156], these concepts were demonstrated by using a hierarchical model to conduct a two-dimensional global/local structural analysis of the side panel of an airplane fuselage. A more detailed discussion of the hierarchical strategy is provided in Section 5.

A hierarchical model of the DCB specimen is created using different models for different regions of the model. The region around the crack front is modeled discretely taking into account the tow architecture of the plain weave composite where as the other regions are modeled using homogenized properties. The models in the hierarchy are ‘joined’ together by implementing a boundary matching routine that specifies multipoint constraints in order to impose continuity at the interfaces. A detailed stress analysis of

the DCB specimen is conducted to study the effect of the complex microstructure on stress distribution and GI distribution. The effect of the microstructure on the stresses and GI as the crack advances is also investigated.

2.6.3 Simulation of Oxidation in Textile Composites

Composite structures are increasingly being used for high temperature applications in the aerospace industry. The extreme operating environments that these materials are subjected to can lead to chemical degradation including oxidation. It is important to understand the behavior of these materials under these conditions so that they can be designed better and provide increased performance. A focal problem that is investigated in this work is the effect of oxidation on the mechanical behavior of textile composites. This will involve a coupled damage progression analysis that accounts for the effect of oxidation on the engineering properties of the composite.

A precursor to the coupled damage progression analysis is the oxidation analysis of the composite which is quite complex because in reality the fiber and matrix both have their own response to high temperature oxidation and aging. In addition, when the two are combined to form the composite, the anisotropic oxidative response is even more complex to simulate because of the fiber-matrix microstructure. Micro-cracks and damage formed at the interface between the fiber and matrix affect the oxidative response of the composite. The task of simulating oxidation of textile composites requires a combination of various strategies. The underlying oxidation model is adopted from the work by Pochiraju, Schoeppner and Tandon[7-9] who have used their model to simulate the oxidation of neat PMR-15 resin with reasonable accuracy compared to experimental observations. The oxidation behavior is represented using a set of transient nonlinear governing equations based on the conservation of mass equation for diffusion. The oxidation model will be implemented using the finite element framework that is developed as part of this work. The finite element formulation imposes limitations on the element size and the time step size which make the simulation very computation intensive. New strategies need to be developed in order to expedite the oxidation analysis. Moreover, it is not practical to discretely model the fibers in the textile

composite. Strategies for determining effective oxidative properties need to be developed and validated. The overall goal is to develop an efficient analysis strategy that can simulate the oxidation behavior in textile composites in a reasonable time frame.

2.6.4 Prediction of Damage Progression in Textile Composites under Oxidation

The overall goal of this work is to use a finite element framework to analyze damage progression in textile composites due to the combined effects of oxidation under high temperature and mechanical loads. Determining the effect of high temperature oxidation and aging on the mechanical behavior of composites is a very complex and challenging problem. There are a number of studies in the literature investigating the different time-dependent physical, chemical and mechanical damage mechanisms [8,157-159] as well as experimental characterization studies[160-165]. But there is still much more work that needs to be done in order to reliably predict the composite behavior using mechanistic approaches. The planned damage progression analysis involves performing an oxidation analysis that simulates the diffusion of oxygen into the composite and tracks how much the material has oxidized. The simulation of oxidation in the textile composite is one of the goals of this work and is discussed in the previous section.

The proposed analysis is a one-way coupled problem where the oxidation is assumed to affect the mechanical behavior of the material and not vice versa. A constitutive theory will be used to determine the amount of damage in terms of strength or stiffness degradation based on the oxidation state of the material in the composite. Figure 2.10 shows a schematic that illustrates the coupled analysis. Both the oxidation analysis as well as the damage progression analysis needs to account for the multiple microstructural scales in the composite. The damage will not affect the oxidation properties in the current implementation. The progressive damage analysis will track the damage state in the composite and calculate the stress state in the composite with respect to time as the oxidation progresses.

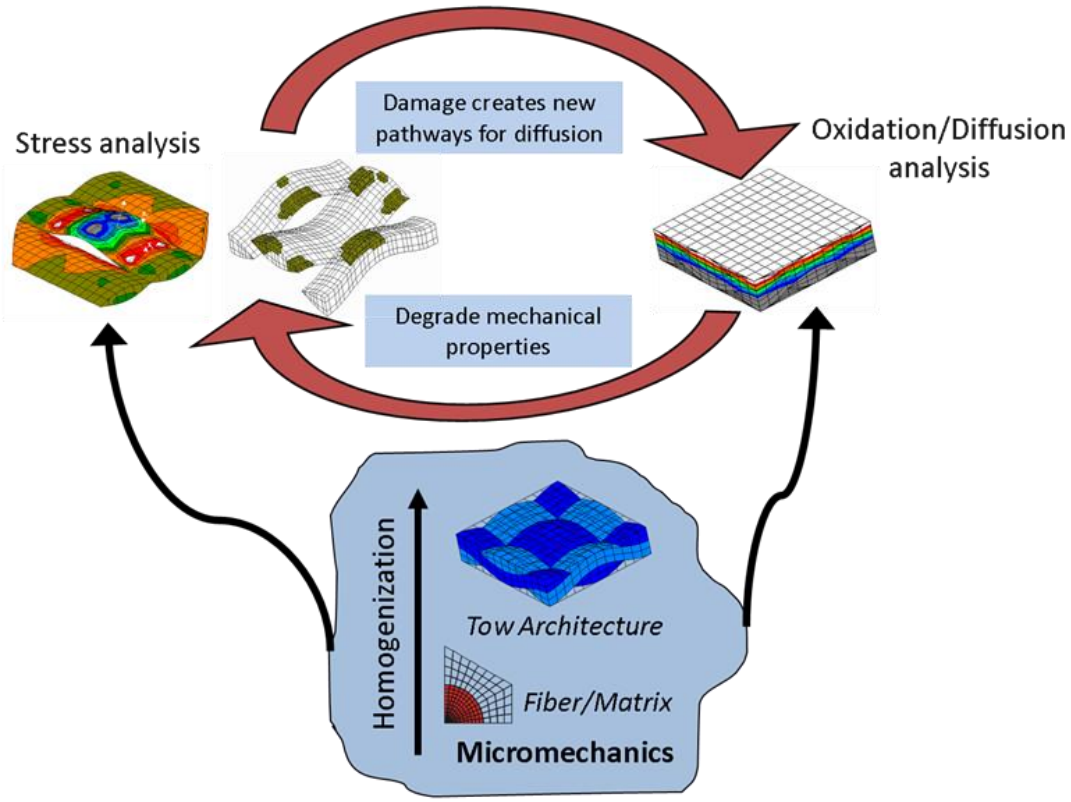

Figure 2.10: Schematic illustrating coupled oxidation/thermo-mechanical

The coupled analysis model will be used to investigate a focal problem. The focal problem chosen for this work is a Graphite/PMR-15 plain weave composite laminate that is loaded uniaxially to a particular strain level and then the top and bottom surfaces are exposed to oxygen for 200 hours. The laminate in the simulation is assumed to be at 288 C. A parametric study will also be performed to study the effect of the number of plies in the laminate on its mechanical behavior. This analysis model will lay the groundwork for fully coupled simulations of the behavior of textile composites under combined mechanical loading and oxidation.

In summary, this part of the research will focus on the following:

1) Develop a coupled analysis model using the finite element framework that will couple the oxidation analysis and the damage progression analysis.

2) Develop a constitutive model to simulate the effect of oxidation on the mechanical properties of the tow and matrix.

3) Use the coupled analysis model to analyze a focal problem

a) Simulate mechanical behavior of a Graphite/PMR-15 plain weave laminate under oxidation.

b) Perform a parametric study on the effect of the number of plies on the mechanical behavior of the configuration.

2.7 Summary

This section gave a brief overview of the finite element method and the software packages and other options available to the finite element method user community. For the analyses described in this work, a user-developed finite element framework would provide the flexibility and freedom to implement the required models. Section 4 describes the framework that was developed to achieve this goal. This section also described the challenges involved in the multi-scale analysis of textile composites including the evolution of models from simple 1-D models to full 3-D models for describing textile composites. A review of global/local analyses was provided as well as a small overview of progressive failure analyses as it pertains to this work. Finally, as part of the literature review, a brief review of the challenges and accomplishments involved in predicting the effect of environmental conditions on the behavior of composites was given. The section concludes by giving the scope of the research in this work. The overall goal of this work is to develop a multiscale/multiphysics analysis framework that can be used to study the mechanical behavior of textile composites under oxidation.

3. THEORY AND EQUATIONS

3.1 Introduction

In this work, the behavior of textile composites to several different phenomena was analyzed. In addition to linear elastic analysis of these materials, damage initiation and progression simulations were also conducted. The diffusion and oxidation behavior of textile composites were also analyzed. The work also includes a coupled mechanical and oxidation analysis that simulates the effect of oxidation on the damage progression. All the analyses performed had some common characteristics which made it convenient to express these otherwise very different analyses in a common analysis framework. This section will start by describing the common aspects of the different analyses and how it can be viewed simply as different instantiation of a common analysis procedure. This will include the generic types of equations as well as strategies to homogenize the analysis region. The theory, governing equations and specific characteristics of the different analyses will be described next. This will include detailed descriptions and the finite element formulations of the mechanical, diffusion, oxidation and the coupled analyses.

3.2 Common Analysis Procedure

One of the common aspects of all the analyses performed in this work is that they are all defined by boundary value problems based on partial differential equations. In this particular work, the finite element method is used to solve the boundary value problems. In this section, the common analysis procedure is described without going into the specific details of the equations involved. The boundary value problems have an analysis domain, which in this work, typically relates to a textile composite structure or a region within the structure. The behavior of the domain as described by the primary variables of the problem is governed by an equation or set of equations. In all these analyses performed in this work, there are a few common aspects related to the underlying boundary value problem. For the sake of convenience, the common aspects are described

using a generic name (where applicable) or its analogous version in the field of solid mechanics.

The following four sets of equations are seen in each of the underlying boundary value problems.

1. Conservation laws

2. Kinematics such as strain-displacement relations or simple gradients as in the case of heat transfer or diffusion.

3. Constitutive relations

4. Boundary conditions (and initial conditions for transient problems)

The specific sets of equations for the different analyses will be described in later on in this section. A very brief overview of the finite element method is given here to show the common steps involved in the procedure regardless the actual type of analysis. For a more detailed description of the finite element method, refer to [166]. To solve the boundary value problem using the finite element method, the first step is to obtain a weak form of the governing equations. Typically, the equation from the conservation law is multiplied by an arbitrary virtual displacement (or the analogue primary variable) and integrated over the domain. The resulting equation is then re-written after using integration by parts to obtain the weak form for the boundary value problem.

The next step is to discretize the weak form statement. This step yields the finite element formulae for the problem. The solution field is assumed over an element based on nodal primary variables (or unknowns). This approximation of the solution field is then used in the weak form statement to derive a set of equations for a finite element. Derivation of the finite element formulation for the different analyses is described later on in this section.

The analysis domain is then discretized into a finite element mesh using elements and nodes. The set of equations obtained from the finite element mesh along with the boundary conditions can then be used to solve for the unknowns. The accuracy of the

solution depends on a number of factors including the mesh chosen for the analysis domain and its refinement and this aspect of the analysis is beyond the scope of this work. The solution can be post-processed to obtain other information (such as the strain and stress for a mechanical analysis).

3.2.1 Homogenization of Periodic Microstructures

When analyzing configurations or materials with periodic microstructure, in many cases it is possible to considerably reduce the analysis effort by using homogenized properties for the material rather that discretely modeling the microstructure. In some cases, it is just not practical to discretely model the microstructure. This is especially true when modeling composite structures. Even with the current state of the art in computing power and FE modeling tools, it is not practical to discretely model the fibers and matrix in the composite structure. In textile composites, there are additional microstructural scales which make the microstructure even more complex. For example, the plain weave textile composite has undulating tows running across each other. It is possible to determine a periodic pattern to the microstructure for most of the textile architectures. While most structures in reality are not truly periodic, the structures or the microstructure in the configurations are assumed to be periodic. The deviations from periodicity seen in the real structure are usually not significant enough to affect the overall response of the structure.

For periodic structures, homogenized properties of the structure can be obtained by analyzing a representative volume element (RVE). The response of the RVE is volume averaged to obtain the effective properties. In general, this strategy to obtain effective properties can be used for different types of analyses including mechanics and diffusion and oxidation. This would involve determining the periodic boundary conditions needed to be applied on the RVE. The particular details regarding the periodic boundary conditions for mechanics and diffusion will be discussed later in this section. In this section, aspects regarding homogenization that are common to the different analyses are discussed.

When the RVE chosen is a full unit cell of the periodic microstructure, then boundary conditions can be obtained by exploiting periodicity. In some cases, the full unit cell has certain symmetries that can be exploited to reduce the RVE to a fraction of the full unit cell. This is especially true for textile composites where the number of degrees of freedom for a full unit cell model can be quite large. Significant savings can be made especially for non-linear analyses where numerous iterations are made. The concept of *Equivalent Coordinate Systems* is useful in identifying the symmetries and constraint conditions [90]. Coordinate systems are equivalent if the geometry, spatial distribution of material, loading, and the various fields that describe the response (e.g., displacement, strains etc.) are identical in the two systems [90]. Some symmetries are destroyed by combined loading though. Periodicity and symmetry conditions were exploited to derive boundary conditions in this work.

The following sections describe the theory, governing equations and the finite element formulation for solid mechanics, diffusion, oxidation and the coupled mechanical-oxidation analysis. It should be noted that each section follows the same general procedure outline in this section. Recognizing these common features also help in implementing a common analysis framework that facilitates the investigation of the behavior of these materials.

3.3 Solid Mechanics

Mechanical behavior of textile composites was analyzed in this work. In addition to linear elastic behavior, nonlinear behavior introduced due to damage initiation and progression in the material was also studied. In this section, the governing equations for the analyses are derived as well as the related finite element formulation.

As described in the previous section, the common analysis procedure requires the four sets of equations. For all the solid mechanics analyses performed in this work, the equations defining the conservation laws, the kinematics and the boundary conditions are the same. But the constitutive relations are quite different for the linear elastic analyses as opposed to the damage progression analysis. All the governing equations and

finite element formulation for the linear analysis are described first followed by that for the damage progression analysis.

For the sake of clarity, index notation will be used to define the equations. A repeated index is a dummy index and denotes summation and a non-repeated index denotes a free index. A comma denotes a partial derivative with respect to the coordinate x. For example, let ϕ, a_i and σ_{ij} be a scalar, vector and a second-order tensor respectively, then:

$$\phi_{,j} = \frac{\partial \phi}{\partial x_j},\ a_{i,j} = \frac{\partial a_i}{\partial x_j} \text{ and } \sigma_{ij,j} = \frac{\partial \sigma_{ij}}{\partial x_j} \tag{3.1}$$

3.3.1 Conservation Laws

For a general 3D body with a volume V bounded by the surface S, the conservation of linear momentum yields the following equations of equilibrium

$$\sigma_{ji,j} + f_i = 0 \tag{3.2}$$

where σ_{ij} is the stress tensor and f_i are the body forces.

In the absence of body moments, the conservation of angular momentum also yields the symmetry of the stress tensor

$$\sigma_{ij} = \sigma_{ji} \tag{3.3}$$

3.3.2 Kinematics (Strain-Displacement Relations)

In this work, infinitesimal strains were used and the strain-displacement relation is given by

$$\varepsilon_{ij} = \frac{1}{2}\ u_{i,j} + u_{j,i} \tag{3.4}$$

where u_i are the displacements and ε_{ij} is the second order strain tensor.

3.3.3 Constitutive Relations

For a linear elastic material, the stress-strain relation is given by Hooke's Law

$$\begin{aligned} \sigma_{ij} &= C_{ijkl}(\varepsilon_{ij} - \varepsilon_{ij}^t) \\ or\ \varepsilon_{ij} &= S_{ijkl}\sigma_{ij} + \varepsilon_{ij}^t \end{aligned} \tag{3.5}$$

where C is the fourth order stiffness tensor and is the inverse of the fourth order compliance tensor S, ε_{ij} is the overall strain tensor, and ε_{ij}^t is the thermal strain tensor. For convenience, the Voigt notation is used to express the components of the 2nd order stress and strain tensors as:

$$\varepsilon_i = \begin{Bmatrix} \varepsilon_{11} \\ \varepsilon_{22} \\ \varepsilon_{33} \\ \varepsilon_{12} \\ \varepsilon_{23} \\ \varepsilon_{13} \end{Bmatrix}, \sigma_i = \begin{Bmatrix} \sigma_{11} \\ \sigma_{22} \\ \sigma_{33} \\ \sigma_{12} \\ \sigma_{23} \\ \sigma_{13} \end{Bmatrix} \tag{3.6}$$

Thus the stress-strain relation can be written as

$$\begin{aligned} \sigma_i &= C_{ij}(\varepsilon_i - \varepsilon_i^t) \\ or\ \varepsilon_i &= S_{ij}\sigma_i + \varepsilon_i^t \end{aligned} \tag{3.7}$$

where C_{ij} and S_{ij} are the stiffness and compliance matrices respectively and ε_i^t is the thermal strain in contracted Voigt notation. For an orthotropic material, the matrices are defined by

$$S_{ij} = \begin{bmatrix} \frac{1}{E_{11}} & \frac{-\upsilon_{12}}{E_{11}} & \frac{-\upsilon_{13}}{E_{11}} & 0 & 0 & 0 \\ \frac{-\upsilon_{21}}{E_{22}} & \frac{1}{E_{22}} & \frac{-\upsilon_{23}}{E_{22}} & 0 & 0 & 0 \\ \frac{-\upsilon_{31}}{E_{33}} & \frac{-\upsilon_{32}}{E_{33}} & \frac{1}{E_{33}} & 0 & 0 & 0 \\ 0 & 0 & 0 & \frac{1}{G_{12}} & 0 & 0 \\ 0 & 0 & 0 & 0 & \frac{1}{G_{23}} & 0 \\ 0 & 0 & 0 & 0 & 0 & \frac{1}{G_{13}} \end{bmatrix} \tag{3.8}$$

$$C_{ij} = S_{ij}^{-1} \tag{3.9}$$

3.3.4 Boundary Conditions

The traction boundary conditions are given by

$$T_i = \sigma_{ij} n_j \quad \text{on S} \tag{3.10}$$

And the displacement boundary conditions are given by

$$u_i = \hat{u} \quad \text{on } \hat{S} \tag{3.11}$$

Where $\hat{u}$ is the specified displacement on the boundary $\hat{S}$.

3.3.5 Weak Form

The equations of equilibrium are multiplied by an arbitrary virtual displacement and integrated over the volume to obtain the total virtual work for the body, which is set to zero

$$\int_V \sigma_{ji,j} + f_i \ \ \delta u_i dV = 0 \tag{3.12}$$

Or

$$\int_V \sigma_{ji,j} \delta u_i dV + \int_V f_i \delta u_i dV = 0 \tag{3.13}$$

The first term in eq(3.13) can be written as

$$\int_V \sigma_{ji,j} \delta u_i dV = \int_V \sigma_{ji} \delta u_{i\ ,j}\, dV - \int_V \sigma_{ji} \delta u_{i,j} dV \tag{3.14}$$

But,

$$\int_V \sigma_{ji} \delta u_{i\ ,j}\, dV = \int_S \sigma_{ji} \delta u_i n_j dS \tag{3.15}$$

Therefore eq(3.13) can be re-written as

$$\int_V \sigma_{ji} \delta u_{i,j} dV = \int_V f_i \delta u_i dV + \int_S \sigma_{ji} \delta u_i n_j dS \tag{3.16}$$

Using eq(3.10)

$$\int_V \sigma_{ji} \delta u_{i,j} dV = \int_V f_i \delta u_i dV + \int_S T_i \delta u_i dS \tag{3.17}$$

Using eq(3.3) and eq(3.4), the following relation can be obtained,

$$\sigma_{ji} \delta u_{i,j} = \sigma_{ji} \delta \varepsilon_{ij} \tag{3.18}$$

By inserting eq(3.18) into eq(3.17), the principle of virtual work statement is obtained as

$$\int_V \sigma_{ji}\delta\varepsilon_{ij}dV = \int_V f_i\delta u_i dV + \int_S T_i\delta u_i dS \tag{3.19}$$

That is, the statement of virtual work principle is

$$\delta W = \delta W^{\text{int}} + \delta W^{ext} = 0 \tag{3.20}$$

Where $\int_V \sigma_{ji}\delta\varepsilon_{ij}dV$ is the internal virtual work and

$-\int_V f_i\delta u_i dV - \int_S T_i\delta u_i dS$ is the external virtual work.

To avoid dealing with tensors and convenience in computations, eq(3.19) can be re-written using the Voigt notation for stresses and strains,

$$\int_V \sigma_k\delta\varepsilon_k dV = \int_V f_i\delta u_i dV + \int_S T_i\delta u_i dS,\ i = 1..3,\ k = 1..6 \tag{3.21}$$

3.3.6 Discretization of Weak Form

The displacement field over an element is assumed in terms of the unknown nodal displacements u_i^α. The subscript *i* denotes the coordinate directions and the superscript $\alpha = 1..n$ indicates the node number and *n* is the number of nodes in the element.

The displacement field is expressed as follows

$$u_i = N^\alpha u_i^\alpha \tag{3.22}$$

where N^α are the interpolation functions.

The nodal displacements in the element are collected in a vector denoted by q_β. In this work, the vector takes the following form for a 3D analysis:

$$q_\beta = u_1^1, u_2^1, u_3^1, u_1^2, u_2^2, u_3^2, ..., u_1^\alpha, u_2^\alpha, u_3^\alpha, ..., u_1^n, u_2^n, u_3^n \tag{3.23}$$

For the 3D analyses in this work, 20 node hexahedral brick elements were used. Each node has three degrees of freedom, which are displacements u_1, u_2 and u_3 along three coordinate directions.

The terms δu_i and $\delta \varepsilon_k$ in eq(3.21) can be written in terms of q_β,

$$\delta u_i = \frac{\partial u_i}{\partial q_\beta} \delta q_\beta \tag{3.24}$$

$$\delta \varepsilon_k = \frac{\partial \varepsilon_k}{\partial q_\beta} \delta q_\beta \tag{3.25}$$

Substituting eq(3.24) and eq(3.25) in eq(3.21) gives

$$\int_V \sigma_k \frac{\partial \varepsilon_k}{\partial q_\beta} \delta q_\beta dV = \int_V f_i \frac{\partial u_i}{\partial q_\beta} \delta q_\beta dV + \int_S T_i \frac{\partial u_i}{\partial q_\beta} \delta q_\beta dS, \; i = 1..3, \; k = 1..6, \beta = 1..3n \tag{3.26}$$

Since eq(3.26) hold for any arbitrary nonzero selection of δq_β,

$$\int_V \sigma_k \frac{\partial \varepsilon_k}{\partial q_\beta} dV = \int_V f_i \frac{\partial u_i}{\partial q_\beta} dV + \int_S T_i \frac{\partial u_i}{\partial q_\beta} dS \tag{3.27}$$

Using eq(3.7) in eq(3.27) gives

$$\int_V C_{kl} (\varepsilon_l - \varepsilon_l^t) \frac{\partial \varepsilon_k}{\partial q_\beta} dV = \int_V f_i \frac{\partial u_i}{\partial q_\beta} dV + \int_S T_i \frac{\partial u_i}{\partial q_\beta} dS \tag{3.28}$$

Eq(3.28) can be re-written as

$$\int_V C_{kl}\varepsilon_l \frac{\partial \varepsilon_k}{\partial q_\beta} dV = \int_V f_i \frac{\partial u_i}{\partial q_\beta} dV + \int_S T_i \frac{\partial u_i}{\partial q_\beta} dS + \int_V C_{kl}\varepsilon_l^t \frac{\partial \varepsilon_k}{\partial q_\beta} dV \qquad (3.29)$$

Replacing ε_k in terms of the unknown displacements q_β gives

$$\int_V C_{kl} \frac{\partial \varepsilon_l}{\partial q_\lambda} q_\lambda \frac{\partial \varepsilon_k}{\partial q_\beta} dV = \int_V f_i \frac{\partial u_i}{\partial q_\beta} dV + \int_S T_i \frac{\partial u_i}{\partial q_\beta} dS + \int_V C_{ij}\varepsilon_k^t \frac{\partial \varepsilon_k}{\partial q_\beta} dV \qquad (3.30)$$

The various terms in eq(3.30) are expressed in matrix form to give a sense of the repeating patterns in the operations involved,

$$\frac{\partial \varepsilon_k}{\partial q_\beta} = B = \left[\begin{array}{ccc|ccc|c|ccc} \frac{\partial N_1}{\partial x_1} & 0 & 0 & \frac{\partial N_2}{\partial x_1} & 0 & 0 & & \frac{\partial N_n}{\partial x_1} & 0 & 0 \\ 0 & \frac{\partial N_1}{\partial x_2} & 0 & 0 & \frac{\partial N_2}{\partial x_2} & 0 & & 0 & \frac{\partial N_n}{\partial x_2} & 0 \\ 0 & 0 & \frac{\partial N_1}{\partial x_3} & 0 & 0 & \frac{\partial N_2}{\partial x_3} & & 0 & 0 & \frac{\partial N_n}{\partial x_3} \\ \frac{\partial N_1}{\partial x_2} & \frac{\partial N_1}{\partial x_1} & 0 & \frac{\partial N_2}{\partial x_2} & \frac{\partial N_2}{\partial x_1} & 0 & ..... & \frac{\partial N_n}{\partial x_2} & \frac{\partial N_n}{\partial x_1} & 0 \\ 0 & \frac{\partial N_1}{\partial x_3} & \frac{\partial N_1}{\partial x_2} & 0 & \frac{\partial N_2}{\partial x_3} & \frac{\partial N_2}{\partial x_2} & & 0 & \frac{\partial N_n}{\partial x_3} & \frac{\partial N_n}{\partial x_2} \\ \frac{\partial N_1}{\partial x_3} & 0 & \frac{\partial N_1}{\partial x_1} & \frac{\partial N_2}{\partial x_3} & 0 & \frac{\partial N_2}{\partial x_1} & & \frac{\partial N_n}{\partial x_3} & 0 & \frac{\partial N_n}{\partial x_1} \end{array}\right] \qquad (3.31)$$

$$\frac{\partial u_i}{\partial q_\beta} = N = \left[\begin{array}{ccc|ccc|c|ccc} N_1 & 0 & 0 & N_2 & 0 & 0 & & N_n & 0 & 0 \\ 0 & N_1 & 0 & 0 & N_2 & 0 & ..... & 0 & N_n & 0 \\ 0 & 0 & N_1 & 0 & 0 & N_2 & & 0 & 0 & N_n \end{array}\right] \tag{3.32}$$

Therefore, the finite element equations in eq(3.30) can be written as

$$\left[K^e\right] q = F^e \tag{3.33}$$

where the element stiffness matrix is

$$\left[K^e\right] = \int_V B^T C B \, dV \tag{3.34}$$

and the element load vector is

$$F^e = \int_V N^T f \, dV + \int_S N^T T \, dS + \int_V B^T C \varepsilon_k^t \, dV \tag{3.35}$$

In the analyses performed in this work, the thermal strains are neglected and therefore eq(3.35) reduces to

$$F^e = \int_V N^T f \, dV + \int_S N^T T \, dS \tag{3.36}$$

Assembling the element stiffness matrices and the load vector will yield the global set of equations

$$K q^G = F \tag{3.37}$$

where K is the global stiffness matrix, q^G is the global displacement vector and F is the global load vector.

3.3.7 Boundary Conditions for Periodic Microstructures

As mentioned in the section 3.2.1, periodic configurations can be analyzed by using just a representative volume element (RVE) or unit cell. They can also be used to obtain effective properties for the periodic configuration or microstructure. The unit cell is a region within the microstructure which can be used to generate the entire microstructure by just duplication and translation of the unit cell. Once the unit cell is chosen for the periodic microstructure, the certain characteristics can be determined based on the fact that each of the unit cells will behave in the same manner. For elasticity, the periodic conditions state that the displacement of one unit cell differ from the other unit cells only by a constant offset, which depends on the volume averaged displacement gradients [90-91]. Further the strains and stresses are identical in all of the unit cells. This can be expressed as

$$u_i\ \ x_\alpha + d_\alpha\ \ = u_i\ \ x_\alpha\ \ + \left\langle \frac{\partial u_i}{\partial x_\beta} \right\rangle d_\beta \tag{3.38}$$

$$\varepsilon_{ij}\ \ x_\alpha + d_\alpha\ \ = \varepsilon_{ij}\ \ x_\alpha \tag{3.39}$$

$$\sigma_{ij}\ \ x_\alpha + d_\alpha\ \ = \sigma_{ij}\ \ x_\alpha \tag{3.40}$$

where d_α is a vector of periodicity [90-91]. The vector of periodicity is a vector from a point in one unit cell to and equivalent point and an adjacent unit cell.

As mentioned earlier, additional savings can be obtained by exploiting symmetries within the unit cell [90]. The periodic boundary conditions are imposed by using multi-point constraints in the finite element analysis.

3.3.8 Damage Initiation and Progression

The damage progression analysis performed in this work is based on a continuum damage strategy. This strategy degrades the strength or stiffness of a material point in the finite element mesh based on the failure criteria. The damage analysis differs with

respect to linear elastic analysis lies in how the constitutive relations evolve as the load on the configuration changes. This section will describe the algorithm for the damage progression analysis used in this work followed by the failure criteria and the property degradation scheme used.

All the analyses performed in this work assume that the configuration is loaded with an increasing strain load. This could also be easily changed to be loaded with a specified displacement without any changes to the underlying algorithm. Figure 3.1 shows the flowchart for the algorithm used in this work. The configuration is assumed to behave linearly until damage is initiated. The failure criterion can be used to determine the load at which damage initiates. This is done by applying an arbitrary load on the model and calculating the expressions in the failure criterion. Since the model is initially linear elastic until the first instance of damage, it is possible to calculate the initial failure load by scaling the load to the point where failure is just triggered. The configuration is then loaded with a load that is a small fraction larger than the load at which damage initiated. This is done to ensure that round-off errors during the numerical calculations do not affect the simulation. This ensures that the load is increased to a value that

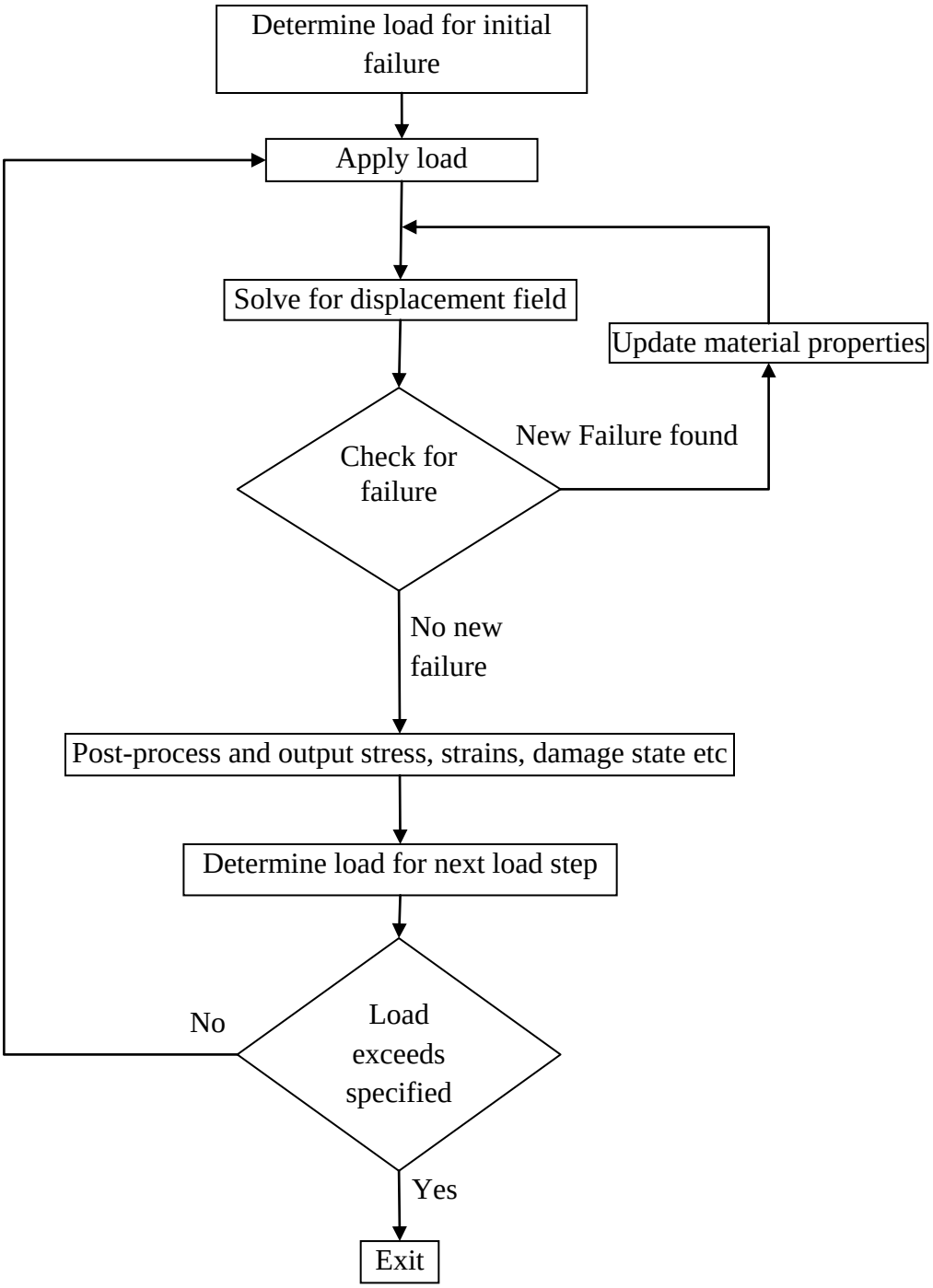

Figure 3.1: Flowchart for damage progression analysis

definitely causes new damage to occur. This point in the algorithm can be considered the beginning of a new load step. The displacement field corresponding to this load is solved

for, by assuming that no damage has initiated yet. The displacement field is used to apply the failure criterion at all the Gauss quadrature (or integration) points. For all the locations that damage is found, the mechanical properties at that integration point are degraded based on the property degradation scheme. The model is solved for the new displacement field based on the new material properties at each integration point. The model is checked again for damage and this procedure is repeated till it does not find any new damage. The next step before moving on to the next load step is determining the load for the next load step. Since we have converged on to a damage state for this current load step, the configuration can be likened to a new linear elastic material till the load is increased and new damage is found. Thus, just as the load for initial failure was determined, the load value for the next occurrence of new damage is determined using the failure criteria. In this manner, the load is increased and the simulation proceeds through the load steps until a specified maximum strain load is reached. Throughout this process, the damage state is recorded and new damage is tracked as the load on the configuration is increased. Other post-process data such as the volume averaged stresses and strains are also recorded. Figure 3.2 gives a schematic of what the stress-strain response would look like as the simulation progresses. The following sections describe the failure criteria and the property degradation scheme that were used in this work.

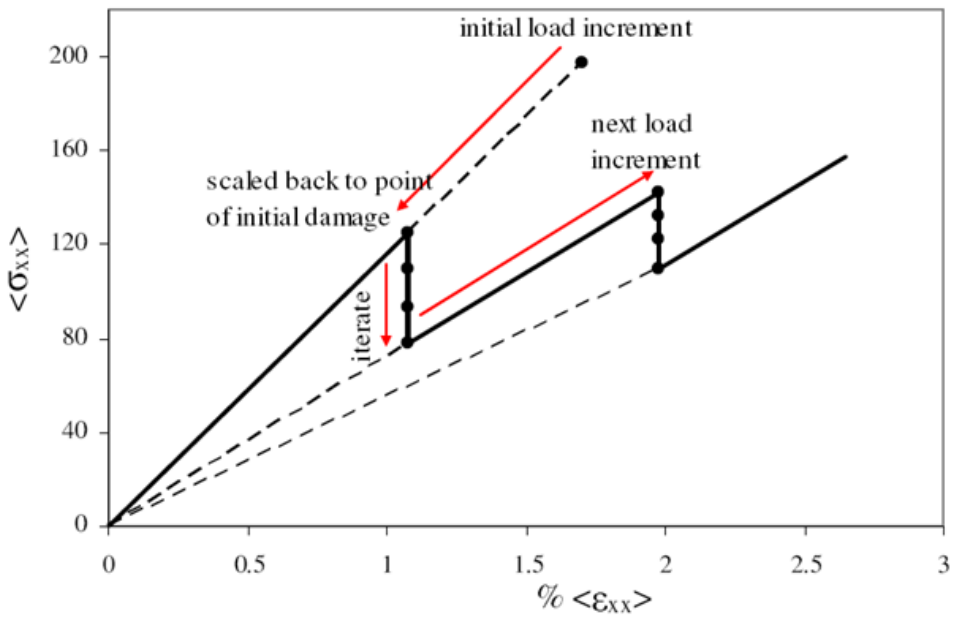

Figure 3.2: Schematic of stress-strain response

3.3.8.1 Failure criteria

There are various failure criteria such as the maximum strain criterion and the maximum strain criterion. Any of these criteria or a combination of these criteria can be use in the damage progression analysis. For the analyses in this research work, the maximum stress failure criteria are used. This means that failure has occurred when any of the stress components in the material coordinates has exceeded its corresponding strength, i.e. when $\sigma_{ij}/S_{ij} > 1$ where σ_{ij} is the stress component in the material coordinates and S_{ij} is the corresponding strength for σ_{ij}. Section 9 gives a detailed description of the failure criteria that are utilized to simulate the microscopic damage progression in this work.

3.3.8.2. Property degradation scheme

Typical property degradations models degrade the engineering properties whenever failure is detected. Some degradation models look at the properties (such as stress, strain) at the centre of the element. In this work, the failure criteria and property

degradation scheme is applied on each integration point of all the elements in the model. The stresses and strains at any material point in the material coordinate system are related by Hooke's law given by eq(3.7). The compliance matrix for an orthotropic material is given by eq(3.8)

Let E_{ij}, G_{ij} and υ_{ij} be the original extensional moduli, shear moduli and Poisson's ratio respectively and $\overline{E}_{ij}$, $\overline{G}_{ij}$ and $\overline{\upsilon}_{ij}$ be the degraded extensional moduli, shear moduli and Poisson's ratio respectively. Say, $a_i, (i = 1..9)$ are the degradation parameters, which specify the amount of degradation. Then a typical property degradation scheme will look like:

$$\begin{aligned} \overline{E_{11}} &= E_{11}/a_1, \quad \overline{E_{22}} = E_{22}/a_2, \quad \overline{E_{33}} = E_{33}/a_3 \\ \overline{G_{12}} &= G_{12}/a_4, \quad \overline{G_{23}} = G_{23}/a_5, \quad \overline{G_{13}} = G_{33}/a_6 \\ \overline{\upsilon_{12}} &= \upsilon_{12}/a_7, \quad \overline{\upsilon_{23}} = \upsilon_{23}/a_8, \quad \overline{\upsilon_{13}} = \upsilon_{33}/a_9 \end{aligned} \tag{3.41}$$

For example, if a_1=8, that implies that the E_{11} modulus is decreased by a factor of 8 from its current value if the material point fails. Note that in this general framework, the diagonal as well as non-diagonal entries of the compliance matrix can be affected independently. The specific details of property degradation scheme used in this work including the degradation factors used for the different materials will be given in Section 9.

3.4 Diffusion

This section describes the governing equations and the finite element formulation for simulating the diffusion behavior in materials. The diffusion behavior through heterogeneous materials was analyzed in this work. This section will follow the same format as the section on solid mechanics and starts by listing the equations for the common analysis procedure. This is followed by the derivation of the weak form and its discretization to obtain the finite element formulation.

3.4.1. Conservation Laws

The conservation of mass law for diffusion yields the following equation

$$\frac{\partial C}{\partial t} + \frac{\partial J_i}{\partial x_i} = 0 \tag{3.42}$$

where C is the concentration of diffusing material and J_i is the diffusion flux.

The differential equation described in Eq(3.42) holds for a material point. When the material being analyzed is homogenous, the concentration field is continuous throughout the domain and can be solved without any modifications. When the governing equation is applied to a configuration that has inhomogeneous regions with dissimilar solids, the concentration is generally not continuous across the interface between the different solids. This issue of discontinuous concentrations is addressed in Ref.[137], where a thermodynamic potential is introduced. The thermodynamic potential is considered to be what drives the flow of a diffusing material through another material. This potential is continuous across the material interface and the concentration is then defined as a function of the thermodynamic potential. When this function is assumed to be linear with C=0 when the potential=0, the function is of the form

$$C = a\bar{C} \tag{3.43}$$

where $\bar{C}$ is the thermodynamic potential and a is a material property. $\bar{C}$ is assumed to have a range from 0 to 1, which means that the concentration is maximum when the potential has a value of 1. That determines a to be the saturation mass concentration of

the diffusing material in the solid, denoted by C^{∞}. Therefore, the thermodynamic potential is the concentration in the material normalized by the saturation concentration of the solid, hereafter referred to as the normalized concentration,

$$\bar{C} = \frac{C}{C^{\infty}} \tag{3.44}$$

The governing equation can now be rewritten as

$$C^{\infty} \frac{\partial \bar{C}}{\partial t} + \frac{\partial}{\partial x_i} J_i = 0 \tag{3.45}$$

3.4.2. Concentration Gradients

Unlike the strain-displacement relationship in solid mechanics, the diffusion analysis uses simple gradients of the concentration, $\frac{\partial C}{\partial x_i}$

3.4.3 Constitutive Relations

The relationship between flux and the concentration gradient is given by Fick's first law,

$$J_i = -D_{ij} \frac{\partial C}{\partial x_j} \tag{3.46}$$

where D_{ij} is the 2nd order diffusivity tensor. The Latin subscripts *i* and *j* denote the coordinate direction and range from 1 to 3 for a three dimensional formulation.

When eq(3.46) is re-written in terms of the normalized concentration,

$$J_i = -C^{\infty} D_{ij} \frac{\partial \bar{C}}{\partial x_j} \tag{3.47}$$

3.4.4 Boundary Conditions

The flux boundary conditions are given by

$$\hat{q} = -n_i J_i \quad \text{on S} \tag{3.48}$$

And the normalized concentration boundary conditions are given by

$$\bar{C} = \bar{C} \text{ on } \hat{S} \tag{3.49}$$

where $\bar{C}$ is the specified displacement on the boundary $\hat{S}$.

3.4.5 Weak Form

The equation of conservation mass is multiplied by a variation of the normalized concentration and integrated over the volume to obtain the weighted integral form,

$$\int_V \delta\bar{C}\left[C^{\infty} \frac{\partial \bar{C}}{\partial t} + \frac{\partial}{\partial x_i} J_i \right] dV = 0 \tag{3.50}$$

where $\delta\bar{C}$ is an arbitrary variation of the normalized concentration.

Integration by parts gives the weak from,

$$\int_V \left[\delta\bar{C} C^{\infty} \frac{\partial \bar{C}}{\partial t} - \frac{\partial \delta\bar{C}}{\partial x_i} J_i \right] dV + \int_S \delta\bar{C} n_i J_i dS = 0 \tag{3.51}$$

Using eq(3.47) and eq(3.48) in eq(3.51) gives the basis for the finite element formulation,

$$\int_V \left[\delta\bar{C} C^{\infty} \frac{\partial \bar{C}}{\partial t} + \frac{\partial \delta\bar{C}}{\partial x_i} C^{\infty} D_{ij} \frac{\partial \bar{C}}{\partial x_j} \right] dV = \int_S \delta\bar{C} \hat{q} dS \tag{3.52}$$

3.4.6 Discretization of Weak Form

Over a typical finite element, the normalized concentration is approximated by

$$\bar{C}(x,t) = N_\alpha(x)\bar{C}_\alpha(t) \tag{3.53}$$

where N_α are the interpolation functions and $\bar{C}_\alpha$ are the nodal normalized concentrations. The subscripts with Greek letters range from 1 to the number of interpolation functions.

After discretizing the weak form using eq(3.53) and $\delta\bar{C} = N_\alpha \delta\bar{C}_\alpha$, the following set of equations are obtained,

$$\int_V \left[N_\alpha C^\infty N_\beta \frac{\partial \bar{C}_\beta}{\partial t} + \frac{\partial N_\alpha}{\partial x_i} C^\infty D_{ij} \frac{\partial N_\beta}{\partial x_j} \bar{C}_\beta \right] dV = \int_S N_\alpha \hat{q} dS \tag{3.54}$$

In matrix form this can be written as

$$M_{\alpha\beta}\dot{q}_\beta + K_{\alpha\beta} q_\beta = F_\alpha \tag{3.55}$$

where

$$M_{\alpha\beta} = \int_V \left[N_\alpha C^\infty N_\beta \right] dV \tag{3.56}$$

$$K_{\alpha\beta} = \int_V \left[\frac{\partial N_\alpha}{\partial x_i} C^\infty D_{ij} \frac{\partial N_\beta}{\partial x_j} \right] dV \tag{3.57}$$

$$F_\alpha = \int_S N_\alpha \hat{q} dS \tag{3.58}$$

$$q_\alpha = \bar{C}_\alpha \text{ and } \dot{q}_\alpha = \frac{d\bar{C}_\alpha}{dt} \tag{3.59}$$

Note that eq(3.54) contains a time derivative term. In order to numerically solve this set of equations, an approximation is used for the time derivative term whereby the solution at a particular instant in time is determined based on the solution history. The following describes this 'time-marching' procedure used to numerically solve eq(3.54). For the sake of convenience, the following generally uses matrix notation and dispenses with the indices. Let the subscript *s* denote the solution at time *s* and the subscript *s+1* denote the solution at time $s+\Delta t$. Using eq(3.55), the following equations can be written for two consecutive time steps, $t=t_s$ and $t=t_{s+1}$,

$$M\dot{q}_s + K_s q_s - F_s = 0 \tag{3.60}$$

$$M\dot{q}_{s+1} + K_{s+1} q_{s+1} - F_{s+1} = 0 \tag{3.61}$$

Using the alpha family of approximations[166] gives

$$(1-\alpha)\dot{q}_s + \alpha\dot{q}_{s+1} = \Delta q / \Delta t \tag{3.62}$$

Multiplying eq(3.62) by ΔtM gives

$$(1-\alpha)\Delta tM\dot{q}_s + \alpha\Delta tM\dot{q}_{s+1} = M\Delta q \tag{3.63}$$

Rearranging the terms in eq(3.63) gives an expression for $\alpha\Delta tM\dot{q}_{s+1}$

$$\alpha\Delta tM\dot{q}_{s+1} = M\Delta q - (1-\alpha)\Delta tM\dot{q}_s \tag{3.64}$$

Multiplying eq(3.61) throughout by $\alpha\Delta t$ gives

$$\alpha\Delta tM\dot{q}_{s+1} + \alpha\Delta t\ \ K_{s+1} q_{s+1} - F_{s+1}\ \ = 0 \tag{3.65}$$

Substituting eq(3.64) into eq(3.65) gives,

$$M\Delta q-(1-\alpha)\Delta t M\dot{q}_s+\alpha\Delta t\ K_{s+1}q_{s+1}-F_{s+1}\ =0 \tag{3.66}$$

And substituting for $M\dot{q}_s$ from eq(3.60) in eq(3.66) gives the governing equations

$$M\Delta q-(1-\alpha)\Delta t\ -K_s q_s+F_s\ +\alpha\Delta t\ K_{s+1}q_{s+1}-F_{s+1}\ =0 \tag{3.67}$$

Using

$$a1=\alpha\Delta t \tag{3.68}$$

$$a2=(1-\alpha)\Delta t \tag{3.69}$$

in eq(3.67) gives

$$M\Delta q-a2\ -K_s q_s+F_s\ +a1\ K_{s+1}q_{s+1}-F_{s+1}\ =0 \tag{3.70}$$

Assuming that the diffusivity does not change with respect to time, we have

$$K_{s+1}\ =\ K_s \tag{3.71}$$

Using eq(3.71), eq(3.70) can be re-written as

$$M\Delta q-a2\ -K_s q_s+F_s\ +a1\ K_s q_s+K_s\Delta q-F_{s+1}\ =0 \tag{3.72}$$

Rearranging to bring all the terms involving the unknowns to the left side gives

$$M+a1K_s\ \Delta q=-(a1+a2)\ K_s q_s\ +a2\ F_s\ +a1\ F_{s+1} \tag{3.73}$$

Eq(3.73) is solved to obtain the solution for the *s+1* time step. Therefore, the finite element formulation for this diffusion model can be described by the following equations

$$\bar{M}\Delta q = \bar{F} \tag{3.74}$$

where

$$\bar{M} = M + a1K_s \tag{3.75}$$

$$\bar{F} = -(a1 + a2)\ K_s q_s\ + a2\ F_s\ + a1\ F_{s+1} \tag{3.76}$$

3.4.7 Boundary Conditions for Periodic Microstructures

As mentioned in the section 3.2.1, periodic configurations can be analyzed by using just a representative volume element (RVE) or unit cell. Similar to how solid mechanics models can be homogenized (in section 3.3.6), RVE models of periodic microstructures can also be used to obtain effective diffusivities. One noticeable difference with the solid mechanics models described in the earlier sections is that they deal with static mechanics whereas the diffusion model described in the previous section simulates a transient behavior. In order to calculate the effective diffusivities, the concentration distribution in the model at steady-state conditions is required. This means that the transient part of eq(3.52) is omitted making it a static model.

As noted in the case of solid mechanics (in section 3.3.6), once the unit cell is chosen for the periodic microstructure, certain characteristics can be determined based on the fact that each of the unit cells will behave in the same manner. For diffusion at steady-state, the periodic conditions state that the concentration gradient and flux distributions are identical in all of the unit cells. This can be expressed as

$$C\ \ x_\alpha + d_\alpha\ \ = C\ \ x_\alpha\ \ + \left\langle \frac{\partial C}{\partial x_\beta} \right\rangle d_\beta \tag{3.77}$$

$$\frac{\partial C}{\partial x_i}\ \ x_\alpha + d_\alpha\ \ = \frac{\partial C}{\partial x_i}\ \ x_\alpha \tag{3.78}$$

$$q_i\ \ x_\alpha + d_\alpha\ \ = q_i\ \ x_\alpha \tag{3.79}$$

where d_α is a vector of periodicity [90-91]. The vector of periodicity is a vector from a point in one unit cell to and equivalent point and an adjacent unit cell.

The configurations analyzed in this work are in general heterogeneous and as mentioned in the previous section, continuity of the normalized concentrations is imposed in order to resolve the issue of discontinuous concentrations at the interface of two different base materials. Therefore all the formulations and models are defined based on normalized concentrations, $\bar{C}$. The actual concentrations can of course always be calculated using eq(3.44). In some ways this is different from the typical homogenization procedure in solid mechanics. The primary variable in solid mechanics is displacements whereas in diffusion, the typical primary variable is concentration, which is generally discontinuous across different base materials. This, as mentioned earlier necessitates the use of normalized concentrations, which is continuous across different base materials. To explain the subtle differences when dealing with normalized concentrations, the procedure to determine the effective diffusivity properties of a composite with circular fibers in a periodic square array is described. This procedure is also used to perform some of the analyses in this work.

The approach described herein is consistent with Whitcomb and Tang's work[137] but some notations have been changed to make it clearer. Consider a discrete unit cell of a periodic square array as shown in Figure 3.3 and assume that the diffusing mass is macroscopically flowing in the horizontal direction and therefore there is no flux across the top and bottom edges. Although the fiber is considered to be impermeable in this work, this formulation is developed assuming that both the matrix and fiber are permeable and have saturation concentrations of D_m, C_m^∞ and D_f, C_f^∞ respectively. The matrix is assumed to be isotropic and the fibers are assumed to be transversely isotropic. Since the constituents are isotropic in the transverse plane and the fibers are arranged in a square array, the resulting microstructure will have the same effective diffusivity in the x and y directions, denoted by D_{eff}. Therefore, in order to obtain the effective

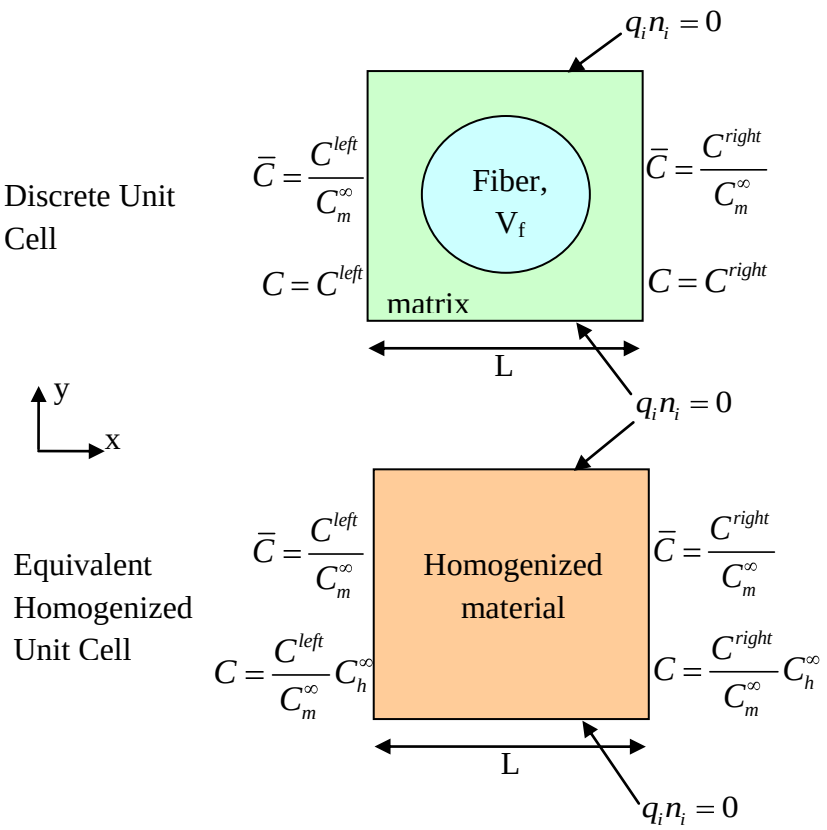

Figure 3.3: Boundary conditions for the discrete unit cell and the equivalent homogeneous unit cell

diffusivity for the microstructure, only one type of configuration needs to be analyzed with an imposed concentration gradient in the x direction. Suppose the concentrations on the left and right are C^{left} and C^{right}, respectively. The respective normalized concentrations are obtained by dividing the concentrations by C_m^{∞}. The finite element model of the configuration can be analyzed by imposing the corresponding normalized concentrations on the left and right edges. The results will show a continuous variation of the normalized concentration across the domain as expected but the actual concentrations will have a discontinuity at the interface between the fiber and the matrix, if they have different saturation concentrations. It is convenient to define an effective property, *d* for the unit cell in terms of volume averaged values of the flux in the x direction, q_x and the normalized concentration gradient, $\frac{\partial \bar{C}}{\partial x}$.

$$\langle q_x \rangle = -d \left\langle \frac{\partial \bar{C}}{\partial x} \right\rangle \tag{3.80}$$

where the angle brackets indicate the volume average of the bracketed term.

The solution can be post-processed to give the volume averaged flux over the unit cell. For this simple geometry and boundary conditions, the volume-averaged normalized concentration gradient is simply $\bar{C}^{right} - \bar{C}^{left} \big/ L$, although for more complicated models, the value can be obtained by post-processing the solution.

An equivalent homogenized material will have a saturation concentration value which is the volume-averaged value of the constituent saturation concentrations.

$$C_h^{\infty} = V_m C_m^{\infty} + V_f C_f^{\infty} \tag{3.81}$$

In the corresponding homogenized unit cell, the normalized concentrations at the right and left will be the same as that in the discrete unit cell as indicated in Figure 3.3. The actual concentrations at the right and left edge in the homogenized unit cell are obtained by using eq(3.44). Therefore the corresponding concentration on the left and right will be $C_h^{\infty} \frac{C^{left}}{C_m^{\infty}}$ and $C_h^{\infty} \frac{C^{right}}{C_m^{\infty}}$ respectively as shown in Figure 3.3. The equivalent concentration gradient can be written as

$$\left\langle \frac{\partial C}{\partial x} \right\rangle = \frac{\left(C_h^{\infty} \frac{C^{right}}{C_m^{\infty}} - C_h^{\infty} \frac{C^{left}}{C_m^{\infty}} \right)}{L} = C_h^{\infty} \frac{\left(\frac{C^{right}}{C_m^{\infty}} - \frac{C^{left}}{C_m^{\infty}} \right)}{L} \tag{3.82}$$

This can be rewritten in terms of the volume averaged normalized concentration gradients, $\left\langle \frac{\partial \bar{C}}{\partial x} \right\rangle$

$$\left\langle \frac{\partial C}{\partial x} \right\rangle = C_h^{\infty} \left\langle \frac{\partial \bar{C}}{\partial x} \right\rangle \tag{3.83}$$

Combining eq(3.80) and eq(3.83) gives,

$$\langle q_x \rangle = -\frac{d}{C_h^\infty}\left\langle \frac{\partial C}{\partial x} \right\rangle \tag{3.84}$$

which gives the expression for effective diffusivity as

$$D_{eff} = \frac{d}{C_h^\infty} \tag{3.85}$$

When the fiber is assumed to be impermeable, i.e. $D_f = 0, C_f^\infty = 0$, the expression for the effective diffusivity simplifies to

$$D_{eff} = \frac{d}{V_m C_m^\infty} \tag{3.86}$$

Under such an assumption, it is observed[137] that the ratio $\frac{d}{D_m C_m^\infty}$ is constant for a fixed fiber fraction, regardless of the value of the matrix diffusivity. Let this ratio be defined by the following,

$$\bar{D} = \frac{d}{D_m C_m^\infty} \tag{3.87}$$

A master curve can be obtained showing the variation of $\bar{D}$ with fiber fraction. This master curve shown in Figure 3.4 is valid as long as the diffusion follows Fick's law. The same is true for hexagonal arrays of impermeable fibers and Ref.[137] gives a simple curve fit for both master curves. This makes it convenient to obtain the effective diffusivity of a composite with impermeable circular fibers for various fiber fractions using the following,

$$D_{eff} = \frac{\bar{D} D_m}{V_m} \tag{3.88}$$

where $\bar{D}$ is obtained using the curve in Figure 3.4, which also describes the formula for the curve fit.

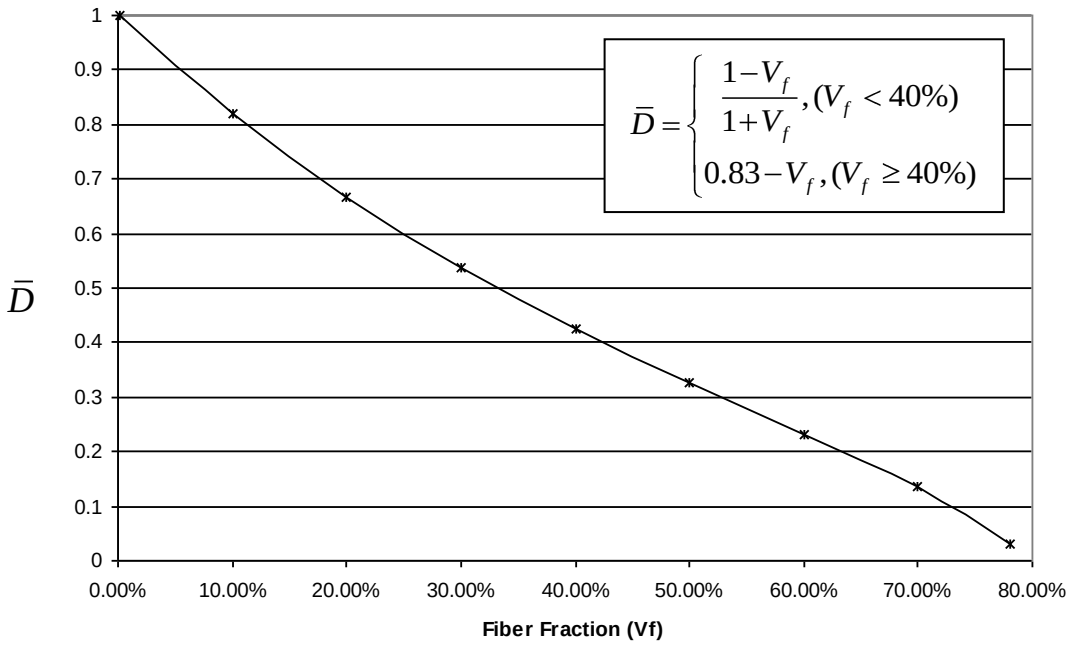

Figure 3.4: Master curve for impermeable circular fibers in square array showing variation of $\bar{D}$ with fiber fraction V_f (refer to eq(3.87) for definition of $\bar{D}$)

3.5 Oxidation

This section describes the governing equations and the finite element formulation for simulating the oxidation behavior in pure resin and in composites. The oxidation model can be considered an extension of the diffusion model as they are both based on the same conservation law. Some of the issues such as using normalized concentration as the primary variable are common to this analysis as well. The common aspects between the two analyses will be highlighted while describing the special circumstances that make this analysis different. This section will follow the same format as the sections on solid mechanics and diffusion and starts by listing the equations for the common analysis procedure. This is followed by the derivation of the weak form and its discretization to obtain the finite element formulation.

3.5.1. Conservation Laws

The oxidation process in a polymer is a combination of the diffusion of oxygen and its consumption by reaction, which also results in the creation of by-products such as carbon dioxide. For the purposes of modeling the oxidation of polymers, the process is assumed to be dominated by the diffusion of oxygen into the polymer. The oxidation model that is used in this research effort is primarily based on the work by Pochiraju et al[7-9] in which they used the conservation of mass law for diffusion with a term to model the rate of consumption of the diffusing oxygen during chemical reaction. The governing equation can be expressed as

$$\frac{\partial C}{\partial t} + \frac{\partial J_i}{\partial x_i} + R = 0 \tag{3.89}$$

where C is the concentration of oxygen, J_i is the diffusion flux and R is the reaction rate term.

This section is also used to completely define the reaction rate term and the related quantities. The reaction rate, R, in general, would depend on the concentration of oxygen, temperature and the availability of un-oxidized polymer. As the oxygen reacts with the polymer, the amount of polymer available for oxidation depletes and the oxygen

will continue to diffuse to the interior of the polymer to react. Depending on the type of polymer, the process also leads to a reduction in the molecular weight of the material due to chemical bond breakage and the release of the oxidation by-products[9]. The amount of polymer available for oxidation is defined by an oxidation state variable called ϕ. The value of the oxidation state variable at which the polymer is considered to be completely oxidized with no more polymer available for reaction is defined as ϕ_{ox}. The oxidation state can be physically defined to be the ratio of the current weight of the material over its original un-oxidized weight. Therefore, the oxidation state ϕ has a range from ϕ_{ox} to 1 where an oxidation state value of 1 denotes the un-oxidized polymer. An oxidation state value between ϕ_{ox} and 1 indicates that the material is partly oxidized and can still undergo more oxidation. To illustrate this, three zones were defined by Pochiraju et al[7-9] as shown in Figure 3.5. Consider that the left end of the idealized material shown in the figure is exposed to oxygen and the oxidation propagates to the right. Zone III is the region of the material that is un-oxidized with an oxidation state of 1 and as the oxidation continues, this zone gets smaller while Zone I which denotes the fully oxidized material with an oxidation state of ϕ_{ox} increases. The zone in

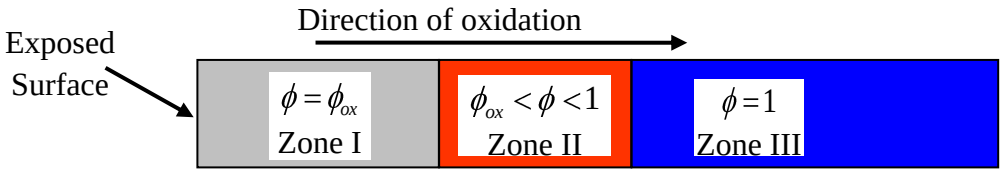

Figure 3.5: Oxidation zones and corresponding values of the oxidation state variable

between where the oxidation state is between ϕ_{ox} and 1 is called the active zone and is denoted by Zone II. The expression for calculating the oxidation state variable is described later in this section.

When $\phi = \phi_{ox}$ at a material point, $R = 0$ and the process simplifies to just diffusion at that point. It is assumed that the effects of ϕ, T and C on R are separable such that the function R can be expressed as

$$R = \left(\frac{\phi - \phi_{ox}}{1 - \phi_{ox}} \right) f(C) R_0(T) \tag{3.90}$$

$R_0(T)$ is the "saturated reaction rate" (as described in Ref[9]), which describes the dependence of the reaction rate on the temperature under saturation conditions. The polymer is considered saturated when it has the maximum amount of oxygen possible for the given temperature and pressure. The leading factor and $f(C)$ in the expression both have a range from 0 to 1. The leading factor models the dependence of the reaction rate on the availability of polymer that can be oxidized such that R is maximum when ϕ has a value of 1 and linearly decreases to zero when $\phi = \phi_{ox}$. The function $f(C)$ models the dependence of the reaction rate on the oxygen concentration. For modeling oxidation in polyimide resin systems like PMR-15 as implemented by Pochiraju, the function $f(C)$ is taken from the work by Colin et al[167-168].

$$f(C) = \frac{2\beta C}{1 + \beta C} \left[1 - \frac{\beta C}{2\ 1 + \beta C} \right] \tag{3.91}$$

The value of β is determined by using weight loss data obtained from specimens aged at two different oxygen partial pressures i.e. at two different saturation conditions, typically in pure oxygen and air. The details of this procedure are given in Ref.[9]. The following ratio is obtained from the experimental work by Abdeljaoued[163],

$$\frac{\text{weight loss}_{\text{air}}}{\text{weight loss}_{\text{pure oxygen}}} = 0.7 \tag{3.92}$$

Assuming that the weight loss is proportional to the reaction rates, the ratio of the weight loss from the two specimens would be the same as the ratio of the reaction rates and would give the following equation,

$$\frac{R(C = 0.79\, mol/m^3, 288°C)}{R(C = 3.74\, mol/m^3, 288°C)} = \frac{R_0(288°C) f(C = 0.79\, mol/m^3)}{R_0(288°C) f(C = 3.74\, mol/m^3)} = 0.7 \tag{3.93}$$

This can be solved to obtain three roots for β of which only one is non-zero and has a value of 0.919.

For modeling neat PMR-15 resin, ϕ_{ox} has a value of 0.187, which is taken from Pochiraju's work [7-9]. This value is determined from experimental weight loss data and the method is described in Ref. [9]. The oxidation state variable can be related to the weight loss of the material as follows

$$\frac{d\phi}{dt} \propto \frac{dW}{dt} \tag{3.94}$$

where W is the weight of the material.

Assuming that the rate of change of weight is proportional to the reaction rate gives,

$$\frac{dW}{dt} \propto -R \tag{3.95}$$

Combining Eq.(8) and Eq.(9) gives the following,

$$\frac{d\phi}{dt} = -\alpha R \tag{3.96}$$

where α is a proportionality parameter that is, in general, time and temperature dependent.

Using Eq.(10), the following expression for calculating ϕ can be obtained

$$\phi = \max\left\{\phi_{ox}, \left(1 - \int_0^t \alpha(\varsigma) R(\varsigma) d\varsigma\right)\right\} \tag{3.97}$$

An issue that arises when analyzing oxidation in heterogeneous materials is that although the oxidation state value for any material has an upper limit of 1, its lower limit for different materials is not necessarily the same. This makes it inconvenient to make comparisons as to how much oxidation has taken place. For example, the same oxidation state value for two different materials need not imply that they are equally close to being fully oxidized or that they have the same amount of material left to oxidize. In order to

make this comparison easier, a new variable is introduced called the oxidation level denoted by Φ. The oxidation level variable linearly scales the oxidation state variable so that all materials have an oxidation level that ranges from 0 to 1. This relation is given by,

$$\Phi = \frac{\phi - \phi_{ox}}{1 - \phi_{ox}} \tag{3.98}$$

For the same reasons described in section 3.4.1, the differential equation described in eq(3.89) is re-written in terms of normalized concentrations,

$$C^{\infty} \frac{\partial \bar{C}}{\partial t} + \frac{\partial}{\partial x_i} J_i + R = 0 \tag{3.99}$$

3.5.2. Concentration gradients

Just as in the diffusion analysis, the oxidation analysis uses simple gradients of the concentration, $\frac{\partial C}{\partial x_i}$

3.5.3 Constitutive Relations

The relationship between flux and the concentration gradient is given by Fick's first law,

$$J_i = -D_{ij} \frac{\partial C}{\partial x_j} \tag{3.100}$$

where D_{ij} is the 2nd order diffusivity tensor. The Latin subscripts *i* and *j* denote the coordinate direction and range from 1 to 3 for a three dimensional formulation. The constitutive relationship is different from that in the diffusion analysis described in section 3.4.3 and that is because the diffusivities of the un-oxidized and oxidized polymer, in general, will be different. The diffusivity of the polymer in the active

oxidizing zone (where $\phi_{ox} < \phi < 1$) is assumed to vary linearly between the un-oxidized polymer diffusivity and the fully oxidized polymer diffusivity and is given the following expression

$$D_{ij} = \left\langle D_{ij} \right\rangle_{un} \left(\frac{\phi - \phi_{ox}}{1 - \phi_{ox}} \right) + \left\langle D_{ij} \right\rangle_{ox} \left(\frac{1 - \phi}{1 - \phi_{ox}} \right) \tag{3.101}$$

Again, eq(3.100) is re-written in terms of the normalized concentration

$$J_i = -C^{\infty} D_{ij} \frac{\partial \bar{C}}{\partial x_j} \tag{3.102}$$

3.5.4 Boundary Conditions

The boundary conditions are defined in the same manner as the diffusion analysis. The flux boundary conditions are given by

$$\hat{q} = -n_i J_i \quad \text{on S} \tag{3.103}$$

And the normalized concentration boundary conditions are given by

$$\bar{C} = \bar{C} \text{ on } \hat{S} \tag{3.104}$$

where $\bar{C}$ is the specified normalized concentration on the boundary $\hat{S}$.

3.5.5 Weak Form

The same procedure is applied as described in section 3.4.5 for the derivation of weak form for diffusion analysis. The difference is in the inclusion of the reaction rate term in the case of the oxidation analysis. The equation of conservation mass is multiplied by a variation of the normalized concentration and integrated over the volume to obtain the weighted integral form,

$$\int_V \delta \bar{C} \left[C^{\infty} \frac{\partial \bar{C}}{\partial t} + \frac{\partial}{\partial x_i} J_i + R \right] dV = 0 \tag{3.105}$$

where $\delta\bar{C}$ is an arbitrary variation of the normalized concentration.

Integration by parts gives the weak from,

$$\int_V \left[\delta\bar{C}C^{\infty} \frac{\partial \bar{C}}{\partial t} - \frac{\partial \delta\bar{C}}{\partial x_i} J_i + R\delta\bar{C} \right] dV + \int_S \delta\bar{C} n_i J_i dS = 0 \qquad (3.106)$$

Using eq(3.102) and eq(3.103) in eq(3.106) gives the basis for the finite element formulation,

$$\int_V \left[\delta\bar{C}C^{\infty} \frac{\partial \bar{C}}{\partial t} + \frac{\partial \delta\bar{C}}{\partial x_i} C^{\infty} D_{ij} \frac{\partial \bar{C}}{\partial x_j} + R\delta\bar{C} \right] dV = \int_S \delta\bar{C}\hat{q} dS \qquad (3.107)$$

3.5.6 Discretization of Weak Form

Again, the same basic procedure is applied as described in section 3.4.6 for the derivation of finite element formulation. On the other hand, there are some details that are quite different from the diffusion analysis. This is because of the reaction rate term and the non-linear expression of the diffusivity in the weak form.

Over a typical finite element, the normalized concentration is approximated by

$$\bar{C}(x,t) = N_{\alpha}(x)\bar{C}_{\alpha}(t) \qquad (3.108)$$

where N_{α} are the interpolation functions and $\bar{C}_{\alpha}$ are the nodal normalized concentrations. The subscripts with Greek letters range from 1 to the number of interpolation functions.

After discretizing the weak form using eq(3.108) and $\delta\bar{C} = N_{\alpha}\delta\bar{C}_{\alpha}$, the following set of equations are obtained,

$$\int_V \left[N_\alpha C^\infty N_\beta \frac{\partial \bar{C}_\beta}{\partial t} + \frac{\partial N_\alpha}{\partial x_i} C^\infty D_{ij} \frac{\partial N_\beta}{\partial x_j} \bar{C}_\beta + N_\alpha R \right] dV = \int_S N_\alpha \hat{q} dS \tag{3.109}$$

In matrix form this can be written as

$$M_{\alpha\beta} \dot{q}_\beta + K_{\alpha\beta} q_\beta + R^*_\alpha = F_\alpha \tag{3.110}$$

where

$$M_{\alpha\beta} = \int_V \left[N_\alpha C^\infty N_\beta \right] dV \tag{3.111}$$

$$K_{\alpha\beta} = \int_V \left[\frac{\partial N_\alpha}{\partial x_i} C^\infty D_{ij} \frac{\partial N_\beta}{\partial x_j} \right] dV \tag{3.112}$$

$$R^*_\alpha = \int_V N_\alpha R \, dV \tag{3.113}$$

$$F_\alpha = \int_S N_\alpha \hat{q} dS \tag{3.114}$$

$$q_\alpha = \bar{C}_\alpha \text{ and } \dot{q}_\alpha = \frac{d\bar{C}_\alpha}{dt} \tag{3.115}$$

Just as in the case of the diffusion analysis, an approximation is used for the time derivative term in eq(3.109) whereby the solution at a particular instant in time is determined based on the solution history. The same ‘time-marching’ procedure from section 3.4.6 is used to numerically solve eq(3.109). Using eq(3.110), the following equations can be written for two consecutive time steps, $t=t_s$ and $t=t_{s+1}$,

$$M\dot{q}_s + K_s q_s + R_s^* - F_s = 0 \tag{3.116}$$

$$M\dot{q}_{s+1} + K_{s+1}q_{s+1} + R^*_{s+1} - F_{s+1} = 0 \tag{3.117}$$

Using the alpha family of approximations[166] gives

$$(1-\alpha)\dot{q}_s + \alpha\dot{q}_{s+1} = \Delta q / \Delta t \tag{3.118}$$

Multiplying eq(3.118) by ΔtM gives

$$(1-\alpha)\Delta tM\dot{q}_s + \alpha\Delta tM\dot{q}_{s+1} = M\,\Delta q \tag{3.119}$$

Rearranging the terms in eq(3.119) gives an expression for $\alpha\Delta tM\dot{q}_{s+1}$

$$\alpha\Delta tM\dot{q}_{s+1} = M\,\Delta q - (1-\alpha)\Delta tM\dot{q}_s \tag{3.120}$$

Multiplying eq(3.117) throughout by $\alpha\Delta t$ gives

$$\alpha\Delta tM\dot{q}_{s+1} + \alpha\Delta t\left[K_{s+1}q_{s+1} + R^*_{s+1} - F_{s+1}\right] = 0 \tag{3.121}$$

Substituting eq(3.120) into eq(3.121) gives,

$$M\,\Delta q - (1-\alpha)\Delta tM\dot{q}_s + \alpha\Delta t\left[K_{s+1}q_{s+1} + R^*_{s+1} - F_{s+1}\right] = 0 \tag{3.122}$$

And substituting for $M\dot{q}_s$ from eq(3.116) in eq(3.122) gives the governing equations

$$M\,\Delta q - (1-\alpha)\Delta t\left[-K_s q_s - R^*_s + F_s\right] + \alpha\Delta t\left[K_{s+1}q_{s+1} + R^*_{s+1} - F_{s+1}\right] = 0 \tag{3.123}$$

Using eq(3.68) and eq(3.69) in eq(3.123) gives

$$M\Delta q - a2\left[-K_s q_s - R_s^* + F_s\right] + a1\left[K_{s+1}q_{s+1} + R_{s+1}^* - F_{s+1}\right] = 0 \qquad (3.124)$$

A Taylor Series expansion is used on the terms in eq(3.124) that are dependent on the unknown solution, (q_{s+1}), which are $K_{s+1}q_{s+1}$ and R_{s+1}^*. Indices will be used in the next few steps in order to make the operations involved clear. Ignoring the higher order terms in the Taylor Series expansion gives the following expression,

$$K_{\alpha\beta\ s+1}\ q_{\beta\ s+1} + R_{\alpha\ s+1}^* \approx K_{\alpha\beta\ s}\ q_{\beta\ s} + R_{\alpha\ s}^* + \frac{\partial\left[K_{\alpha\beta\ s}\ q_{\beta\ s}\right]}{\partial q_\zeta}\Delta q_\zeta + \frac{\partial\ R_{\alpha\ s}^*}{\partial q_\beta}\Delta q_\beta$$

(3.125)

The partial derivatives in the expression above are very complex and therefore the aim is to obtain an approximation for the expression. It is assumed that for sufficiently small time steps, the error is minimal and certain approximations can be made. Similar approximations have been made in Pochiraju's oxidation model [7-9]. One approach to obtain an approximate expression for $\frac{\partial\ R_{\alpha\ s}^*}{\partial q_\beta}$ is by assuming that only $f(C)$ from eq(3.90) depends on C. This would make it simpler to take a derivative of R_α^* with respect to the nodal variables, q_β. This approach will be evaluated in future work but for this work, it is assumed that if the time step is sufficiently small that $R_{\alpha\ s+1}^*$ in eq(3.125) can be approximated by $R_{\alpha\ s}^*$ (or mathematically, $\frac{\partial\ R_{\alpha\ s}^*}{\partial q_\beta} = 0$). The remaining partial derivative in eq(3.125) can be expressed as

$$\frac{\partial\left[\ K_{\alpha\beta}\ _s\ q_\beta\ _s\right]}{\partial q_\zeta} = \ K_{\alpha\beta}\ _s \frac{\partial\ q_\beta\ _s}{\partial q_\zeta} + \ q_\beta\ _s \frac{\partial\ K_{\alpha\beta}\ _s}{\partial q_\zeta} \qquad (3.126)$$

The term $\frac{\partial\ K_{\alpha\beta}\ _s}{\partial q_\zeta}$ is not convenient to compute because $K_{\alpha\beta}$ depends on ϕ, which is a complex function of the solution (see eq(3.97)). Again, it is assumed that for sufficiently small time steps, Eq.(39) can be approximated by assuming $\frac{\partial\ K_{\alpha\beta}\ _s}{\partial q_\zeta} = 0$. Thus eq(3.126) becomes

$$\frac{\partial\left[\ K_{\alpha\beta}\ _s\ q_\zeta\ _s\right]}{\partial q_\zeta} = \ K_{\alpha\zeta}\ _s \qquad (3.127)$$

Therefore eq(3.125) becomes

$$K_{\alpha\beta}\ _{s+1}\ q_\beta\ _{s+1} + \ R^*_\alpha\ _{s+1} \approx \ K_{\alpha\beta}\ _s\ q_\beta\ _s + \ R^*_\alpha\ _s + \ K_{\alpha\beta}\ _s \Delta q_\beta \qquad (3.128)$$

Substituting eq(3.128) in eq(3.124) gives

$$M\Delta q - a2\left[-K_s q_s - R^*_s + F_s\right] + a1\left[(K_s q_s + R^*_s) + K_s \Delta q - F_{s+1}\right] \approx 0 \qquad (3.129)$$

Rearranging to bring all the terms involving the unknowns to the left side gives

$$M + a1K_s\ \ \Delta q \approx -(a1+a2)\left[K_s q_s + R^*_s\right] + a2\ \ F_s\ \ + a1\ \ F_{s+1} \qquad (3.130)$$

Eq(3.130) is solved to obtain the solution for the *s+1* time step. For sufficiently small time steps, it is seen that this approximation is reasonable because a parametric study with different time step sizes showed the model appearing to converge to the same solution. Therefore, the finite element formulation for this oxidation model can be described by the following equations

$$\bar{M}\Delta q = \bar{F} \tag{3.131}$$

where

$$\bar{M} = M + a1K_s \tag{3.132}$$

$$\bar{F} = -(a1+a2)\left[K_s q_s + R_s^*\right] + a2\ F_s + a1\ F_{s+1} \tag{3.133}$$

To arrive at this formulation, a number of approximations were made to simplify the nonlinearity. Typically, when solving a nonlinear equation numerically, a 'residual' is driven to zero by iterating. In this implementation, there is no iterating at each time step in order to drive a 'residual' to zero. This is because it was found that the even without iterating, the results were found to be reasonably close to that from Pochiraju's model.

An important part of the oxidation analysis is post-processing the results of the simulation to provide a measure of the oxidation behavior. The oxidation behavior is visualized in terms of the growth of the oxidation layer. The oxidation layer initiates from the surfaces exposed to the oxygen and grows into the interior as the material becomes oxidized. Although ideally the material is said to have started oxidizing when the oxidation level drops below 1, the oxidation layer thickness is defined by the point at which the oxidation level, Φ, dips below 0.99, indicating that 1% of the oxidizable material has oxidized. Therefore, an element is assumed to have started oxidizing if the oxidation level at each of the material integration points falls below 0.99. If the oxidation state is above 0.99, the element is assumed to be un-oxidized and if it is below 0.01 it is assumed to be fully oxidized. A post-processing routine was written that

calculated the growth of the oxidation layer in the 1D model. This involved extrapolating the oxidation state values from the integration points to the nodal points, averaging the extrapolated values at a node if the node shared elements of the same material and solving for the location in the model where the oxidation level value met the specified upper and lower limits. This routine was also generalized to work for 2-D and 3-D models. Note that the prescribed upper and lower limits of 0.99 and 0.01 respectively are valid only for a completely oxidizable material such as neat resin. When dealing with homogenized material such as a tow, the entire material does not oxidize because the fibers are assumed to be inert and therefore the prescribed limits will be different. In such a case, the upper limit that defines the oxidation layer thickness is the oxidation level when 1% of the resin in a homogenized tow material point is oxidized. This upper limit is given by

$$\Phi_{upper} = 1 - 0.01 V_m \tag{3.134}$$

The model described in this section was implemented and the oxidation layer growth was simulated for neat PMR-15 resin using a 1D model. The results were compared with that from Pochiraju's simulation. For a 200-hr simulation, it was found that both models agree closely in predicting the Zone I thickness. The difference is negligible in the beginning of the simulation and grows to a maximum difference at 200 hours when the current model predicts a thickness 107 microns compared to 104 microns predicted by Pochiraju's model. Both models predict the Zone II thickness to be almost constant throughout the 200 hr simulation. Pochiraju's model gives a Zone II thickness of 19 microns while the current model under predicts by 21% with a value of 15 microns. The cause of this difference could be the implementation of the two models. Pochiraju's 1D model[9] uses a modified implementation of *ode15s* and *Pdepe* solvers in MATLAB to solve the governing equation, eq(3.89). The current model on the other hand uses a standard one-dimensional finite element implementation based on eq(3.131). For the purposes of investigating the effect of oxidation on the mechanical response of the composites using this material system, it is assumed that the thickness of Zone I alone or the overall thickness (Zone I + II) that is of primary concern. Thus, if the overall

thickness is considered, the difference between the two models is around 21% in the beginning and drops to about 2% at 200 hours, which is assumed to be negligible for the purposes of this particular research effort.

The various material input properties required for specifying the equations in the oxidation model are:

1. The diffusivities for the oxidized and un-oxidized material, D_{ox}, D_{unox}
2. Saturated reaction rate, R_0
3. Dependence of reaction rate on concentration, $f(C)$ and the constant β
4. Value of oxidation state when fully oxidized, ϕ_{ox}
5. Weight-reaction proportionality parameter, α

3.5.7 Boundary Conditions for Periodic Microstructures and Homogenization

The oxidation response in polymers and PMCs is a nonlinear transient behavior. Just as in the case of diffusion, in order to simulate oxidation for periodic microstructures, the transient part of the behavior needs to be removed effectively looking at the microstructure at steady-state conditions. Under oxidation behavior, steady-state conditions imply that all the material in the microstructure is oxidized. But when all the material is oxidized, the behavior reverts to typical steady-state diffusion behavior. Therefore, it is not intuitive to obtain the effective oxidation material properties in this manner. Instead, other strategies are explored for simulating oxidation in periodic microstructures.

In order to model oxidation in a textile composite, it is necessary to obtain effective properties for the tows because it is impractical or even impossible to discretely model the entire microstructure. This section will describe approaches for obtaining effective oxidation material properties for tows.

When trying to replace a heterogeneous material with a homogenized material in model, it is reasonable to assume that some or possibly all of these properties might change. It can also be expected that there could be more than one way that these properties can change to demonstrate the same overall behavior as a discretely modeled heterogeneous microstructure. There are at least two approaches for achieving this goal. One is to use a multi-scale analysis that keeps track of the 'local' information such as oxidation state and actual average concentration in the constituent matrix in the homogenized material. Given this information, it would be possible to calculate the reaction rate R at a particular material point in the tow's constituent matrix using eq(3.90). Next, the effective reaction rate for the larger scale homogenized tow is determined by a simple rule of mixtures and plugged into the governing equations. When the equations for a time step are solved, the calculated concentrations are transformed back to the local scale using a rule of mixtures in order to keep track of the oxidation state of the constituent matrix. Thus, a continuous transfer of information between the two scales needs to be maintained throughout the simulation. For this work, another approach is used where effective oxidation properties for the homogenized material are determined thereby eliminating the need to go back and forth between the two scales. A few assumptions are made in order to determine the effective material properties, D_{ox}, D_{unox}, $R_0, f(C), \beta, \phi_{ox}$ and α. These assumptions and the procedure to determine the properties are described in the remainder of this section.

In this work, the fibers in the tows are idealized to be in a square array and the fibers are assumed to be impermeable and do not oxidize. While there are other factors that can influence the oxidation behavior in composites such as the properties of the fiber/matrix interface or interphase, they are not taken into account for the homogenization model described in this work. Cracks in the matrix or along the fiber/matrix interface can also affect the oxidation behavior by allowing rapid ingress. Depending on the type of damage that is observed in these composites, it might be possible to account for their effects in the homogenized model. For example, if the damage is diffuse, the homogenized properties can be degraded appropriately or if the damage is confined to

certain areas, cracks can be introduced in the homogenized model. Since this model does not consider factors such as the effect of damage, fiber/matrix interface or cracks in the composites, the only oxidation material property that is different when considering axial and transverse growth is the diffusivity. The axial diffusivity is largely governed by a rule of mixtures and exhibits simple behavior. Therefore, particular attention is not paid to the axial oxidation behavior. Moreover, in realistic applications, the surfaces exposed to oxidizing environments are mostly parallel to the fibers. The laminate configurations that are analyzed in this work are chosen based on these considerations and therefore, the oxidation behavior is depends on the transverse oxidation material properties.

3.5.7.1 Diffusivities for the oxidized and un-oxidized material D_{ox}, D_{unox}

The diffusivities on its own only define the mass flow of oxygen in the material. It will be assumed that the oxidation state continues to have a linear effect on the effective diffusivities of the homogenized material. The effective diffusivity can be determined by just modeling the diffusion without the need for modeling the oxidation behavior. The procedure for determining effective diffusivity as described in section 3.4.7 is used to obtain the effective diffusivities for the oxidized and un-oxidized material.

3.5.7.2 Saturated reaction rate, R_0

Since the matrix is the only material that is oxidizing, the effective saturated reaction rate would be expected to be related to the amount of matrix in the unit cell. It is assumed that the relationship follows a rule of mixtures (with the fiber having a reaction rate of zero). That is

$$R_0 = V_m R_0^{matrix} \tag{3.135}$$

3.5.7.3 Dependence of concentration on reaction rate on $f(C)$ and β

The term $f(C)$ models the dependence of the reaction rate on the oxygen concentration. Colin's expression[167-168] given in Eq.(4), which is used as $f(C)$ to model the neat PMR-15 polymer will be used for the homogenized tow as well. It is assumed that the same expression models the behavior of the homogenized tow. As mentioned in the previous section, to determine the value of β the ratio of the weight loss of the material at two different saturation conditions is needed. Due to lack of access to experimental data on oxidation weight loss for unidirectional laminates, it is assumed that the ratio of weight loss is the same as that of the neat PMR-15 polymer. Therefore, β has the same value as that of the neat resin, which is 0.919.

3.5.7.4 Oxidation state when fully oxidized, ϕ_{ox}

This is a property that is calculated by determining the weight loss of the material when oxidized. For example, a value of 0.2 implies that the fully oxidized material weighs about 20% of its original weight. Due to lack of access to weight loss data for unidirectional laminates, an estimate for ϕ_{ox} is obtained based on the assumption that the fiber does not lose weight during oxidation. Therefore, the effective ϕ_{ox} would be given by

$$\phi_{ox}^{eff} = 1-(1-\phi_{ox}^{m})V_m \tag{3.136}$$

3.5.7.5 Weight-reaction proportionality parameter, α

In general, the proportionality parameter α is time and temperature dependent. The value of α for the neat resin is determined by examining the oxidation layer growth. On comparison of the simulation results with the experimental results, Pochiraju [9] found that the oxidation behavior was better simulated when the proportionality parameter was linearly decreased over time from 0.01 to 0.0033 for the first 40 hours of oxidation and then remains constant at 0.0033. The value of α for the homogenized tow is assumed to follow the same as that of the neat PMR-15 resin.

3.6. Coupled Mechanical-Oxidation Analysis

A coupled mechanical-oxidation analysis model was developed to predict damage initiation and progression in textile composites under an oxidizing environment. Although the analyses performed in this work assumes only one-way coupling, the underlying analysis model forces no such restriction and can account for full coupling between the mechanical and oxidation analysis. This section describes the coupled analysis model used in this work followed by the constitutive relations used to the couple the two analyses.

One component of the coupled analysis is the oxidation analysis that simulates the diffusion of oxygen into the composite and tracks how much the material has oxidized. The second component is the damage progression analysis that can track the damage in the material and degrade the properties of the damaged regions. The theory and finite element formulation behind both the oxidation analysis and the damage progression analysis is provided in the previous sections and they are adapted to use in this coupled analysis model. The coupling between the two analyses is enabled by constitutive relations. The full coupling requires a constitutive relation relating the oxidation state to the mechanical properties and another constitutive relation relating the mechanical state to the oxidation material properties. In this work, all the configurations that were analyzed assumed only a one-way coupling with the oxidation state affecting the mechanical properties of the model. The remainder of this section describes the algorithm for this one-way coupled model. The implementation and the details involved with performing an actual coupled analysis on a textile composite configuration will be explained in a later section.

Since the analysis assumes only one-way coupling and the mechanical state does not affect the oxidation material properties, the oxidation analysis can be performed independent of the damage progression analysis. Therefore, the output from the oxidation simulation can be used by the model as and when needed. The oxidation analysis output contains the oxidation state distribution in the configuration at different times in the simulated oxidation time period. The damage progression analysis described

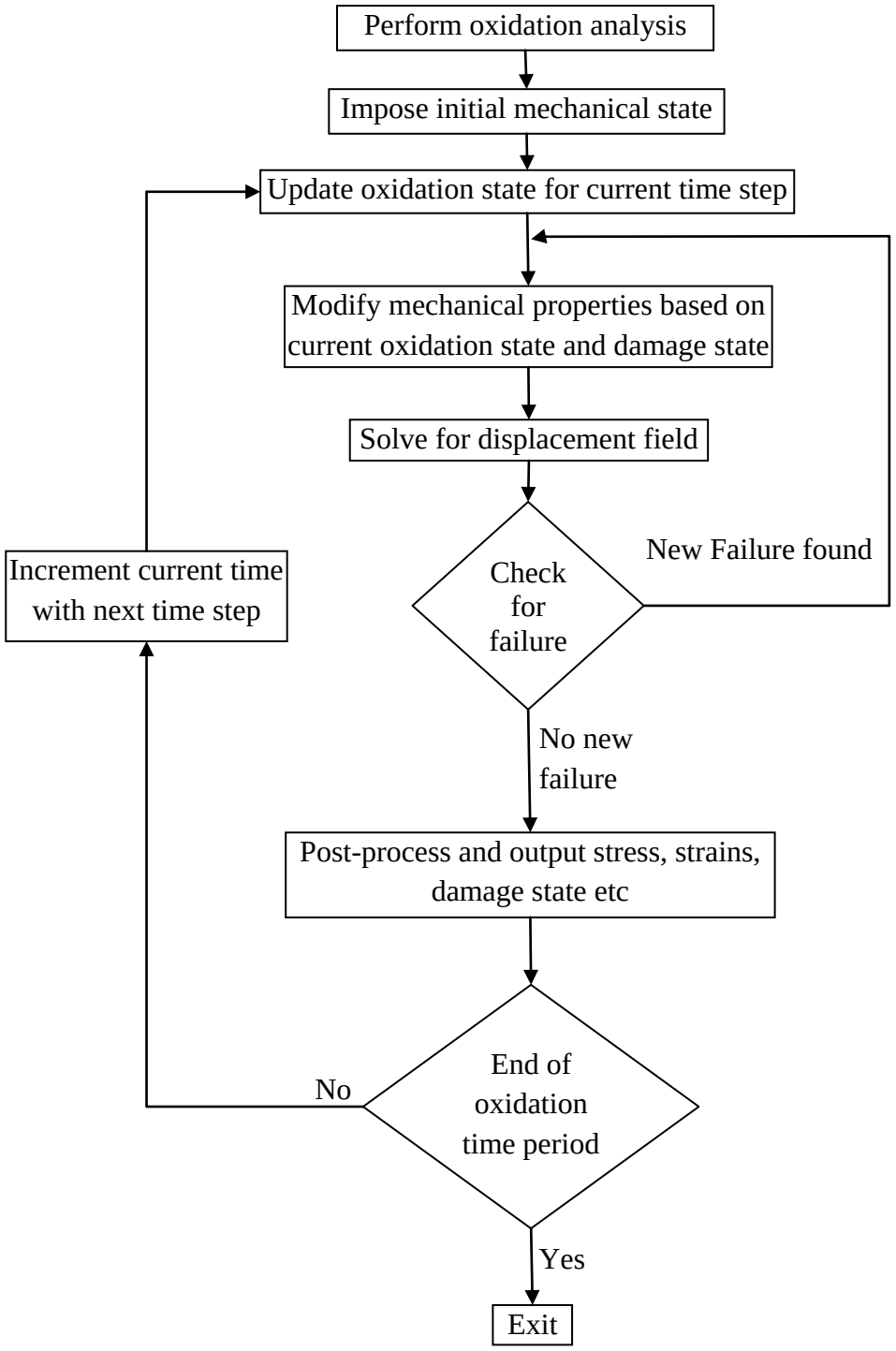

Figure 3.6: Algorithm for one-way coupled oxidation-damage progression analysis

in section 3.3.8 is a quasi-static analysis where the loading is ramped up but is essentially time-independent. On the other hand, all the coupled models analyzed in this work assume a constant mechanical loading while the configuration is undergoing oxidation. Therefore, the damage progression analysis cycles through each of the time data-points in the simulated oxidation time period and performs the following steps – Load the oxidation state for the particular time data-point, modify the mechanical properties and iterate to converge upon the final damage state for the corresponding time data-point. This is illustrated in the flowchart for the algorithm shown in Figure 3.6.

3.6.1 Constitutive Relations

Experimental results show that oxidation causes damage in the oxidized material which can ultimately affect the mechanical properties of the composite [9]. Oxidation is found to affect the mechanical properties of fibers [9]. But it is not trivial to characterize the damage and its effects on the mechanical properties of the composites. The underlying mechanisms and the properties of the fiber/matrix interface and interphase have not been fully understood yet. Shrinkage of the matrix due to oxidation is theorized to be among the factors causing delaminations on the fiber matrix interface [153]. These cracks can further affect the oxidation behavior by allowing oxygen to penetrate the material faster. But the effects of the mechanical or physical damage on the oxidation behavior are not being considered in the simulations used in this work. This section will describe the type of constitutive relations used in the simulations that were performed in this work.

This constitutive relation or degradation scheme is similar in some respect to the property degradation scheme based on mechanical damage. They are similar in the sense that the engineering moduli are modified to account for the effect of the oxidation. The constitutive relation quantifies the amount of damage in terms of strength and stiffness degradation based on the oxidation level of the material in the composite (see eq(3.98)).

Let E_{ij}, G_{ij} and υ_{ij} be the original extensional moduli, shear moduli and Poisson's ratio respectively and $\overline{E}_{ij}$, $\overline{G}_{ij}$ and $\overline{\upsilon}_{ij}$ be the degraded extensional moduli, shear moduli and Poisson's ratio respectively. b_i $(i = 1..9)$ are the percentages by which the nine

engineering properties change when the material is completely oxidized. Remember that the oxidation level, Φ ranges from 1, which means un-oxidized to 0, which means fully oxidized. The amount of degradation is assumed to vary linearly with the oxidation level. Therefore, a typical property degradation scheme will look like:

$$\begin{aligned}
&\overline{E_{11}} = (1+(1-\Phi)b_1)E_{11}, \quad \overline{E_{22}} = (1+(1-\Phi)b_2)E_{22}, \quad \overline{E_{33}} = (1+(1-\Phi)b_3)E_{33} \\
&\overline{G_{12}} = (1+(1-\Phi)b_4)G_{12}, \quad \overline{G_{23}} = (1+(1-\Phi)b_5)G_{23}, \quad \overline{G_{13}} = (1+(1-\Phi)b_6)G_{33} \\
&\overline{\upsilon_{12}} = (1+(1-\Phi)b_7)\upsilon_{12}, \quad \overline{\upsilon_{23}} = (1+(1-\Phi)b_8)\upsilon_{23}, \quad \overline{\upsilon_{13}} = (1+(1-\Phi)b_9)\upsilon_{33}
\end{aligned} \tag{3.137}$$

For example, if E_{11} is reduced by 20% when the material is fully oxidized, then $b_1 = -0.2$. If the E_{11} property needs to be degraded for a material that has an oxidation level of 0.3, the new modulus, according to eq(3.137) would be given by

$$\overline{E_{11}} = (1+(1-\Phi)b_1)E_{11} = (1-0.7\times 0.2)E_{11} = 0.86E_{11} \tag{3.138}$$

Note that in this general framework, the diagonal as well as non-diagonal entries of the compliance matrix can be affected independently.

Similarly, the strength can also be degraded based on the amount of oxidation the material has undergone. In this work, the strengths under compression are assumed to be the same as the strengths under tension. Let S_i, $(i = 1..6)$ denote the original strengths of the material in the different stress components (in Voigt notation) and $\overline{S_i}$, $(i = 1..6)$ be the degraded strengths. Let the strength degradation parameters, d_i, $(i = 1..6)$ be the corresponding factors by which the strengths would be degraded if the material was fully oxidized. Again, a linear dependence on the oxidation level, Φ is assumed. Therefore, the strength degradation scheme will look like the following

$$\overline{S_i} = (1+(1-\Phi)d_i)S_i \tag{3.139}$$

The specific details of property degradation scheme used in this work including the degradation factors used for the different materials will be given in Section 9.

The two degradation schemes involved with the coupled analysis, that is, one based on the stress state/mechanical damage, and the other based on the oxidation, need to be aggregated to provide the overall mechanical properties of the material based on the oxidation level and the mechanical damage. At each time step, this overall set of properties will be used to perform the stress analysis in the damage progression model, and then check for new damage based on the failure criteria. In this work, a procedure has been implemented to combine the two degradation schemes. This procedure in the coupled analysis algorithm would correspond to the box in Figure 3.6 that is labeled 'Modify mechanical properties based on current oxidation state and damage state'. Let us consider the procedure for a material point in the configuration. The procedure takes the initial mechanical properties for the material and the current oxidation and damage state as input and returns the modified mechanical properties. The procedure is as follows. The initial mechanical properties are modified following the degradation scheme based on the oxidation level. At the end of this first step, the compliance matrix has been modified according to eq.(3.137), and the strengths have been modified according to eq.(3.139) In the second step the new properties are then modified again based on the degradation scheme based on mechanical damage. Therefore, at the end of the second and final step, the properties obtained from the first step are then modified according to eq.(3.41). In reality, the order of the steps do not matter and the overall elastic moduli can be summarized as follows

$$\begin{aligned}
&\overline{E_{11}} = \left[\frac{(1+(1-\Phi)b_1)}{a_1}\right]E_{11}, \quad \overline{E_{22}} = \left[\frac{(1+(1-\Phi)b_2)}{a_2}\right]E_{22}, \quad \overline{E_{33}} = \left[\frac{(1+(1-\Phi)b_3)}{a_3}\right]E_{33} \\
&\overline{G_{12}} = \left[\frac{(1+(1-\Phi)b_4)}{a_4}\right]G_{12}, \ \overline{G_{23}} = \left[\frac{(1+(1-\Phi)b_5)}{a_5}\right]G_{23}, \quad \overline{G_{13}} = \left[\frac{(1+(1-\Phi)b_6)}{a_6}\right]G_{33} \\
&\overline{\upsilon_{12}} = \left[\frac{(1+(1-\Phi)b_7)}{a_7}\right]\upsilon_{12}, \quad \overline{\upsilon_{23}} = \left[\frac{(1+(1-\Phi)b_8)}{a_8}\right]\upsilon_{23}, \quad \overline{\upsilon_{13}} = \left[\frac{(1+(1-\Phi)b_9)}{a_9}\right]\upsilon_{33}
\end{aligned} \tag{3.140}$$

The overall strengths would be simply those given by eq.(3.139) because the degradation scheme based on mechanical damage does not modify the strengths of the material.

3.7 Summary

The common aspects of some of the different analyses were discussed in this section and a common analysis procedure was determined that can be used to help design an analysis framework. The procedure is then used to derive the theory and equations involved in the different analysis models used in this work. The finite element formulations for the models were derived and the algorithms for the analysis were discussed. It also discusses the strategies involved in analyzing periodic configurations and obtaining effective properties for periodic microstructures. The models described in this section are implemented in a finite element analysis framework that is described in the next section.

4. DESIGN OF FINITE ELEMENT FRAMEWORK

4.1 Introduction

Based on the requirements of the analysis models used in this work and the fact that the models are not convenient to implement in commercial codes, it was determined that a finite element framework would be designed to serve the needs of this work. This section describes the design of the framework including its salient features. The major components of the framework will be discussed along with a brief description of what would be required to implement a new analysis method or tool. Please note that basic knowledge of object oriented programming and C++ is recommended for reading certain sections of this section.

4.2 Why Object-Oriented Design?

The goal was to design a robust framework that can be enhanced and extended in the years to come by future users and lives beyond the term of this research work. The framework was developed keeping the following features in mind:

- Flexible: It should provide a collection of basic building blocks and functions which can be used to build different tools in the framework. The re-use of these primitive classes and functions leaves less work for the developer to do.
- Accessible: Having open/free access to the source code goes a long way in being able to understand how a program works. This would help other students and researchers understand how the different implemented methods work. Understanding how the software works also makes it easier to tailor tools to work for specific needs. Another aspect of having full access to the source code is that it makes it a lot easier to interface with external utilities.
- Extensible: With the framework essentially being a research code, users should be conveniently able to extend the framework to be able to perform their specific types of analyses. By being able to build on what is already present rather than starting

from scratch, the users can easily implement their own analysis methods or functions or post-processing tools as needed.

Keeping these requirements in mind, the object-oriented programming paradigm appeared to be the most favorable option. As described in section 2.1.1, object-oriented programming became increasingly popular through the 90's and eventually, a number of finite element packages were developed using object-oriented programming languages such as C++. Older programs written in FORTRAN, which had been the language of choice for scientific and numerical tasks, tend to be monolithic and difficult to maintain and extend even though some of them have very good functionality. On the other hand, the object-oriented programming paradigm provides superior features in terms of ease in designing, maintaining, modifying, and extending the software. By following an object oriented philosophy, the developers also run a smaller risk of unknowingly propagating errors to other parts of the code while enhancing its functionality.

The object oriented design philosophy allows for the requirements listed above using features such as encapsulation, data abstraction, inheritance and polymorphism. These features are described here very briefly. *Encapsulation* is the ability to store data and function in a single unit, known as a *class* in object oriented terminology. In comparison to the terminology used in regular procedural programming, the *class* is similar to *structs* or basic data types such as *int* or *char*. The instantiation of a particular data type is called a *variable* in regular procedural programming. Similarly, the instantiation of a *class* is known as an *object*. *Abstraction* allows representing essential features without including the background details or explanations. Classes use the concept of abstraction and are defined as a list of abstract attributes. *Inheritance* allows a class to have the same behavior as another class and extend or tailor that behavior to provide special action for specific needs. The new class that inherits behavior from an existing class is called the derived class or child class and the existing class is called the parent class. Simply stated, *polymorphism* is the ability to use a general interface to manipulate things of various specialized types. These features make it possible to build software using software components that correspond to real-world high level entities. There are several books

that describe the object-oriented programming design and C++ in particular [169]. Jun Lu et al [20] details the advantages of using an object oriented design for finite element programs. Following a good object oriented design philosophy makes the code a lot simpler, flexible and allows for extensibility, reusability and reliability.

4.3 Framework Design

The finite element framework, which is called ‘BETA’, is a successor to the existing in-house finite element code, "ALPHA". The new framework has several enhancements over the existing in-house code in order to meet the needs of this work. Rather than building the new framework from scratch, a number of the classes and subroutines from the existing code was adapted and enhanced to build BETA. Simply stated, the framework is a collection of libraries or modules that can be used to build a program to perform a step in the finite element analysis. The libraries consisted of different classes, data-structures and subroutines. This section will give an outline of the main modules that make up the BETA framework. There are four modules or libraries that are required to perform a basic structural finite element analysis – Core_library, Math_library, FEM_library and Utility_library. The following sub-sections will give a description of each module.

4.3.1 Core_library

The core_library contains the parent classes that define entities in a finite element analysis such as the model, mesh, elements, nodes, materials, loads and constraints. Each of these parent classes only contain the common data and functionality that is required by all types of FEM analyses, but not enough information required for specific analyses such as a 3D structural stress analysis. In order to achieve specific functionality such as that for a stress analysis, appropriate classes would need to be derived or inherited from the parent class using the *inheritance* feature of the C++ language. The new derived class would contain the required functionality and data for performing a stress analysis. The classes present in the core_library, many of which are self-explanatory, are:

- *Node* : class that defines a node in a finite element mesh

- *BasicElement* : parent class that defines an element in a finite element mesh
- *BasicMesh* : parent class that defines a finite element mesh. This class contains a list of nodes and elements.
- *Material* : parent class that defines a material in the finite element model
- *Load* : parent class that defines a load applied on the finite element model
- *Constraint* : parent class that defines a constraint applied on the finite element model
- *BasicModel* : parent class that defines a finite element model. Just like the different components that make up a finite element model, this class contains pointers to a finite element mesh and a list of materials, loads and constraints, as illustrated in Figure 4.1.
- *ElementWorkspace* : parent class for a data structure used as a temporary workspace for storing information when performing calculations such as the element stiffness matrix.
- *Factory* : parent class that contains the functionality to create objects of specific elements, materials and models.

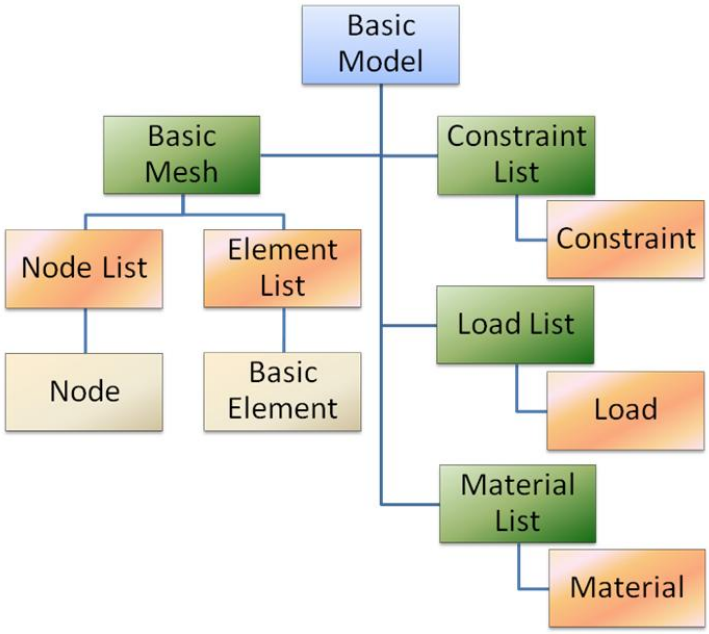

Figure 4.1: Illustration of different members that are part of the BasicModel class

4.3.2 Math_library

The math_library contains the classes that define the set of equations associated with the finite element model such as the global stiffness matrix and the global load vector. This library also contains the finite element solvers and interfaces to external solvers libraries. The main classes in this library are:

- *Equations* : this is the main class that handles the equations related to the finite element model. This class contains pointers to the sparse matrix, the load vectors and other vectors related to the global set of equations. This class also contains the functionality to assemble the set of equations for the finite element model as well as other routines such as those to calculate the residual. The BasicModel class contains an Equations class data member. This Equations data member acts as the important link between the finite element model and the global set of

equations it represents. The Equations class also acts as the interface between the model and the finite element solver.

- *LargeMatrix* : parent class that define the large sparse matrices such as the global stiffness matrix of the finite element model. The *LargeMatrix* class itself does not provide any storage ability or functionality to solve the set of equations defined by the sparse matrix and a load vector. The classes that are derived from the *LargeMatrix* class implement the actual storage and solving capability. The derived classes can also serve as interfaces to external solvers such as the PARDISO solver [36] in Intel's Math Kernel Library (MKL)[170]. One such class is described below.
- *MKLPardisoSymmMatrix* : This class is derived from the *LargeMatrix* class to implement the PARDISO solver for symmetric sparse matrices available through Intel's Math Kernel Library (MKL). The PARIDISO [36] solver is a parallel direct solver that uses the OpenMP parallel programming paradigm.
- *AdditionalEquation* : This class defines additional constraint equations that are added to the finite element model. This class is instrumental in the handling of multi-point constraints (MPCs) in the finite element model.
- *Matrix* : This class is used to for storage of matrices that are much smaller compared to the global stiffness matrix, such as the compliance and stiffness matrix, or the element stiffness matrix. This class also has the functionality to perform matrix operations such as multiplication.

Other solvers that have been implemented in the BETA framework include a serial as well and parallel (for 2 processors only) iterative conjugate gradient solver, a direct symmetric matrix solver from the Watson Sparse Matrix Package [171] and the symmetric matrix solver from PETSc [45-46].

4.3.3 FEM_library

The FEM_library is primarily a collection of specialized classes derived from the classes in the Core_library module. It contains the specialized classes required to perform a

structural stress analysis. For example, the *ElasticityModel* class which is a part of the FEM_library, is derived from the *BasicModel* class. The *ElasticityModel* class contains additional capabilities compared to the *BasicModel* class such as the functions to post-process data such as stresses and strains. Similarly, the *ElasticityElement3D* class is derived from the *IsoElement* class, which in turn is derived from the *BasicElement* class. The *IsoElement* class brings new functionality in terms of the ability to handle numerical integration and isoparametric formulations. Because of this, the *IsoElement* class serves as the ideal starting point for the development of many different element classes such as those for elasticity as well as diffusion and heat transfer. Figure 4.2 shows the inheritance tree indicating some of the element classes that have been derived from the *BasicElement* class. The *ElasticityElement3D* class adds the capability to calculate the element stiffness matrix and the associated finite element expressions that are specific to modeling elasticity problems. The *ElasticityModel* class also has the functionality to read and implement multi-point constraints, which are used in this work to analyze models with periodic or symmetry boundary conditions. There are also classes in the FEM_library that allow the element classes to use numerical integration to evaluate the finite element expressions. The *ElasticMaterial* class, which is derived from the *Material* class, contains the data members to store the engineering properties of the materials in the finite element model. It also has the functionality to calculate

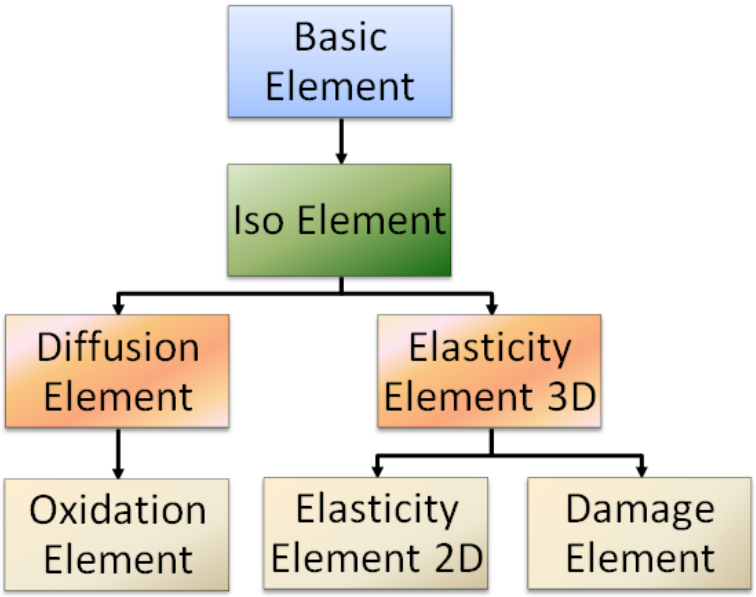

Figure 4.2: Inheritance tree for the BasicElement class

the material compliance and stiffness matrix as well as calculate the stress state given a strain state. The FEM_library also contains the *FactoryFEM* class that is derived from the *Factory* class in the Core_library. The *FactoryFEM* class contains the functions that can create objects of specific elements such as the *ElasticityElement3D* or *ElasticityElement2D*.

Overall, the classes in the FEM_library along with the classes in the Core_library form the basic building blocks for a finite element analysis package.

4.3.4 Utility_library

The Utility_library consists of support functions and classes that are perform tasks that are not essentially associated with the finite element analysis. They do not depend on the classes in any of the other modules in the BETA framework and can be used independently. On the other hand, all the other modules in the framework are dependent on the Utility_library. They provide higher level functions for performing certain tasks thereby making the coding simpler and more readable. For example, consider a task that requires searching for a file from a list of possible directories and opening the file when

it is found. This task would typically take a few lines of code. On the other hand, this could be converted into a subroutine. Therefore, rather than inserting this block of code into the source code each time this step needs to be performed, the utility function could be used which would take a lot less number of lines.

One of the more important classes in the Utility_library is the *FileManager* class. This class handles all functionality related to opening and closing of files for the analysis. This includes input files and output files. It keeps track of the working directories and other directories in the search path. This way, the developer can focus on the details of the finite element analysis rather than spend valuable time on low-level steps such as file-operations.

Another important utility class is the *Stopwatch* class and its accompanying subroutines. These functions handle the timing requirements for the BETA framework. Knowing how much time is spent in different steps of the analysis is helpful in making enhancements to make the code more efficient.

4.3.5 Using the Framework

The ability to re-use the classes and routines available in the framework libraries makes it very convenient for the user to implement their own finite element analysis tool. The framework has been developed so that it can be used in both the Windows as well as the UNIX/LINUX platform. The differences between the two platforms are accounted for by developing functions that check for the platform using compiler directives that conditionally compile parts of the code based on the platform. In this manner, the functions and classes in the BETA framework can be used safely without worrying about portability issues. Take for example the utility function to search for and open a file in one of the directories in the BETA path. This involves changing the working directories to each one in the BETA environment variable until it finds the file. In the Windows platform, the C++ system function to change directories is '*_chdir*' whereas in the UNIX/LINUX platform, the corresponding function is '*chdir*'. The utility function for changing directories in the BETA framework has been implemented such that the line in

the source code with the appropriate function is compiled when the application is built in any particular platform. Therefore, calling the same function will work in both platforms and only one copy of the source code needs to be maintained rather than a separate copy for each platform. The same technique is used to make the source compatible between 32-bit and 64-bit machines.

Although the BETA framework is portable across different platforms, the source code development is typically done in the Windows platform because of its user-friendly environment and ease with debugging. When the application is required on another platform, the source code is simply copied over and compiled using the appropriate compiler. The Microsoft Visual Studio environment is used to maintain and develop applications using the BETA framework. A Visual Studio *solution* contains all the settings for the compiler and linker and other such information to generate the executable. The BETA framework contains a few standard *solutions* that can be used to build finite element applications such as those for 1D rod or beam FEA or 3D elasticity. When the user needs to build a finite element application that implements a new specialized method that is not already present in the BETA framework, a new *solution* needs to be created that contains the necessary source files that implement the new method. The new source files could include new subroutines or classes derived from the existing classes in the BETA framework. The new *solution* could also require a new Factory class if a new Material, Element or Model class was developed.

For example, the analyses performed in this work required implementation of a damage progression analysis method. The theory behind the damage progression analysis is described in Section 3. Note that most of the underlying finite element formulations for the damage analysis are the same as the elasticity analysis. Therefore, the new classes do not need to be developed from scratch. Instead the new classes can inherit from the classes that are used for the elasticity analysis and only the new functionality needs to be implemented in the derived classes. Some of the new classes that were implemented are the DamageModel, DamageElement and the DamageMaterial classes. The DamageModel class was inherited from the ElasticityModel class. One of the functions

that were implemented in the new DamageModel class was the executive that implements the algorithm illustrated in Figure 3.1. The DamageElement class was inherited from the ElasticityElement3D class and only the functionality that had to do with accounting for damage in the element had to be specifically implemented. Similarly, the DamageMaterial class was derived from the ElasticMaterial class and it added certain functionality such as degrading the material properties based on the amount of damage. This type of software design avoided

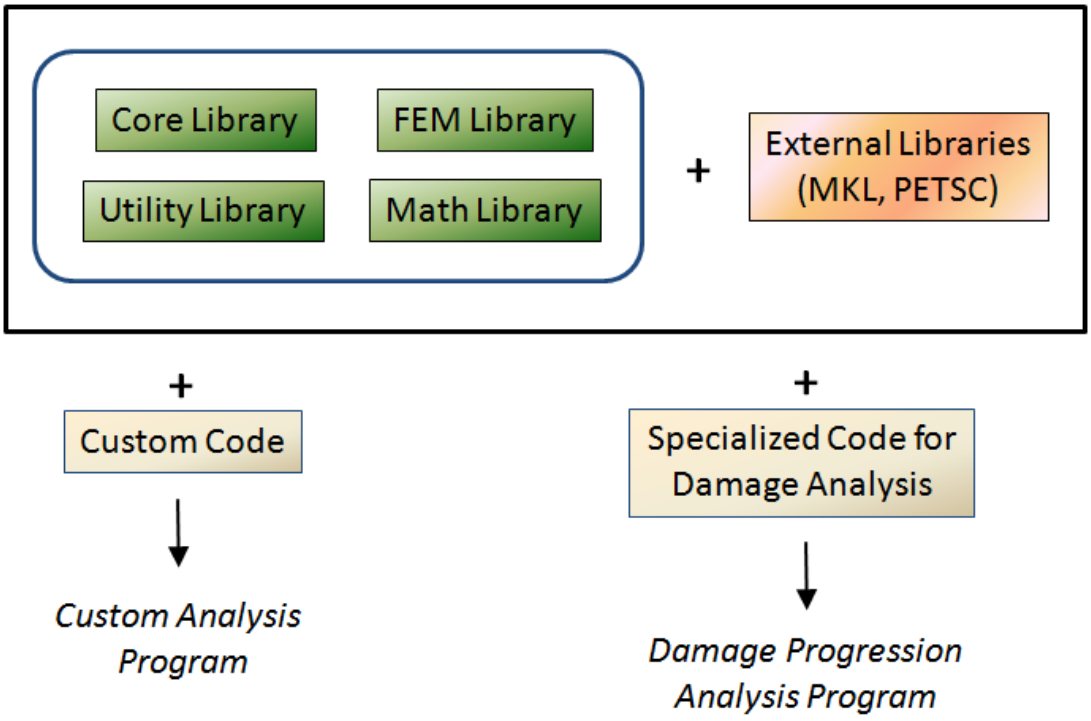

Figure 4.3: Using BETA to implement a specialized method

repeating huge blocks of code and allowed code re-use whenever possible. This makes it easier to manage because a change made in a block of code in a parent class would propagate to all the derived classes. Figure 4.3 gives an illustration of the components required to build a specialized FEA program using the BETA framework.

The BETA framework has been used to implement the B-Spline finite element method, which can potentially give a more accurate result for a smaller number of degrees of

freedom than a standard analysis. Owens [172] has evaluated the performance of B-Spline FEA using 2D and 3D elasticity configurations. In particular, the oxidation model, the damage progression model and the coupled analysis model which was described in Section 3 and used for studying the behavior of textile composites in this work was developed using the BETA analysis framework.

4.4 Other Applications

The framework is also used to build tools other than the main finite element analysis program. The framework is used to build tools for visualizing the results from the finite element analysis. One such tool is the 'Plotter', which was built using the classes and the functions from the BETA framework. Plotter is used to visualize finite element meshes as well as results such as displacement and stress contours. Plotter was also implemented in a manner similar to how the specialized analysis methods were implemented, where new classes were derived from the existing classes in the framework.

Plotter uses OpenGL and Microsoft Foundation Classes to implement a Windows version of the software with a GUI. This make it convenient for the user to visualize the results interactively and change different settings such as contour limits instantaneously. *Plotter* also has a command-line version for cases when it is more convenient to generate a collection of figures automatically. The command-line version of Plotter generates figures as files in the GIF or PostScript format. These files can then be modified further using any of the various advanced image editing software available.

One of the advantages of a visualization tool based on the BETA framework over commercial applications is that it can have direct access to the data structures in the framework or any specialized method developed by a user using the framework. This gives the user full control over how to visualize or perform operations on the data from a specialized analysis method.

The framework can also be used to develop non-standard post-processing techniques. Post-processing utilities can be developed that are specialized for a particular type of analysis. One such post-processing utility was developed to study the behavior of textile

composites. Full 3-D finite element models of textile composites attempt to model the geometry as truly as possible. Since these models make a lot fewer assumptions than the much simpler models described in Section 2.2.1, it also inadvertently gives less basis for developing an intuitive understanding of the textile composite behavior. The full 3-D models give a tremendous amount of raw numerical information but it is harder to quickly extract the important details regarding the behavior. For example, the stress contours for the 3D stress state in a 5 harness satin weave shown in Figure. 2.2 give a lot of detailed information, but no framework for interpretation. The post-processing utility that was developed digests the massive amount of output data and converts it into comprehensible modes of behavior. The full 3D finite element results are post-processed to obtain stress resultants, such as the axial force or moment in the tow. The post-processing subroutine automatically detects and traverses the tow under consideration while tracking the stress resultants across the cross-section. Figure 2.6 illustrates typical results for an elastic analysis. It can be seen that both Fx and Fz have highest values where the tow undulation is maximum. Since these stress resultants are obtained from refined 3D models, the results are much more reliable than one could obtain by using a simplified model. It should be noted that these post processing techniques are not meant to eliminate the details. These techniques were used by Goyal [5] in various ways to investigate textile behavior.

4.5 Summary

The BETA framework was developed to serve the needs of the analysis requirements of this work. An object oriented design using the C++ language was chosen due to the numerous advantages it gives over the older procedural programming design. An analysis environment that was developed in-house also gives full control over the analysis as compared to commercial finite element packages. A brief description of the framework was provided in this section. Some of the specific implementations that were developed using the framework were also discussed.

5. MULTISCALE ANALYSIS OF WOVEN COMPOSITE DCB

5.1 Introduction

The finite element framework that was developed as part of this work is used to analyze a Double Cantilever Beam (DCB) specimen fabricated with woven composite. Such a configuration contains many microstructural scales such as fiber/matrix, tow architecture and laminate as illustrated in Figure 2.9. The problem becomes impractical to solve if the entire configuration is to be modeled at the same length scale as its complex microstructure. A literature review showed no previous work on FE simulation of a DCB test that considered complex microstructure. Shindo et al [173] used a micromechanics model to obtain effective properties for a plain weave composite and then used these properties to conduct an FE analysis of the DCB specimen. Numerical simulation of such a test has a number of challenges because of the complexity of the microstructure. In many cases homogenizing the microstructure of a laminate could give an incorrect prediction for the response of the material. For example, the flexural stiffness for both a $[90_n/0_n]_s$ and a $[0_n/90_n]_s$ lay-up would be the same if the material was homogenized.

In order to perform the multiscale analysis, a hierarchical strategy is implemented where the natural hierarchical character of model descriptions and simulation results are exploited to expedite analysis of problems. Hierarchical techniques were used in the development, organization, and management of finite element models, and for the post-processing of the results from the analyses. The next section gives a brief overview of the hierarchical strategy. This is followed by a description of the configuration and the modeling. Finally, the results of the multiscale stress analysis on the DCB specimen are presented.

5.2 Hierarchical Analysis Strategy

When conducting a detailed stress analysis of the DCB specimen, the region around the crack tip would be modeled discretely at the lamina scale with the tow and matrix or maybe even at a smaller fiber/matrix scale. The region away from the crack tip can be modeled at a larger microstructural scale assuming that the homogenized properties

simulate the load transfer to the crack tip region accurately. When there are multiple scales in a single problem, managing the information from each scale can become intractable. The information could include model attributes such as the mesh, material properties, load and boundary conditions or analysis results like displacements and stresses. The book-keeping and transfer of this information between different scales in a finite element analysis takes up considerable effort on the part of the analyst. There are many factors that govern how quickly one can perform analysis of a structural configuration. When using finite elements, the steps typically consist of defining a solid model, converting the solid model into a finite element mesh, preparing the non-geometric data input (such as material properties and boundary conditions), using a finite element solver to solve the equations and provide the solution in terms of displacements, stresses, etc., and most importantly interpret the results. Each of these steps can be quite time consuming in terms of computing power and human involvement. Certain hierarchical aspects involved in analyzing a problem can be exploited to reduce the analysis time. This strategy, which was introduced in an earlier work [156] can be applied to solve a problem faster and makes it easier for the analyst to manage the models and its results. The strategy was developed and implemented in collaboration with Tang and Whitcomb. In the previous work [156], these concepts were demonstrated by using the hierarchical environment to conduct a two dimensional global/local structural analysis of the side panel of an airplane fuselage. The system was also used to conduct a micro mechanical analysis on unidirectional composites that have a non-uniform spatial distribution of the fibers.

An analysis environment using this strategy to store and handle information at different scales can be used to better manage, manipulate and control a multi-scale analysis. Commercial software such as DesignSpace by AnSys [114], SIMBA (Simulation Manager and Builder for Analysts), developed by Sandia Labs [116] and NextGRADE by NASA [174] builds FE models from various components but they do not address data flow between different models in a multiscale analysis. One of the most important characteristics of this strategy is inheritance. Inheritance is a term that is closely related

to hierarchies. Here, the concept of inheritance is used to create a hierarchy of analysis models. In this work, the term “hierarchical strategy” is used to convey the idea that analysis models can be organized and managed hierarchically in order to rapidly set up a new analysis model. New models are derived from an existing model whose information is either inherited or overridden by the new model. That is, the analytical tools are integrated such that a new model can be derived from an existing model without starting from scratch. For example, an initial step in analyzing a complex structure would be to use a coarse model. Depending on the results of the first analysis, the analyst might decide to refine a certain part of the coarse model to get a more detailed stress distribution. The analyst could also decide during the design process to make changes to certain parts of the structure. In these cases, all the analyst has to do is specify the ‘difference’ or the ‘changes’ that need to be made to the existing model. These ‘changes’ are known as the Components in the terminology used in this hierarchical strategy whereas the new model that includes properties from the existing model as well as the component is known simply as the model. The existing model is known as the base model while the new model is called the derived or child model. The inheritance applies to different aspects of the model from geometric mesh information or material properties to load or boundary conditions to even solutions of analysis models. All the analyst needs to do is specify the ‘component’ and the system takes care of building the new model. Therefore, changes in geometry, material properties, simplifying assumptions, loads, etc. can be propagated through a collection of models via inheritance. The hierarchical strategy shares much with classical global/local methods, but supplies much more “infrastructure” to expedite analysis, especially parametric analysis.

One of the most important aspects of this philosophy is the sharing of data by models in the hierarchy. This feature makes it ideal for cases like global/local analysis where results from a global analysis are used to provide the boundary conditions for the local model. Efficient data flow mechanisms are required and recursive functions were developed that traverse the hierarchical tree to implement this flow. This kind of

recursive strategy can be used to access data belonging to any model in the hierarchy. The recursive strategy is designed such that it can be used to perform tasks on particular models or a collection of models in the hierarchy. This mechanism gives a model in the hierarchy the ability to ‘interrogate’ another model for information. Many of the features of the hierarchical strategy such as inheritance are built on the backbone provided by this mechanism.

A robust as well as efficient mechanism was designed for implementing inheritance of geometry. This involved automatic mesh generation for a model based on the information from its base model and the component. The mesh generation follows a z-order component mesh association. This means that a component lower in the hierarchy replaces any part of a component higher up in the hierarchy that occupies the same region in 3D space. This concept can be illustrated by a simple two dimensional case shown in Figure 5.1. Three components are used to build hierarchical models and the corresponding model at each level is shown on the right. Thus, a component can replace elements over a number of components in its model path and not just its immediate parent model alone. The procedure to generate the mesh for a hierarchical model is more difficult when dealing with complicated geometries. At present, the system can handle inheritance of rectangular parallelepiped regions.

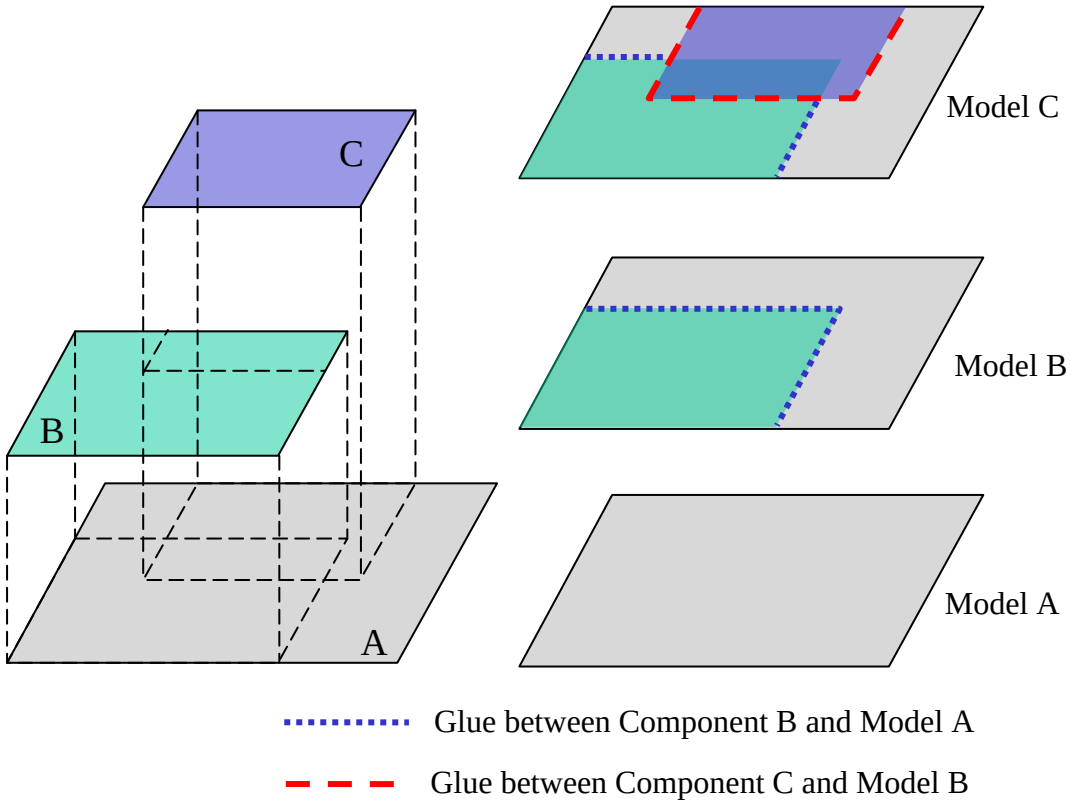

Figure 5.1: Inheritance of geometry and ‘joining’ components

When creating an analysis model, the different components in the hierarchical model needs to be ‘glued’ in order for it to behave as a single structure. In this system, the components are ‘digitally glued’ by imposing multi-point constraints between nodes on the boundary interface in order to impose continuity of displacement. Again, Figure 5.1 shows that nodes in one component could be slaved to nodes in a component a few levels down the model path. This process is automated to achieve considerable savings in the analyst’s effort. The strategy used in analyzing this problem utilizes a robust boundary matching and sorting algorithm. The boundaries of the components are detected and matched with the corresponding component. The nodal positions of the more refined component boundary are then expressed in terms of the local coordinates of the boundary elements on the matching component. With this information, the nodes of

the more refined component (which is usually the smaller microstructural scale) are then slaved to the master nodes on the other component by generating multi-point constraints that impose continuity at the interface between the different components of the model. Joining of dissimilar meshes at the interface is a common feature offered in most modern FEA. Alternate methods of imposing continuity such as using Interface elements [111] can be implemented into the system. A detailed discussion of the implementation of the inheritance is given in reference [156]. Several strategies are integrated into the analysis environment: classical homogenization of periodic media, spatially varying homogenization, macro elements [101-102], in situ homogenization [175] and various global/local methods for local refinement of models. A key characteristic of the environment is the ability to use various techniques in the same simulation and to easily change the techniques in the simulation as deemed necessary.

5.3 Configuration

The DCB specimen is assumed to be made of a laminate with 10 plies and plain weave tow architecture is assumed for the woven laminate. Figure 5.2 gives the dimensions of the DCB specimen that was analyzed. Aluminum tabs were added to the top and bottom surfaces to represent the hinges on the DCB. Owing to symmetry, only a quarter of the specimen needs to be modeled. Figure 5.2 also shows the finite element model for the DCB laminate and the boundary conditions that were imposed. Three-dimensional 20-node isoparametric elements were used for all the models. The crack length (a_0) was taken to be 75mm. A load of 1N was evenly distributed along the edge of the tab.

The laminate is assumed to be fabricated using S2 Glass and SC-15 Epoxy. The orthotropic properties of the tows were calculated using an FE micromechanics model assuming a 78.5% fiber volume fraction. The tow fraction of the weave was 63.6% making the overall fiber fraction of the laminate 50%. Figure 5.3 shows the finite element model and dimensions for a plain weave full unit cell. The waviness ratio for the laminate was assumed to be 0.15. Effective properties for the weave were used to model the regions away from the crack tip. The effective properties of a plain weave laminate (with symmetric stacking) were calculated using an FE micromechanics model that used

only 1/32 of the unit cell by employing symmetry conditions. Table 5.1 gives the material properties that were used for the finite element models.

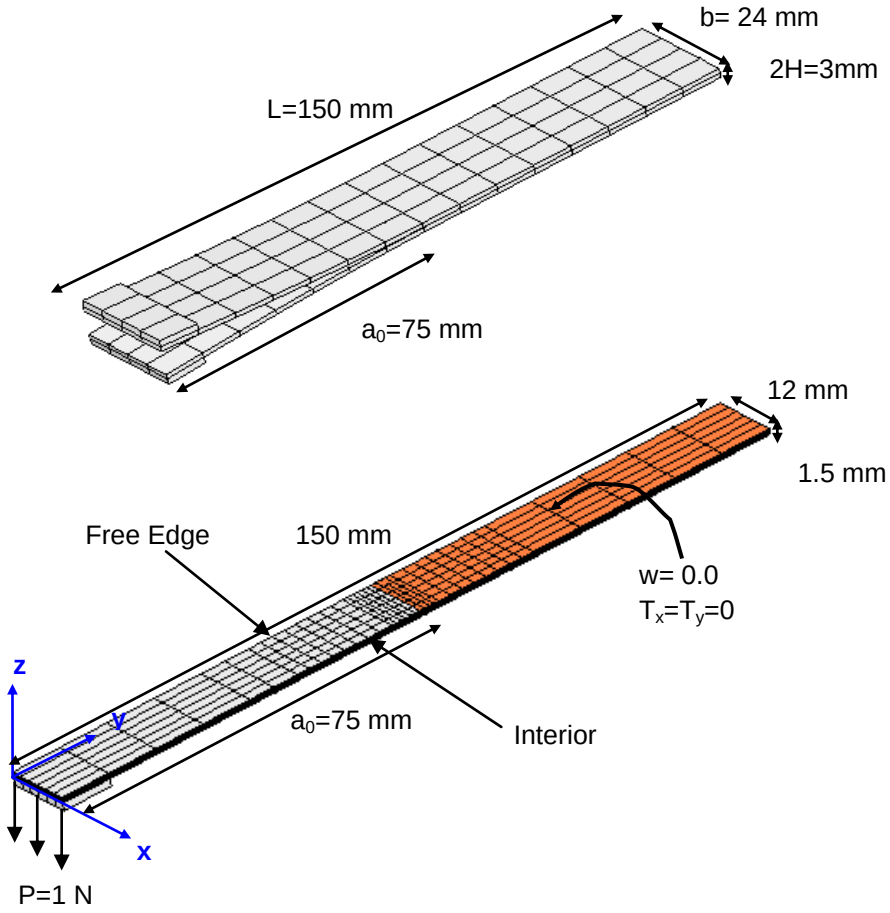

Figure 5.2: Finite element model of DCB laminate

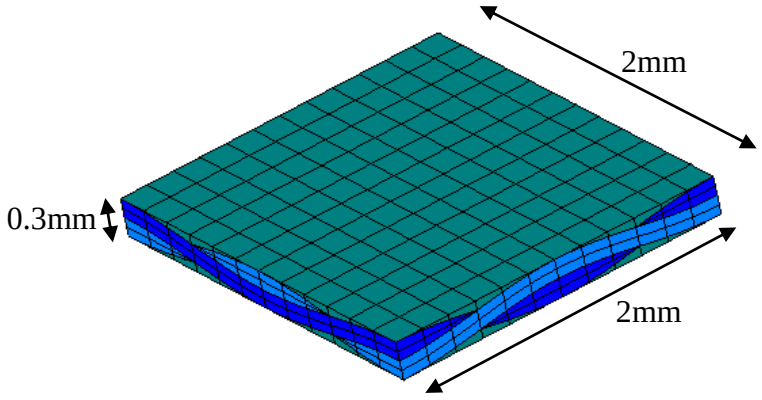

Figure 5.3: Finite element model of plain weave unit cell

Table 5.1: Material Properties used in DCB finite element model

Material	Mechanical Properties
S2 Glass/Epoxy Tow	E_{11}=76.42 GPa , E_{22}=E_{33}=20.18 GPa, υ_{12}= υ_{13}=0.26 , υ_{23}=0.33, G_{12}=G_{13}=7.4 GPa, G_{23}=4.03 GPa
Neat Epoxy (SC-15)	E= 2.82 GPa, υ=0.395
Effective Weave Properties	E_{11}=E_{22}=30.1 GPa, E_{33}=10.6 GPa, υ_{12}=0.114, υ_{13}=υ_{23}=0.418, G_{12}=4.5 GPa, G_{13}=G_{23}=2.6 GPa

5.4 Analysis of DCB Specimen

Although the finite element analysis will not give the theoretical value of the stress at the crack tip, which is infinity, it is useful in identifying the trends in the stress variation due to its complex microstructure and loading. In addition to the stress distribution, the effect of the microstructure on the strain energy release rate (G_I) is also investigated. The method used to calculate the G_I is described in the next section. The other modes, G_{II} and G_{III}, do not exist since the geometry, material and loading are symmetric about the delamination plane.

The microstructure of a woven composite is at a larger scale than that of a tape laminate where fibers are aligned unidirectionally in a lamina. In general, the size of the microstructural scale can be defined by the size of the smallest periodic unit cell that can be used to homogenize the microstructure. In woven composites, there are at least two scales: a fiber tow scale and a larger woven layer scale where the tows form a weave. Due to the complex structure of the weave, the crack tip region should not be modeled using homogenized properties. At the very least, the tow architecture has to be considered. One could also go to a lower scale and consider the fiber/matrix scale in the tows. A thorough simulation of a DCB test would have to consider the effect of free edges and free surfaces of the laminate specimen. One difference with respect to a tape laminate specimen is that in a woven composite specimen, the complex tow architecture would affect the stresses at the crack front. The undulation of the tows as seen in the unit cell of a plain weave (Figure 5.3) would be expected to cause a varying stress distribution along the crack front, whereas in the case of a tape laminate there is no such undulation of tows.

Based on these considerations, a hierarchy of models was generated for conducting the multi-scale stress analysis of the DCB specimen. Figure 5.4 illustrates the hierarchy of different meshes that were used in the analysis. At each level, the component mesh was provided and the system generated the new mesh by inheriting the rest of the information from its parent mesh. This saved a considerable amount of time involved in model generation. A coarse mesh (Mesh 1) made of rectangular parallelepiped (or brick) elements was taken as the starting point for building the hierarchy of meshes. Mesh 2 was generated by providing the system with a mesh for the aluminum tab. From this mesh onwards, the hierarchy splits three ways depending on which part of the DCB is the region of interest. The right-most branch in the hierarchy shown in Figure 5.4 zooms in on the crack front in the interior of the DCB. An intermediate interior mesh was generated before the tow architecture was introduced (Mesh 3) in order to provide for a gradual refinement towards the length scale of the weave's microstructure. Mesh 3 discretely models the tows and matrix in the woven composite. The component mesh is

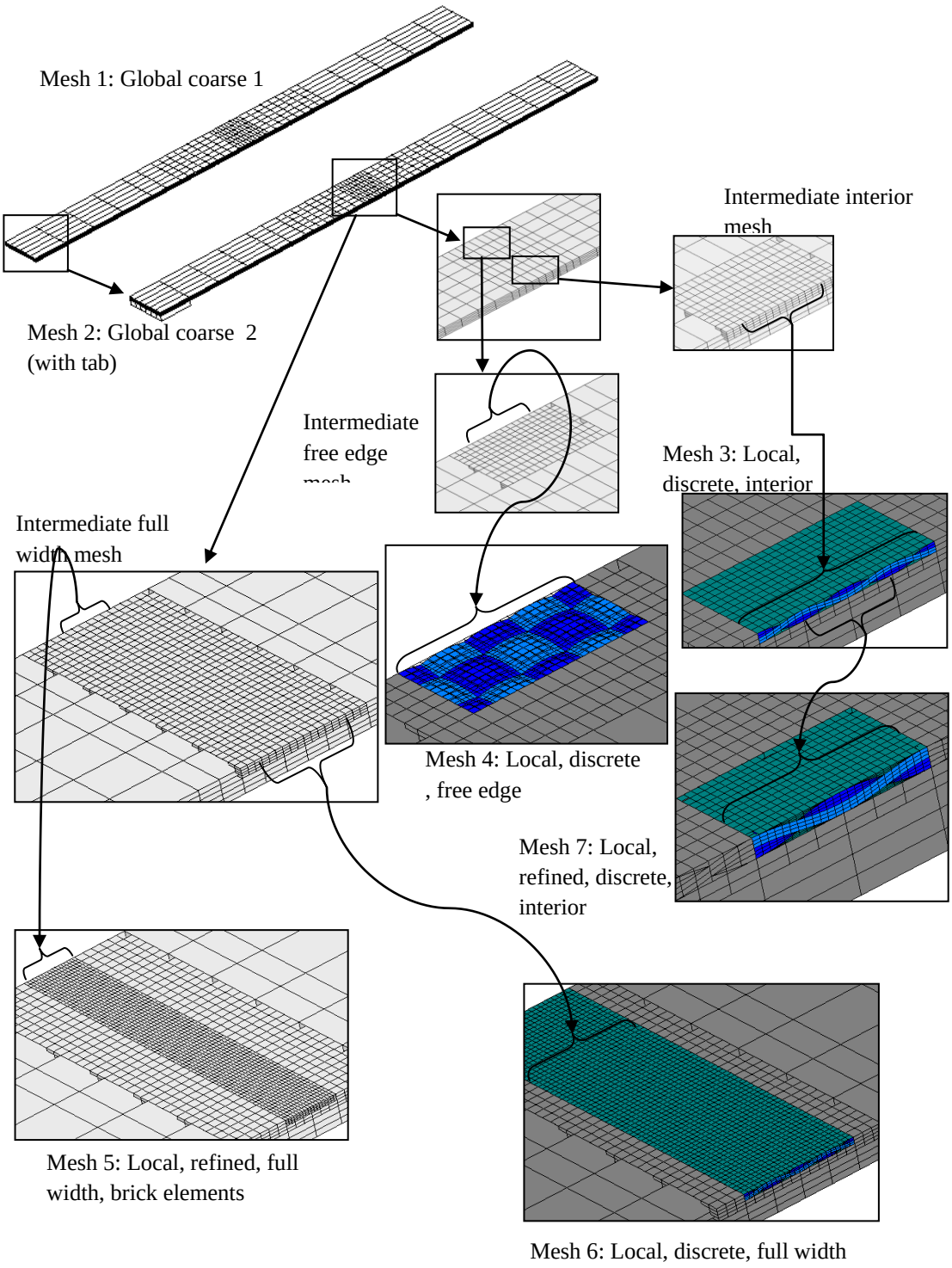

Figure 5.4: Hierarchy of finite element meshes (Mesh 7, 8 and 9 are not used in the current study)

made of two full unit cells that model the top ply in the bottom half of the DCB specimen. The other branch in the hierarchy (to its immediate left) refines the region on the crack front near the free edge. By way of an intermediate mesh, Mesh 4 in the hierarchy is created by using a discrete mesh similar to that used in Mesh 3. The matrix in Mesh 4 has been made transparent to show the underlying tows. The remaining branch models the full width of the model in order to verify the results obtained using the other branches as well as obtain the variation of stresses along the entire width of the DCB specimen. Again an intermediate full width mesh is used to bridge the variation in refinement. The hierarchy then splits into two more branches. Mesh 5 is generated using a refined mesh made of rectangular parallelepiped (or brick) elements. Mesh 6 is generated using a discrete mesh that spans the full width of the DCB along the crack front. Meshes 5 and 6 are considerably larger than the models in the other two branches since the entire width of the crack front is modeled using a refined mesh. In order to make comparisons of the results obtained using the discrete models that account for the variation in material properties with that using effective properties, the same meshes seen in Figure 5.4 were used to generate the models using effective properties.

The boundary-matching and model-joining algorithm is currently limited in the sense that it cannot be used to interface a general boundary or surface. The current implementation limits this feature to only flat surfaces and one of the surfaces in the interface has to be made of rectangular element faces. Due to these limitations, models using Mesh 7 cannot be currently analyzed.

5.5 Calculation of Strain Energy Release Rate

The strain energy release rate (G_i) distribution was calculated from the finite element analysis results using a post-processing routine. The Virtual Crack Closure Technique [176] was used to obtain the G_i distribution. The procedure for calculating the G_I uses the energy required to close the delamination over a short distance, Δa. The closure energy involves products of delamination front nodal forces and relative displacements behind the delamination front. The delamination front nodal forces can be determined by

actually closing the delamination over Δa. Another technique, which requires only a single solution, assumes that the current delamination front nodal forces are the same as they would be if the delamination length was reduced by Δa. The single solution method was used herein.

The strain energy release rate calculation will be illustrated for the 20-node element, since this element was used for all of the analyses. Figure 5.5 shows a schematic of the delamination front region. The nodes of interest for the strain-energy release rate calculations are indicated by the filled circles. Because it is not appropriate to close the delamination over part of an element, there are four sets of nodes (indicated by the letters a, b, c and d) which are used to calculate the closure energies. The relative displacements are obtained by subtracting the displacements at nodes a_i' and b_i' from the displacements at nodes a_i and b_i, respectively. Since only the lower half of the DCB specimen was modeled, the relative displacements were obtained by doubling the

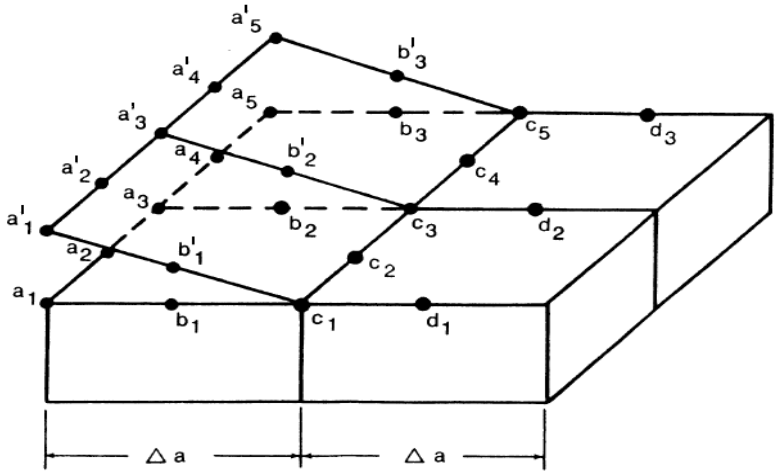

Figure 5.5: Schematic of the delamination front region

displacements at nodes a_i and b_i. The forces are equal to the nodal forces transmitted across the delamination plane at nodes c_i and d_i. The forces are obtained by evaluating

$\int C_{ij}\varepsilon_i \frac{\partial \varepsilon^i}{\partial q^\alpha} dV$ for all elements which are connected to nodes c_i or d_i. There are two sets of energy products. One of the sets of energy products consists of the relative displacements for nodes a_i and a_i' multiplied by the forces for nodes c_i. The other set of energy products consists of the relative displacements for nodes b_i and b_i' multiplied by the forces for nodes d_i. The energies equal ½ of these products.

Strain-energy release rate is a measure of energy per unit area. Hence, the energy products must be normalized by the appropriate areas. Unfortunately, there is not a simple exact way to determine the appropriate areas. The primary complication is that the midside nodes and corner nodes are "weighted" differently by the assumed element shape functions. The result is that, even if the strain-energy release rates are actually constant along the delamination front, there would be much larger energy products for the midside nodes than for the corner nodes. For example, in Figure 5.5, the energy products associated with nodes c_2 and c_4 would be much larger than for that associated with nodes c_1 and c_3. An approximate solution to this dilemma is as follows. The strain energy release is not calculated for locations like c_2 and c_4 along the delamination front. Instead, the energy products associated with those locations are split evenly between the adjacent nodes. For example, the energy associated with location c_3 along the delamination front becomes

$$\bar{E} = \bar{E}_{a_3 a_3' c_3} + \bar{E}_{b_2 b_2' d_2} + \frac{1}{2}\left[\bar{E}_{a_2 a_2' c_2} + \bar{E}_{a_4 a_4' c_4}\right] \tag{5.1}$$

$\bar{E}$ denotes the energy products associated with G_I and the subscripts indicate the nodes involved. The area is approximated by the product of Δa times the distance between the midside nodes on either side of the corner node being considered. For example, the area for node c_3 is Δa times the distance from node c_2 to node c_4.

5.6 Results and Discussion

This section presents the results of the stress analysis on DCB specimen. An initial coarse mesh (Mesh 2 in Figure 5.4) using effective properties of the weave is used to model the DCB. Additional hierarchical models are then used to incorporate the complex microstructure of the weave. The effect of the microstructure on the stress distribution and the G_I distribution are presented. The results of the interior and free edge models are compared with a larger model that uses a refined model along the full width of the beam. The stresses for all the models are extrapolated from the integration points to the nodal points. The stresses at a node are averaged between adjacent elements that have the same material properties.

5.6.1 Stress Distribution

A coarse model using Mesh 2 (Figure 5.4) was analyzed using the effective properties of the plain weave. The mesh was relatively coarse at the region near the crack front (2mm x 1mm x 0.3mm) but this model gave the a general trend of the stress distribution in the composite DCB specimen. The distribution of the out of plane normal stress (σ_{zz}), which is the component of main interest in this problem, is shown in Figure 5.6. Stress concentrations are seen at the crack tip which is what is expected when the two free ends of the double-cantilever beam are pulled apart. It was seen that the high stress gradients existed within an element's length on either side of the crack front. The maximum σ_{zz}

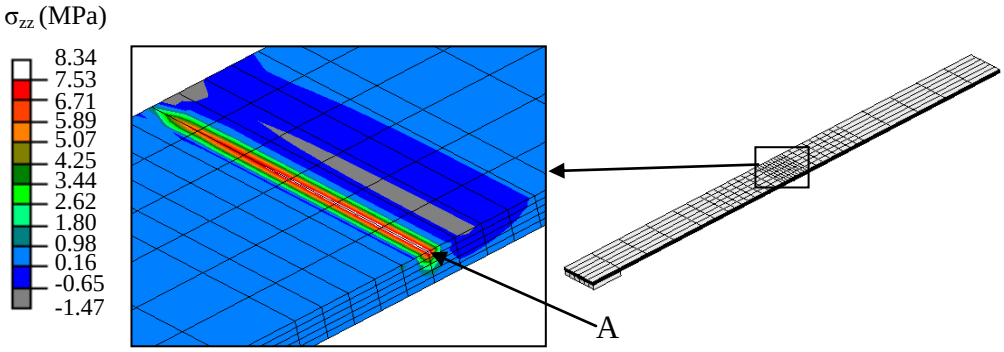

Figure 5.6: Distribution of σ_{zz} around crack front for the coarse global model with homogenized properties

stress component, which is indicated by location A in Figure 5.6, was calculated to be 8.34 MPa.

Two hierarchical models using Mesh 3 (Figure 5.4) were analyzed to obtain the stress distribution around the crack front in the interior. One model incorporated the variation in the material properties within the weave (discrete model) while the other used effective properties (homogeneous model) for the weave in all the elements. The elements near the crack front are refined such that the element size was down to 0.166mm in the x and y direction as opposed to 1mm and 2 mm respectively in the coarse global model. The refined model with homogenized properties gave a maximum σ_{zz} around three times as large (25 MPa). Figure 5.7 shows the distribution of σ_{zz} in the crack tip region at the interior of the DCB (using Mesh 3 in Figure 5.4). It is seen from the contour plots that the stress distribution along the crack front in the homogeneous model is almost constant. On the other hand, the discrete model with the tow and matrix properties has a high degree of variation. This can be attributed to the undulation of the tows in the woven composite and thus resulting in the variation of the material properties in the region around the crack front. The line plot in Figure 5.7 gives the stress variation along the crack front. It is seen that the maximum stress in the discrete model is over 2.5 times higher than in the homogeneous model. The periodic pattern of the stress distribution seems to be influenced by the pattern of the tows at the crack front. It can be seen that the highest stresses are in those regions where the tows that aligned along the long axis of the DCB are closest to the crack front. The other peak in the curve is when the tows aligned with the crack front are closest to the crack front. This suggests that the delamination would initiate in these regions and then propagate to the other regions in the crack front. This is reaffirmed by the results from the strain energy release rate calculations to be shown later in this section. No experimental work could be found in the literature that has reported such a behavior in crack propagation. There are slight undulations in the σ_{zz} distribution for the homogeneous model. This is attributed to the varying refinement within the mesh. It should be noted that the results obtained near the interface of the local model and the global model (on the left edge in Figure 5.7) are not

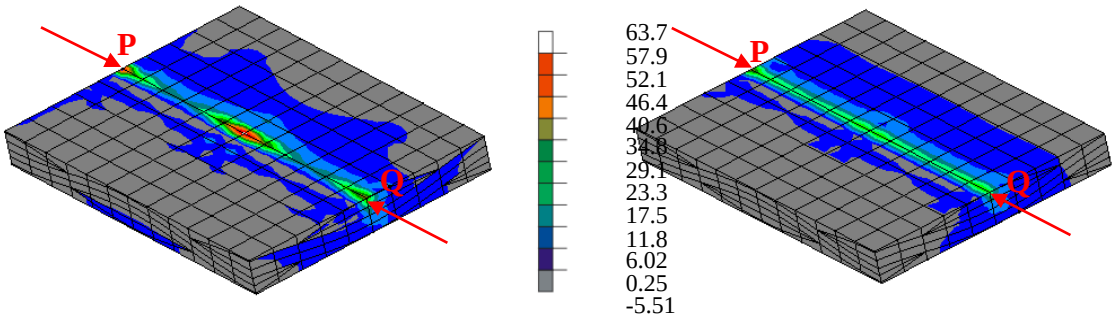

Discrete model σ_{zz}(MPa) Homogeneous model

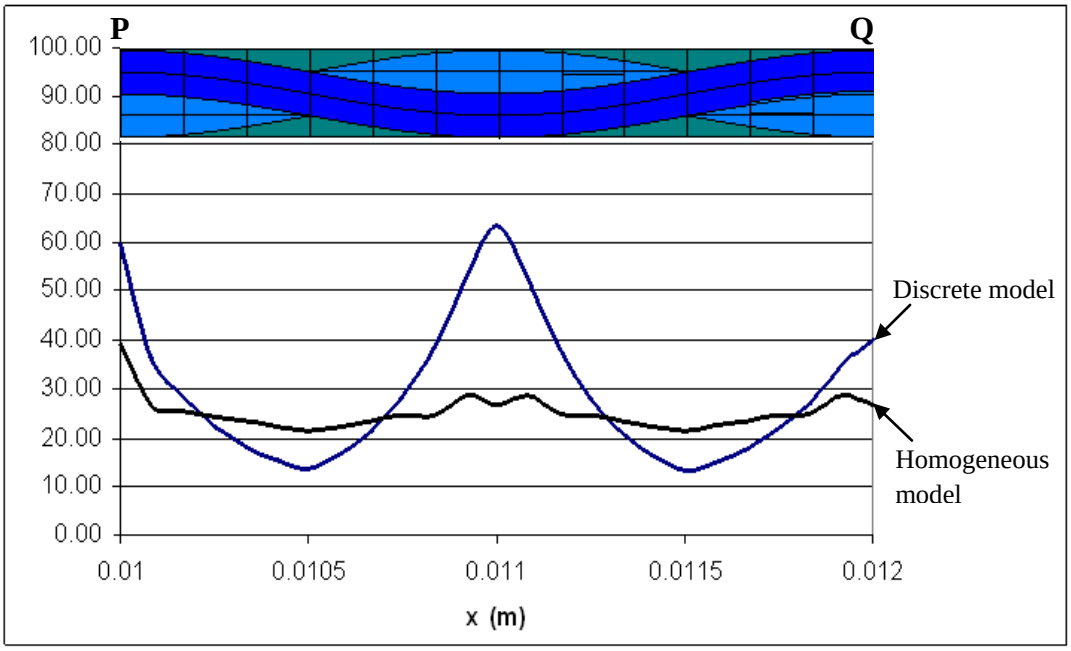

Figure 5.7: Comparison of σ_{zz} (MPa) distributions at the interior of crack front

reliable. This is due to the errors that propagate from the boundary where the multi-point constraints are used to 'join' the local model to the global model. Further verification has been conducted to check the reliability of the results obtained from the smaller hierarchical models and they are presented later on in this section.

The undulation of the tows along the x-direction causes the variation seen in Figure 5.7. The microstructure of the woven composite should also have an effect on the stresses as the crack front advances. This is illustrated by the woven mat in Figure 5.8. The

configuration of the tows at the locations indicated by A and B are similar except that they are offset by a half periodic length in the direction along the crack front. It is known

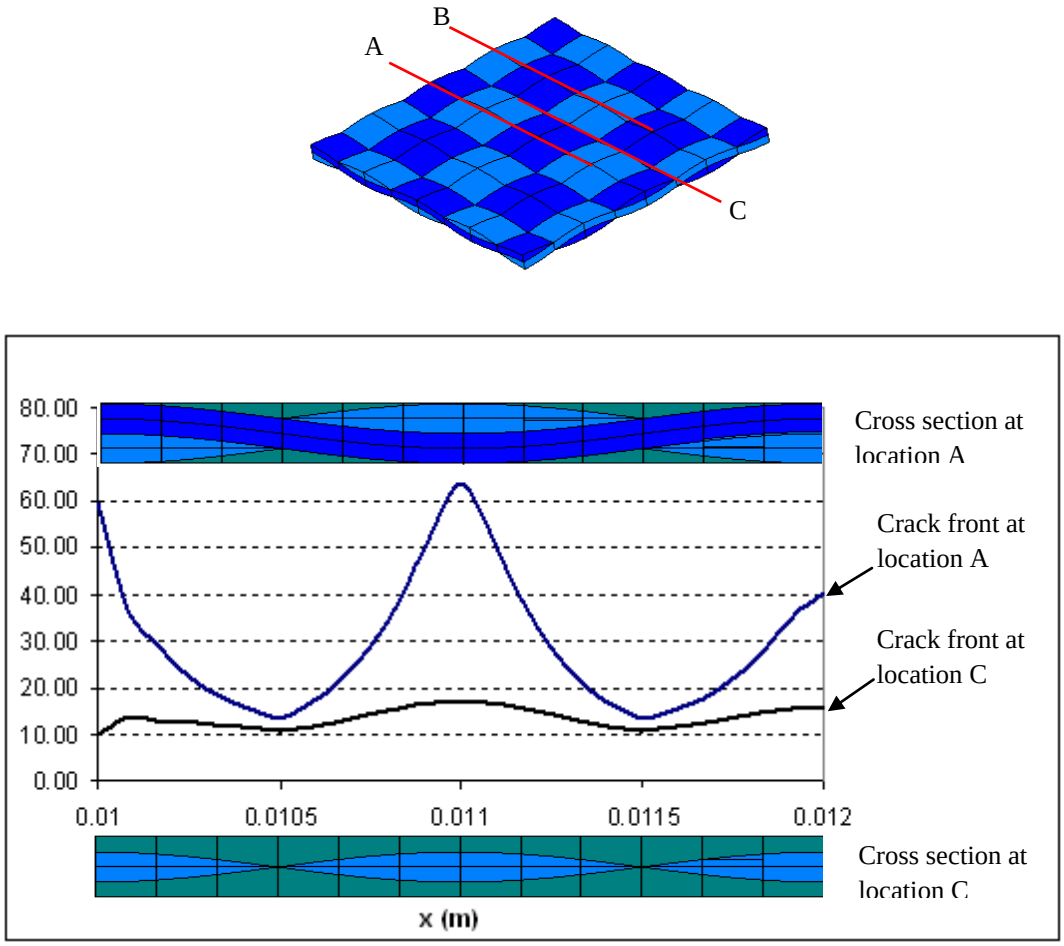

Figure 5.8: Comparison of stress distribution (MPa) when crack front is advanced by quarter periodic length

that the stresses at the crack front are affected by the crack length of the DCB specimen but in the case of a woven composite these stresses are also affected by its microstructure or the tow architecture. Therefore, the stress distribution can be expected to be almost identical if the phase shift and crack length is accounted for. This is not the case when the crack front is at location C, where the configuration of the tows is different from that at locations A and B. To determine the change in stress state when the

crack-tip location changes, a new model was generated where the boundary conditions are specified such that the position of the crack tip is advanced by a quarter periodic length. Figure 5.8 compares distribution of σ_{zz} when the crack front is located at the two different positions. To make the results comparable, the loading is such that moments at the crack tip are the same for both configurations. Since the crack front moves by only 0.5mm, the load changes only by 0.66%. The line plot gives the variation along the crack front for both configurations. The corresponding cross-sections at the different locations are also given. The σ_{zz} stress component is much less when the crack front is at location C. The σ_{zz} distribution at location C also has a periodic pattern similar to the distribution when the crack front is a location A but the amplitude is almost $1/8^{th}$ while the peak stress is close to a quarter of that at location A. This is because the tows aligned along the DCB are closer to the crack front when it is positioned at location A than when it is at location C. It is evident from the crack front cross sections for the two configurations that location A has a higher tow fraction thus contributing more to the stiffness in the region. As a result, the mean σ_{zz} is much higher for location A than that for location C. This suggests that the rate at which the crack would grow would vary as the crack advances, since the local microstructure is changing.

The stress state in the interior of the DCB specimen is considerably different from that at the free edges. The analysis of the coarse global model (Mesh 2) shows the σ_{zz} stress component (Figure 5.6) remains almost constant along the crack front except for the region near the free edge. A discrete hierarchical model using Mesh 4 (Figure 5.4) was generated to obtain the stress distribution near the free edge. This model gives the effect of the free edge up to a distance of 2mm from the free edge. A discrete model using Mesh 6 was also generated to get the stress distribution along the entire width of the beam. As shown by Figure 5.9, the stress distribution remains oscillatory as it approaches the free edge although its magnitude drops. The effect of the free edge appears to be gradual. For example, at 3mm into the DCB specimen, the peak σ_{zz} stress component is still 6.25% less than the corresponding value at the center of the beam. It can be seen that there is very good correlation between the results from the full width

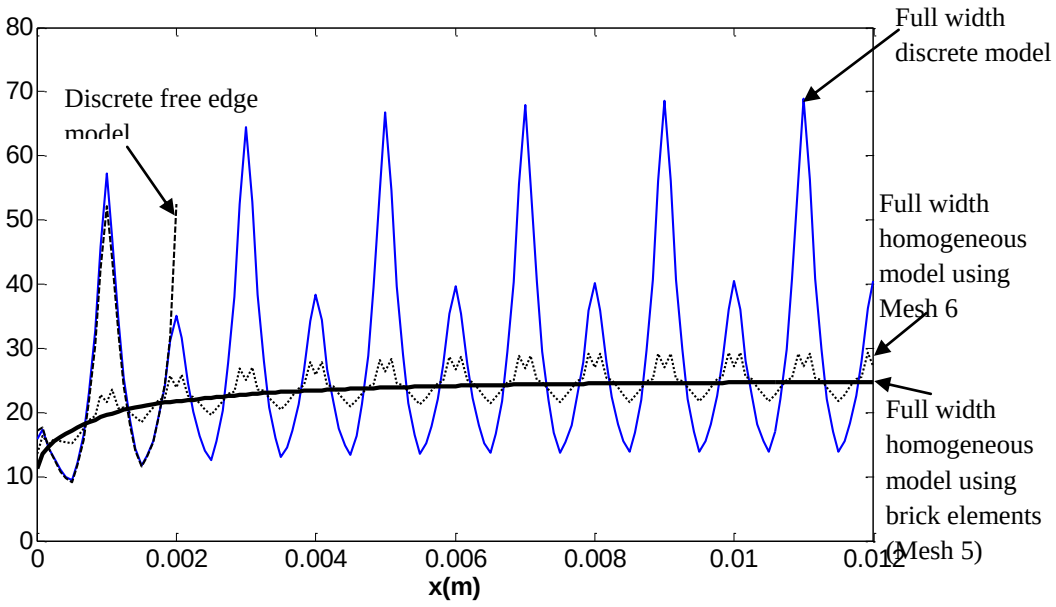

Figure 5.9: Comparison of σ_{zz} distribution (MPa) along entire crack front

discrete model and the free edge discrete model except near the boundary of the local model where it interfaces with the global model. The stress distribution is compared with the corresponding homogeneous model using Mesh 6. The slight undulation seen in the case for the homogeneous model is due to the varying mesh refinement within the model (since the same mesh was used for the homogeneous case). Another homogeneous model using only brick elements was generated (Mesh 5) to confirm this. It can be seen that this curve is smooth and does not have any undulations.

5.6.2 Strain Energy Release Rate Distribution

The strain energy release rate (G_I) for a DCB made of a typical orthotropic material would be almost constant sufficiently away from the free edges. The homogeneous hierarchical models using Mesh 3, 4 and 6 were used to determine the G_I distribution along the crack front. As shown in Figure 5.10, the G_I distribution obtained from the full width homogeneous model starts from 1.51 J/m^2 at the free edge and gradually increases and approaches a constant value of around 5.43 J/m^2. Note that the smaller local models (the free edge homogeneous model and the interior homogeneous model) give a fairly

accurate distribution of the G_I as long as the region of interest is away from the boundary of the local model where the MPCs are used to join them to the global model.

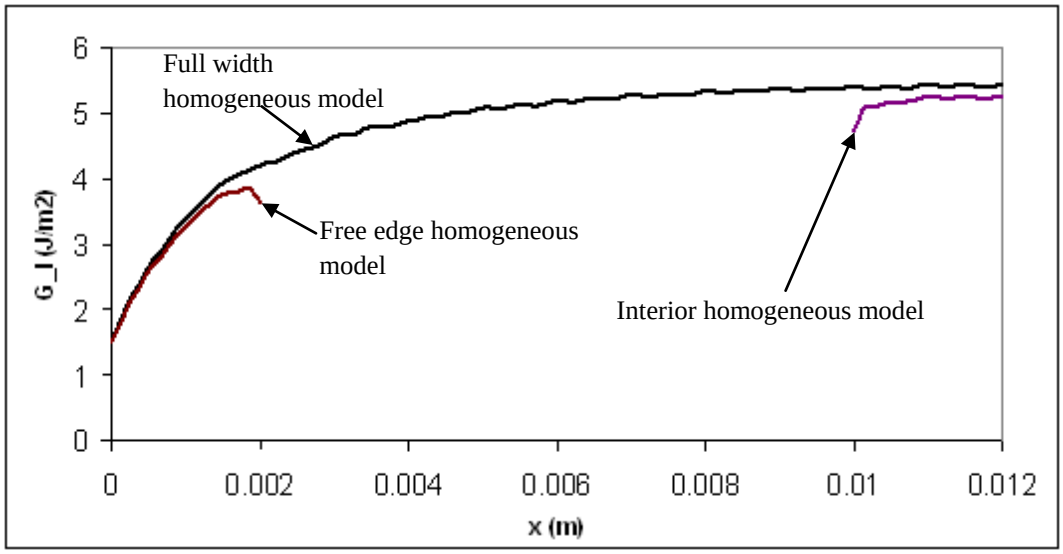

Figure 5.10: G_I distribution along crack front predicted by three homogeneous models

When the tow architecture is taken into consideration, the G_I distribution obtained is considerably different. The G_I distribution from the interior discrete model is compared with that from the corresponding homogeneous model. As shown in Figure 5.11, the G_I follows a periodic pattern similar to the stress distribution. As mentioned earlier, the values near the boundary of the local model are not expected to be accurate. The G_I reaches a maximum of almost two times the homogeneous G_I value and its position corresponds to the point on the tow (aligned along the DCB) where it is closest to the crack front. Similarly the other maximum corresponds to the point where the tow aligned along the crack front is closest to the crack front. The minimum G_I is seen in between two peaks where they contribute the least to the stiffness along the length of the beam due to the matrix pocket. This periodic nature seems to indicate that the crack propagation would not be uniform. It is also interesting to note that the mean G_I obtained from the discrete model is higher (over 5%) than the G_I obtained from the homogeneous model.

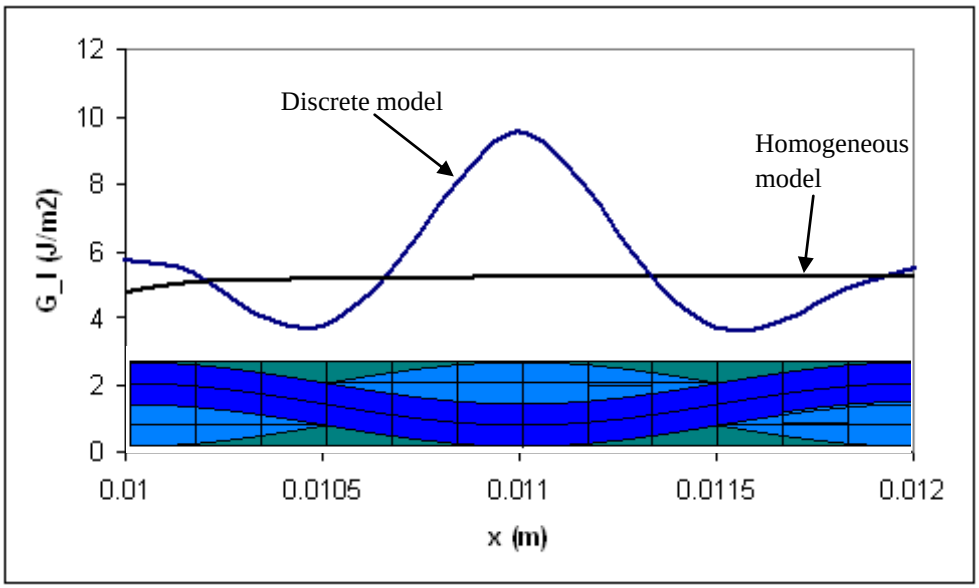

Figure 5.11: Comparison of G_I distributions at the interior of crack front

As seen with the stress distribution results, the G_I distribution is expected to vary when the crack front position changes. This is shown in Figure 5.12 where the G_I distribution for two configurations is plotted. It is seen that as the crack front location moves from A to C (Figure 5.8), the G_I still follows a periodic pattern but the amplitude is less than that when the crack front is at location A. The maximum G_I when the crack front is at location C is 5.75 J/m^2 which is almost 10% more than the G_I value obtained using the homogeneous model. Again, the values at the left edge of the local model should be ignored because of errors that propagate from the boundary where the multi-point constraints are imposed. The diminished periodic pattern of the G_I distribution suggests that the crack propagation rate varies as the crack grows.

As expected, the G_I distribution near the free edge also is considerably different from that obtained when using effective properties. Models using the discrete free edge and interior and full width meshes were used to calculate the G_I distribution for the configurations when the crack front is at locations A and C. In both cases (Figure 5.13) it can be seen that the G_I drops considerably as it reaches the free edge but it still maintains

is oscillatory pattern. Again, the G_I reaches higher peaks when the crack front is at location A rather than location C.

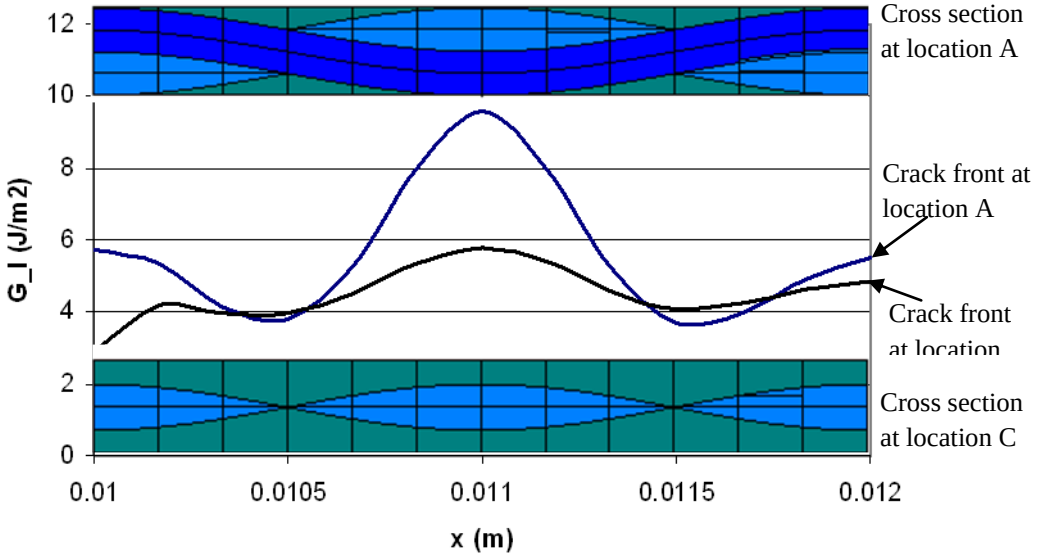

Figure 5.12: Comparison of G_I distribution when crack front is advanced by quarter periodic length

It can be seen that the G_I distributions from the free edge and interior models are in close agreement with the results from the larger full width model in Figure 5.13(a) except when close to the boundaries of the local models. Similarly in Figure 5.13(b), the general trend of the G_I distribution is obtained away from the boundary of the local models where the error is not too large. Thus, the hierarchical models with the smaller local models are reliable for obtaining a good estimate of the G_I distribution along the regions of interest on the crack front. The full width model took over 6 hours to run on a single-processor desktop computer while solving 180666 equations. On the other hand, the smaller models such as the free edge and interior models took less than an hour to solve 50922 equations. This shows a considerable savings in analysis time when compared with running models that have large refined local models. More savings could be achieved if the discrete meshes had varying refinement such that only regions close to the crack front were highly refined. For the models analyzed in this work, the time taken to solve the equations dominated the run times. Therefore, run times when using the

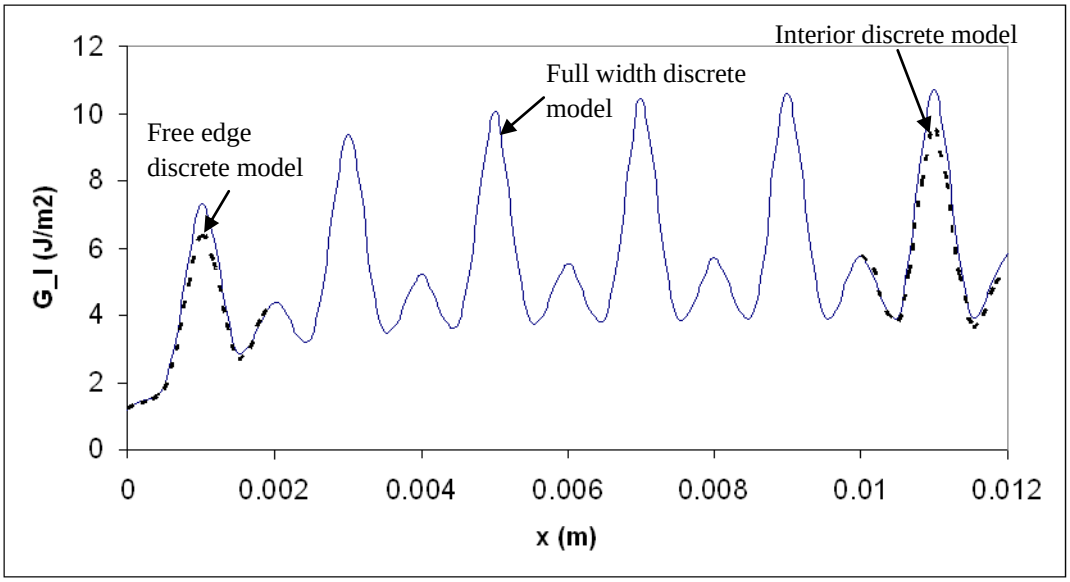

a) Crack front at location A

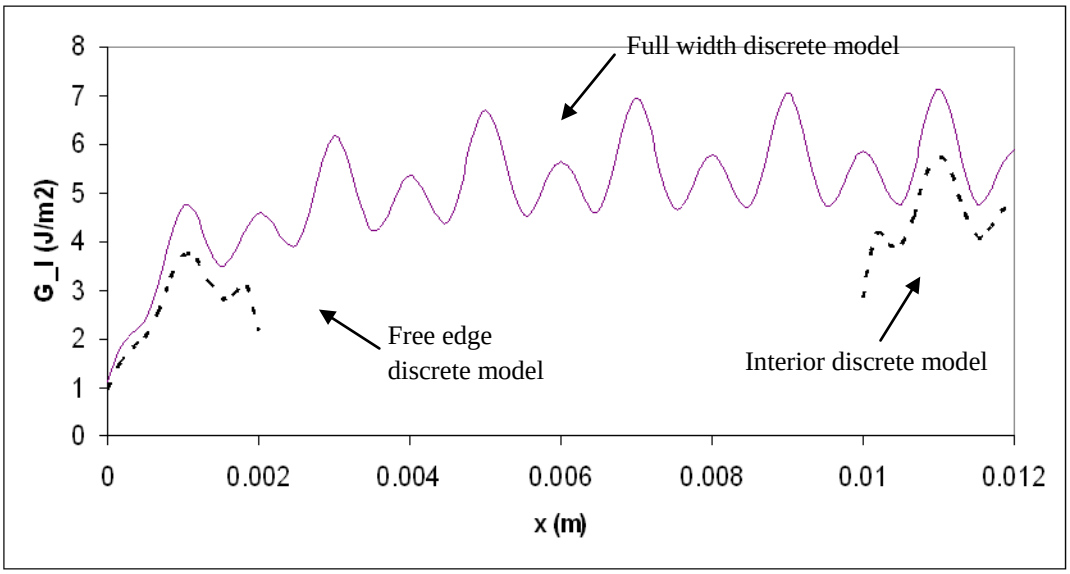

b) Crack front at location C

Figure 5.13: G_I distribution along entire crack front

hierarchical system and conventional FEA approach would be comparable because the solver as such does not utilize any hierarchical characteristics. On the other hand, major savings were obtained in the time taken to generate the models. In a conventional approach, it would be an elaborate and time-consuming task to identify the boundaries and interfaces to the different regions of the model and 'join' those using MPCs to generate a single model. On the other hand, when using the hierarchical system, this step is completely automated. The true potential is in the ability to generate and manage multiple models in a single hierarchy.

5.7 Summary

This section describes the use of a hierarchical strategy to perform a multiscale analysis of a woven composite DCB specimen that contains multiple microstructural scales (fiber/matrix, tow architecture, laminate). The strategy exploits the natural hierarchical character of model descriptions and simulation results to expedite analysis of problems. Hierarchical techniques were used in the development, organization, and management of finite element models, and for the post-processing of the results from the analyses. Models in the hierarchy are 'joined' together by implementing a boundary matching routine that specifies multi-point constraints in order to impose continuity at the interfaces. The effect of the complex microstructure on the stress distribution and the G_I distribution was presented. It was seen that the stresses and G_I distribution follow a periodic pattern corresponding to the undulation of the tows in the woven composite, which suggests that the delamination would initiate in certain regions and propagate to the rest of the crack front. The effect of the microstructure on the stresses and G_I as the crack advances was also investigated. The results suggested that there would likely be significant variation in the growth rate as the crack advanced.

6. IMPLEMENTATION AND VALIDATION OF OXIDATION MODEL

6.1 Introduction

The theory and the finite element formulation of the oxidation model were described in Section 3. The simulation of the oxidation behavior, as will be explained in this section, is a computationally expensive process and in some cases not even feasible for modeling complex configurations. This section is divided into two major sections. The implementation of the oxidation model is described first. This includes special approximations and strategies used to enhance the efficiency of the oxidation analysis. These strategies reduce the analysis time to a fraction of the standard implementation while giving reasonable results. The rest of the section discusses the tests conducted to validate the optimizations and strategies implemented to expedite the oxidation simulation.

6.2 Implementation of Oxidation Model

The oxidation model used herein is adopted from the work done by Pochiraju, Schoeppner and Tandon[7-9] who have used this model to simulate the oxidation of neat PMR-15 resin with reasonable accuracy compared to experimental observations. Section 3 describes the theory behind the model and goes through the equations to derive the finite element formulation. It also describes approaches to obtain effective oxidation material properties that can be applied to periodic microstructures. The oxidation analysis is inherently more computation intensive than a simple diffusion analysis because of the complex governing equations. The oxidation state variable needs to be calculated for each integration point in the mesh at every time step. The oxidation model appears to require a more refined mesh and a smaller time step size compared to a corresponding diffusion model. This makes it even more important to explore methods to speed up the oxidation analysis without losing required accuracy.

As with typical mechanical analyses, the accuracy of the solution depends on several factors, one of which is the element size. In the case of transient analyses like diffusion or oxidation, the solution also depends on the time step size. Depending on the material

properties and other values in the finite element formulas, there are limits to the element size and time step size beyond which meaningless results are obtained. Analyses were performed using COMSOL Multiphysics to confirm that other finite element packages had the same limitations. In addition to the basic approximation for the time integrations, there are several approximations made in the finite element formulation to handle the nonlinearity in the governing equations. The accuracy of these approximations depends on parameters such as the time step size as well.

In general, the optimal time step size need not be constant throughout the simulation because of the nonlinear oxidation behavior. This means that the time step size can potentially be ramped up or down as the simulation is in progress so as to maintain the optimal time step size. To summarize, the following optimizations can be made to an oxidation simulation in order to make it run more efficiently:

1. Optimal element size
2. Optimal time step size
3. Optimal time step size ramping

Parametric studies were conducted to determine the optimized parameters for the materials that would be analyzed in this work. The latter part of this section will discuss the results of these parametric studies.

The remainder of this section describes the oxidation behavior in neat PMR-15 resin. Certain characteristics of the oxidation behavior can be exploited to develop a strategy to speed up the analysis. For this purpose, oxidation of a simple configuration is considered. The simple configuration is a block of neat resin that is exposed to oxygen on one pair of opposite surfaces that are 40 mm apart and protected from oxygen on the other surfaces. This configuration can be analyzed using a 1-D model. Moreover, taking advantage of symmetry, only half of the block needs to be modeled. Table 6.1 gives the material properties used to model the neat PMR-15 resin. For a complete description of the different oxidation material properties, refer to Section 3.5. A uniform element size of 1micron and time step size of 0.15 minute was used for the simulation.

Figure 6.1 shows the predicted oxidation layer growth for the configuration over a period of 200 hours. Section 3.5.6 describes how the oxidation layer growth is determined. It can be seen that the resin oxidizes very quickly in the initial 20 hours or so and then gradually slows down to where the oxidation layer grows almost linearly. Also note that the thickness of zone II or the active zone remains fairly constant throughout the entire process.

Table 6.1: Oxidation material properties for neat PMR-15 resin

	Neat PMR-15 resin
Diffusivity D_{unox} D_{ox}	 53.6×10^{-6} mm^2/min 78.22×10^{-6} mm^2/min
R_0	3.5 mol/(m^{3}min)
ϕ_{ox}	0.187
C^{∞}	0.79 mol/m^3
α	0.01-0.0067(t/40) : t < 40 0.0033 : t > 40 (t in hours)
$f(C)$	$\frac{2\beta C}{1+\beta C}\left[1-\frac{\beta C}{2\ 1+\beta C}\right]$
β	0.919

The difference between oxidation and diffusion-only is that for oxidation, the oxygen molecules do not diffuse as quickly because they are consumed in oxidizing the material. Thus, the reaction term in the governing equations gives the effect of a ‘moving barrier’ that allows almost no oxygen to cross over to the other side of the active zone until there is a sufficient level of oxidation within the active zone. This is evident by looking at the concentration profiles across the model at different snap shots during the simulation. Figure 6.2 shows the concentration profiles in the model at t=2.5 hrs, 50 hrs and 100 hrs. It can be seen that all the profiles have a similar shape. The profiles drop almost linearly from the exposed edge up to the ‘moving barrier’ and the concentration is practically zero for the rest of the model. The difference in each profile is that as time passes, the location of the ‘moving barrier’ shifts in the direction of the oxygen flow. This

movement of the barrier is very slow compared to the diffusion-only process. This is illustrated in Figure 6.2 by the concentration profile of the corresponding diffusion model at 15 minutes. It shows that with only 15 minutes of diffusion, the oxygen concentration at every point in the model has already surpassed that of the oxidation model at 2.5 hours. Even after 100 hours of oxidation, the oxygen concentration is still practically zero past 0.06 mm whereas the corresponding concentration from the diffusion model after 15 minutes is more than 0.025 at 0.06 mm. This also explains why there is a close to linear drop of the concentration from the exposed edge to the 'moving barrier'. In each snapshot of concentration profile in the oxidation process, the region to the left of the moving barrier can be considered as a diffusion only region with fixed concentration boundary conditions – the specified concentration at the exposed

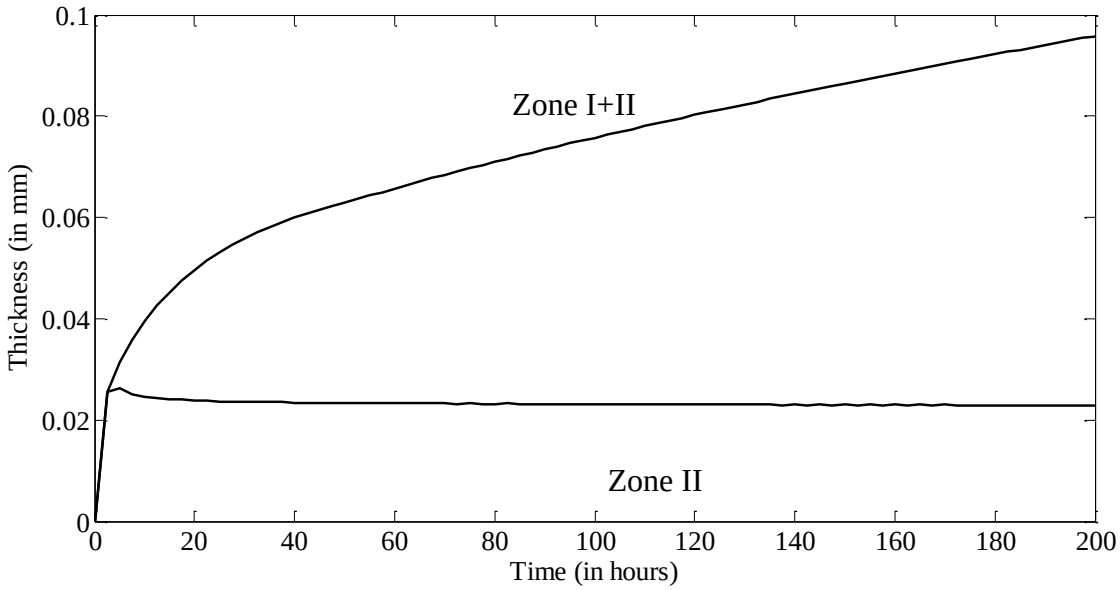

Figure 6.1: Predicted oxidation layer growth (Zone I+II, Zone II) in neat PMR-15 resin

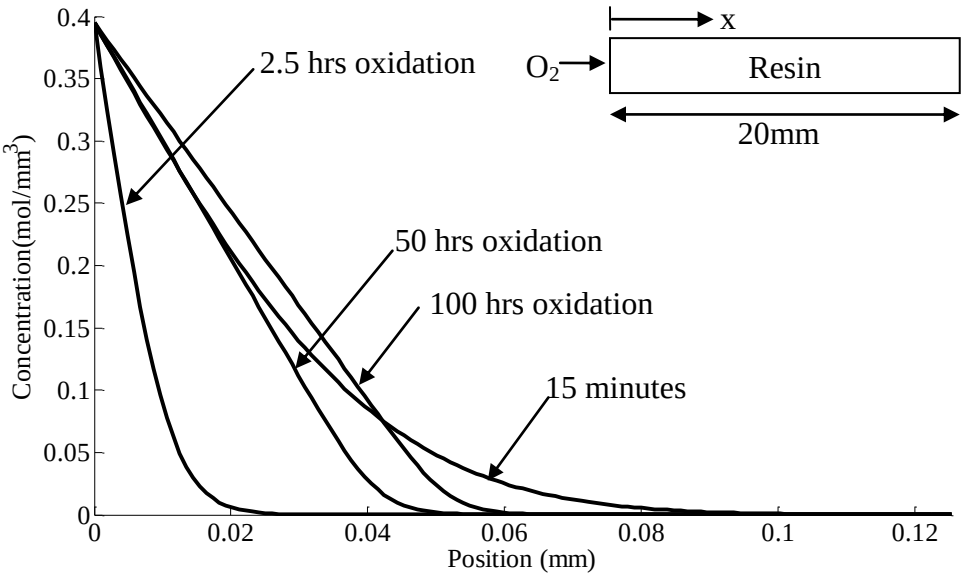

Figure 6.2: Concentration profiles for oxidation and diffusion models.

boundary and zero concentration at the location of the barrier. Since the barrier is moving very slowly, the concentration profiles at the various time steps look very similar to that for the corresponding diffusion-only problem at steady-state, which is a nearly linear variation of the concentration. Examination of this behavior gave way to a strategy to further expedite the oxidation simulation. This strategy was called the *Adaptive Meshing Strategy* and is described in detail in the next section.

6.2.1 Adaptive Meshing Strategy

The fact that the concentration of oxygen in the un-oxidized region of the material is practically zero can be exploited to speed up the analysis by constraining the degrees of freedom(dof) in most of the un-oxidized region to zero. This can lead to a considerable reduction in the number of unknowns to be solved for, especially in the initial period of oxidation because most of the material is un-oxidized at that time. The challenge is in determining which regions of the material should be constrained and developing an efficient algorithm so that this can be automated. The regions very close to the active zone should not be constrained since the active zone is slowly moving to the interior of

the material with each time step and that can affect the solution. Also, the regions should not be permanently constrained because that implies that those regions will never get oxidized, which is not the case.

Based on these requirements, the following algorithm was developed to automatically determine the regions to be constrained. A very small concentration value close to zero is chosen, say C^0, in order to determine which regions are to be constrained. If the concentration at a node is more than C^0, then that location is assumed to be inside the oxidation layer or close to it and therefore the dof for that node is left unconstrained. On the other hand, if the concentration at a node is less than C^0, then the node is assumed to be in the un-oxidized region and far enough from the active zone, therefore that dof is constrained. This check is not performed at every time step. Instead, the check is performed every 15 or 20 time steps or some optimal number of time steps (say, N) chosen depending on the rate the active zone is moving. Therefore, once a check is performed, the constrained dofs remain constrained for the subsequent time steps until the time step right before the next check. In this time step preceding the check, all the artificial constraints are removed and the full system of equations is solved. This allows a minute amount of oxygen to enter the previously constrained region. In the next time step, the check is performed, at which time some of the previously constrained dofs will be unconstrained because the oxygen concentration has increased by a small amount. This cycle is repeated throughout the simulation. This strategy speeds up the analysis by a large factor because in the standard analysis, every time step involves solution of the entire system of equations whereas in the adaptive mesh analysis, the entire system of equations is solved only every N time steps. During the other time steps, the system of equations solved is much smaller. The check to determine the region to be constrained is also performed only every N time steps and the computation effort used for the check is miniscule compared to the savings obtained by solving a smaller set of equations. In addition to those savings, whenever the check is performed and a region of the un-oxidized material is constrained, the corresponding elements are also deactivated thereby speeding up the finite element assembly process as well.

The choice of the value of C^0 has an effect on the analysis because if the value is too large, regions that are close to the active zone will be constrained whereas if the value is too small, a smaller region is constrained and the strategy is not used to its maximum potential. Similarly, the number of time steps that is skipped before a check, *N*, also has an effect on the efficiency of the simulation. Parametric studies were performed by varying the two parameters, C^0 and *N* on 1-, 2- and 3-D models. The results of this parametric study are presented in the validation section of this section.

6.3 Optimization and Validation

This section discusses the results of the tests conducted to optimize model parameters as described in the earlier sections of this section. The optimizations of the standard oxidation model are discussed first followed by the validation of the Adaptive Meshing Strategy.

6.3.1 Optimization of Model Parameters

Parametric studies were conducted to determine the optimal element size and time step size as well as the time step size ramping. In order to make comparisons, parametric studies were also conducted on corresponding diffusion models. Optimal element size and time step size were determined by analyzing the same configuration described in section 6.2. The diffusivity of the material for this parametric study was assumed to be 53.6×10^{-6} mm^2/min, which is the diffusivity of the un-oxidized PMR-15 resin. It is important to note that this parametric study is not extensive and does not look all the possible parameters. Therefore, the results from this parametric study, in essence, are valid only for material properties and other model parameters used in the study. In order to analyze other material systems, it would be advisable to determine the optimal parameters for that specific system.

One-dimensional models were analyzed using various element sizes and time step sizes. The reference solution was assumed to be that obtained from using linear elements with a size of 1 micron and a time step size of 0.15 minutes. The variation of average concentration in the model with time was compared for the different models. It was

observed that the effect of the element size and time step size on the results were independent of each other. The element size was kept constant at 1 micron and models were analyzed with varying time step sizes and it was found that the time step size could be raised to over 10 minutes before any noticeable difference in the results were observed. When the time step size was kept constant at 0.15 minutes, the element size could be increased to at least 40 microns without any noticeable change in the results. A model with an element size of 40 microns and a time step size of 10 minutes also yielded the same behavior as the reference model. This behavior was seen for both linear and quadratic elements. In some instances, the nodal concentrations drop below zero but they are still considered numerical zeros and these negative concentrations do not have any significant effect on the results. The same results were obtained when a parametric study was conducted on two dimensional models with eight-node quadratic elements. A parametric study was also conducted to determine the effect of diffusivity on the allowable time step size. As expected, when the diffusivity is increased, the oxygen takes less time to saturate the material and the optimum time step size required in order to get a converged solution becomes smaller. It was also found that increasing the element size while keeping the time step size and diffusivity constant, eventually results in negative nodal concentrations.

Similar to what was done for the diffusion analysis, the optimal mesh size and time step size were determined by analyzing the configuration described in section 6.2 using the material properties in Table 6.1. The reference solution was assumed to be that obtained from using linear elements with a size of 1 micron and a time step size of 0.15 minutes. The oxidation layer thicknesses were calculated for all the models and compared to determine the accuracy. The oxidation layer consists of a fully oxidized layer (Zone I) and the active reaction layer (Zone II). Although the Zone II layer is defined by having an oxidation level in between 0 and 1, for all the oxidation models described in this paper, a tolerance of 1% is allowed on those limits. Therefore, an element is assumed to have started oxidizing and is in Zone II if the oxidation level at each of the material integration points falls within a lower limit of 0.01 and an upper limit of 0.99. If the

oxidation state is above 0.99, the element is assumed to be un-oxidized and if it is below 0.01 it is assumed to be fully oxidized. A post-processing routine was written that calculated the growth of the oxidation layer along a line in a model. This involved extrapolating the oxidation state values from the integration points to the nodal points, averaging the extrapolated values at a node if the node shared elements of the same material and solving for the location on the prescribed line where the oxidation level value met the specified upper and lower limits.

Figure 6.3 shows the effect of the size of linear elements on the oxidation layer growth with a constant time step size of 0.15 minutes. It shows that the models using 4-micron and 8-micron size elements closely agree with the model using 1-micron elements whereas the model using 12-micron elements over predicts the thickness. The model with 8-micron elements shows a distinct oscillation in the curve. This is believed to be caused due to errors from extrapolation of the oxidation state values from the integration points to the nodal points. Nevertheless, it can be seen that upper bound of the curve is very close to the results of the 1-micron size model. The model with 4-micron elements shows slight oscillations as well but it is able to predict the thickness growth very well.

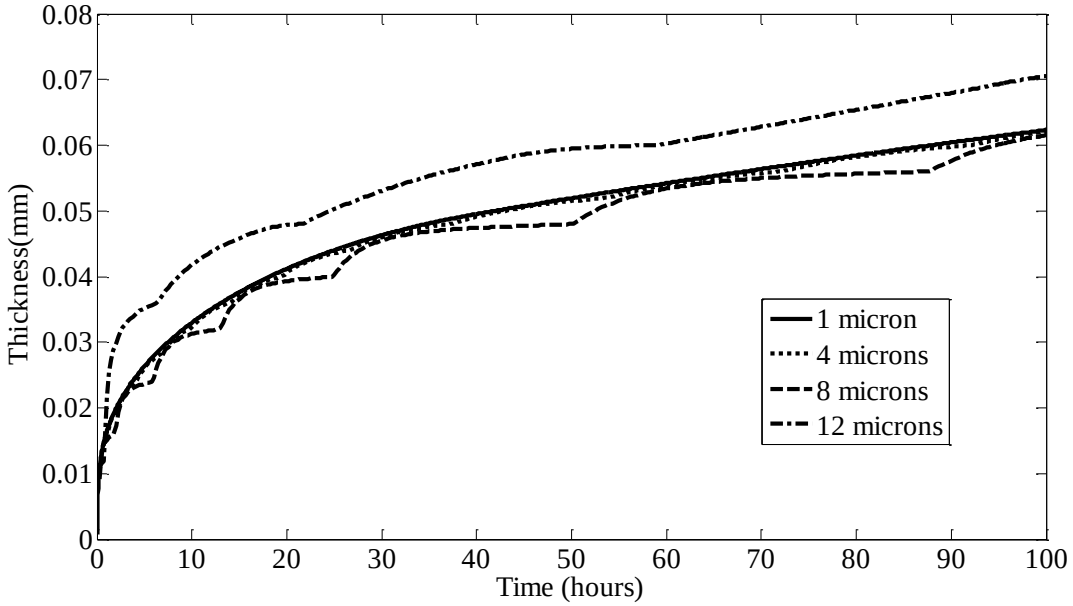

Figure 6.3: Effect of element size on oxidation layer growth (Zone I+II) for neat resin (using linear elements and time step size of 0.15 mins)

The effect of the time step size was also investigated by keeping the element size constant and varying the time step size. Figure 6.4 shows the oxidation layer growth for different models when the element size is kept constant at 2 microns and the time step size varies from 0.15 mins to 0.8 mins. It can be seen that the time step size can be doubled from 0.15 mins to 0.3 mins without any perceivable effect on the results. When the time step size is raised to 0.5 mins, some difference can be seen in the initial part of the simulation while the latter part still predicts the oxidation growth fairly well. Increasing the time step size to 0.8 mins affects the results considerably especially during the initial part of the simulation. This kind of behavior for the effect of time step size on the predicted oxidation growth was seen for both linear and corresponding quadratic elements. The trends also show that the time step size is more critical to the initial part of the simulation where the oxidation growth is nonlinear. For many of these models, the nodal concentrations calculated would be numerical zeroes that go below zero. When the program encounters such values, they are converted to zero so that it

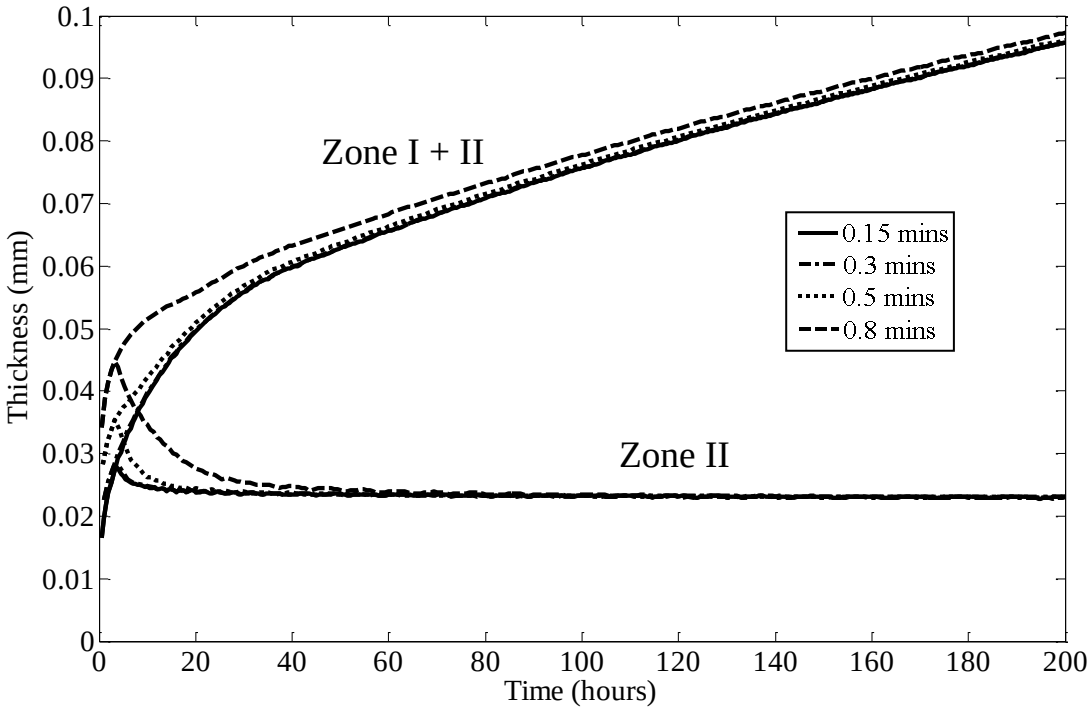

Figure 6.4: Effect of time step size on oxidation layer growth for neat resin (using 2 micron linear elements)

does not use negative concentrations in the calculation of the reaction terms and the oxidation state, which would physically mean a reversal of the oxidation process.

In order to speed up the analysis, the behavior of the model when the time step size is gradually increased was investigated. As seen from the results of the previous parametric study, a time step size of no more than 0.3 minutes was required to accurately model the initial part of the simulation where layer growth is highly nonlinear. The layer growth behavior becomes close to linear once the model has undergone oxidation for 40 hours, which is when the time-dependent material property, α changes from decreasing linearly with respect to time to a constant value of 0.0033. Based on this, a parametric study was conducted where the models used a time step size of 0.3 mins for the initial 40 hours of the simulation and for the other 160 hours, the different models used different time step sizes. The reference model used a time step size of 0.15 mins for the entire 200 hours. All the models used elements with a size of 2 microns. Figure 6.5 shows that when the

time step size is ramped up from 0.3 minute to 1 minute, the predicted oxidation growth curve is barely distinguishable from that of the reference model. The results are fairly reasonable even when the time step size is ramped up to 5 mins. As shown in Figure 6.5,

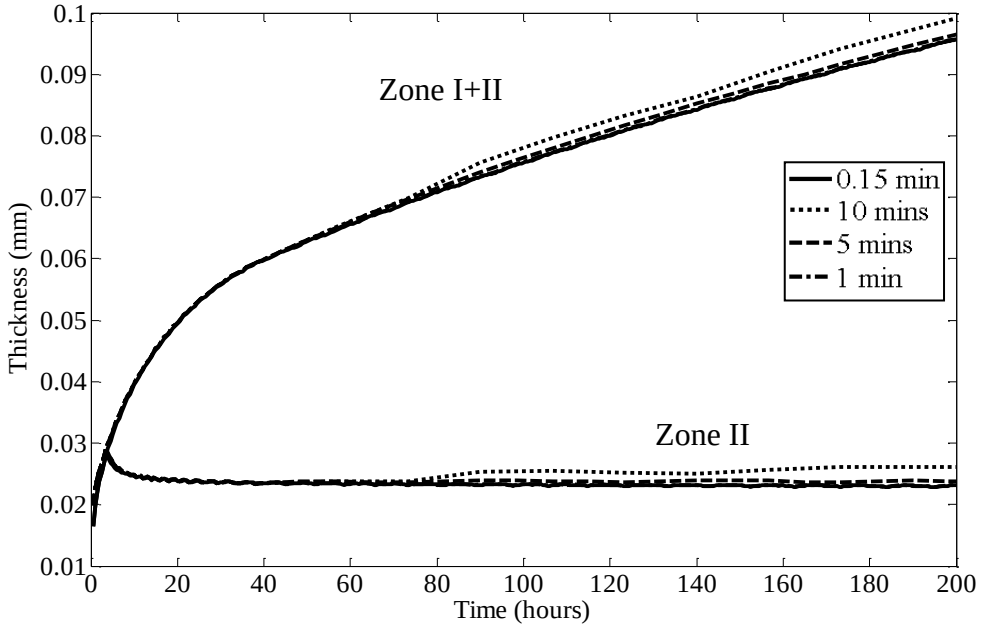

Figure 6.5: Oxidation layer growth (Zone I+II, Zone II) for neat resin (using 2 micron linear elements and time step size of 0.30 mins for the first 40 hours and different ramped time step sizes thereafter)

the differences in the curves are considerable when the time step size is ramped to 10 mins. Figure 6.5 show that the models also predict the Zone II thickness fairly well. Ramping up the time step size tremendously reduces the computational time required for the analysis compared to using a constant time step size of 0.3 minutes. A constant time step size of 0.3 mins used for simulating 200 hours of oxidation takes up 40,000 time steps whereas using a model that uses 0.3 mins for the first 40 hours and 5 mins for the remaining 160 hours takes up only 9920 time steps. This makes a computational savings of over 75%.

6.3.2 Validation of Adaptive Meshing Strategy

Parametric studies were performed to determine the optimal parameters for the Adaptive Meshing Strategy as well as potential computational savings. The one-dimensional configuration in section 6.2 is analyzed using the Adaptive Meshing Strategy described in section 6.2.1. The two parameters that were varied were C^0 and *N*. All the models in this particular parametric study use 1 micron size elements and time step size ramping where the first 40 hours use 0.3 minute time steps and the remaining 160 hours use 1 minute time steps. The oxidation layer growth from the different models is compared with a reference model that uses the standard oxidation analysis. Figure 6.6 shows the oxidation layer growth for models that have a constant C^0 of 0.01 and three different *N* values of 50, 100 and 200. It shows that for *N* values of 50 and 100, the oxidation layer growth predicted is very close to that of the reference model. Even for the model with an *N* value of 200, it is seen that there is close agreement till about 40 hours after which the time step size is ramped up to 1 minute. This indicates that the value of the threshold concentration, C^0 is too high and that the oxidation front is creeping up to the constrained region and the active region of the mesh is not re-evaluated quickly enough. That is why for lower *N* values such as 50 or 100, the prediction of oxidation layer growth is much better. This means that if the threshold concentration, C^0 is lowered, that would make the constrained region smaller thereby taking it longer for the oxidation front to reach the region. Therefore, lowering C^0 should allow increasing *N* while maintaining the accuracy. This was validated by analyzing a similar set of models as earlier except with a C^0 value of 1e-3. Figure 6.7 shows that *N* value of 200 does a very good job of predicting the oxidation layer growth whereas when C^0 had a value of 1e-2, an *N* value of 200 did a very poor job of predicting the layer growth. Moreover, even an *N* value of 300 does a good job and it is only when it is increased to 400 that the accuracy of the prediction even starts to deteriorate. This same trend was seen when the C^0 was lowered even further to 10^{-4} and 10^{-5}. On the other hand, when C^0 is lowered, the constrained region is reduced and the maximum potential of the Adaptive Meshing Strategy is not achieved. Figure 6.8 shows computational time savings achieved when

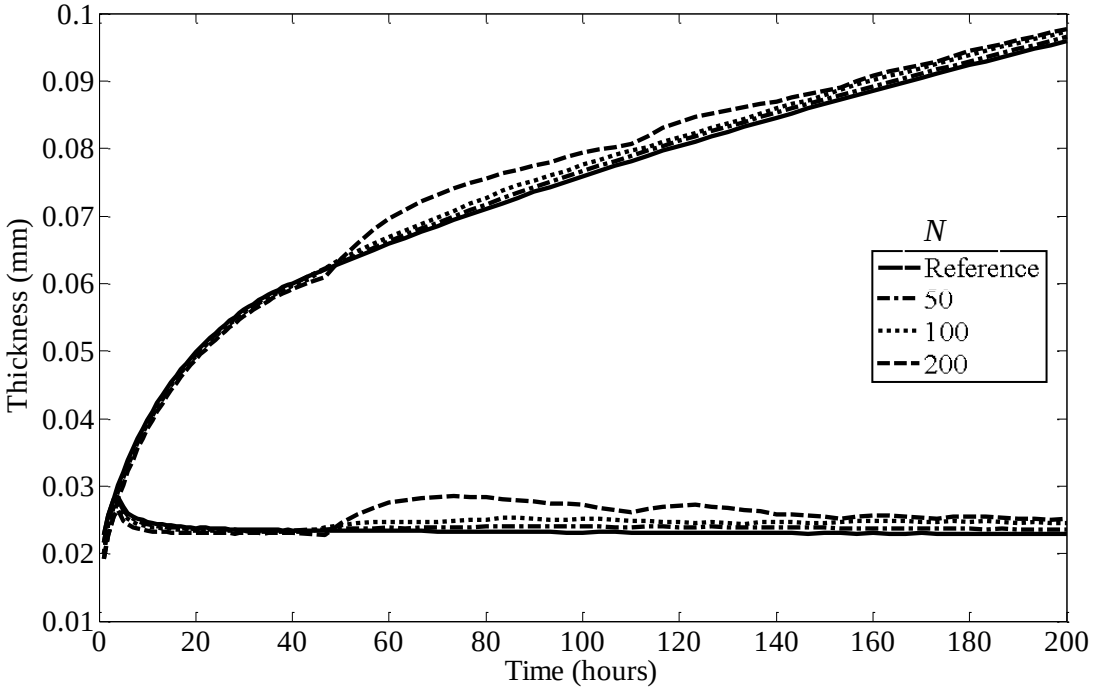

Figure 6.6: Oxidation layer growth (Zone I+II, Zone II) for neat resin (using C^0=10^{-2} and different N values)

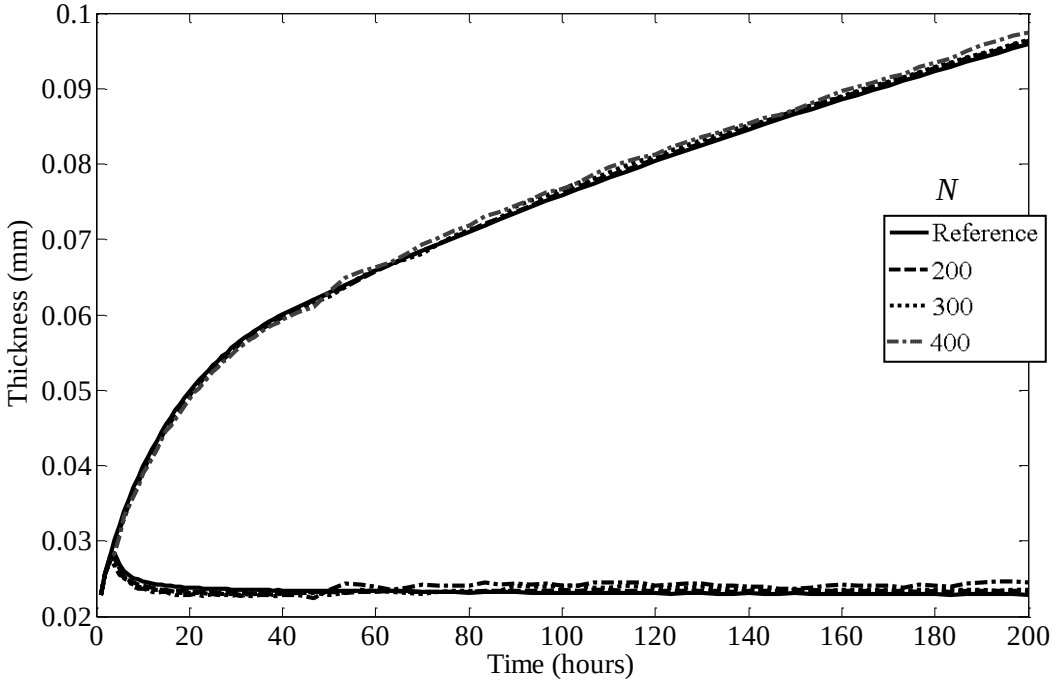

Figure 6.7: Oxidation layer growth (Zone I+II, Zone II) for neat resin (using C^0=10^{-3} and different N values)

using the Adaptive Meshing Strategy compared to the corresponding standard analysis with time step size ramping. The computation time savings is defined by

$$\text{computational time savings} = \left(1 - \frac{\text{time taken by Adaptive Meshing Strategy}}{\text{time taken by standard analysis}}\right) \times 100 \quad (6.1)$$

Due to constraints with the computational resources, it was not possible to obtain accurate timings of the analysis but it still gives a good sense for the trends in the savings achieved when the value of C^0 is lowered. As illustrated in the figure, as the value of C^0 is lowered from 1e-2 to 1e-5, the computation time savings decreased from ~68% to ~58%.

In order to see how this analysis strategy fares when the dimensionality of the model is increased, the same configurations were analyzed using 2D and 3D models. The 2D mesh had dimensions of 200 x 10 elements using 8-noded 2D elements of size 1 micron. The 2D model had a total of 6421 dofs. The 3D model had dimensions of 5 x 5 x 200 elements using 20-noded brick elements of size 1 micron. The 3D model had a total of 26496 dofs. Again constraints on the computational resources prevented accurate timings of the analyses but it did give the same kind of trend for all the models analyzed. Figure 6.9 shows the computational time savings achieved when C^0 was kept at a constant value of 1e-3 and the value of N has been varied for the corresponding 1D, 2D and 3D models. The results were not conclusive enough to determine any strong trends. In general, it was seen that the percentage savings reduced for the 2D model compared to the 1D model. On the other hand, the 3D models generally gave a better percentage savings compared to the 1D models. It is estimated that this trend is due to the nature of the system of equations related to 1D, 2D and 3D models. For all the analyses performed in this work other than this parametric study, C^0 was chosen to be 0.0001 mol/m^3 and N was chosen to be 20 time steps.

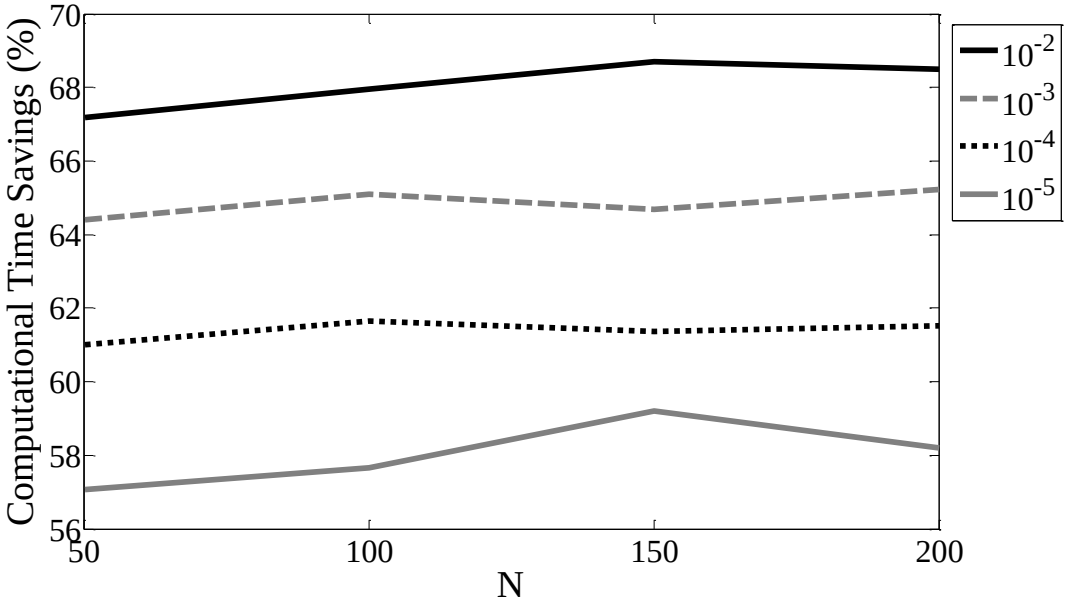

Figure 6.8: Computational time savings for parametric study of 1D expedited analysis models with various C^0 and N values)

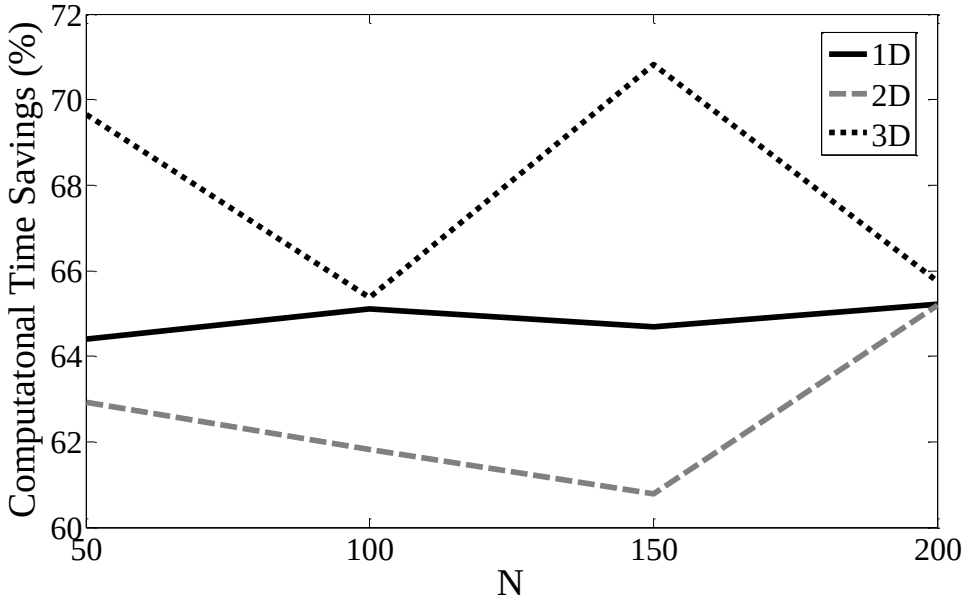

Figure 6.9: Computational time savings for parametric study of 1D, 2D and 3D expedited analysis models with $C^0=10^{-3}$ and various N values)

6.4 Summary

This section described the specific details regarding the implementation of the oxidation model for the simulation of oxidation in neat PMR-15 resin. It discusses the optimization of different mesh parameters including element size, time step size as well as the effect of changing the time step size during the simulation. Unfortunately, in spite of all these optimizations, the oxidation analysis is still very computationally expensive. Upon study of the oxidation behavior another analysis strategy is introduced to speed up the oxidation simulation. The latter half of this section describes the parametric studies performed to optimize the different model parameters as well as validate the Adaptive Meshing Strategy.

7. VALIDATION OF HOMOGENIZED OXIDATION PROPERTIES

7.1 Introduction

When simulating oxidation in a configuration made of composites, it is not practical to discretely model all the matrix and fibers in the composite because of modeling and computational challenges. The same situation is true in the case of textile composites. Similar to what is done in order to perform structural analysis of textile composites, homogenized properties are used to avoid modeling a microstructural scale thereby making the analysis tractable. The necessity is even more severe when simulating oxidation because the finite element formulation requires very refined meshes. Therefore, even discretely modeling the tow architecture scale in a single unit cell creates a very large model. Strategies for determining homogenized oxidation properties for unidirectional laminates or tows are described in section 3.5.7. In this section, the homogenization strategies are validated using various configurations so that they can be reliably used later to model oxidation in textile composites. The next section describes the material properties and the configurations analyzed. This is followed by the results of the analyses and a discussion of the accuracy of the homogenized properties.

7.2 Material Properties and Configurations

Three configurations were analyzed to determine the accuracy of the homogenized oxidation properties. The expressions described in section 3.5.7 were used to determine homogenized oxidation properties for tows with a fiber fraction of 28.49% and 50%. Table 6.1 specifies the material properties for the neat PMR-15 resin and Table 7.1 specifies those computed for the homogenized tows.

For a more accurate calculation of the diffusivity at V_f=50%, the actual value of $\bar{D}$ in Figure 3.4 obtained from micromechanics (which is 0.3254) is used rather than calculating the value using the formula for the curve fit (which is 0.33). Mesh refinement and time step sizes were determined such that the analyses were computationally efficient while giving accurate results as described in the previous section. The three configurations are described next.

Table 7.1: Oxidation material properties for the homogenized tows

	Homogenized tow (Vf=28.49%)	Homogenized tow (Vf=50%)
Diffusivity D_{unox} D_{ox}	 41.71 x10^{-6} mm^2/min 60.87 x10^{-6} mm^2/min	 34.88 x10^{-6} mm^2/min 50.90 x10^{-6} mm^2/min
R_0	2.50 mol/(m^3min)	1.75 mol/(m^3min)
ϕ_{ox}	0.4186	0.5935
C^{∞}	0.564 mol/m^3	0.395 mol/m^3
α	0.01-0.0067(t/40) : t < 40 0.0033 : t > 40 (t in hours)	
$f(C)$	$\frac{2\beta C}{1+\beta C}\left[1-\frac{\beta C}{2\ 1+\beta C}\right]$	
β	0.919	

7.2.1 Configuration A

This configuration is a unidirectional laminate idealized as having fibers arranged in a "square array" with twenty fibers in the x direction and infinite dimensions in the y and z directions. This is illustrated in Figure 7.1 showing a single layer of fibers from an infinite stack of such layers. Although the sketch shows a finite z dimension, the configuration is actually infinite in the z direction. The fibers are identical and have a diameter of 10 microns. The fiber volume fraction of the laminate is 50%. The laminate is exposed to air on both the left and right surfaces. Therefore, the composite begins oxidizing from the outer surface with the oxygen making its way into the interior of the laminate. By taking into consideration the symmetries, this configuration can be analyzed by modeling just ten fibers in a two-dimensional model as shown in Figure 7.1. The analysis region is also shaded in the sketch of the configuration. The left edge of the model is exposed to air whereas the right edge is impermeable. The ten fibers in the matrix are modeled discretely and the results from using this model will provide the reference solution. The fibers are modeled as voids since the fibers are assumed to be impermeable. The same configuration is analyzed in two other ways to test the accuracy of the effective properties. One is to model the configuration completely using

homogenized properties for the microstructure. Since this involves only one homogenized material in a simple one dimensional geometry, this can be analyzed using a 1D finite element model. The other way is to use a mixed model with three unit cells on the extremes modeled discretely and the four interior unit cells modeled using homogenized properties. Figure 7.2 shows a schematic of this model. This method will test the accuracy of the homogenized properties in models with heterogeneous materials.

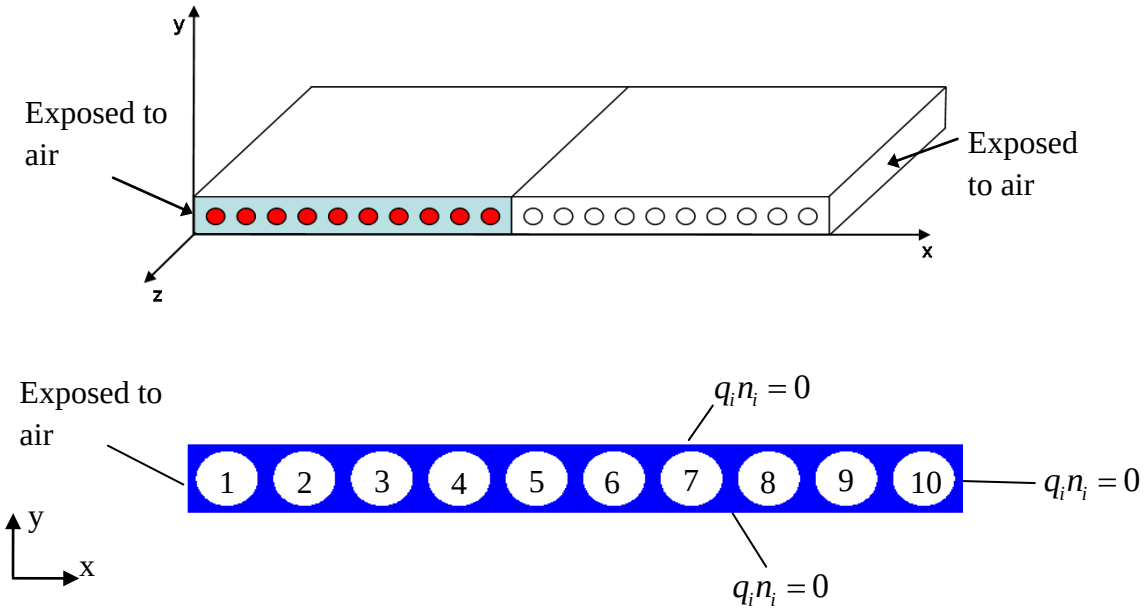

Figure 7.1: Schematic and analysis region for configuration A with the numbering for each unit cell.

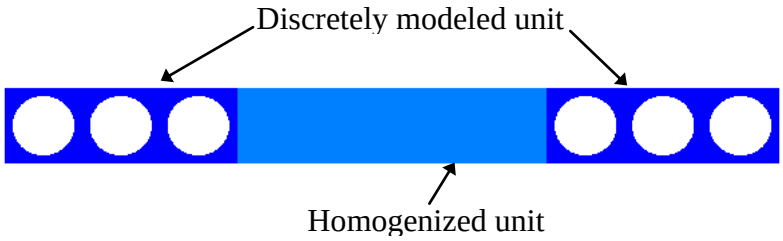

Figure 7.2: Mixed model for configuration A

7.2.2 Configuration B

This configuration is slightly more complex than the previous one in that the laminate is infinite only in the z direction. This can be considered as a square tow with 36 fibers packed in a square array as illustrated in Figure 7.3. Again, all the fibers have a diameter of 10 microns and are packed with a fiber fraction of 50%. The tow is exposed to air on all four lateral surfaces and starts oxidizing as the oxygen makes diffuses into the tow. Utilizing symmetry conditions, only the shaded region in the sketch needs to be modeled, as shown in Figure 7.3. The left and bottom edges in the analysis model are exposed to air while the right and top edges are specified to be impermeable.

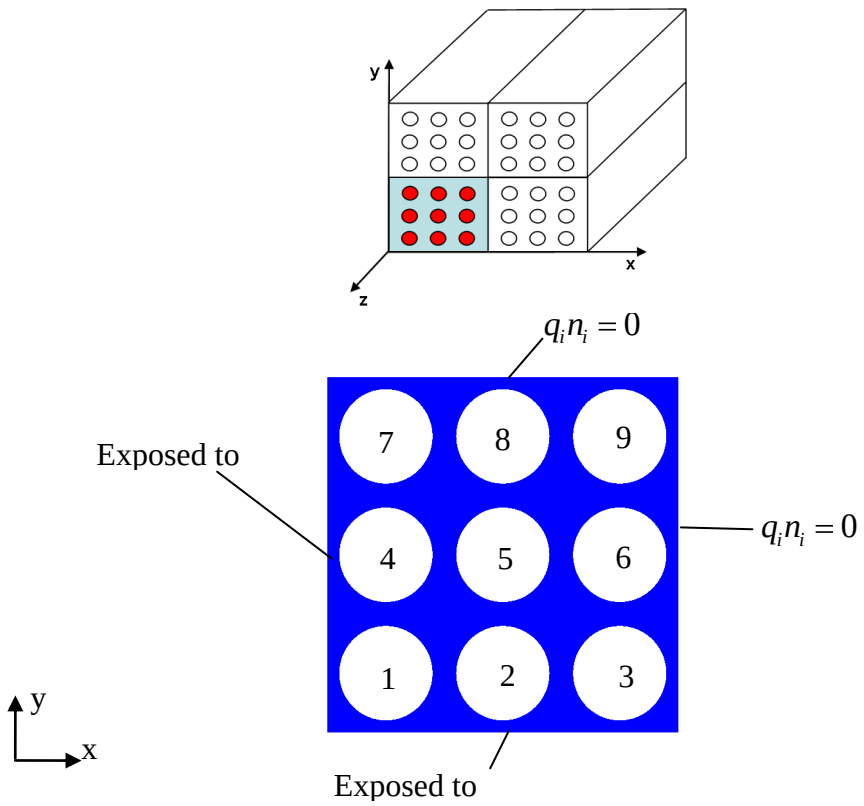

Figure 7.3: Schematic and analysis region for configuration B with the numbering for each unit cell.

7.2.3 Configuration C

This configuration considers a slightly more realistic situation with an irregular distribution of fibers. A computer generated random microstructure was used to represent the microstructure in a tow (see Figure 7.4). The two dimensional microstructure assumes that the fibers run exactly parallel to each other in the z-direction. This, of course, is not what happens in a typical tow but this configuration would be a reasonable precursor to modeling the much more complex (if at all achievable) realistic microstructure of a tow. The configuration C has 160 identical fibers with 10 micron diameter like the previous configurations but with an overall fiber fraction of 28.49%. The analysis region is assumed to be a square with a side of 210 microns. The configuration is assumed to be exposed to air from the bottom edge and all the other surfaces are impermeable. Three idealizations are used to model the configuration. The first one discretely models the random microstructure shown in Figure 7.4. This idealization also brings to light the computational challenges involved in analyzing the oxidization behavior of complex microstructures. The second

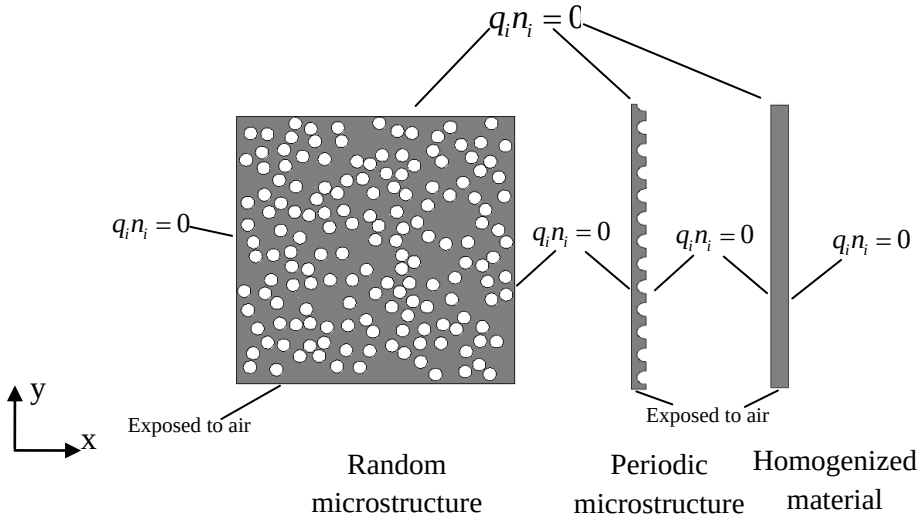

Figure 7.4: Analysis regions for the different configuration C idealizations.

idealization uses a periodic microstructure. It is not possible to create a perfect square region using an array of 160 square unit cells because $\sqrt{160}$ is not a rational number. A close approximation was chosen using a square with a side measuring 12.5 square unit

cells (or 207.54 microns). Although the height of the periodic model is a half unit cell longer than the discrete model, this difference does not have any effect on the oxidation growth behavior for the 200 hour simulations that are analyzed in this work. Even after 200 hours of oxidation, the oxidation front in a pure resin advances less than 100 microns and the un-oxidized material on the other side of the front has insignificant influence on the oxidation growth up to that point. For a periodic idealization, it is possible to analyze just a fraction of the configuration by taking advantage of symmetry. To analyze the idealized periodic configuration, a model with a width of a half unit cell and a height of 12.5 unit cells was chosen. The third idealization uses a homogenized material to model the configuration. The simple boundary conditions and the single homogenized material in the idealization allow the third configuration to be modeled using 1D elements.

7.3 Results and Discussion

Before determining the accuracy of the effective oxidation material properties, diffusion analyses were run for both configurations A and B to validate the accuracy of the effective diffusivities. Oxidation analyses were conducted for all three configurations (A, B and C). The results from the diffusion modeling are discussed first followed by that of the oxidation modeling.

7.3.1 Diffusion Modeling

The diffusion behavior was simulated using the un-oxidized PMR-15 resin diffusivity to model the material in the discrete models, which is 53.6×10^{-6} mm^2/min. For the models that used homogenized materials, the corresponding effective diffusivity of the un-oxidized resin was used, which for the case of a 50% fiber fraction tow is 34.88×10^{-6} mm^2/min.

Diffusion analyses were conducted on all three models representing configuration A: discrete model which serves as the reference solution, a fully homogeneous model and a mixed model as shown in Figure 7.1 and 7.2. The two-dimensional models that generated the results shown in Figure 7.5, 7.6 and 7.7 used meshes with a maximum

element length of 1.41×10^{-3}mm and a time step size of 0.15 minutes. Figure 7.5 shows the concentration profiles in the discrete and mixed model at 5 hrs. It is seen that the concentration profiles are almost exactly the same in the first three unit cells on the left which is modeled discretely in both the discrete and mixed models. This shows that the

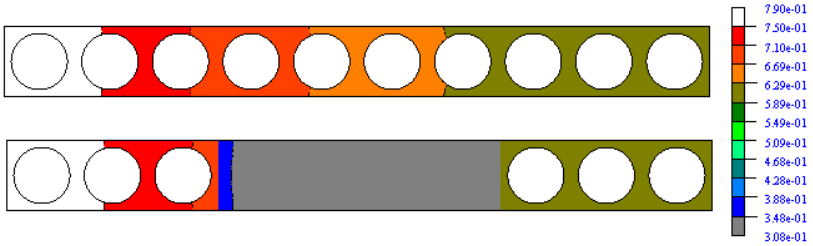

Figure 7.5: Concentration profiles in discrete and mixed models for configuration A under diffusion at 5 hours.

effective properties in the homogenized region did not cause an adverse effect on the concentration profile in the discretely modeled region. The homogenized material has a different saturation concentration compared to the neat PMR-15 material as shown in Table 7.1, which is calculated using Eq.(48). The normalized concentration distribution will be continuous throughout the model based on the finite element formulation as explained in section 3. On the other hand, since the homogenized material has a different saturation concentration as compared to the neat resin, the concentration distribution (which is calculated using Eq.(13)) will have a discontinuity at the interface between the discrete and homogenized region. It is not convenient to make reasonable comparison between the two models by just looking at the concentration profiles. When the models compared have homogenized properties, it is perhaps more reasonable to compare volume averaged concentrations.

Figure 7.6 shows the volume averaged concentration for the entire model as it grows over time. It shows that the curves from the homogeneous and mixed model fall exactly on top on the curve from the discrete model. To take a closer look at the results, the concentrations were averaged over each of the 10 unit cells in the configuration. The unit cells are numbered as shown in Figure 7.1. Figure 7.7 shows the average concentrations

in each unit cell at three snapshots in the simulation: 15 mins, 150 mins and 375 mins into the simulation. For each snapshot, the average concentrations from the three different models are shown. The first three columns for each unit cell denote the average concentrations for t=15 mins, the next three for t=150 mins and the last three columns for t=375 mins. For each set of three columns, the first one denotes the discrete model, the second denotes the homogeneous model and the last one denotes the mixed model. The results show that both the models that use effective properties agree very well with the discrete model.

Configuration B was analyzed for diffusion using both the discrete model and the fully homogenized model. The two-dimensional models that generated the results shown in Figure 7.8 and 7.9 used meshes with a maximum element length of 1.41×10^{-3}mm and a time step size of 0.15 minutes. Figure 7.8 shows the average concentration in the entire model as it grows over time. The two models agree closely. The homogeneous model under predicts the average concentration in the beginning of the simulation and the difference reduces as time progresses. It is not surprising that the error reduces as the simulation progresses because both models are approaching the same steady state condition. Similar to the previous configuration, the average concentration was determined for each of the nine unit cells at two different times through the simulation. The unit cells are numbered as shown in Figure 7.3. Figure 7.9 shows the average concentration from the discrete and homogeneous in each unit cell at t=1.5 and 15 minutes. The results in Figure 7.9 repeat the trend from Figure 7.8 in that the homogeneous model under predicts the concentrations and the predictions become closer in agreement as the simulation progresses. In this configuration, the concentration profile is more complicated than the earlier one because the oxygen is flowing in from two directions. This kind of complex loading appears to have an effect on how well the diffusion is modeled by the effective properties. Although it does not do a perfect job in simulating the oxygen flow in the beginning, the accuracy increases very quickly as the simulation progresses.

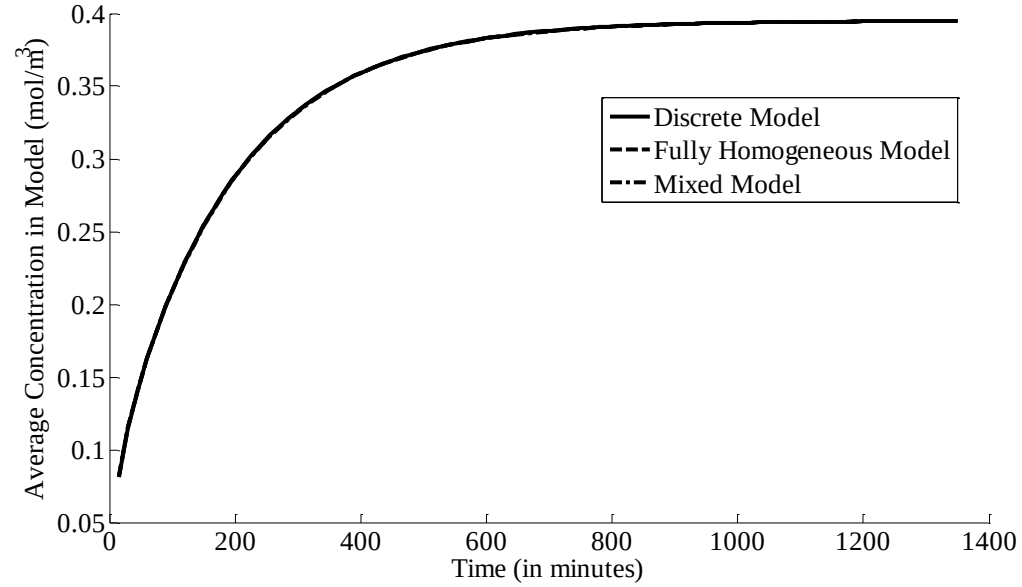

Figure 7.6: Variation of average concentration in configuration A with time

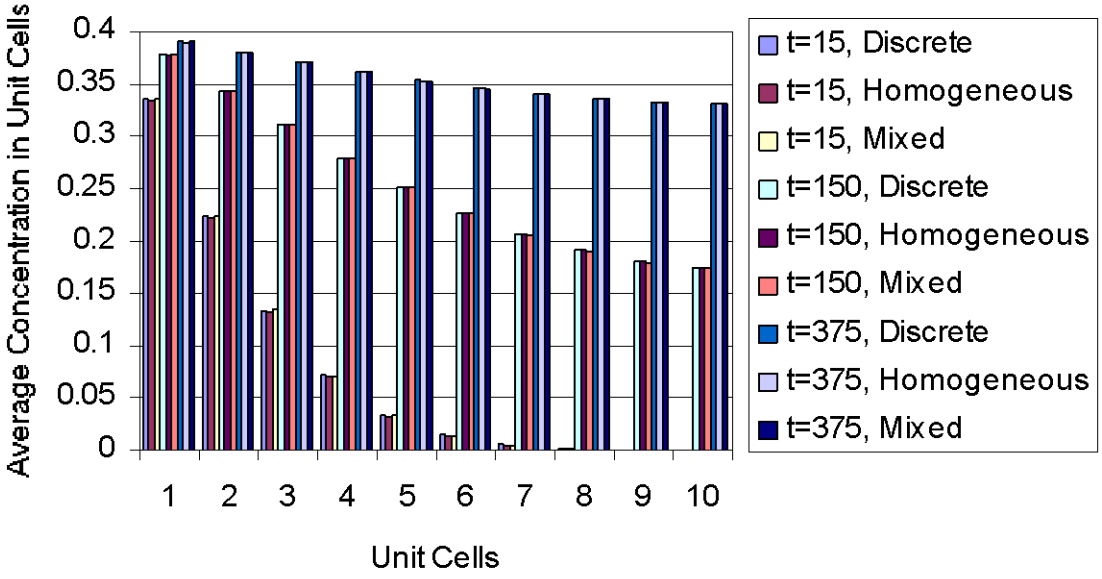

Figure 7.7: Variation of average concentration in each unit cell in configuration A at different times (in minutes)

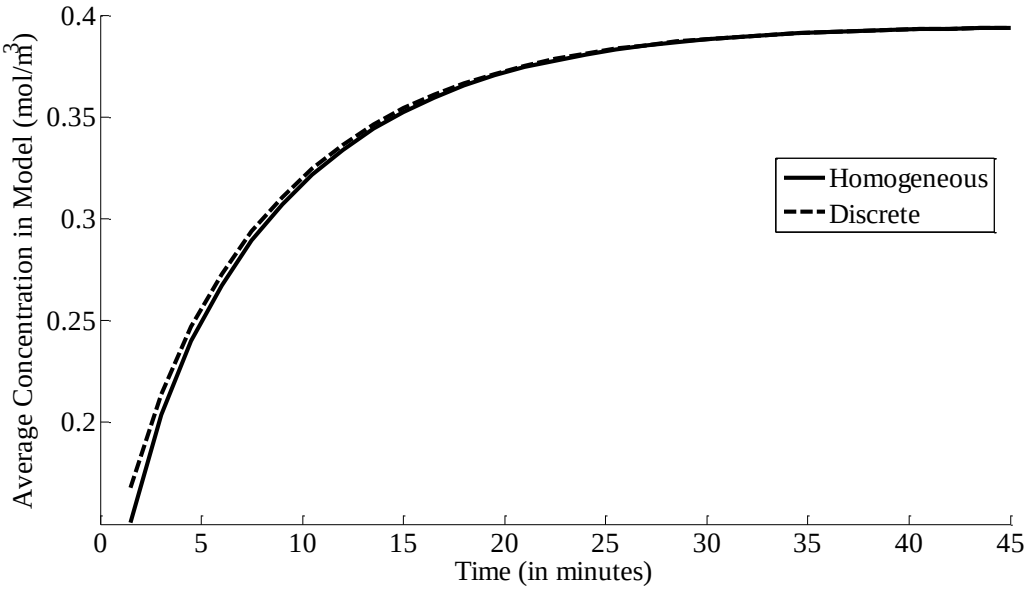

Figure 7.8: Variation of average concentration in configuration B with time

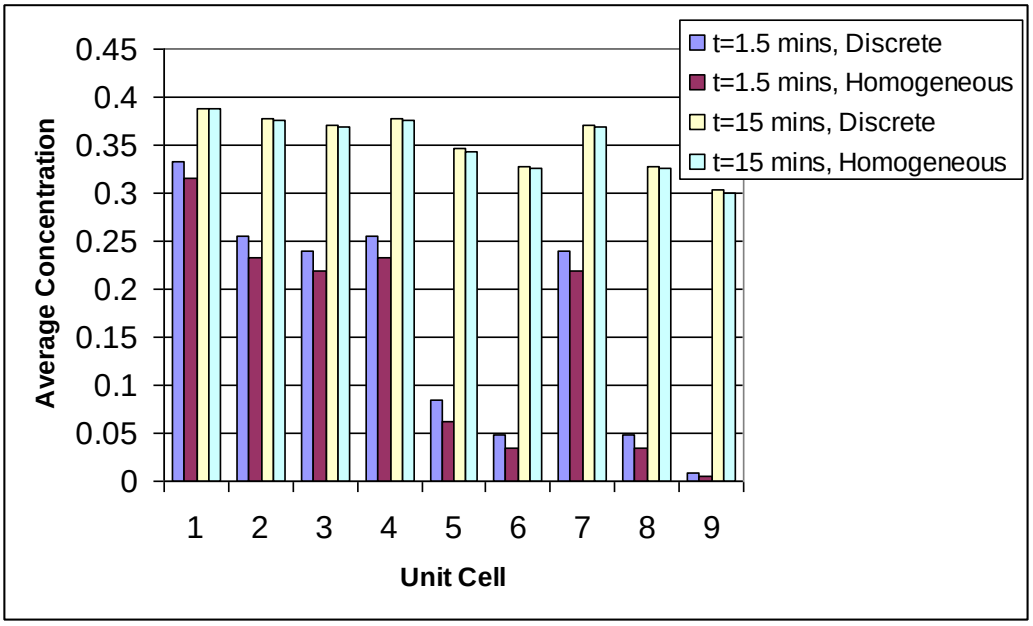

Figure 7.9: Variation of average concentration in each unit cell in configuration B at different times (in minutes)

7.3.2 Oxidation Modeling

This section discusses the results from the oxidation simulation of configurations A, B and C. In the oxidation analysis, there are primarily two types of data that are of interest – the concentration and the oxidation state. For configuration A and B, the concentration distribution will be discussed first followed by the oxidation state. For configuration C, only the oxidation state results are presented.

Figure 7.10 shows the concentration profiles in the discrete and mixed model at 200 hrs. It is seen that the concentration profiles are almost exactly the same in the first three unit cells on the left which are modeled discretely in both the discrete and mixed models. This shows that the effective properties in the homogenized region did not cause an adverse effect on the concentration profile in the discretely modeled region. There is, as expected, a discontinuity in the concentration at the interface between the discrete and homogenized region just as seen in the diffusion analysis of configuration A.

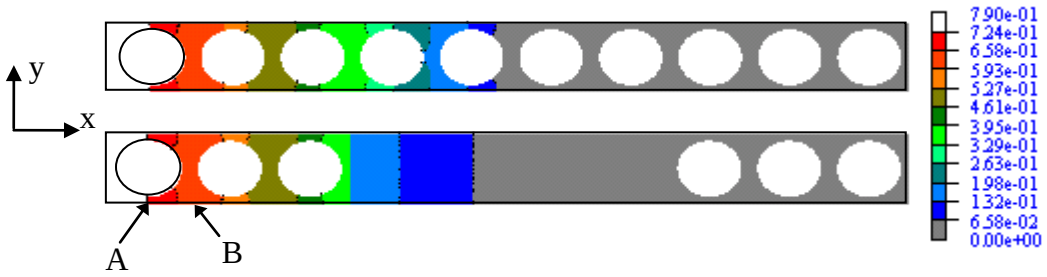

Figure 7.10: Concentration profiles in discrete and mixed models for configuration A at 200 hours.

Just as the results for the diffusion analysis were presented, Figure 7.11 shows the average concentration growth in the model over time. The plot shows that the discrete model appears to have spurts of increase in the average concentration. This can be explained by the fact that the discrete model has fibers that are impermeable and do not oxidize. When the oxygen diffuses from the left end, the cross sectional area of the polymer material through which it can diffuse varies. The area decreases to a minimum where the fiber takes up the most space in the cross section (indicated by A in Figure

7.10) and increases to a maximum when there is no fiber in the cross section (indicated by B). Therefore, when the oxygen is diffusing through the constricted regions, the process slows down and this effect shows up in the concentration growth. When the oxidation front (or the 'moving barrier' as described in the previous section) passes the constricted pathways, the process speeds up for a while till the next constricted pathway comes along. The homogeneous model has no such spurts in the growth of the average concentration because the model assumes that it is all one homogeneous material without any impermeable fibers. On the other hand, the mixed model does show the spurts in concentration growth in the first part of the curve because the mixed model does have three discrete fibers modeled in the left end where the oxygen is entering the material. Although there are these oscillations when the fibers are discretely modeled, it is clearly seen that the models with the effective properties do follow the same general trend and appears to follow the mean line of the oscillating curves.

Figure 7.12 shows the difference in the average concentration from the discrete and homogeneous in each unit cell at t=150 minutes and t=200 hours. While the homogeneous models always under predicted the average concentrations in the diffusion only analysis (see Figure 7.7 and 7.9), no such correlation was seen in the oxidation analysis. This can be attributed to the same reason for seeing spurts in the growth of the average concentration. As seen in Figure 7.11, depending on the simulation time, the homogeneous model fluctuates between under predicting and over predicting the average concentration. This same effect is what is seen in Figure 7.12.

The Zone I and II thicknesses are measured for all the three models for configuration A: the fully discrete model, fully homogenized model and the mixed model. The zone thicknesses for the discrete and mixed models are assumed to be the thicknesses along the top or bottom edges of the model. Note that the model is symmetric about the horizontal mid-axis and therefore the oxidation layer growth will be symmetric about that line. Figure 7.13 shows growth of the oxidation layer (Zone I + II) for the three models as well as the variation of the active zone layer (Zone II). It can be seen that the effective properties do a good job in predicting the growth in both the homogenous and

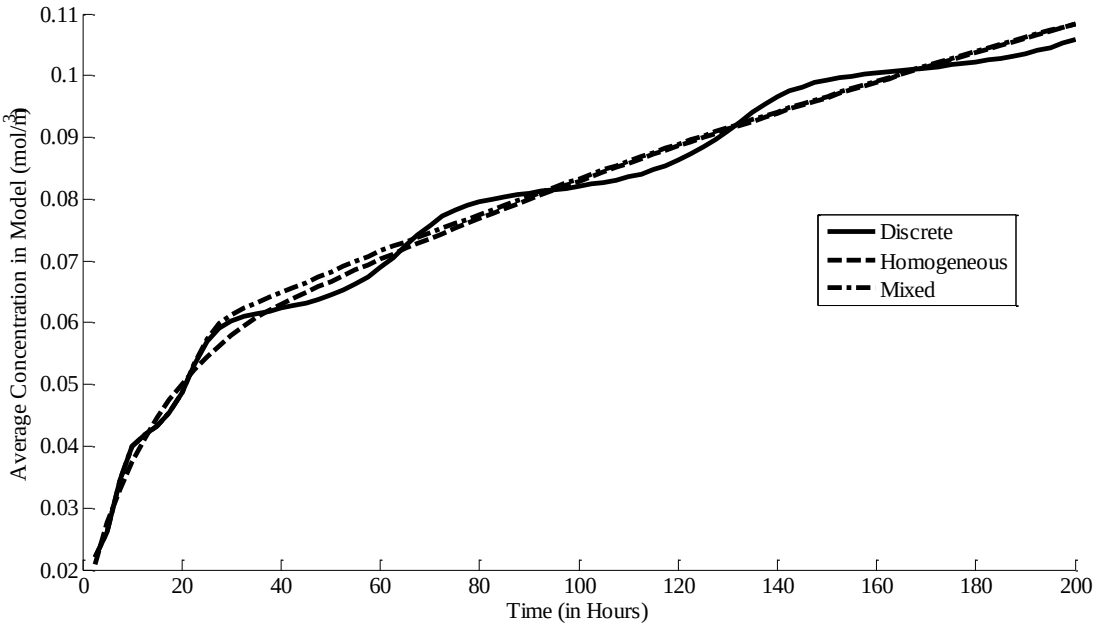

Figure 7.11: Variation of average concentration in configuration A with time under oxidation

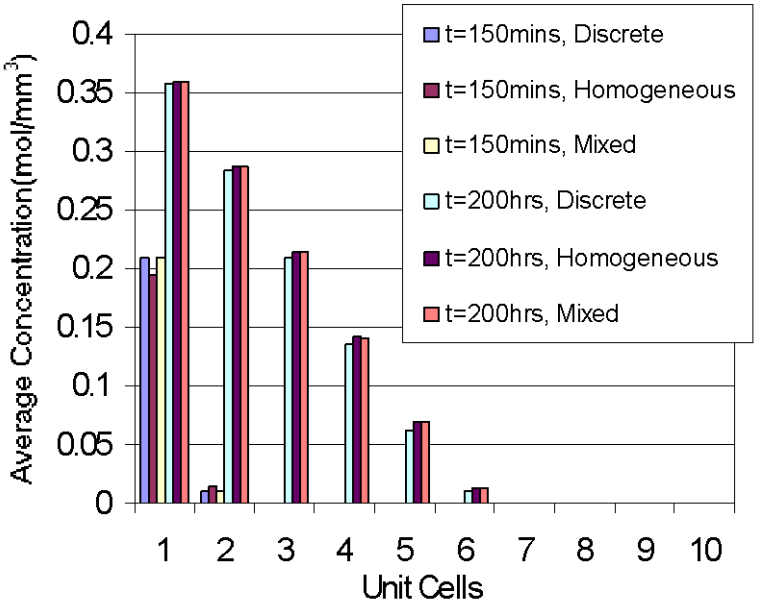

Figure 7.12: Variation of average concentration in each unit cell in configuration A at different times under oxidation.

mixed model. The Zone II thickness is also found to be predicted fairly well considering that the Zone II thickness according to the discrete model appears to fluctuate erratically. Figure 7.14 shows the evolution of the oxidation layer in the discrete and mixed models. The three zones, Zone I (Fully oxidized), Zone II (Oxidizing) and Zone III (Un-Oxidized) are color-coded by grey, red and blue respectively. Figure 7.14 shows the state of oxidation at six different times during the simulation, t= 150 mins, 25 hrs, 50 hrs, 100 hrs, 150 hrs and 200 hrs. The snapshots in Figure 7.14 shows what has already been conveyed by Figure 7.13 in that the effective properties are able to simulate the oxidation layer growth fairly well for configuration A.

Next, the oxidation analysis was performed for configuration B using two models – a discrete model and a homogeneous model. Figure 7.15 shows the concentration distribution in the two models at time, t=150 mins. The homogeneous model has the fibers drawn in light gray in order to expedite comparisons with the discrete model. While the concentrations contours do not exactly match, the contours in between the fibers do in some sense resemble corresponding contours in the homogeneous model. Figure 7.16 shows the growth of average concentration in the two models as simulation progresses. Similar to the concentration growth in discrete model for configuration A, it can be seen that the concentration growth for configuration B follows a similar oscillating trend. The plot shows that the homogeneous model under-predicts the average concentration for most of the simulation. It is understandable that the homogeneous model is not able to reproduce the wavy nature of the concentration growth in Figure 7.16 because that effect is caused by the microstructure. The homogenous model on the other hand, does not have such a microstructure.

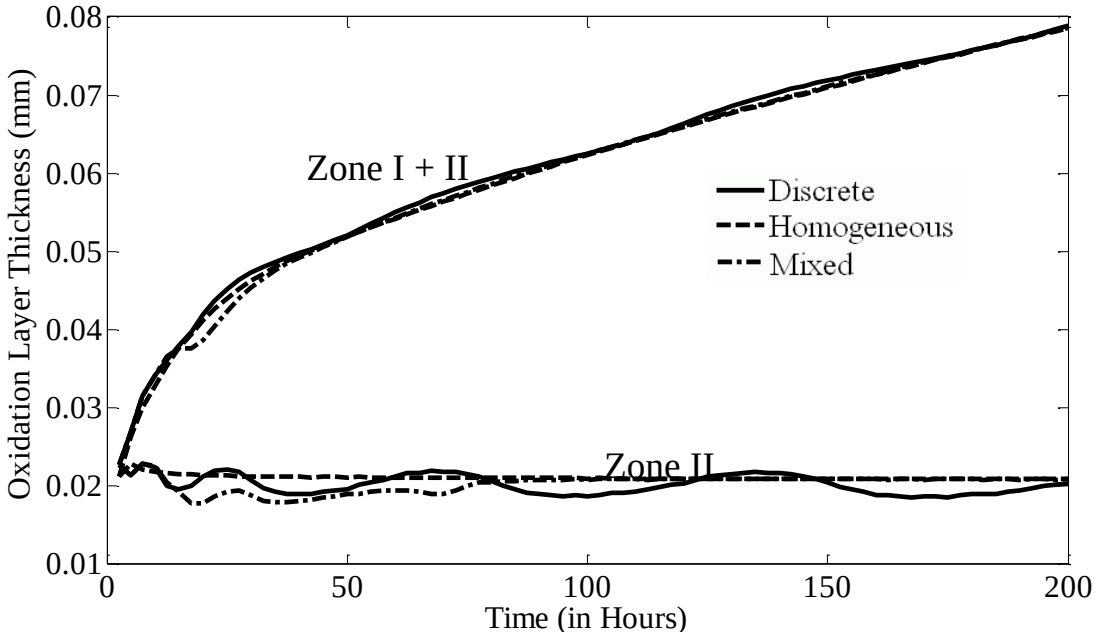

Figure 7.13: Oxidation layer growth (Zone I+II and Zone I) for configuration A

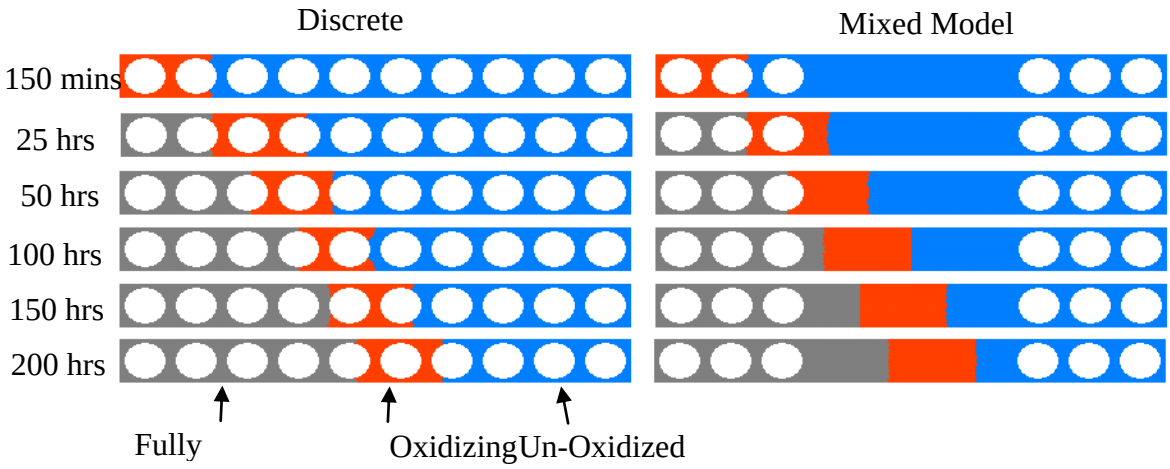

Figure 7.14: Evolution of oxidation layer in discrete and mixed model for configuration A

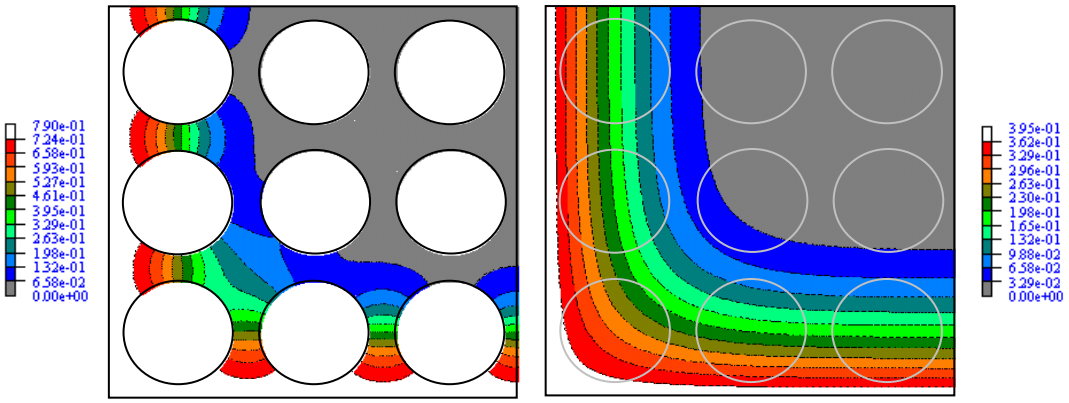

Figure 7.15: Concentration profiles in discrete and mixed model at t=150 mins for configuration A

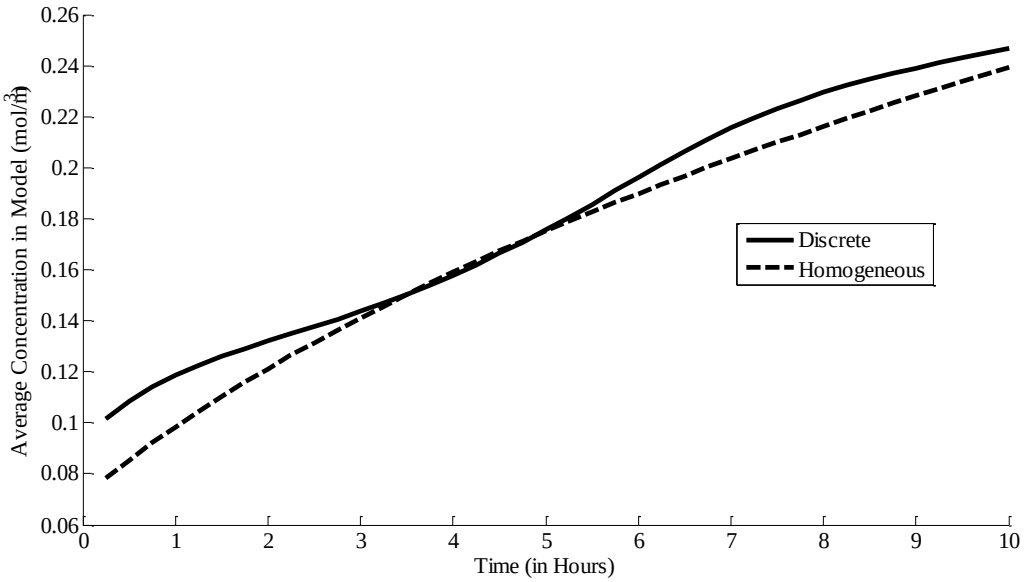

Figure 7.16: Variation of average concentration in configuration B with time under oxidation

The oxidation state from the two models is compared next. Figure 7.17 shows the oxidation state at different times in the simulation. As shown in Figure 7.15, the

homogeneous model has the fibers drawn in light gray in order to expedite comparisons with the discrete model. The oxidation states for t=15 mins, 2.5 hrs, 5 hrs and 10 hrs are shown. The figures show that the homogeneous model is able to predict the oxidation layer growth fairly accurately.

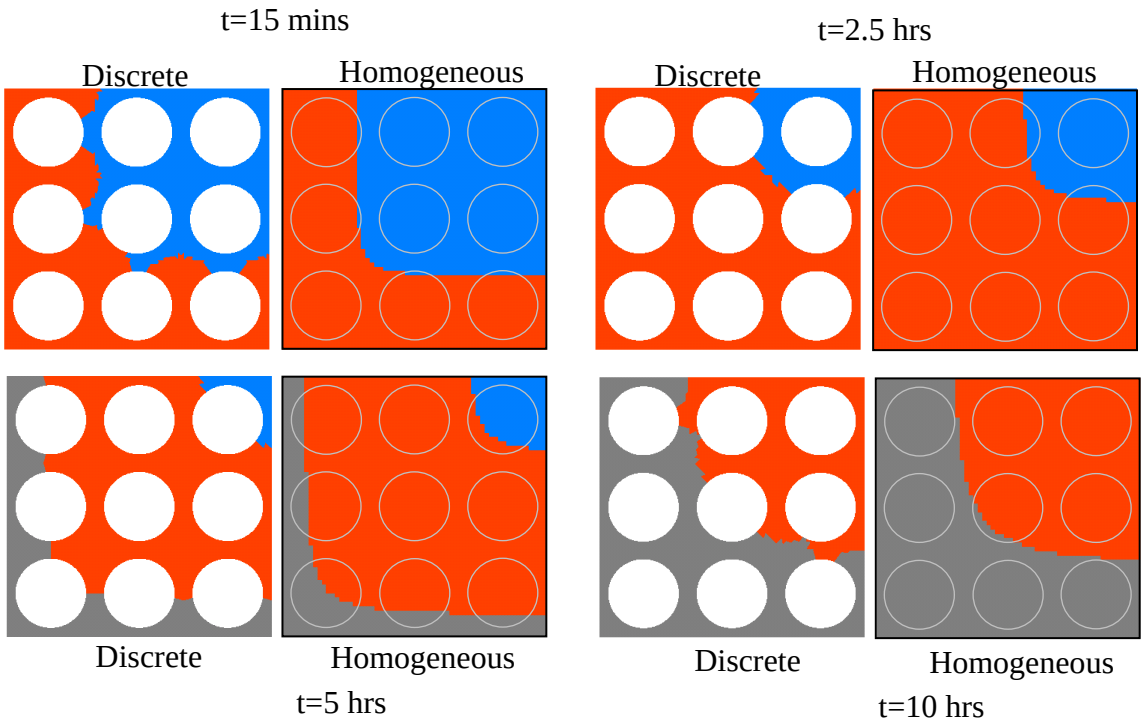

Figure 7.17: Evolution of oxidation layer in discrete and homogeneous models for configuration B

The discrete models that have been considered so far model only 9 or 10 fibers but the discrete model for configuration C models 160 fibers. This makes it a considerably larger model and more time-consuming compared to the previous models. Figure 7.18 shows the contour plots of the oxidation state in the discrete and periodic models after undergoing 75 hours of oxidation. As expected the oxidation profile is irregular for the model with the discrete microstructure. Nevertheless, the variation in thickness and location of the oxidation layer from the exposed edge varies no more than 5% across the width. It is interesting to note that the periodic model predicts relatively the same

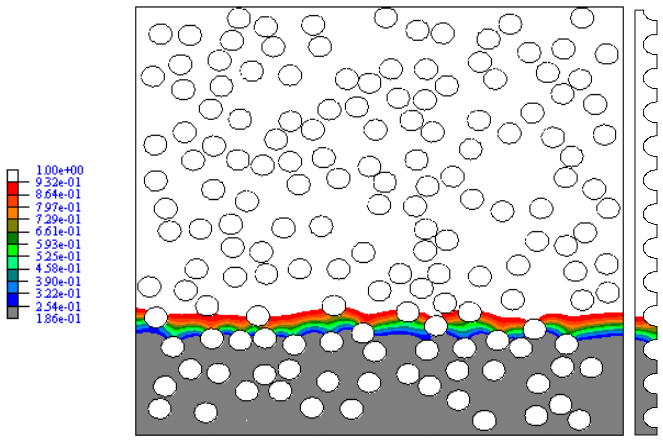

Figure 7.18: Oxidation state profiles in discrete and periodic model at t=75 hours for configuration C

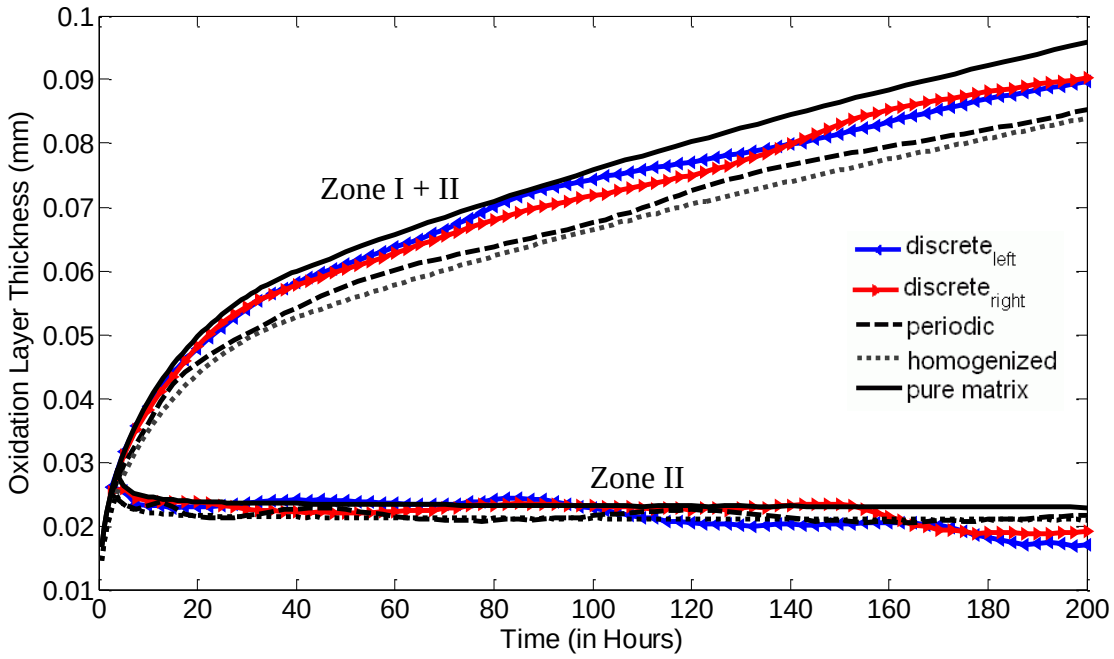

Figure 7.19: Oxidation layer growth (Zone I+II and Zone I) for configuration C

amount of oxidation growth as the random model which indicates that for this fiber volume fraction and distribution of fibers, the oxidation growth can be idealized by using a periodic array. While Figure 7.18 shows the oxidation state distribution at a single snapshot from the entire simulation, Figure 7.19 gives a sense of how the oxidation state evolved during the entire simulation. Figure 7.19 gives the oxidation layer growth over time for the random, periodic and homogenized idealizations. It shows the oxidation layer growth along the two edges (right and left) of the discrete model. While the two curves do not fall right on top of each other, they are very close. The curve from the periodic model is very close to the curves from the discrete model and follows the same trend but slightly under predicts the oxidation growth. The homogeneous model also follows the same trend but under predicts the growth even further. To make an easy comparison with the behavior if there were no fibers at all (i.e. pure resin), the oxidation growth curve from pure resin oxidation analysis (using a 1D model) is also included. This shows that the pure resin oxidizes slightly faster than when there are fibers in the resin which is expected since the fibers are assumed to be impermeable and do not oxidize.

A typical homogenization process in structural mechanics results in being able to use a less refined homogenized model to replace the actual microstructure. This was generally found to be the case for the oxidation analysis as well. As discussed in the previous section, it is possible optimize the mesh parameters and use larger elements and time steps. In some configurations, including the ones described in this section, the element size is restricted by the need model the discrete geometry accurately. This restriction is greatly reduced when modeling homogenized regions. It is also easier to generate the models when a complex microstructure can be replaced by a simpler homogenized geometry. Another advantage is that sometimes a two dimensional model can be replaced with a one dimensional model that is much less computationally intensive. This was made use of when analyzing configuration A with a fully homogeneous model. The goal of this work is to eventually be able to correlate the effect of the oxidation on the mechanical response and damage progression of the composite. Keeping this in mind,

tracking the regions of oxidized or oxidizing material in the composite is what would be considered to impact the mechanical response. For the material system being considered in this work, the thickness of the active zone is found to be practically constant and the variation of oxidation state within this zone can be inconsequential in this regard, but this need not be the case for other composite systems. Further work needs to be performed in order to determine if some accuracy of the oxidation state variation in the active zone can be given up in exchange for better computational efficiency as long as the oxidation layer thicknesses are predicted with reasonable accuracy.

7.4 Summary

To simulate the oxidation of the textile composite, it is important to be able to use homogenized oxidation properties for the tow because it is practically impossible to discretely model all the fibers in a composite. Effective oxidation material properties were calculated for a unidirectional laminate/tow using the expressions described in section 3.5.7. Three configurations were analyzed to test the accuracy of the effective oxidation properties. The fibers were assumed to be impermeable and do not oxidize. All the configurations had 10 micron diameter circular fibers. Two of the configurations had the fibers in a square array packing with 50% fiber fraction whereas the third configuration had random microstructure with an overall fiber fraction of 28.5%. The configurations were discretely modeled to provide a reference solution. Idealizations with fully homogenized materials as well as mixed idealizations (both discrete and homogenized regions) were used to determine the accuracy of the effective properties. The concentration of oxygen in the model as well as the oxidation state of the materials in the composite was compared to the reference model. It was seen that the effective oxidation properties performed reasonably well for both configurations and were able to simulate the oxidation layer growth.

8. OXIDATION ANALYSIS OF TEXTILE COMPOSITES

8.1 Introduction

One of the primary goals of this work is to study the effect of oxidation on damage progression in textile composites. A precursor to the complete damage progression is the oxidation analysis of the textile composite. The information from the oxidation analysis will be used to degrade the mechanical properties of the textile composite in the damage progression model. In this work, the mechanical damage is assumed to not have an effect on the oxidation behavior. Therefore, the oxidation model and the damage progression model are only coupled in one direction, where the oxidation behavior has an effect on the damage model and not the other way round. As discussed in the previous section, simulating the oxidation behavior is a computationally intensive task. Conventional oxidation analysis of textile composites would require a full 3-D model and in spite of the savings from the adaptive meshing strategy described in Section 7, a full 3-D oxidation analysis would be exceedingly time-consuming. This section describes a hybrid modeling strategy developed to make oxidation analysis feasible. The validation of the strategy is also described followed by the simulation of oxidation of a plain weave composite configuration using the hybrid strategy. This section also describes the information that is generated from the hybrid modeling strategy, which can then be used in the coupled damage progression model to predict the mechanical behavior of the composite under oxidation.

8.2 Hybrid Model

Textile composites have multiple microstructural scales – the fiber/matrix scale, the tow architecture scale and laminate scale. As mentioned in the previous sections, it is not practical to discretely model all the fibers in the composite because of modeling and computational challenges. Effective oxidation material properties that are derived in Section 3 and validated in Section 7 are used to model the tows in the textile composite. The adaptive meshing strategy described in Section 6 gives considerable savings compared to the standard finite element method but unfortunately, it is not enough to

make the 3-D analysis of textile composites feasible. Given the length scales involved and the limitations on the element size, the mesh would require a huge number of elements. This would make generating the models extremely challenging, and analyzing the models practically impossible. Moreover, considering that the overall goal of this research effort is to couple the oxidation analysis with the damage progression analysis, the combination would be prohibitively expensive. In an effort to make this more feasible, a hybrid analysis was developed to make the oxidation analysis more efficient.

The strategy applies to composite laminates that are exposed to oxygen from the top or bottom (or both) surfaces, but not the lateral surfaces. The strategy is illustrated in Figure 8.1, which shows a $1/8^{th}$ unit cell of a plain weave symmetrically stacked 2-ply laminate. The hybrid analysis takes the three-dimensional model and divides it up into individual analysis domains in the in-plane dimensions as shown in Figure 8.1. The strategy assumes that because of the boundary conditions applied on the model, the oxidation behavior will be such that the neighboring domains do not have an effect on each other, essentially assuming that oxygen does not flow from one domain to another. Therefore, the individual domains can be analyzed separately. Each individual domain is

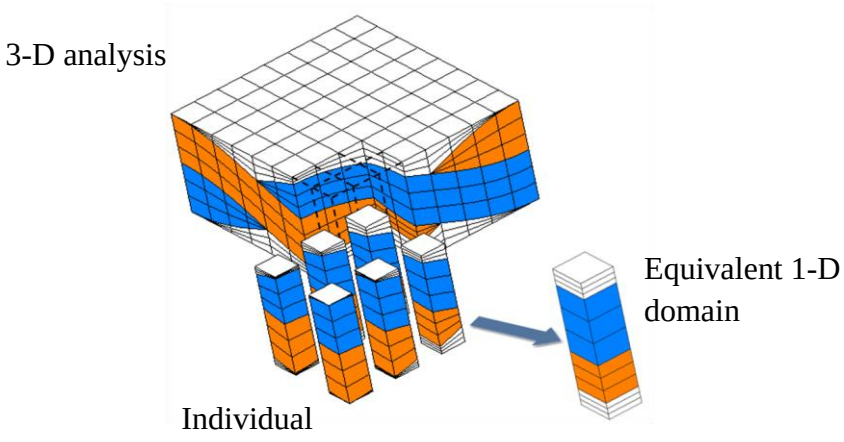

Figure 8.1: Schematic of hybrid model for analyzing textile composites

a three dimensional heterogeneous analysis region with curved material boundaries because of the undulation of the tows in the textile composite. The model assumes that the change in the diffusivity due to the undulation is not significant because the rotation

angles in actual composites are relatively small. The analysis also assumes that the undulations of the tows are not significant enough to cause an impact on the oxidation behavior. This assumption has been validated and is discussed in the next section. Based on this assumption, the individual 3-D domain can be converted into an equivalent domain with straight horizontal material boundaries based on the volume fraction of the different constituents in the domain as illustrated in Figure 8.1. Since the new equivalent domain has no inclined material boundaries, it can be analyzed with a simple 1-D model. Thus, the 3-D model shown in Figure 8.1 can be replaced by an array of 64 1-D models, thereby reducing analysis time significantly. The hybrid model is implemented in the finite element analysis package in such a way that the input to the model is the same as the conventional 3-D model. Additional pre-processing work is not required and the array of 1-D models is automatically generated and analyzed without the need for human interaction. Moreover, the 1-D models can be run in parallel on multi-core processors, thereby increasing the efficiency even further. This hybrid modeling strategy was validated by using a 2-D configuration. The validation including discussion of some of the oxidation behavior is described in the next section.

8.3 Validation of Hybrid Model

A simple 2-D heterogeneous configuration with two materials was chosen where the material boundary is straight but at an angle to the horizontal edge as shown in Figure 8.2(a). The bottom edge is assumed to be exposed to oxygen whereas the other three edges are assumed to be impermeable. The configuration has the dimensions 200 microns x 100 microns. The material in the lower region is assumed to be neat PMR-15 resin and the other material is assumed to be a homogenized graphite/PMR-15 tow with a fiber fraction of 55.6%. The 2-D plane in the configuration is assumed to be the plane perpendicular to the fiber axis in the tow and therefore only the transverse diffusivities of the tow will be used in the 2-D analysis. The material properties of the tow are calculated using the formulas described in Section 3.5.7. The material properties of the resin are given in Table 6.1 and that of the homogenized tow using the aforementioned formulas are given in Table 8.1. The region is first divided into two domains and

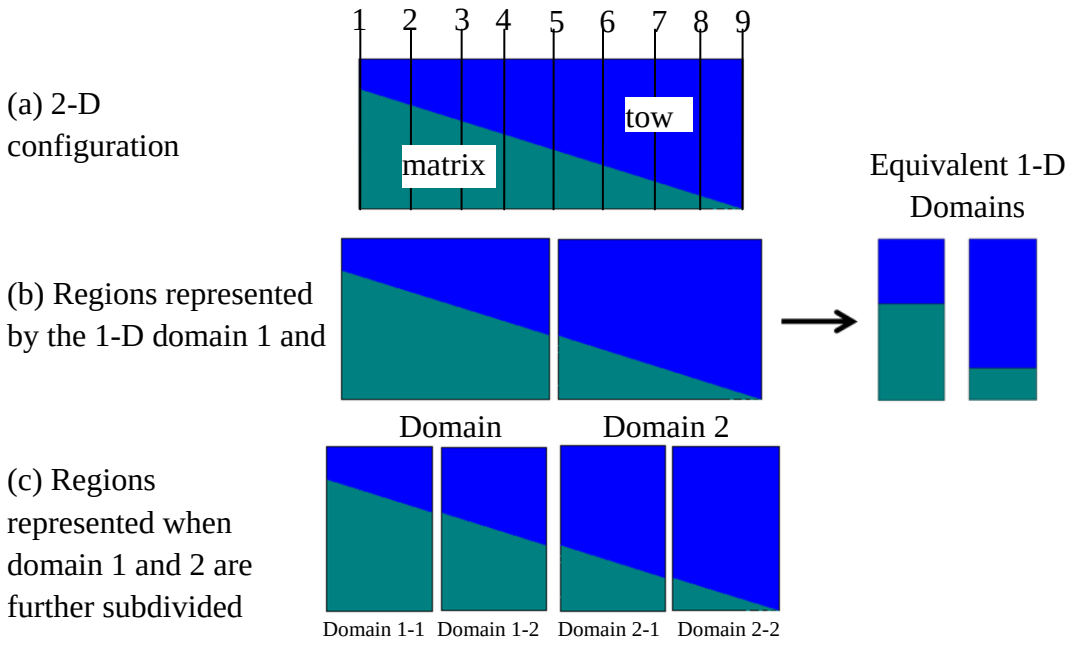

Figure 8.2: 2-D configuration for validating hybrid model

converted into equivalent 1-D models as shown in Figure 8.2(b). To compare the oxidation layer growth predicted by the 1-D models with the behavior in the actual 2-D model, the oxidation layer growths along different vertical lines (numbered in Figure 8.2(a)) in the 2-D model are compared. Figure 8.3(a) plots the oxidation growth given by the equivalent 1-D domain 1 model along with that along lines 1, 3 and 5. It shows that the 1-D result agrees very closely with that of line 3 and not so much with that of lines 1 and 5, which are on the extreme edges of domain 1. Similar trends are seen in Figure 8.3(b), which shows corresponding plots for domain 2. The domains are then further subdivided into domains 1-1, 1-2, 2-1 and 2-2 as shown in Figure 8.2(c). The corresponding oxidation growth plots for domains 1-1, 2-1, 1-2, and 2-2 are shown in Figure 8.3(c), (d), (e), and (f) respectively. As expected, these results show that the equivalent 1-D domain models perform better at simulating the oxidation layer growth when the domain size is reduced.

Table 8.1: Oxidation material properties for the homogenized tow (V_f=55.6%)

	Homogenized tow (Vf=55.6%)
Transverse Diffusivity D_{unox} D_{ox}	33.07 x10^{-6} mm^2/min 48.27 x10^{-6} mm^2/min
R_0	1.554 mol/(m^{3}min)
ϕ_{ox}	0.639
C^{∞}	0.3507 mol/m^3
α	0.01-0.0067(t/40) : t < 40 0.0033 : t > 40 (t in hours)
$f(C)$	$\frac{2\beta C}{1+\beta C}\left[1-\frac{\beta C}{2\ 1+\beta C}\right]$
β	0.919

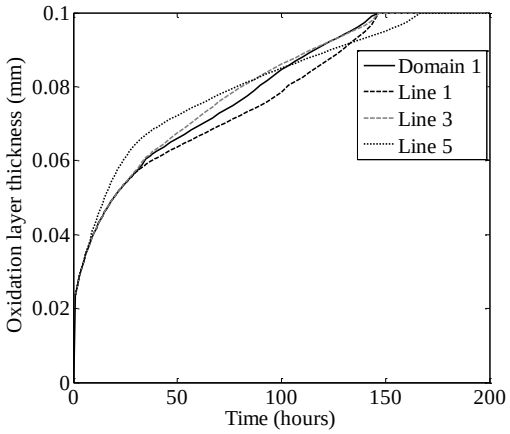

(a) Domain 1

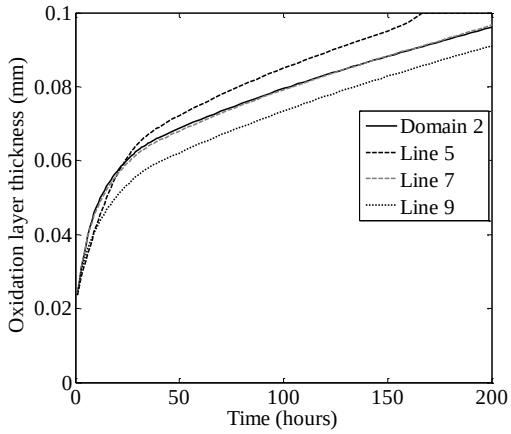

(b) Domain 2

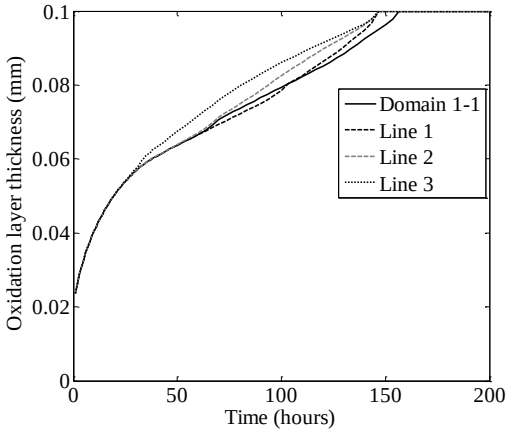

(c) Domain 1-1

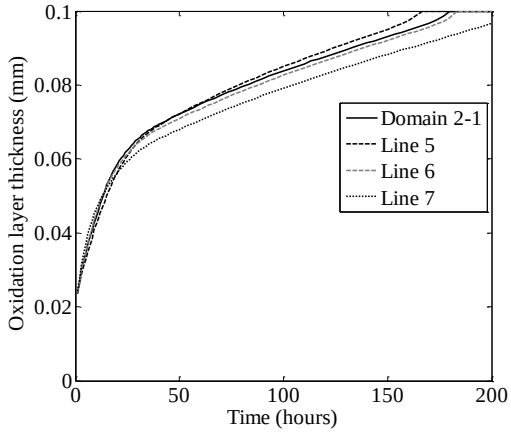

(d) Domain 2-1

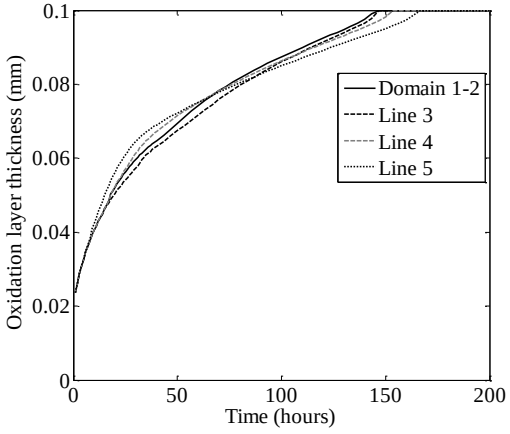

(e) Domain 1-2

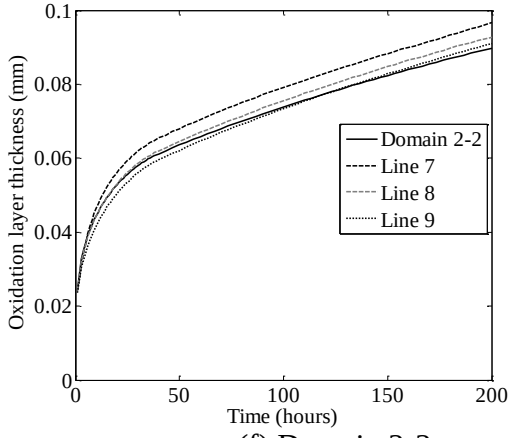

(f) Domain 2-2

Figure 8.3: Comparison of the oxidation layer growth from the different 1-D models with the growth in the 2D configuration

One interesting behavior that was noticed during the validation was that when simulating oxidation of a heterogeneous model with neat matrix and tow, the predicted oxidation growth seems counter-intuitive when compared to that of a model with neat matrix alone. Consider the equivalent 1-D configuration for domain 1 shown in Figure 8.4, which is a heterogeneous model with neat resin and homogenized tow. Figure 8.5 compares the predicted oxidation layer growth for the configuration in Figure 8.4 with that of a pure resin model. One would intuitively expect that since the model with the tow is assumed to have inert and impermeable fibers, this would slow down the oxidation layer growth compared to a neat resin model that has no fibers. But Figure 8.5 shows that the model with the resin and tow has a faster oxidation layer growth. On

Figure 8.4: Equivalent 1D configuration for domain 1

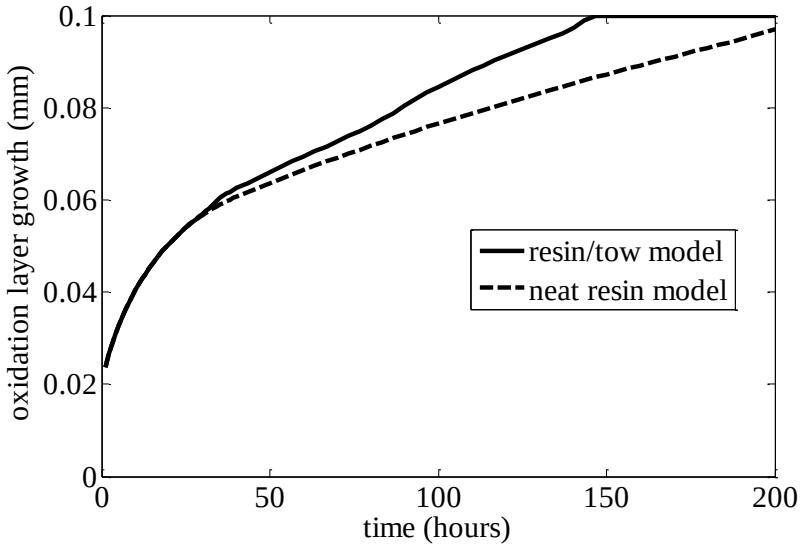

Figure 8.5: Comparison of oxidation layer growth in the domain 1 (resin/tow) model and neat resin model

further investigation, it was seen that a number of factors influence this behavior. The tow in the model acts like a pseudo-barrier allowing the resin to saturate with oxygen much faster than the tow. Until the oxidation front reaches the vicinity of the material boundary, both the models behave in the same manner because the tow has no effect on the matrix that is being oxidized ahead of it. But once the tow begins to oxidize as well, the interface conditions regulate the flow of oxygen from the matrix into the tow and free oxygen starts to build up in the matrix. This is evidenced in Figure 8.6 which shows the oxygen concentration profile in the model at 100 hours. Figure 8.6 shows that the resin region in the resin/tow model (from 0 to 0.06 mm) has more oxygen than the same region in the neat resin model. The oxygen in the tow region (from 0.06 to 0.1 mm) is also more than that in the same region for the neat resin model. This could be due to a combination of factors. First, note that at 100 hours, the oxidation front has crossed the material boundary but is not too far from it. The material boundary is at 0.06mm and the oxidation front at 100 hours can be considered to be around 0.08mm, beyond which the oxygen concentration is practically zero. Secondly, the tow has less amount of resin that can be oxidized and therefore the maximum reaction rate is also less than that of the neat

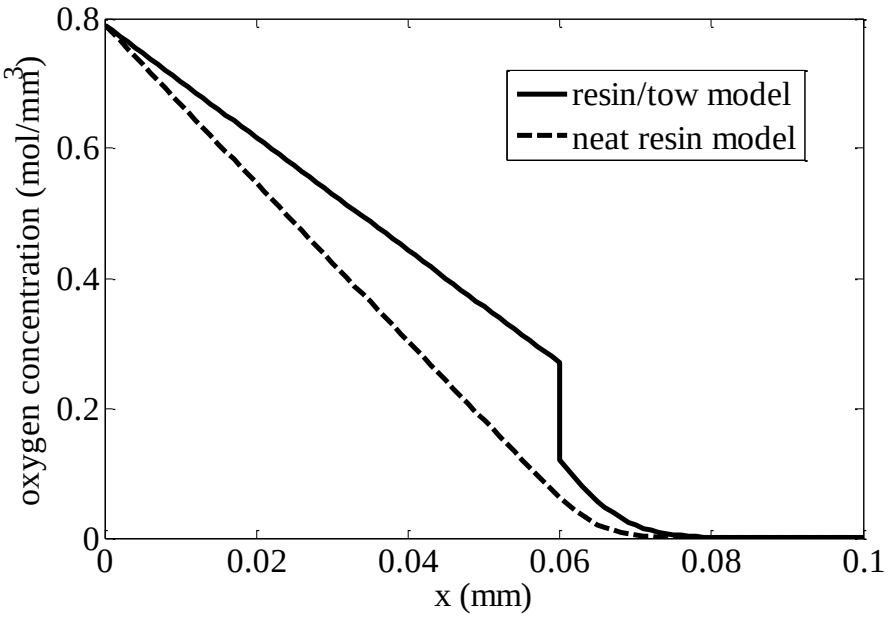

Figure 8.6: Comparison of concentration profile in the resin/tow model and neat resin model at 100 hours

resin. That also means that the region consumes less oxygen (for oxidation) than the neat resin. Since the reaction rate in the tow is less than that in the neat resin and the oxidation front is fairly close to the material boundary, the tow region between the material boundary and the oxidation front also starts accumulating more oxygen than the corresponding region in the neat resin. Figure 8.7 gives the amount of free oxygen in the model throughout the simulation. It shows that until about 60 hours, the resin/tow model and the neat resin model have the same amount of free oxygen, but after 60 hours the

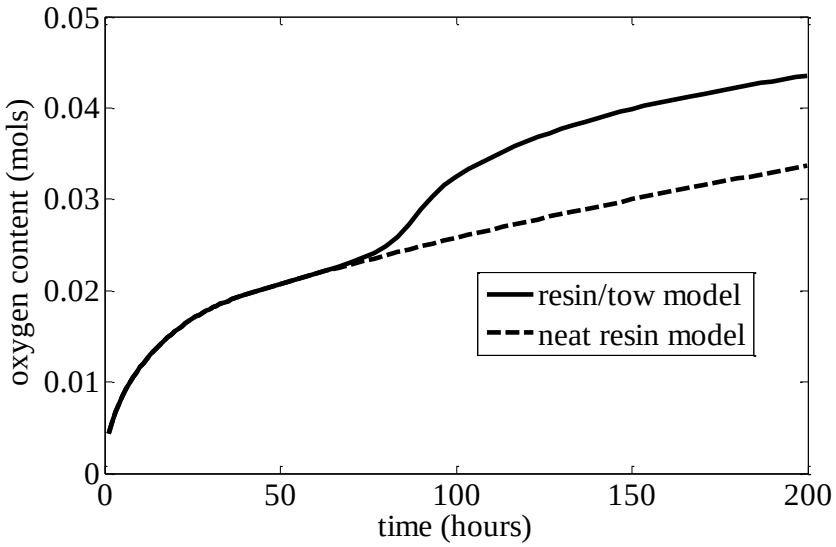

Figure 8.7: Comparison of amount of free oxygen in the resin/tow model and neat resin model

resin/tow model builds up more oxygen in its material. This is not to be confused with the amount of oxygen consumed in oxidizing the polymer in the resin and tow regions. The neat resin model is expected to consume more oxygen than the resin/tow model because it has more material that can be oxidized and this is shown in Figure 8.8. Once the oxygen starts to build up in the matrix, it becomes fully oxidized more quickly and all the incoming oxygen is directed into the tow region, which is then used up to oxidize the polymer in the tow. Also note that an oxidation level of 0.99 at a material point in the neat resin region indicates that 1% of the resin in the material has oxidized. On the other hand, saying that 1% of the resin in a material point in the tow region corresponds to an oxidation level defined by eq(3.134), which for this model is 0.99556. Figure 8.9 shows

the oxidation level profile in the model at 100 hours. The inset plot in Figure 8.9 shows a close up of the oxidation state of the two models between 0.08mm and 0.095mm. It shows that the oxidation level in the resin/tow model dips below 0.99556 at about 0.085mm (at location A) whereas in the neat resin model, it dips below 0.99 at about 0.077mm (at location B). This snapshot of the simulation at 100 hours shows what the oxidation profile in the two models looks like when the oxidation layer thickness in the resin/tow model is larger than that in the neat resin model. Overall, this oxidation behavior in the resin/tow model is due to a combination of factors such as the effective oxidation properties of the tow as well as the diffusion behavior in heterogeneous models and the relatively slow movement of the oxidation

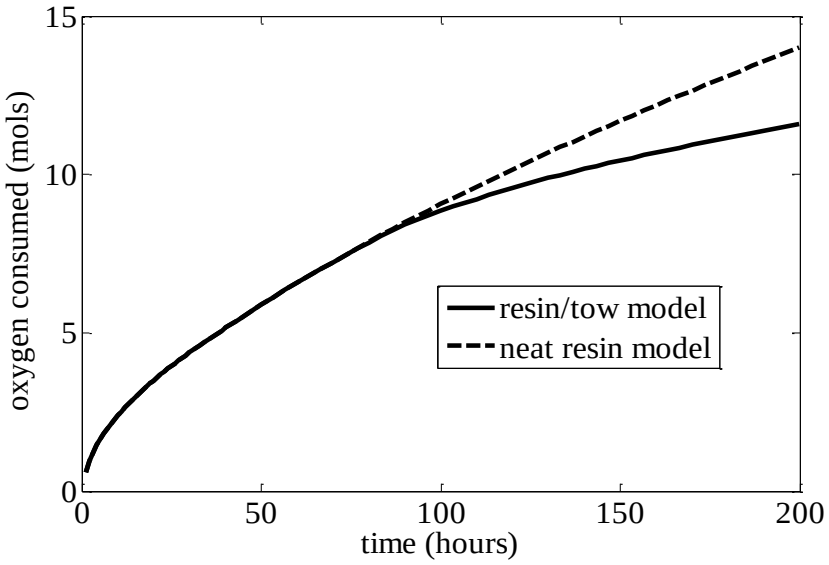

Figure 8.8: Comparison of amount of oxygen consumed in the resin/tow model and neat resin model

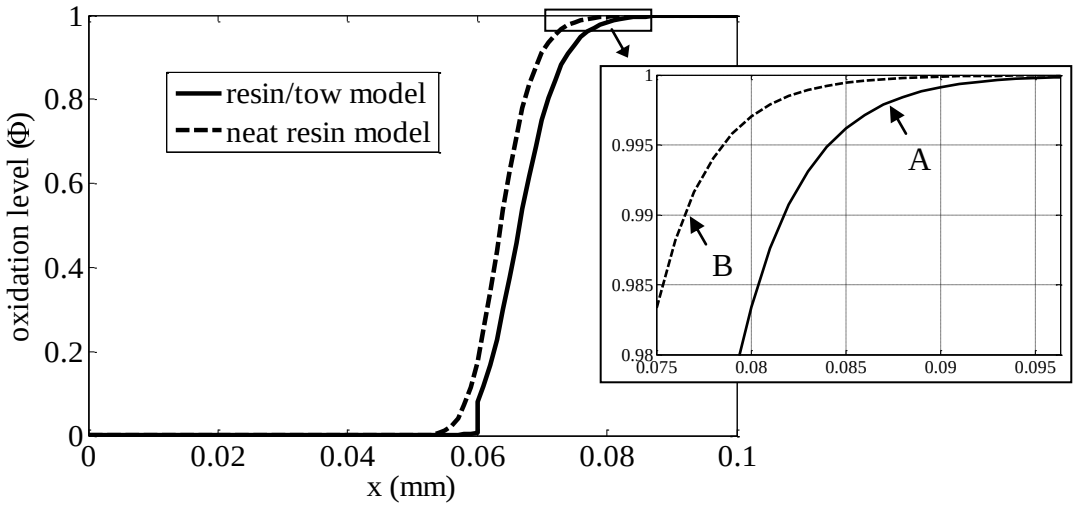

Figure 8.9: Comparison of oxidation level (Φ) profile in the resin/tow model and neat resin model at 100 hours

front into the interior of the material. It would also depend on the volume fraction of the constituent materials and the configuration of the materials in the heterogeneous model. Therefore, the location of the material boundary in the configuration also has an impact on the oxidation behavior.

8.4 Oxidation Analysis of Plain Weave Laminate

Now that the hybrid modeling strategy has been validated, it can be used to simulate the oxidation behavior in textile composites and eventually coupled with the damage progression analysis to predict the mechanical behavior under oxidation. The configurations that are examined in this work are plain weave laminates exposed to oxygen at the top and bottom surfaces and the oxidation behavior is simulated only for 200 hours. As discussed later in this section, after 200 hours of oxidation of the laminates with the material system that is considered in this work, the oxidation layer thickness does not exceed more than the thickness of a single ply. Therefore, based on the oxidation model implemented in this work, the growth of the oxidation layer would be the same regardless of whether it is a 2-ply laminate or if it has more than 2 plies. On the other hand, although the oxidation layer growth is the same, the number of plies could have an impact on the mechanical behavior and this is discussed in the next section.

The hybrid model was used to simulate the oxidation behavior in a symmetric two-ply graphite/PMR-15 plain weave laminate. Both the top and bottom surfaces are exposed to oxygen. The composite is chosen to have a waviness ratio of 1/3. A full unit cell of the configuration is shown in Figure 8.10(a). By exploiting symmetry, it is possible to analyze the configuration using only $1/8^{th}$ of the full unit cell as shown in Figure 8.10(b) with a transparent matrix. The hybrid modeling technique is used on the reduced domain, which is automatically subdivided into an array of 64 1-D model as described in the previous section. Since both the warp and fill tows have the same oxidation material properties and the effects of the undulation are assumed to be insignificant, the four quadrants in Figure 8.10(b) are essentially identical, therefore the results from the corresponding 1-D models in the different quadrants will be the same. Additionally, within one quadrant (i.e. $1/32^{nd}$ of the unit cell), based on the same assumptions of ignoring the effects of undulation, the region is symmetric about the plane as shown in Figure 8.10(c). Therefore, the only unique results from the analysis are those from the 10 domains numbered in Figure 8.10(d). Figure 8.11 gives the predicted oxidation layer

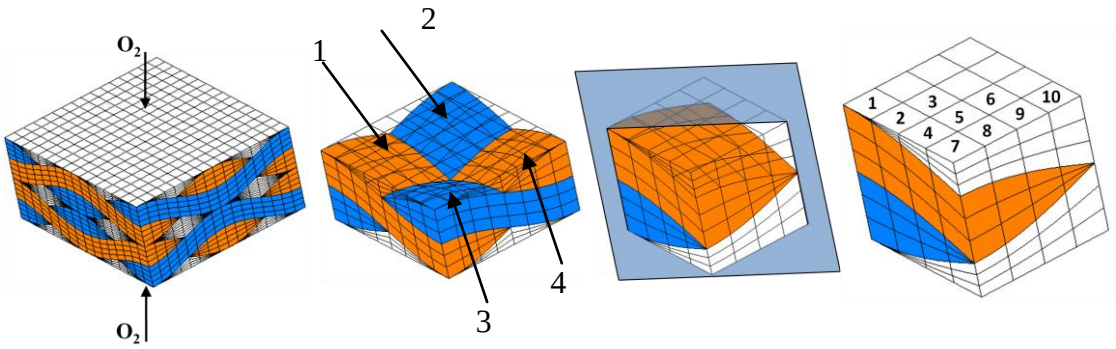

(a) Full unit cell (b) 1/8th unit cell (c)1/32nd unit cell (d) Unique domains in model

Figure 8.10: Configuration and analysis domains for simulating oxidation in plain weave composite

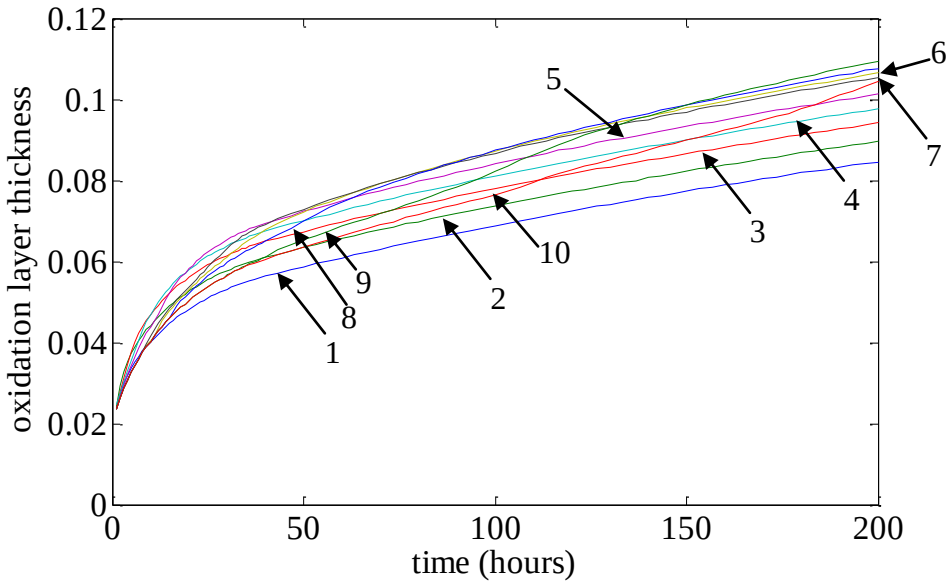

Figure 8.11: Oxidation layer growth in the 10 unique domains

growth for the 10 domains. It shows that there is considerable variation in the oxidation layer growth behavior of the 10 domains. At the end of 200 hours of oxidation, the thickest layer is 0.11 mm (in Domain 9) which is only slightly larger than half the thickness of a single ply. Figure 8.10(c) shows that domain 10 has the largest amount of matrix with a very small region of tow in the middle whereas domain 1 has the largest

amount of tow with a very small region of matrix at the two ends. Although domain 10 has the largest amount of matrix, it is not the domain that has the thickest oxidation layer. This is because, as discussed earlier in section 8.2, in heterogeneous models the oxidation behavior is not very straightforward and depends on a number of factors such as the location of the material boundaries and the oxidation properties of each of the constituent materials. In each of the ten unique 1-D domains representing the weave microstructure, the material boundaries are at a different distance away from the exposed surface. This results in a varied oxidation behavior from the 1-D models. Since domain 10 is almost all resin with a small region of tow in the middle, its oxidation behavior would be expected to be close to that of a neat resin. Similarly, since domain 1 is almost all tow with a small region of matrix at the two ends, its oxidation behavior would be expected to be close to that of a homogenized tow model. However, as explained earlier with the heterogeneous configuration, the behavior is not always close to that of the corresponding homogeneous model. Figure 8.12 shows the layer growth for domains 1 and 10 as well as for a neat resin model and a homogenized tow model. It shows that domain 10 follows the same behavior as a neat resin model but once the oxidation front reaches the tow material, domain 10 has a slightly faster oxidation layer growth. For domain 1, the oxidation layer is only slightly thicker than that in an all tow model. Overall, the analysis shows that the oxidation front does not advance uniformly throughout the composite. At the end of 200 hours of oxidation, domain 1 has the smallest

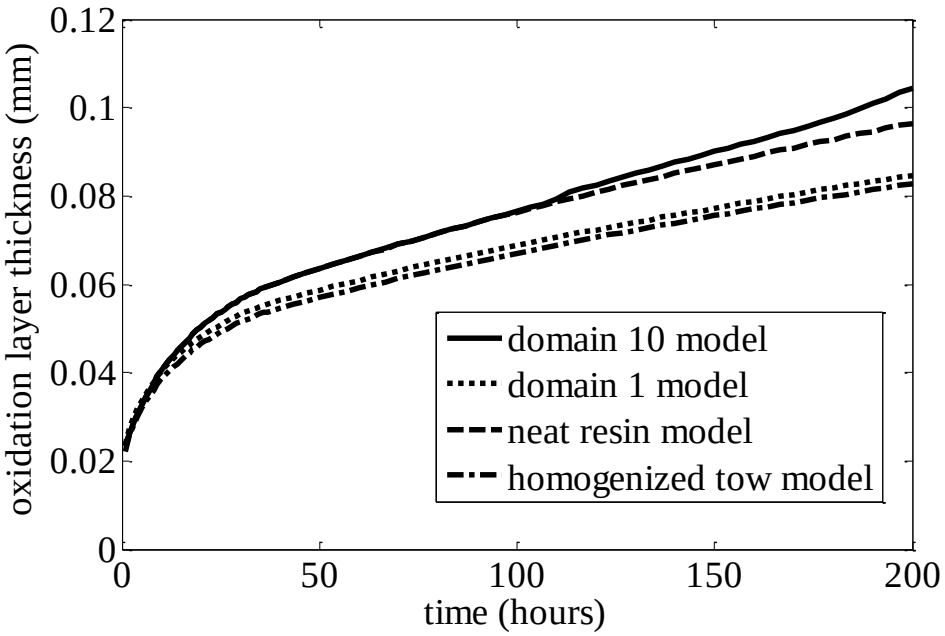

Figure 8.12: Comparison of oxidation layer growth in domains 1 and 10 with that of a neat resin model and homogenized tow model

oxidation layer with a thickness of 84.5 microns and domain 9 has the largest oxidation layer with a thickness of 110 microns. That is a range of over 25 microns, which is over 30% of the domain 1 layer thickness. Therefore, it can be said that the tow architecture plays a significant role in the variation.

8.5 Storage of Oxidation Behavior Data from Hybrid Model

The oxidation behavior of the laminate is eventually used in the coupled damage progression model in order to predict the mechanical behavior under oxidation. In order to do this, the results from the oxidation analysis need to be passed on to the damage progression model. The results consist of the distribution of the oxidation level property in the laminate at different time steps in the simulation. The oxidation level data at the different time steps is needed by the damage progression model in order to degrade the mechanical properties of the composites based on how much of the material has oxidized. The value of the oxidation level at each integration point in the all the elements of the finite element model is kept track of in the memory and can be written to a file, similar to how the stress distribution in a model can be written to a file. If the oxidation

model and the damage progression model used the same discretization for the analysis domain, i.e. the same finite element mesh, then the information transfer is straightforward. The oxidation level distribution file can be read in by the damage progression model and all the oxidation level information would be available for performing the mechanical property degradation.

However, when a hybrid model is used for the oxidation analysis, the information transfer to the damage progression model is not so straightforward. In the hybrid model, each individual 1-D domain is an approximation of the actual 3-D region that it represents in the laminate. Due to this reason, the oxidation level value distribution in the 1D model is not an exact representation of what the distribution would be if the actual 3-D domain was analyzed. For example, Figure 8.13 shows a 3D domain and its equivalent 1D domain. Point A in the 3D domain would be the geometrically equivalent point to Point B in the equivalent 1D domain, but note that the two points are located in different material regions of the models. Point A is located in the matrix region where as Point B is located in the tow region. However, because of the characteristic oxidation behavior, the mismatch in the geometry is only an issue when the oxidation front is in the vicinity of the material boundaries. Even when the oxidation front is near the material boundary, it is seen that errors due to this mismatch is not significant because the rotation angles of the tow in the laminates are not large enough.

Another issue has to do with the amount of information that has to be transferred from the oxidation model to the damage progression model. For example, using the hybrid strategy on the 3D domain shown in Figure 8.10(b) would result in 64 1D domains. Assuming that the oxidation level distribution is post-processed and outputted by each 1D model at 88 different time steps throughout the oxidation simulation, this would result in the creation of 88 x 64 = 5632 data sets. During the coupled simulation, at each of the 88 time steps, 64 different files need to be opened and the oxidation level information of each element in all the 1D models need to be read in. A strategy was sought that could reduce the number of file I/O operations as well as the amount of data that had transferred during the coupled analysis while maintaining reasonable accuracy.

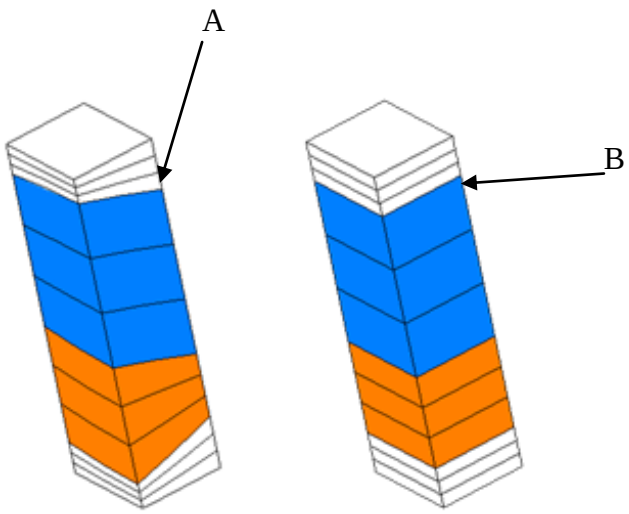

Figure 8.13: 3D domain and equivalent 1D domain in hybrid modeling strategy

The approximations that were made in the developed strategy and a description of the data that is transferred from the hybrid oxidation model to the damage model are described in the remainder of this section.

Note that the value of the oxidation level at a material point can vary from 1 to 0 as described in section 3.5.1. A value of 1 denotes that the material is un-oxidized and a value of 0 denotes that the material is fully oxidized. Typically, a significant majority of the model is made up of either fully oxidized or un-oxidized material. A small fraction of the model has oxidation levels in the range between 1 and 0, which ideally denotes the active zone, or that the material has started oxidizing but it is not fully oxidized yet as shown in Figure 3.5. Therefore, instead of storing the oxidation level information for each element in the 1-D model, just the dimensions of the active zone is stored to represent the oxidation level profile for a particular time step. In this manner, the oxidation level profile in a 1D domain for all of the 88 time steps can be effectively compressed into a single file using only a fraction of the information. When the data is read in during the coupled simulation, the oxidation level profile is approximated using a linear variation of the oxidation level within the active zone. These approximations are

made based on a few assumptions. The active zone is assumed to be very small compared to the fully oxidized and un-oxidized region. Although the actual variation of the oxidation level in the active zone is not linear, the linear variation assumed in this model is assumed to be reliable for the material systems considered in this work. The simple linear approximations employed here are assumed to be reliable for the purposes of predicting mechanical behavior in the composites. Figure 8.14 shows the predicted oxidation level profile in a block of neat resin at 100 hours. The dotted line shows the approximated oxidation level profile. The location where the approximated oxidation

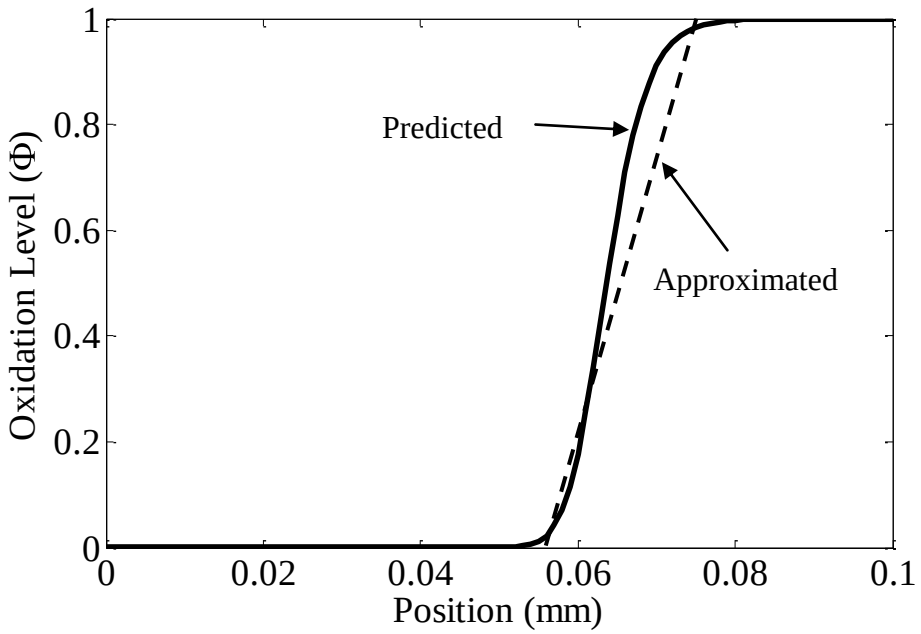

Figure 8.14: Oxidation Level profile in neat resin 1-D model at 100 hours

level starts lowering from 1.0 is determined by the thickness of the oxidation layer or in other words the dimensions of the oxidation zones. The instructions to determine the dimensions of the different zones and the oxidation layer thickness are described in section 3.5.6. The location of the point where the approximated oxidation level reaches 0 is also similarly determined by the dimensions of the active zone (typically it is the location where the predicted oxidation level reaches 0.01). During the initial stages of

oxidation when there is no fully oxidized material, the predicted oxidation level does not drop all the way to 0. In this case, the linear approximation is based on the value of the predicted oxidation level at the location in the model that is exposed to oxygen. This is illustrated in Figure 8.15, which shows the oxidation level profile in neat resin at 1 hour. The predicted oxidation level at the exposed surface after 1 hour of oxidation is 0.1812 and as shown in Figure 8.15, both the predicted profile and the approximate profile have the same oxidation level value at the exposed end. When analyzing heterogeneous models, the oxidation level profile is more complicated in that the profile is piece-wise continuous with the predicted oxidation level continuous within a single material. For example, in the heterogeneous configuration shown in Figure 8.4, the material boundary is at 0.06 mm. Figure 8.16 shows the predicted oxidation level profile for that configuration at 70 hours. The approximated oxidation

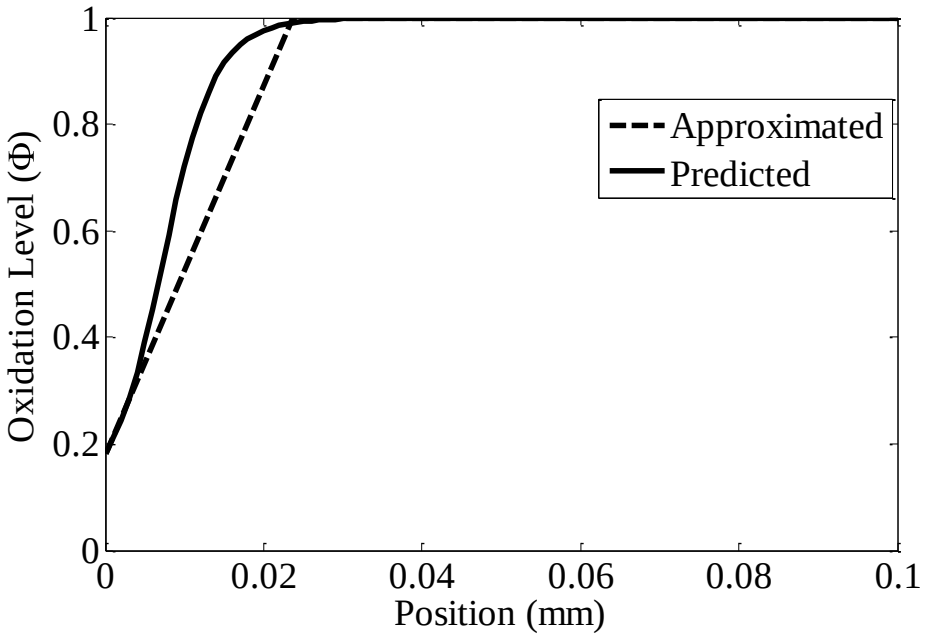

Figure 8.15: Oxidation Level profile in neat resin 1-D model at 1 hour

level profile is also maintained as a piece-wise oxidation level profile for each material region. The approximated oxidation level value in either material region at the material boundary is same as the corresponding predicted oxidation level value for that location.

In order to save the approximated oxidation level profiles for the required time steps so that it can be used by the damage progression model in the coupled simulation, the oxidation level information for each material region in the 1D domain is stored using just four values – the beginning and end locations, and the beginning and end oxidation level values. This information is then used in the coupled damage progression model to determine the oxidation level at each integration point and degrade the mechanical properties based on the constitutive relations.

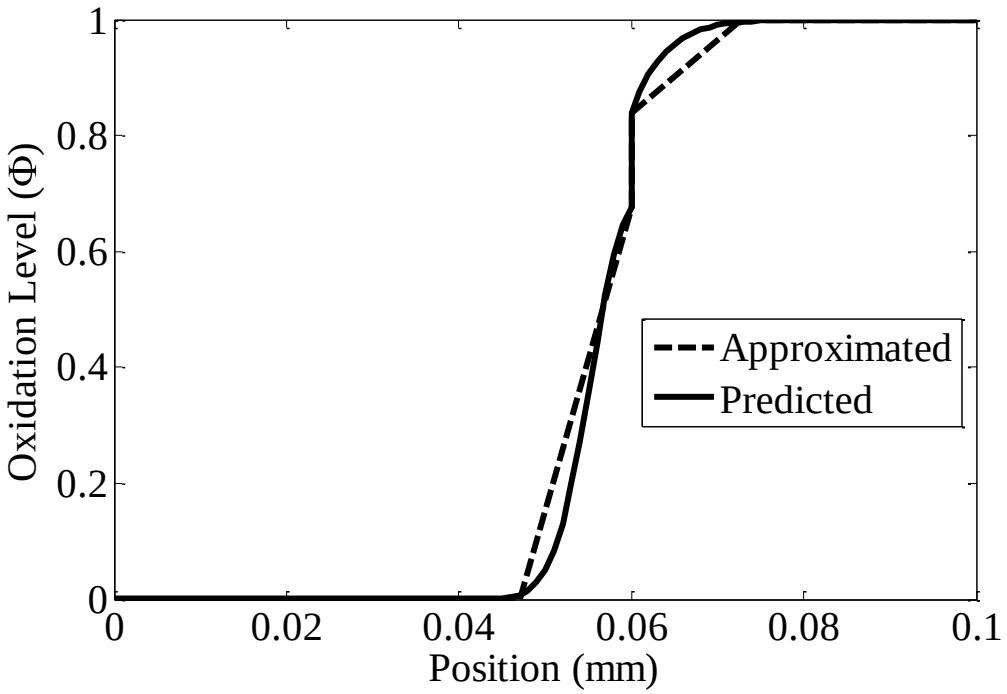

Figure 8.16: Oxidation Level profile in heterogeneous 1-D model (see Figure 8.4) at 70 hours

8.6 Summary

A conventional oxidation analysis of textile composites would require a full 3-D model. Based on the element size requirements, a finite element model of a textile composite would be very large, making it prohibitively expensive to simulate the oxidation behavior. This is in spite of the computational savings made possible by the adaptive meshing strategy described in Section 7. In order to make the oxidation analysis of

textile composites more feasible, a hybrid modeling strategy is developed. The strategy involves dividing the full 3-D model into an array of representative 1-D models, which can be easily analyzed. Since the 1-D models are independent from each other, they can be run on multi-core processors making the analysis even more efficient. This section describes the hybrid modeling strategy and its validation. The hybrid model is then used to simulate oxidation in a plain weave Graphite/PMR-15 composite. The section also describes how the oxidation information from the hybrid model is maintained so that it can be used by the damage progression model for prediction of the mechanical behavior.

9. PREDICTION OF DAMAGE IN TEXTILE COMPOSITES IN OXIDIZING ENVIRONMENTS

9.1 Introduction

The previous sections have laid the groundwork in order to be able to build the framework so that the effect of oxidation on the mechanical behavior of textile composites can be predicted. The last three sections describe the challenges and appropriate strategies for simulating the oxidation behavior in textile composites. Section 3 described the governing equations and finite element formulations required for the damage analysis, oxidation analysis and the coupled oxidation-damage progression model. This section begins with a brief overview of the different damage mechanisms in textile composites. This is followed by a description of how the coupled analysis model was used to predict the damage initiation and progression in the textile composites in oxidizing environments. The configurations that will be analyzed will be described including the material properties and the constitutive model that was used to implement the coupled analysis model. This will be followed by the results and discussion of the analysis and the parametric studies.

9.2 Damage Mechanisms in Textile Composites

Textile composites fail under different types of loadings exhibiting different types of damage mechanisms [177]. One common damage mechanism is transverse cracking in the matrix and tows. Other damage mechanisms seen in the tows are inter- and intra-tow delamination, fiber buckling and fiber breakage etc. Resin pockets in the composite can develop transverse matrix cracks (transverse to the loading direction) independent of the matrix cracks in the tows. Quaresimin et al. [177] observed three main damage mechanisms in twill weave composites under fatigue loading. They are layer delaminations, transverse matrix cracking and fiber failure. Figure 9.1 shows the micrographs illustrating these damage mechanisms. Quaresimin et al. [177] analyzed a number of laminates with different stacking sequences and saw that all three damage

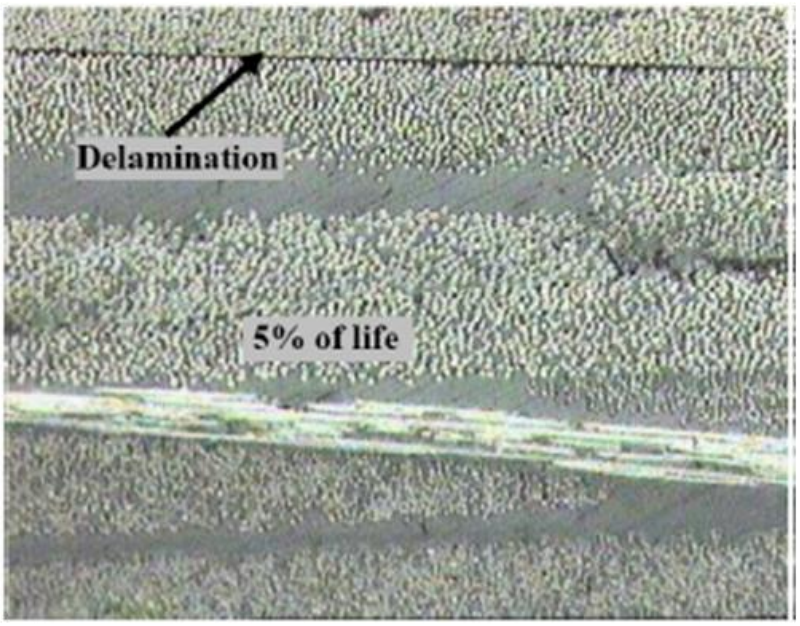

(b) Delamination

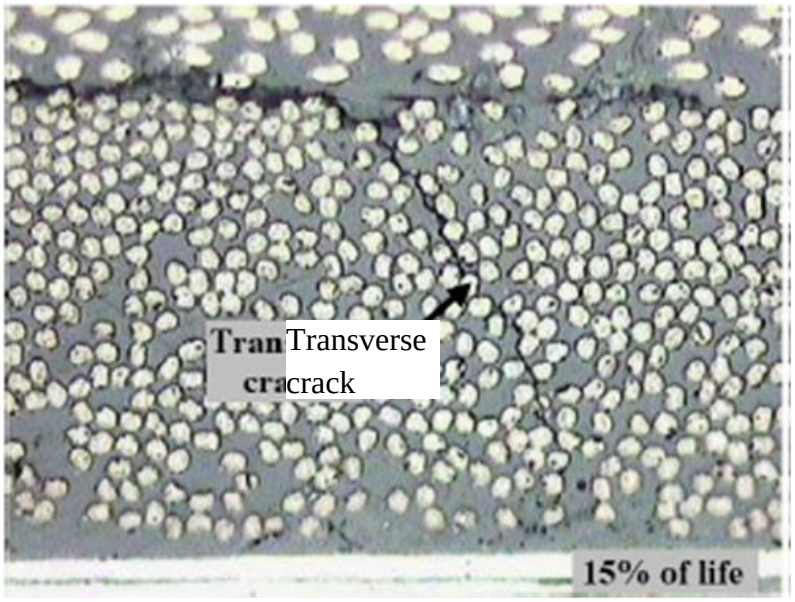

(b) Transverse matrix crack

Figure 9.1: Damage Mechanisms in woven composites [177]

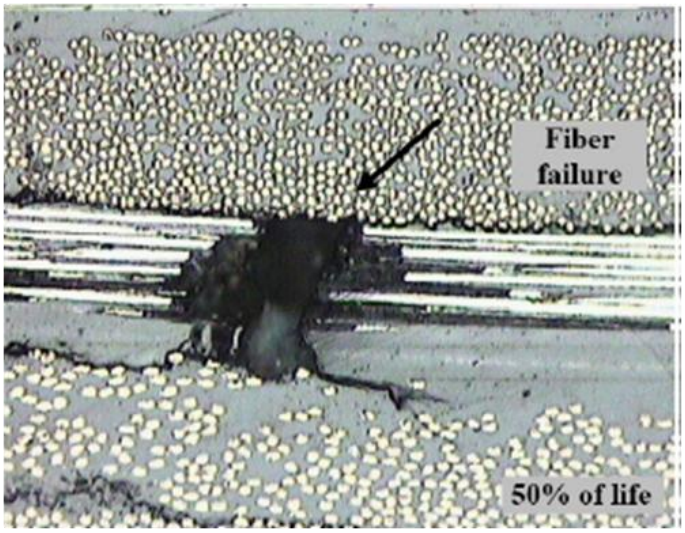

(c) Fiber Failure

Figure 9.1: Continued.

mechanisms were present under different types of fatigue loadings, but the sequence of appearance was different. It was also seen that only one predominant mechanism generally dictated the laminate behavior.

Figure 9.2 shows a schematic of the different damage modes in a tow. The mode under which damage occurs in the material depends on which material allowable is exceeded. The failure criteria that are used in this work are discussed in the next section. The damage modes in the tows can be classified into four types as shown in Figure 9.2. The "1" direction denotes the fiber direction whereas the "2" and "3" directions are in-plane and out of plane transverse directions respectively. The coordinate axes defined by the "1", "2" and "3" direction are the principal coordinate axes of the tow, which is assumed to be transversely orthotropic. The finite element model of the composite accounts for the undulation of the tows and therefore the rotation angles for the material vary depending on the location of the material point in the tow. As illustrated in Figure 9.2, fiber breakage occurs under failure mode 11 and this damage mode is generally caused by excessive σ_{11} stress in the tow. This failure mode is what generally causes the

ultimate failure of the composite. Transverse matrix cracking is generally one of early damage mechanisms seen in the tows. This type of damage mode is caused by excessive σ_{22} or σ_{12} stress components and classified as failure modes 22 and 12 respectively. Failure mode 33 and 13 can be caused by either σ_{33} or σ_{13} stress components and can result in intra- or inter-laminar delaminations. Figure 9.2 also shows the damage mode 23 which is caused by σ_{23} stress.

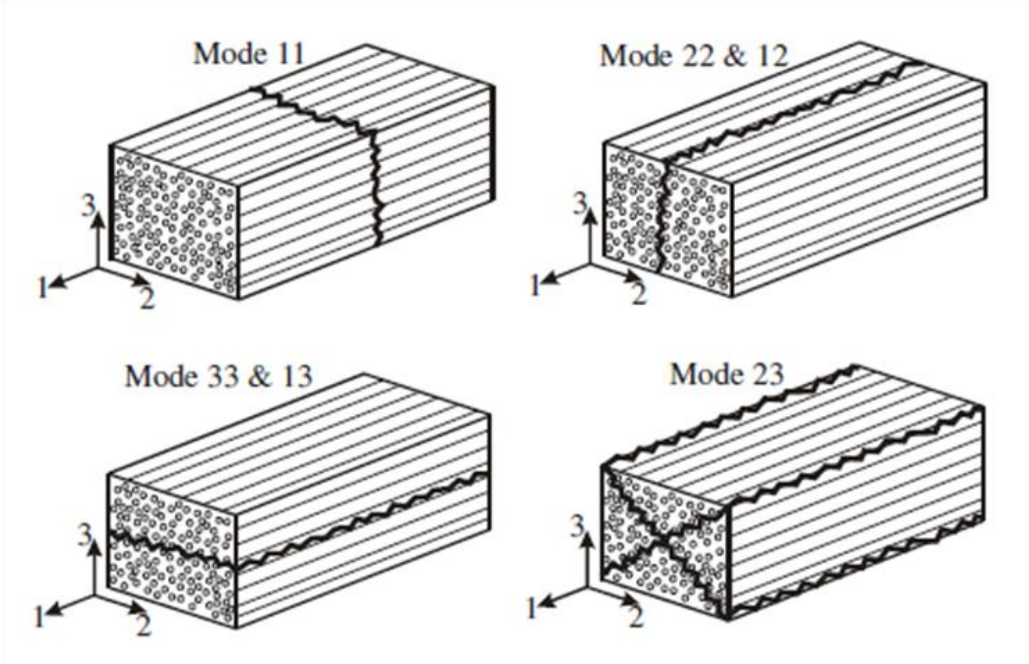

Figure 9.2: Schematic of different damage modes in the tow of textile composites [5]

9.2.1 Failure Criteria for Tows and Matrix

As mentioned in the previous section, the condition for damage to occur and more specifically, which type of damage mechanism is in action, is determined based on what failure mode has been triggered. In order to determine if a failure mode has been

triggered, a suitable failure criterion is required. This section defines the failure criteria employed in all the models used in this work.

Depending upon the property degradation scheme used, a material point in the matrix will be assumed to be isotropic or anisotropic after the damage has occurred. Since the matrix is initially isotropic, the global coordinate system and the material coordinate system are the same. On the other hand, the principal coordinate system is not necessarily the same as the global coordinate system. Moreover, the property degradation scheme used in this work assumes that the material will become anisotropic after mechanical damage. Therefore, it was assumed that there is no significant effect of choosing the maximum stress criterion over the principal stress criterion. In this particular work, the stress in the global coordinate system was used in the maximum stress criterion to determine failure modes in the matrix. However, future enhancements to the model should provide the option of choosing the maximum principal stress criterion if the material is not damaged.

In the case of the tow material, the maximum stress criterion for anisotropic materials was used, which says that the failure occurs when any of the stress components in the material coordinates system exceeds its corresponding strength. The tows can fail under one or more damage modes such as fiber breaking and transverse cracking. The modes strongly affect the mechanical behavior of the structure. In this work, the tows are assumed to be transversely isotropic before any damage occurs. However, the tow in general would no longer be transversely isotropic after it has failed and its mechanical properties have been degraded. But the stress in the local coordinate system of the tow is continued to be used for the maximum stress failure criterion. If σ_{ij} are the stress components in the material coordinates system of the tow and S_{ij} are the corresponding strength values, then the failure criteria used in this work can be summarized as below:

For isotropic matrix:

Max stress criterion

For transversely isotropic tow:

Max stress criterion (9.1)

$\sigma_{ij} / S_{ij} > 1$ Material point has failed in mode *ij*

$\sigma_{ij} / S_{ij} \leq 1$ Material point has not failed

The strength properties of the materials analyzed in this work is listed in section 9.3.1 which defines the all material properties used in this work.

9.3 Configuration

The coupled analysis framework was used to investigate the mechanical behavior of a plain weave Graphite/PMR-15 composite in an oxidizing environment. The waviness ratio of the composite is assumed to be 1/3 and the fiber volume fraction in the tow is assumed to be 55.6%. The reason for choosing this fiber volume fraction was because of the availability of experimental engineering properties for this particular material system in the literature. The volume fraction of the tows in the composite is assumed to be 63.6% and therefore the overall fiber fraction in the composite is 35.36%. The laminate consists of two plies and is assumed to be symmetrically stacked and infinite in the in-plane directions. Figure 9.3 shows the full unit cell of the configuration. The laminate is assumed to be loaded under uniaxial stress conditions in the x-direction at a temperature of 288C. The material properties used to model the configuration will be assumed to be those at 288 C. However, in this current implementation of the coupled analysis model, the effects of thermal expansion and the shrinkage of resin under oxidation will be ignored. The configuration will be loaded to a pre-determined strain level and maintained at that level. The configuration is then exposed to oxygen from the top and bottom surfaces while the lateral surfaces are assumed to be impermeable. The laminate will be exposed to the oxygen for 200 hours at 288C. The damage in the laminate throughout this simulation will be tracked and the mechanical behavior will be recorded. The number of plies in the laminate was changed in a parametric study to determine its

effect on the mechanical behavior. Any changes from this basic configuration will be described as required when discussing the results of the parametric study.

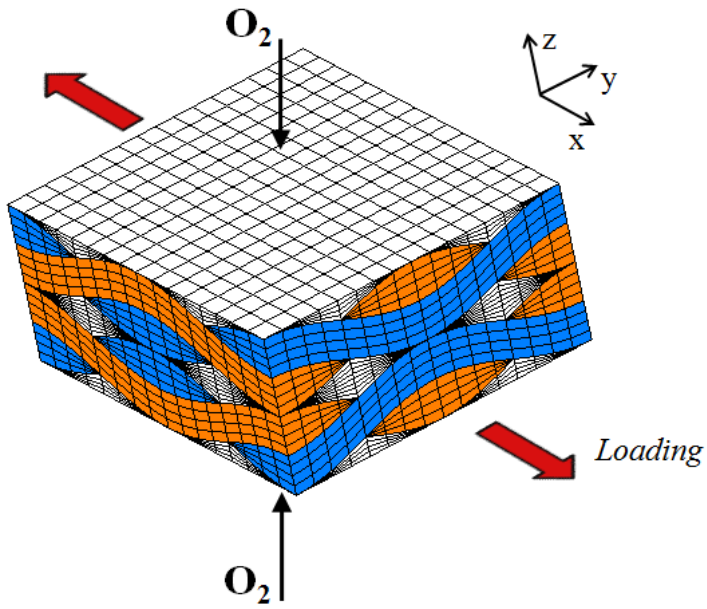

Figure 9.3: Two-ply plain weave composite configuration

Exploiting symmetry conditions in this configuration allows reducing the analysis domain from a full unit cell to just $1/8^{th}$ of the unit cell as shown in Figure 9.4. For all the results discussed in this section, the analysis domain, which is the $1/8^{th}$ unit cell, is part of the bottom ply in the configuration. Therefore, the bottom surface of the model in Figure 9.4 is traction-free and exposed to oxygen.

9.3.1 Material System

The material system used for all the analyses discussed in this section is Graphite/PMR-15 composite. The coupled model requires both the oxidation material properties as well as the mechanical properties for the tow and matrix in the composite. Note that the configuration is assumed to be at a temperature of 288 C throughout the entire simulation. The coupled model also requires the degradation schemes for the matrix and

the tow, for both the oxidation as well as mechanical damage. These degradation schemes are described in the next section.

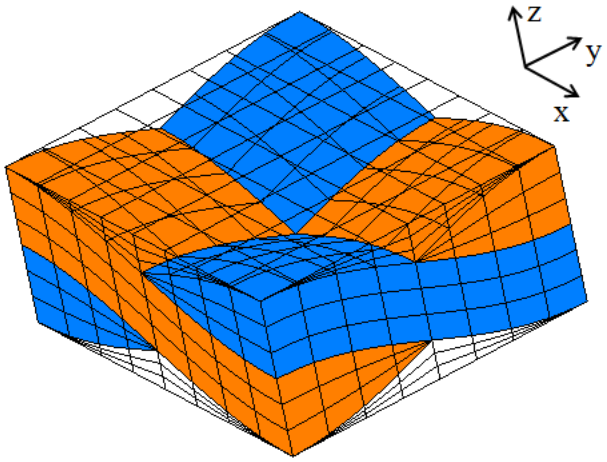

Figure 9.4: Analysis domain ($1/8^{th}$ unit cell) with transparent matrix

The oxidation material properties that are used in these models have already been described in the previous sections that discuss the oxidation behavior in composites. The oxidation material properties for the neat PMR-15 resin were obtained from ref [9]. The oxidation material properties for the tow were determined using the homogenization strategies described in Section 3. Table 6.1 gives the oxidation material properties for the neat PMR-15 resin and Table 8.1 gives the corresponding properties for the tow.

Obtaining the mechanical properties for the Graphite/PMR-15 material system at 288 C is not easy since they tend to change over time and it may not be appropriate to use property data from different sources or manufacturers over different time periods. That being the case, it is also very difficult to obtain the entire set of required mechanical properties from one source in the literature. Moreover, some of the required properties at 288 C are unavailable due to the lack of appropriate experimental techniques to determine them. The resin and the tow are also assumed to be linear elastic materials although elasto-plastic behavior of the polyimide resin would be expected to be more prominent at 288 C. Overall, the set of mechanical properties for the material system

used in this work was chosen from a combination of different sources in the literature and based on certain assumptions and estimates that are described below.

The mechanical properties of the neat PMR-15 resin were chosen based on experimental data from Pochiraju and Tandon [153]. The Young's modulus of the neat resin was found to be 2.096 GPa and the Poisson's ratio is assumed to be 0.30 in Pochiraju and Tandon's work [153]. Based on the assumption that the neat matrix is isotropic, the Young's modulus and Poisson's ratio can be used to calculate the shear modulus. Pochiraju and Tandon [153] also provide the normal strength at room temperature and 288 C. The shear strength of the neat PMR-15 resin is calculated by scaling the strength at room temperature based on the change in normal strength from room temperature to 288 C. Table 9.1 contains the elastic moduli for neat PMR-15 resin that were used in this work. The strength properties that were discussed in this paragraph are provided under Set 1 in Table 9.2. The properties under Set 2 and the need for an additional set of strength properties are discussed in the next paragraph.

The Graphite/PMR-15 tow is assumed to be transversely isotropic and therefore its elastic behavior is defined by five independent properties. The engineering properties for the tow were harder to obtain because the configuration requires properties at 288 C. The elastic moduli chosen were interpolated from work performed by Odegard and Kumosa [149], which looked at the effect of temperature on some of the engineering properties of a Graphite/PMR-15 unidirectional laminate (Vf=55.6%). Of the five independent properties required, E11, E22, v12 and G12 were obtained by interpolating from the data in Ref [149]. The Poisson's ratio in the transverse plane, v23, at 288 C was assumed to be the same as that at room temperature. The elastic moduli for the tow material are summarized in Table 9.1. All the strengths properties of the tow at 288C were not available in the literature. It is relatively difficult to determine all the strength properties for the tow. These properties, especially the matrix-dominated properties, are hard to determine, because of many factors like the material interface properties that influence the strengths. The σ_{22} strength and σ_{12} strength were interpolated from Odegard and

Kumosa's work[149]. Since, the tow is assumed to be transversely isotropic, the σ_{33} strength is the same as the σ_{22} strength and the σ_{12} strength is the same as the σ_{13} strength. Due to lack of experimental data for the fiber-dominated σ_{11} strength, the corresponding strength from a Graphite/epoxy material system was used. However, the σ_{11} strength is only consequential only during fiber-breakage which occurs during final failure of the composite. Therefore, this assumption was not considered to be significant because this work is more concerned with the damage initiation and progression then the final failure of the composite. Also, due to lack of experimental data for the σ_{23} strength, it was assumed to be the σ_{23} stress corresponding to the same strain level at which the σ_{12} stress mode failed. These strength properties for the tow are summarized under Set 1 in Table 9.2. Note that the σ_{22} strength of the tow in Set 1 is considerably lower than the normal strength of the neat resin. This would indicate that the tows would fail before the neat resin pockets in the composite. It is common for a composite to have a lower transverse tensile strength than the tensile strength of the neat resin [178]. However, since the properties for this material system were compiled from different sources and therefore as mentioned before, not particularly reliable, another set of assumed strengths were also chosen for the material system. In this new set of properties, the normal and shear strength of the neat resin were scaled down based on typical strength ratios between resin and tow transverse strengths in Graphite/Epoxy material systems. This additional set of strength properties for the material system used in this work is defined as Set 2 in Table 9.2. Having two sets of material properties would also give another perspective on the damage initiation and progression behavior based on the change in engineering properties.

Table 9.1: Elastic properties for the Graphite/PMR-15 material system [149,153]

	Resin Neat PMR-15	Tow Graphite/PMR-15
E11	2.096 GPa	124.05 GPa
E22=E33	2.096 GPa	6.2 GPa
G12=G13	0.806 GPa	1.62 GPa
G23	0.806 GPa	1.929 GPa
v12=v13	0.3	0.485
v23	0.3	0.607

Table 9.2: Strength properties for the Graphite/PMR-15 material system [149,153]

	Set 1		Set 2	
	Resin Neat PMR-15	Tow Graphite/PMR-15	Resin Neat PMR-15	Tow Graphite/PMR-15
S11	41	2550	12	2550
S22	41	18.91	12	19
S33	41	18.91	12	19
S12	73.72	36.83	12	37
S23	73.72	43.85	12	44
S13	73.72	36.83	12	37

All strengths in MPa

9.3.2 Constitutive Relations

This section describes the different constitutive relations that are required to implement this coupled oxidation-damage progression model. This includes the mechanical property degradation schemes both due to mechanical loading as well as due to the effect of oxidation. The section also talks about how the two degradation schemes are combined and used in the coupled model to obtain the overall mechanical properties of the material based on the oxidation and damage state.

9.3.2.1 Property degradation scheme based on mechanical damage

When a failure mode is triggered during the damage analysis, the engineering properties are degraded to account for the change in mechanical behavior. This operation is conducted based on a property degradation scheme, which has been briefly discussed in section 3.3.8.2. In this work, the failure criteria and the property degradation scheme is

applied on each integration point within every element in the model. The property degradation scheme is implemented such that a material point that has already failed under a particular mode can fail under another mode. In such a case, the material properties are degraded based on which failure mode prescribes the larger degradation.

Different property degradation schemes have been proposed in the literature by several researchers such as Whitcomb et al. [118], Blackketter et al. [82], Tamma et al. [124] and Zako et al. [123]. All these models share certain similarities and differences. They are similar in the sense that each of them controls the amount of degradation under different failure modes for both the tow and the matrix. Goyal [5] performed a comparison of the different degradation schemes and developed a common framework that allowed implementation of a wide variety of degradation schemes.

For all the damage progression models in this work, the degradation scheme by Blackketter [82] was used. This type of degradation scheme has been widely used by many researchers [118-121] to predict initiation and progression of damage. The engineering properties are degraded as specified in eq(3.41). The degradation scheme used is different for the tow and the matrix.

In the degradation scheme for the tow material, the values of the degradation parameters, a_i (i=1 to 6) are 1, 5 or 100. Note that the value of the parameters in a_i will be different under different damage modes. Table 9.3 gives the values of the degradation factors for the tow material under this scheme. The "1" is the local fiber direction of the tow and "2" and "3" are the local transverse directions of the tow. An a_i value of 1 indicates that the modulus has not been degraded. An a_i value of 5 indicates the modulus has been degraded to 20% of its original value and similarly an a_i value of 100 indicates the modulus has been degraded to 1% of its original value. The reason that some of the moduli are degraded to 1% of the original rather than an absolute zero is to avoid numerical instabilities[82]. The shear moduli were not reduced to less than 20% of the original value under mode σ_{22} and σ_{33} failure because it is assumed that some shear stiffness remains due to frictional resistance still present on the failure plane [82].

For the matrix material, the property degradation was assumed to be the same under all the failure modes. The tensile moduli and Poisson's ratios of the matrix are reduced to 1% of its original value whereas the shear moduli are reduced to 20% of its original value. The matrix is therefore assumed to become anisotropic after failure. Table 9.4 gives the degradation factors for the matrix material.

Table 9.3: Degradation parameters (a_i) for engineering elastic properties of the tow [82]

	Mode σ_{11}	Mode σ_{22}	Mode σ_{33}	Mode σ_{12}	Mode σ_{23}	Mode σ_{13}
E11	100	1	1	1	1	1
E22	100	100	1	100	100	1
E33	100	1	100	1	100	100
G12	100	5	1	100	100	1
G23	100	5	5	1	100	1
G13	100	1	5	1	100	100
v12	100	1	1	1	1	1
v23	100	100	1	100	100	1
v13	100	1	1	1	1	1

Table 9.4: Degradation parameters (a_i) for engineering elastic properties of the matrix [82]

	All Modes
E11	100
E22	100
E33	100
G12	5
G23	5
G13	5
v12	100
v23	100
v13	100

9.3.2.2 Property degradation scheme based on oxidation

The effect of oxidation on the mechanical behavior of the composites is considered in the coupled analysis models used in this work. In reality, the mechanical behavior is probably more tightly coupled with the oxidation behavior than what is assumed in the

current model because the mechanical damage can affect the oxidation behavior by allowing more oxygen to penetrate the composite material. This can further affect the mechanical behavior because more oxidation will cause more damage in the composite. These complex effects are not considered in this current work. In this work, the oxidation is assumed to affect the mechanical behavior, but not the converse.

A simple constitutive relation or property degradation scheme was developed to account for the effect of oxidation on the mechanical behavior and is described in section 3.6.1. For a general orthotropic material, the engineering moduli are modified according to eq(3.136). Unlike the property degradation scheme for mechanical damage, there is no failure criteria on which the degradation scheme is based.

While the property degradation scheme due to mechanical damage typically reduces the value of the moduli, the same is not necessarily the case for the property degradation scheme for oxidation. Experimental work has shown that the stiffness of the fully oxidized matrix is typically larger than that of the un-oxidized material [9]. There is not enough data in the literature in order to determine all the degradation parameters, b_i. In order to implement the degradation scheme for this work, the best available data in the literature was used where appropriate and estimates based on certain assumptions were used to the remaining parameters. The values of b_i chosen for the matrix and tow materials in this work are given in Table 9.5. Experiments showed that the elastic modulus of the neat PMR-15 resin increased by about 20% when fully oxidized [9]. The same amount of increase is assumed to apply for the shear moduli. The Poisson's ratio is assumed to remain constant based on the assumption that the matrix remains isotropic after oxidation. The same challenges exist for obtaining accurate characterization data for tows or unidirectional laminates. The fiber is assumed to be impermeable and unaffected by the oxidation. Simple micromechanics analyses showed that effective tow properties were changed by a very small amount when the matrix moduli were increased by 20%. Since the change was insignificant, the degradation properties (b_i) for the tow were assumed to be zero, meaning that the elastic properties of the tow were assumed to

remain constant after oxidation. Therefore, an undamaged material point in the tow was assumed to remain transversely isotropic after the material was oxidized.

As mentioned in Section 3.6.1, the property degradation scheme based on oxidation also degrades the strength properties of the materials in the composite as defined by eq(3.138). There is no data in the literature that can be used to determine the strength degradation parameters, d_i. Due to this limitation, for all the models analyzed in this work, strength properties are assumed for the fully oxidized matrix and tow. Table 9.6 gives the values of the strength degradation parameters chosen for the matrix and tow. The strengths for all stress components in the matrix are assumed to drop to half its value. In the case of the tow material, the σ_{11} strength, which is the strength in the fiber direction, is assumed to drop to 95% of the original value whereas all the other strengths drop 50%.

Table 9.5: Parameters (b_i) for degrading engineering elastic properties of the matrix and tow

	Engineering property affected	b_i	
		Matrix	Tow
1	E11	+0.2	0.0
2	E22	+0.2	0.0
3	E33	+0.2	0.0
4	G12	+0.2	0.0
5	G23	+0.2	0.0
6	G13	+0.2	0.0
7	v12	0	0.0
8	v23	0	0.0
9	v13	0	0.0

Table 9.6: Parameters (d_i) for degrading strength properties of the matrix and tow

	Strength property affected	d_i	
		Matrix	Tow
1	S11	-0.50	-0.05
2	S22	-0.50	-0.50
3	S33	-0.50	-0.50
4	S12	-0.50	-0.50
5	S23	-0.50	-0.50
6	S13	-0.50	-0.50

The overall mechanical moduli of the material are obtained by combining the two degradation schemes, both based on mechanical damage as well as oxidation, as described in Section 3.6.1. The expressions for the overall properties at a material point are given by the eq(3.139). Note that although the degradation scheme chosen in this work assumes that the matrix remains isotropic after oxidation, the overall mechanical properties obtained after accounting for mechanical damage need not necessarily represent an isotropic material. The parameters, a_i, have a value of 1 if the material is not damaged and therefore in such a case, the matrix would remain isotropic. On the other hand, if the matrix is damaged under any mechanical failure mode, the matrix becomes anisotropic. Similarly, the tow need not remain transversely isotropic after the mechanical properties have been modified using eq(3.139).

9.4 Results and Discussion

The coupled analysis model was used to simulate damage initiation and progression in the configuration described in section 9.3. The basic configuration described in Section 9.3 is a two-ply laminate at 288 C with the top and bottom surfaces exposed to oxygen. The laminate is assumed to be infinite in the in-plane directions and has a uniaxial load in the x-direction. As described in Section 9.3.1, two sets of material properties were chosen to model the Graphite/PMR-15 material system. This section will discuss the results from the analyses performed using both sets of properties. A parametric study was also performed where the number of plies in the laminate was increased. The parametric study looked at two-, four- and six-ply laminates for both the sets of material properties. The results of this parametric study will be described in this section as well.

9.4.1 Two-Ply Laminate

The damage progression behavior of the laminate under mechanical load alone (i.e. no oxidation) is first discussed. The laminate is assumed to be quasi-statically loaded uniaxially while maintained at a temperature of 288 C. Since two sets of material properties were chosen to define the Graphite/PMR-15 material system, the damage analyses were performed on two models, one for each material property set. Note that the two sets of material properties have the same elastic moduli. The difference between the two sets of material properties is in the strengths properties as shown in Table 9.2. Figure 9.5 shows a plot of the volume averaged σ_{xx} versus the volume averaged ε_{xx} for both the models. As expected, the stress-strain behaviors are different for the two models. Figure 9.5 shows that the initial damage in the model using Set 1 properties causes a significant drop in load (indicated by A) compared to the initial damage in the model using Set 2 properties (indicated by B). This difference in behavior can be explained by looking at where the initial damage occurs. In the case of Set 1, in which the transverse tow strengths are much lower than the matrix strengths, damage initiated in the fill tow under compressive σ_{33} damage mode. The observation that parts of the fill tow closer to the laminate mid-plane are under compression can be explained by

considering that warp tows are being stretched because of the load and therefore pushing on the fill tows in between. When the material properties of the damaged area in the fill tow are degraded, the amount of load carried by the tow reduces. In the case of Set 2, in which the resin has the lowest strengths, the damage initiates in the matrix pockets under

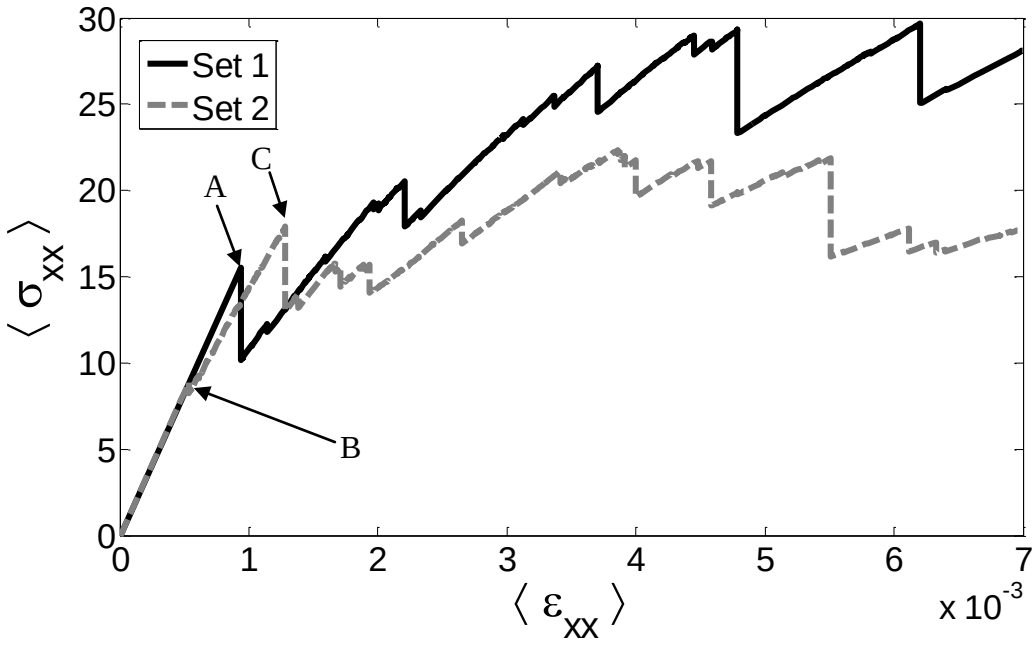

Figure 9.5: Volume averaged stress-volume averaged strain curves for the two-ply laminate without oxidation

tensile σ_{33} damage mode but since the matrix doesn't carry as much load as the tows, the load drop is not as significant as that seen in the model with Set 1 properties. This explanation can be confirmed by looking at the damage evolution in the two models.

Figure 9.6 shows the evolution of damage in the different constituents of the model using Set 1 material properties. It shows the location of the initial damage in the fill tows at a volume averaged ε_{xx} strain level of 0.0935% strain. The initial damage occurs under compressive σ_{33} damage mode. It can be seen that the matrix is the last constituent in the composite to have significant failure. Looking at the column for 0.6% strain in

Figure 9.6 shows that the there is significant transverse damage in the fill and warp tows but there is hardly any damage in the matrix. This behavior was also expected based on the fact that the Set 1 material properties have the transverse tow strengths much lower than that of the matrix.

In comparison, Figure 9.7 shows the evolution of damage in the model using Set 2 material properties. In this case, it shows that the damage initiates in the matrix under tensile σ_{33} mode near the mid-plane of the laminate at a volume averaged ε_{xx} strain level of 0.0473%. Note that the damage initiates at a much lower strain level when using Set 2 material properties versus those in Set 1. Although the initial damage in the Set 2 model is in the matrix, the first significant drop in load is at a strain level of 0.128% (indicated by C in Figure 9.5) and it is caused by damage in the fill tow under compressive σ_{33} failure mode. In comparison, the first significant drop in the Set 1 model occurs at 0.0935% strain (indicated by A in Figure 9.5) under the same type of failure mode. The reason why the damage in the fill tow occurs at a higher strain level in the Set 2 model could be explained as follows. When the Set 2 laminate is at 0.0935% strain, there is already some damage in the matrix pockets. This would make the matrix pockets more compliant and thereby effectively reducing the constraints on the fill tow. The fill tows would be allowed to deform more freely than before matrix damage occurred and therefore relieving the σ_{33} stresses in the fill tow. Thus, a larger load would be required to raise the σ_{33} stress in the fill tow enough to cause damage.

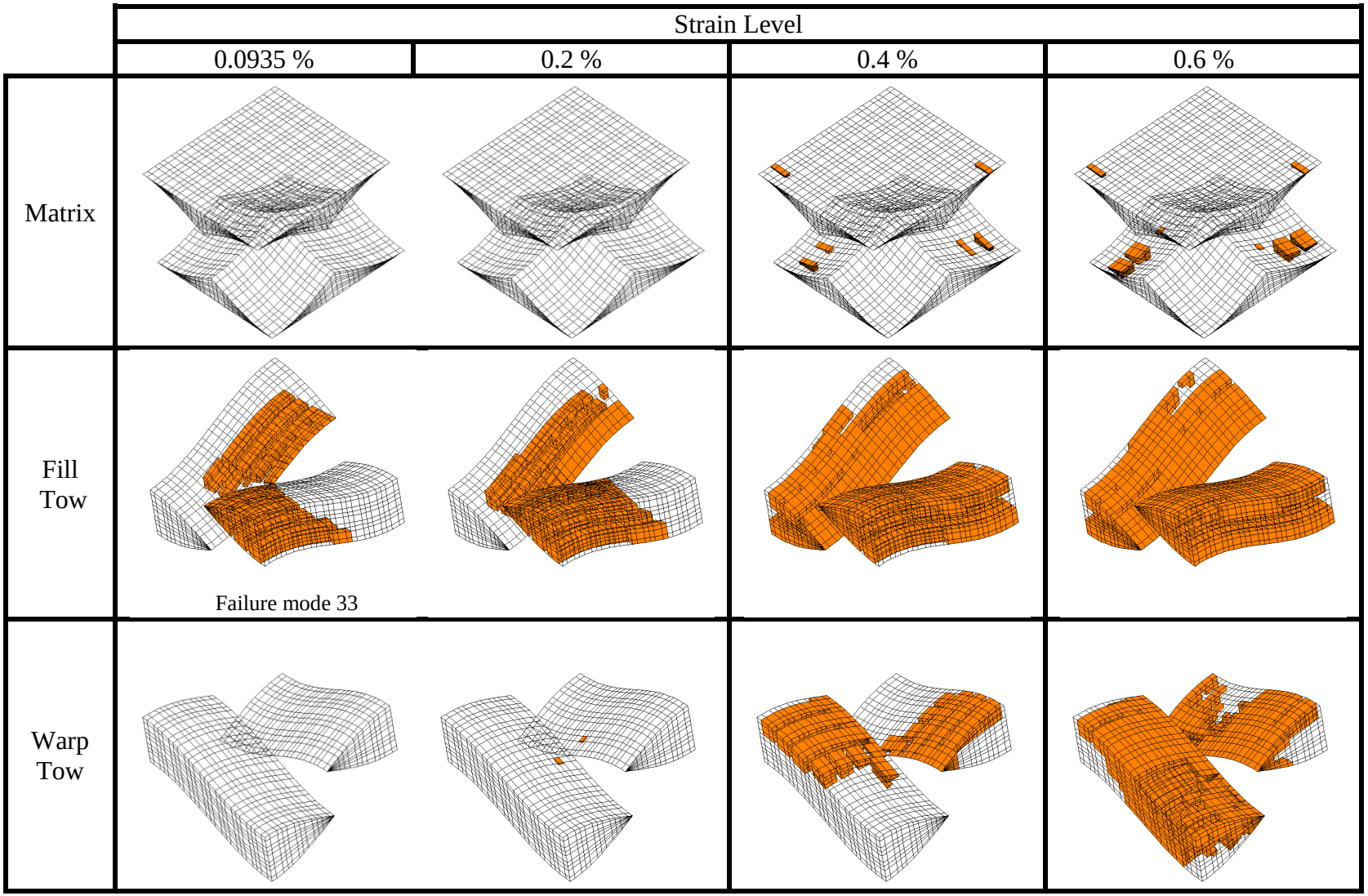

Figure 9.6: Evolution of damage in the two-ply laminate configuration without oxidation using Set 1 material properties

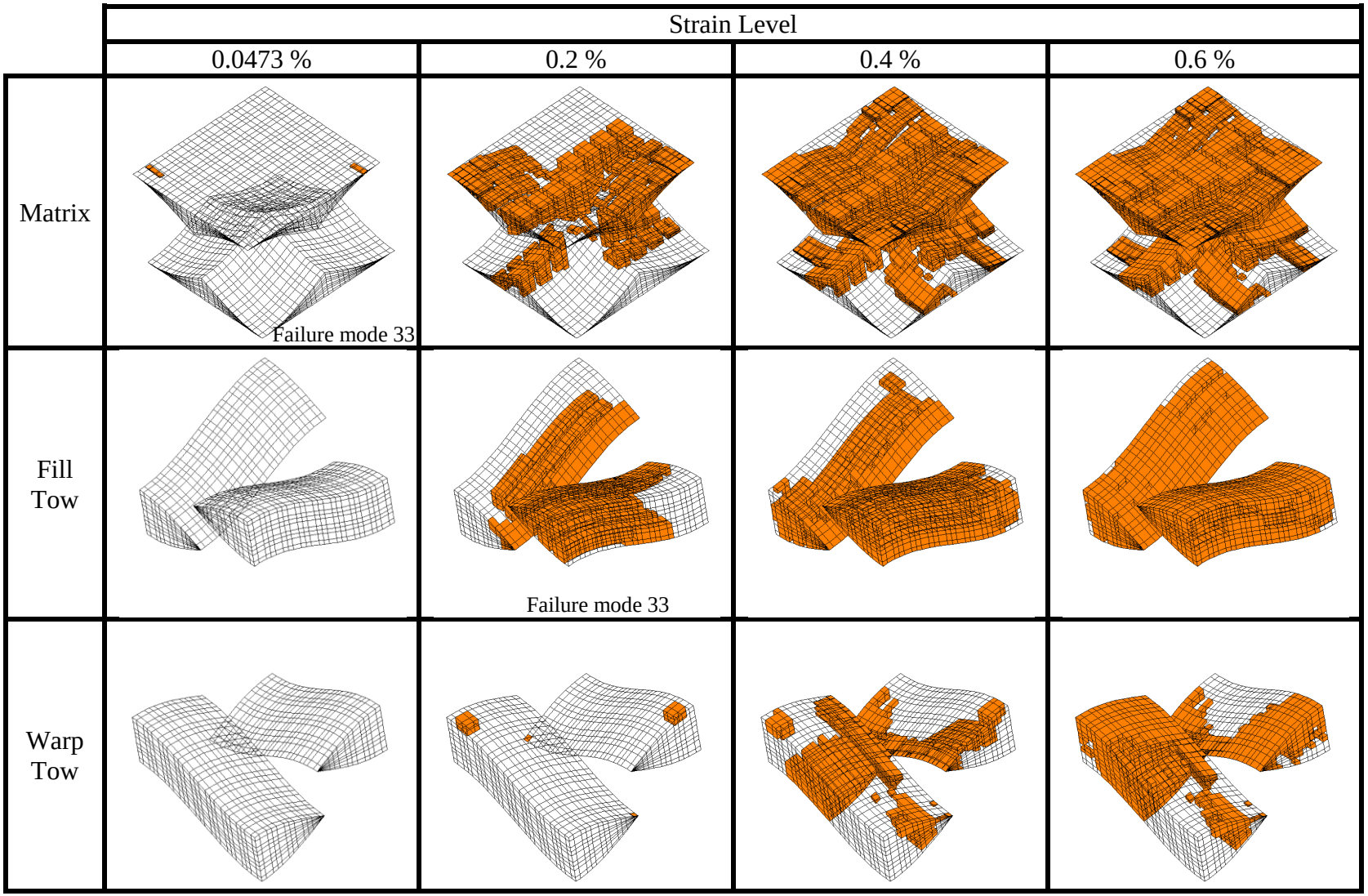

Figure 9.7: Evolution of damage in the two-ply laminate configuration without oxidation using Set 2 material properties

In comparison to the evolution of damage in the Set 1 model, the matrix has much more damage at 0.6% strain. Also, there are slight differences between the damaged locations in the tows. This is probably because of the manner in which the load is transferred when different locations in the laminate start to fail.

The results discussed up to this point considered only the effect of damage due to mechanical loading. Now the results from the coupled models are discussed. The coupled models simulate the mechanical behavior when the laminate is under a fixed mechanical loading and is then exposed to oxygen from the top and bottom surfaces for 200 hours. These simulations are performed at different fixed mechanical loads. Similar simulations are performed on models with each set of material properties to determine the effect of the properties on the behavior.

The behavior of the model using Set 1 material properties is discussed first. As illustrated in Figure 9.6, damage due to a mechanical-only load initiates at a strain level of 0.0935%. A coupled model simulation was performed at a strain level of 0.09% to see if the oxidization would initiate any damage. It was seen that there was no effect of oxidation on the damage behavior throughout the 200 hours. This is because, as shown in Figure 9.6, all the initial damage is located in the top half of the fill tow in the model, which implies that the stress failure index is highest in that region of the fill tow. This region in the model corresponds to the interior of the laminate because the analysis domain represents the lower half of the laminate. After 200 hours of oxidation, the oxidation front has not reached the interior of the laminate far enough to affect the engineering properties of the tow to cause damage. As defined in Table 9.5, the change in engineering moduli is not significant enough to affect the stresses. The changes in the strength properties are significant, but the regions with the stress concentrations are either not oxidized, or not oxidized enough to cause damage in the fill tows.

The simulations were also performed at strain levels of 0.2% and 0.4%. Since the configuration is assumed to be already loaded to a constant strain level, the configuration should also be assumed to have the damage that would have ordinarily occurred without the influence of oxidation. This initial damage state for a particular load level is assumed

based on the corresponding damage state for the model from the standard damage progression analysis. In the model with Set 1 material properties at a strain level of 0.2%, the damage at the beginning of the oxidation simulation is almost entirely in the fill tow as shown in Figure 9.6. There is no damage at all in the matrix. The only other damage in the configuration is one integration point in each warp tow that has failed in the σ_{33} damage mode as shown in Figure 9.6. Figure 9.8 shows the evolution of damage as the oxidation progresses for 200 hours. After one hour of oxidation, there is new damage under σ_{22} and σ_{33} failure modes in the bottom region of the fill tow where the oxygen is slowly making its way into the interior of the laminate. The simulation also shows some slight damage in the matrix pocket closer to the exposed surface of the laminate. There is also some damage in the σ_{22} failure mode in the lower half of the warp tow, which can be explained due to the oxidation front creeping into the interior of the laminate. The more interesting behavior is that regions of the top half of the warp tow fails in the σ_{33} damage mode. This is interesting because the damage is seen after only one hour of oxidation, at which time the oxidation front has not reached even close to the top half of the model. This can be explained by the redistribution of the load in the configuration after material damage. As mentioned earlier, even before oxidation began, there was damage in the fill tow. Figure 9.8 shows that after only one hour of oxidation, there is significant damage in the fill tow, which renders most of the fill tow incapable of carrying load. This increases the load on the warp tow. The effect of the external load on the laminate is to straighten the undulating warp tows, which causes a tensile σ_{33} in the top half of the tow. When the load on the warp tow increases, it also increases the σ_{33} stress in the top half of the tow making it exceed the strength. This behavior shows that the influence of oxidation on the mechanical behavior is not always localized and in some cases, its effect can be seen in the interior of the laminate where the material has not been oxidized.

Figure 9.9 shows the initial damage state in the two-ply laminate at 0.4% strain before oxidation begins. It shows that there is very little damage in the matrix pockets. The fill

tow on the other hand has considerable damage in the σ_{22} and σ_{33} failure modes. Figure 9.9 also shows that warp tow has some damage in the top half under mainly the σ_{33} failure mode. As the oxidation progresses, some build-up of σ_{11} damage is seen in the lower matrix pocket as shown in Figure 9.9. There is little new damage in the fill tow since most of the tow was already damaged before the oxidation began. The warp tow sees considerable new damage under the σ_{22} failure mode in the bottom half of the tow as oxidation progresses. This can be explained by the fact that the fill tow is mostly damaged and much of the load is now carried by the warp tow. Therefore, the warp tow would experience higher stresses. In addition to the higher stresses, the oxidation causes the strengths to drop by 50% thereby increasing the potential of failure.

Figure 9.10 shows the plot of the volume averaged σ_{xx} with the volume averaged ε_{xx} for the Set 1 model indicating the drop in the volume average σ_{xx} at the end of 200 hours of oxidation for the two simulations discussed earlier. It shows that for the 0.2% strain level simulation, the volume averaged σ_{xx} stress reduced from the point labeled A to A' indicating a drop of 15% at the end of 200 hours of oxidation whereas in the case of the 0.4% strain level, the corresponding stress dropped over 22% indicated by the line B-B'. Figure 9.11 shows the volume averaged σ_{xx} for all three simulations normalized with the initial volume averaged stress as the oxidation progresses over 200 hours. As mentioned earlier, at the 0.09% strain level, there was no new damage due to oxidation and therefore there was no drop in the volume averaged stress. Instead, there was a slight increase in the volume averaged stress due to the fact that the stiffness in the matrix increases when oxidized but the increase is so small that it is not noticeable in Figure 9.11. In the case of the 0.2% strain level, a significant part of the stress drop occurs in the beginning of the oxidation process within the first two hours. This indicates that the damage that occurred in the remaining 198 hours was not significant enough to reduce the load in the laminate. In the case of the 0.4% strain level, a major portion of the stress drop occurs at a single time step at 53.33 hours when the stress drops to 78.3% of the

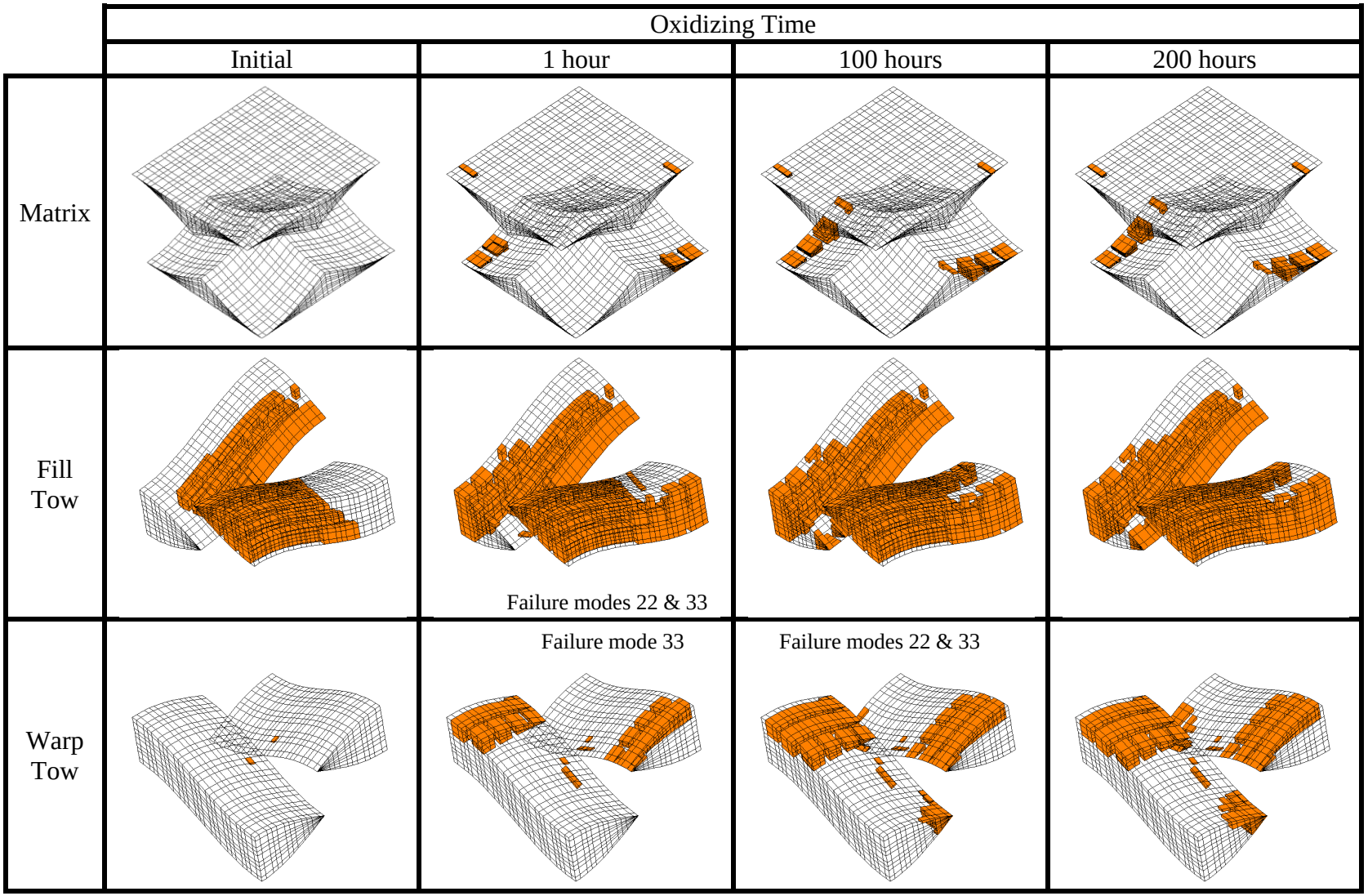

Figure 9.8: Evolution of damage due to oxidation in the two-ply laminate at 0.2% strain using Set 1 material properties

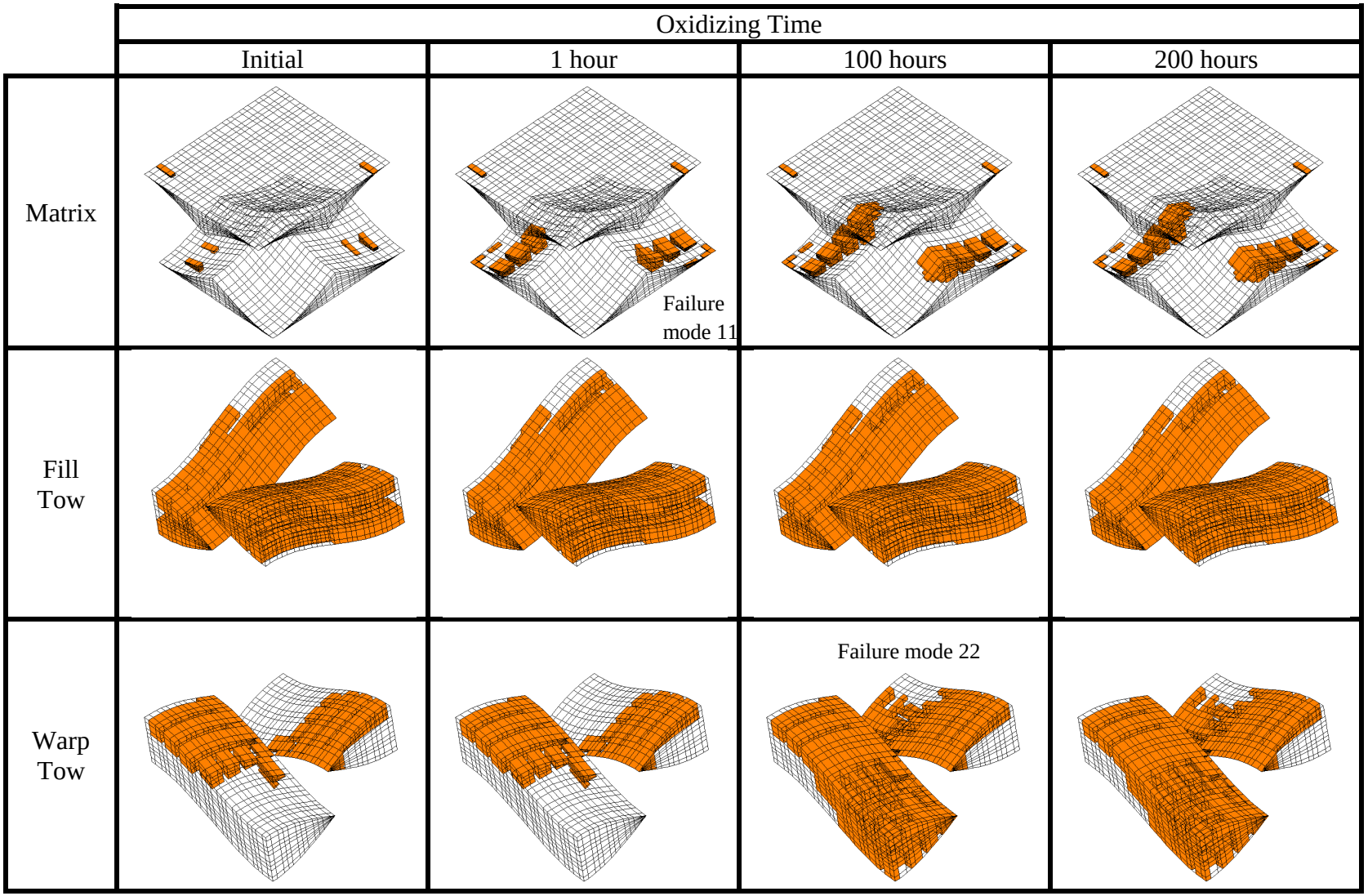

Figure 9.9: Evolution of damage due to oxidation in the two-ply laminate at 0.4% strain using Set 1 material properties

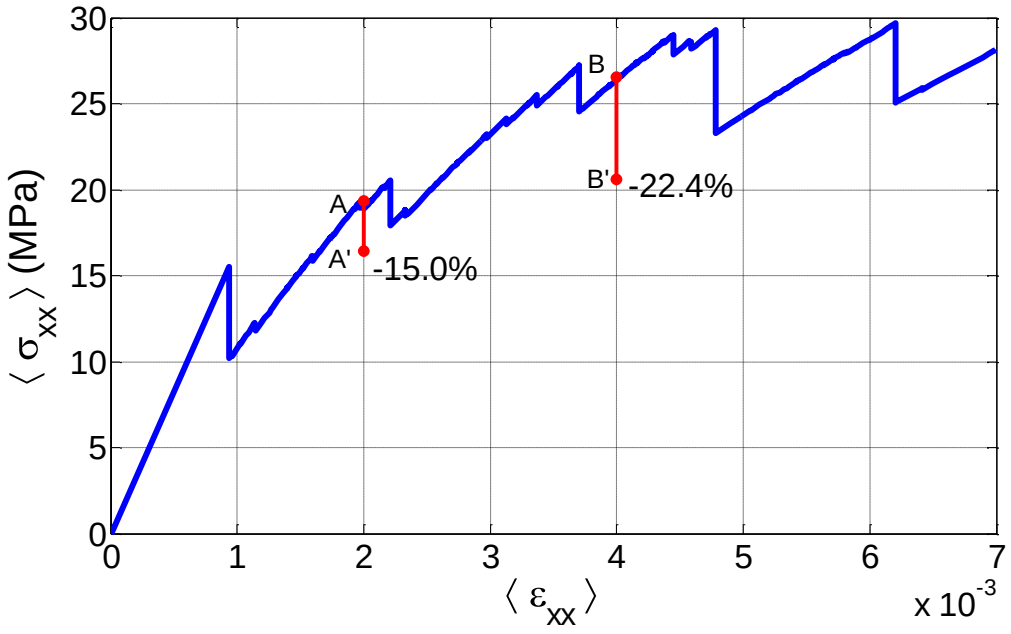

Figure 9.10: Volume averaged stress-volume averaged strain for the Set 1 material two-ply laminate showing drop in stress after 200 hours of oxidation

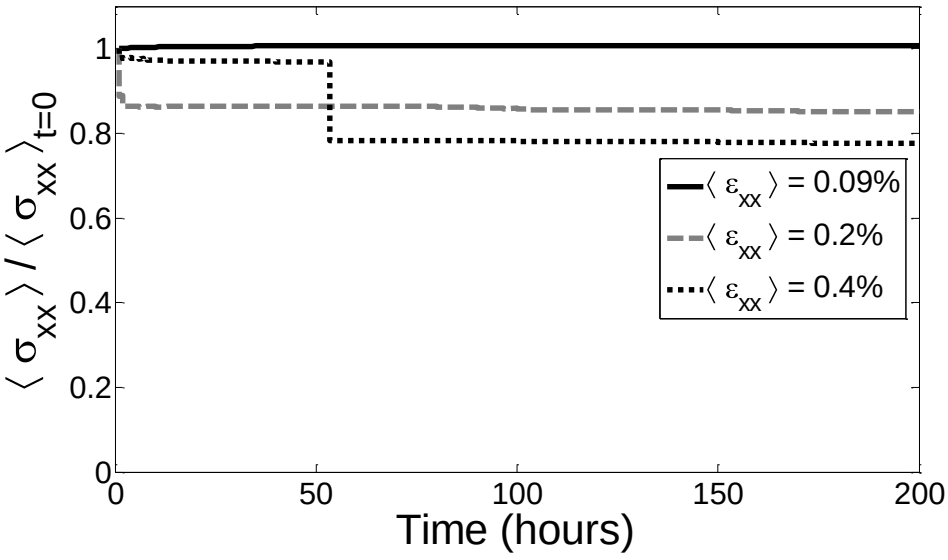

Figure 9.11: Variation in volume averaged stress due to oxidation for the Set 1 material two-ply laminate at different strain levels

initial stress. The damage that occurs before and after that point accounts for just 0.7% of the total drop in load.

The results from the simulations of the laminate using the Set 2 material properties are discussed next. Similar to the simulations on the laminates with Set 1 material properties, three simulations were performed with strain levels of 0.1%, 0.2% and 0.4%. In the simulation with 0.1% strain, the initial damage, as shown in Figure 9.12, is confined to mostly the inter-laminar matrix pocket. There is also slight damage under σ_{33} failure mode in the top part of the warp tow. The coupled analysis shows that there is no new damage caused due to the effect of oxidation. This is similar to the model with Set 1 material properties and 0.09% strain, where the stress state in the oxidized materials is not significant enough to cause new damage. With 0.2% strain, the initial damage is, as expected, more widespread than that in the case with 0.1% strain. As shown in Figure 9.13, the damage in the inter-laminar matrix pocket has increased in addition to new σ_{11} failure in the bottom matrix pocket. The fill tow has σ_{22} and σ_{33} failure in regions from the bottom to the top, with more damage in the latter. Figure 9.13 also shows that the damage in the warp tow increased. The simulation predicted that the damage in the lower matrix pocket grows mostly under σ_{11} and σ_{22} failure modes. The simulation also predicts, as shown in Figure 9.13, that there is new damage in the bottom part of the fill tow under the σ_{22} failure mode. This can be explained as a direct effect of the oxidation of the tows which reduces the strength by as much as 50%. The warp tow also has new damage growth as an effect of the oxidation. As shown in Figure 9.13, the warp tow starts to see damage in the lower part of the tow under σ_{22} failure mode as the oxidation progresses. The warp tow also starts to have σ_{33} damage at the location indicated by A as the oxidation simulation nears the end of 200 hours. A similar simulation was performed for a constant strain level of 0.4%. In this case, the initial damage state is more extensive compared to the simulation with 0.2% strain. The matrix, fill tow and warp tow have considerable damage as shown in Figure 9.14. As expected, the coupled analysis predicted growth in the damage in the lower matrix pocket due to

oxidation. Most of this damage occurs under σ_{11} failure mode along with σ_{22} and σ_{33} failure modes. In the case of the fill tows, the oxidation causes additional damage in the lower part of the tow under σ_{22} failure mode, as shown in Figure 9.14. Additional damage is also seen in the warp tow as an effect of the oxidation. The new damage in the warp tow occurs under σ_{22}, σ_{33} and σ_{13} failure modes.

Similar to Figure 9.10, Figure 9.15 shows the plot of the volume averaged σ_{xx} versus volume averaged ε_{xx} for the Set 2 model indicating the drop in the volume average σ_{xx} at the end of 200 hours of oxidation for the two simulations discussed earlier. Line A-A' shows that for the 0.2% strain level simulation, the volume averaged σ_{xx} stress dropped 13% at the end of 200 hours of oxidation whereas in the case of the 0.4% strain level, the corresponding stress dropped over 13.3% (indicated by line B-B'). Figure 9.16 shows the volume averaged σ_{xx} for all three simulations normalized with the initial volume averaged stress as the oxidation progresses over 200 hours. Just as the model with Set 1 material properties at the 0.09% strain level, there was no new damage due to oxidation and the volume averaged stress actually increases slightly, although it is not noticeable in Figure 9.16. In the case of the other two strain levels, the drop in volume averaged stress is more gradual than the behavior seen in the corresponding models with Set 1 material properties. Although there are some sudden drops in the volume averaged stress as seen in Figure 9.16, they are not as significant as the drops seen in Figure 9.11. This behavior is attributed to growth in the matrix damage observed in the Set 2 laminates that is not seen in the Set 1 laminates.

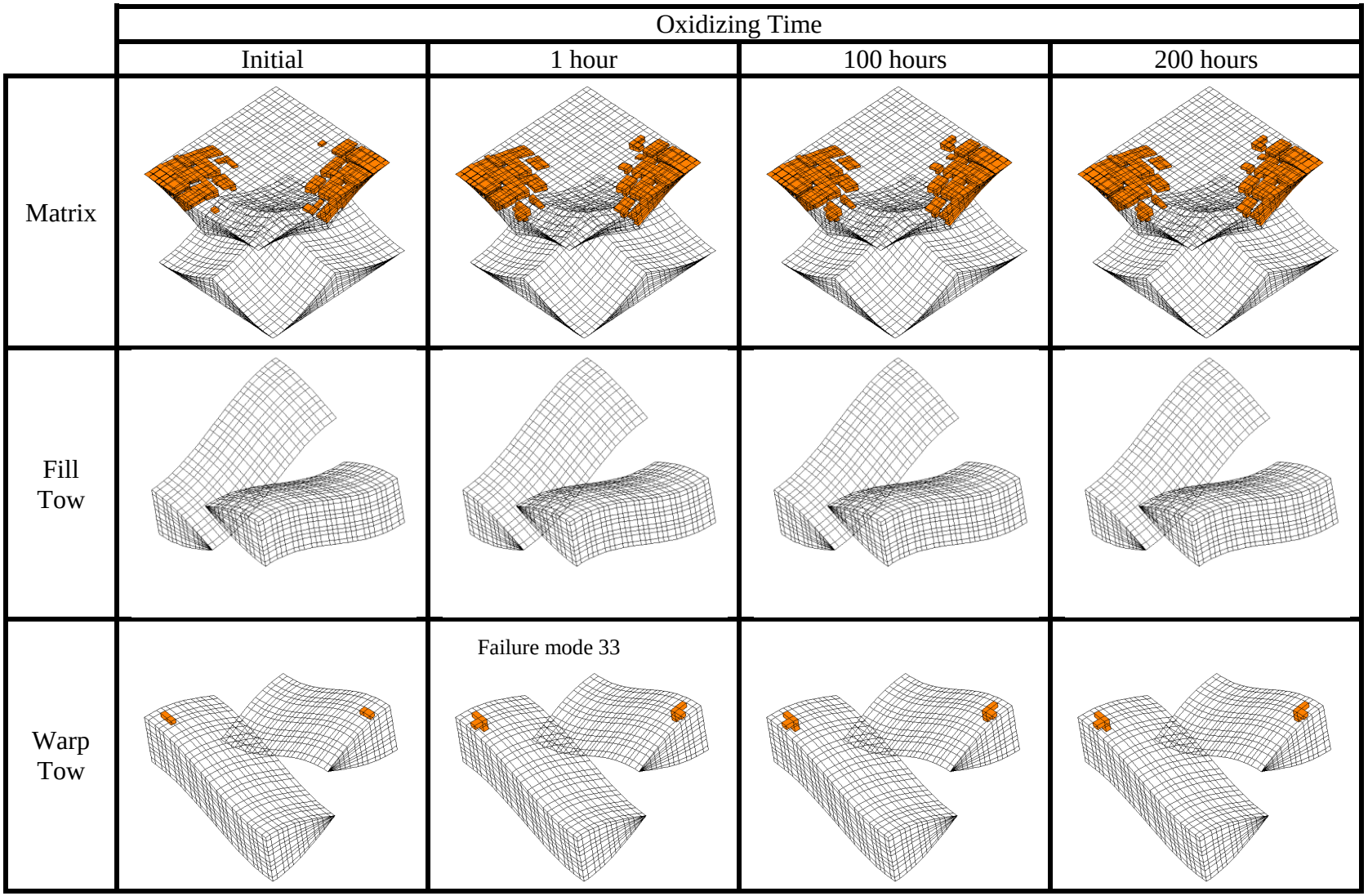

Figure 9.12: Evolution of damage due to oxidation in the two-ply laminate at 0.1% strain using Set 2 material properties

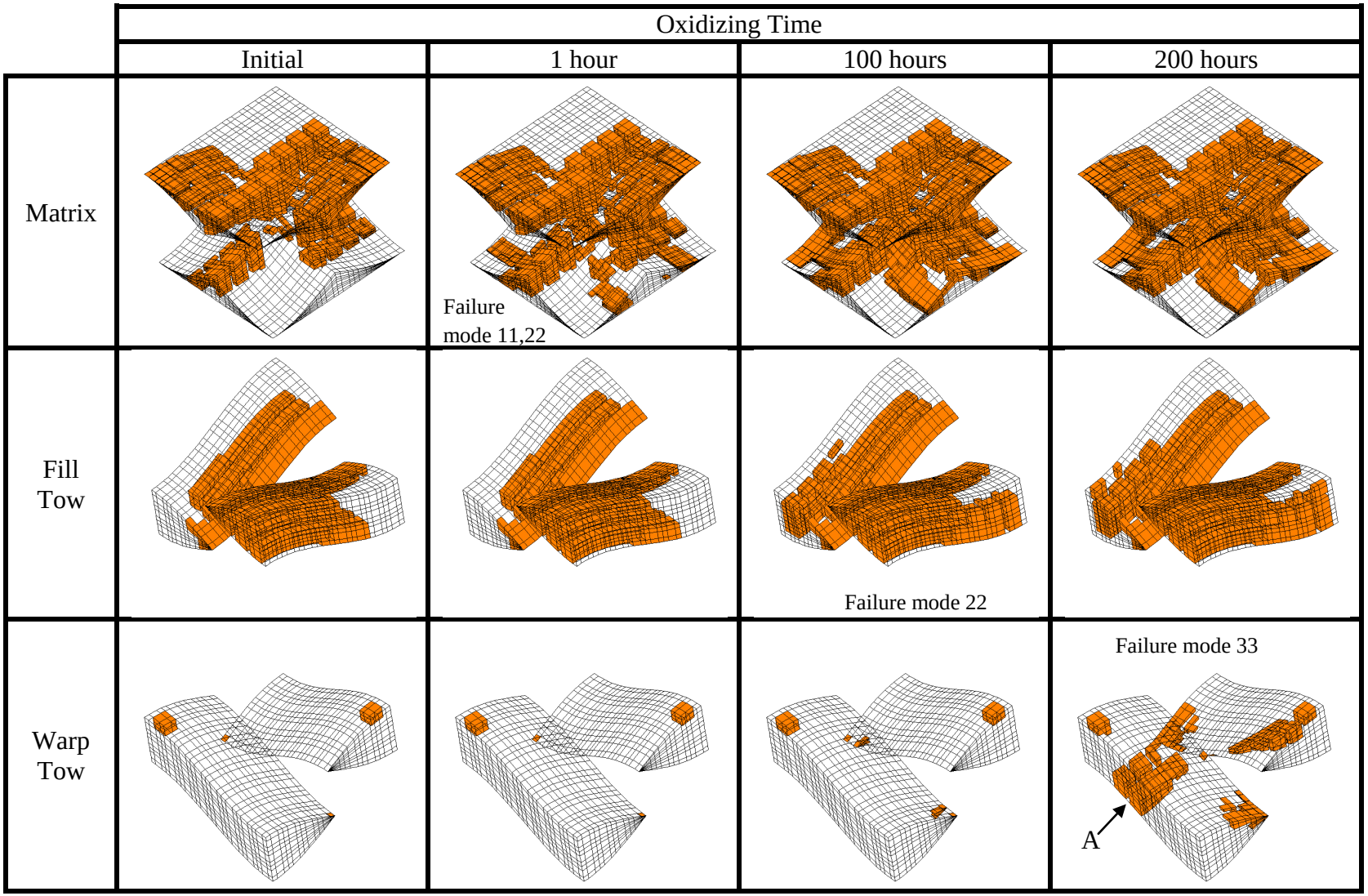

Figure 9.13: Evolution of damage due to oxidation in the two-ply laminate at 0.2% strain using Set 2 material properties

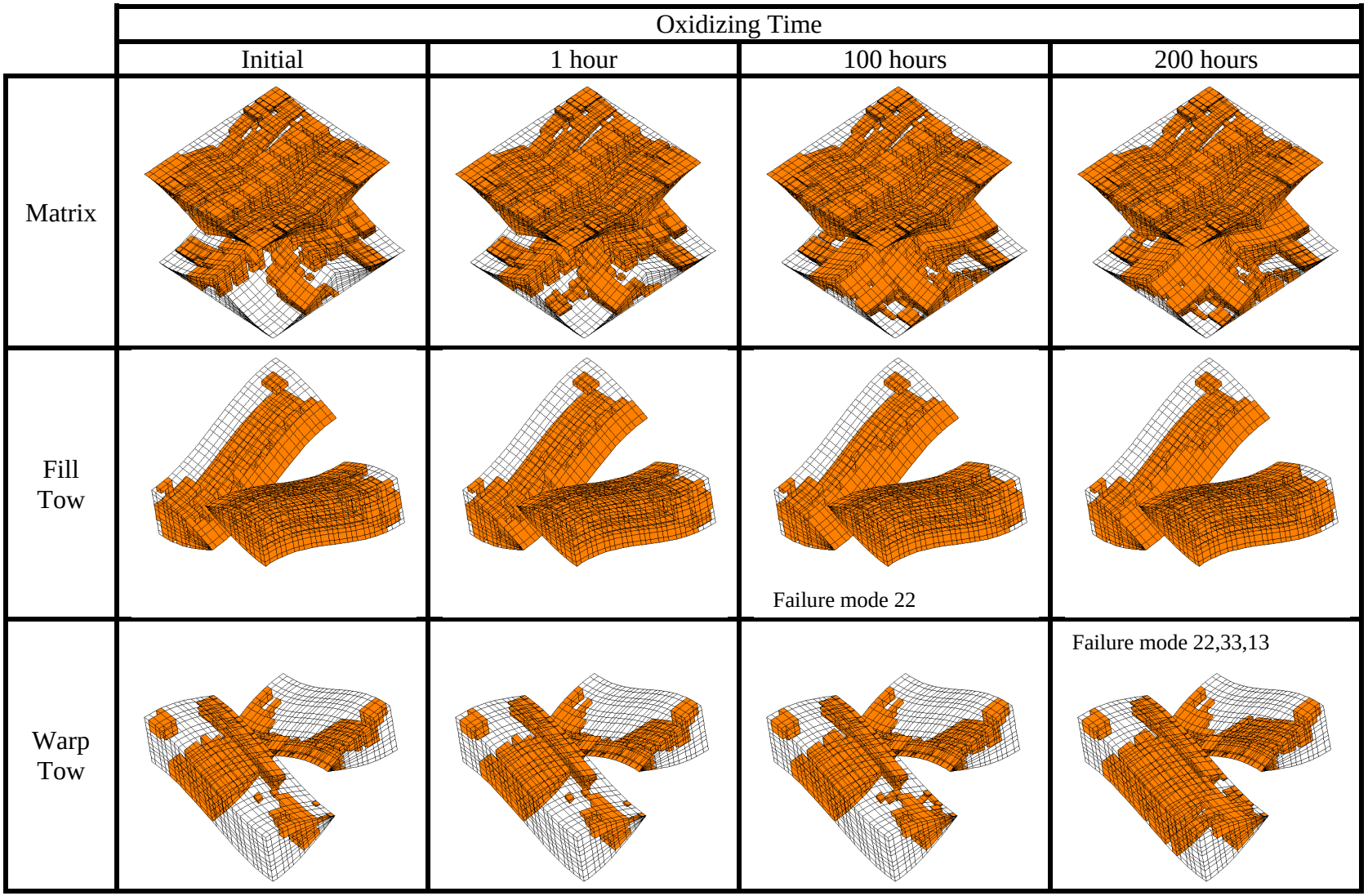

Figure 9.14: Evolution of damage due to oxidation in the two-ply laminate at 0.4% strain using Set 2 material properties

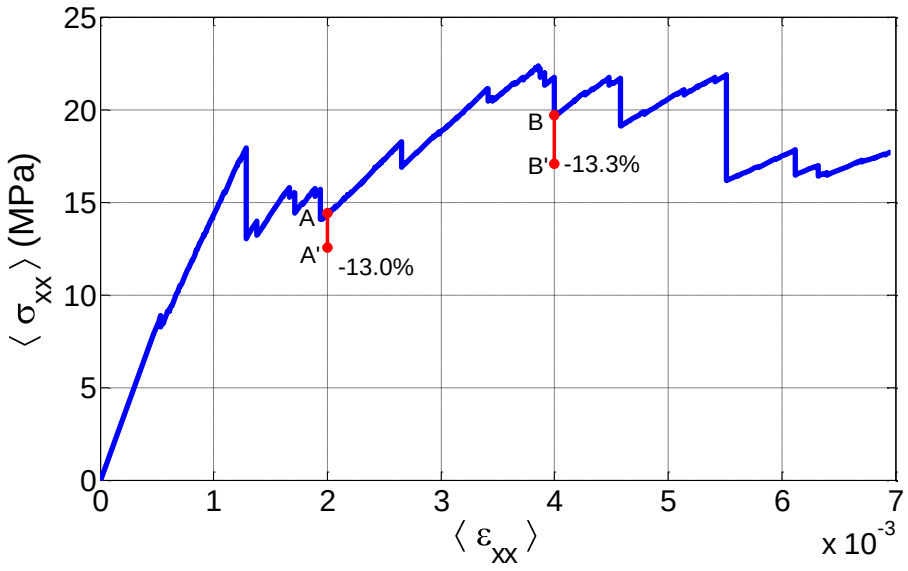

Figure 9.15: Volume averaged stress-volume averaged strain for the Set 2 material two- ply laminate showing drop in stress after 200 hours of oxidation

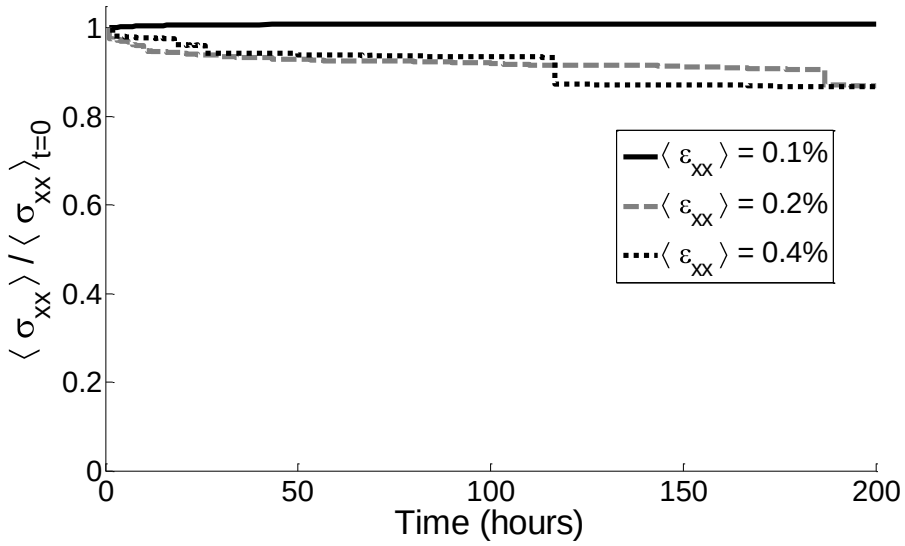

Figure 9.16: Variation in volume averaged stress due to oxidation for the Set 2 material two-ply laminate at different strain levels

9.4.2 Effect of Number of Plies in Laminate

A parametric study was conducted to see if the number of plies in the laminate had any significant effect on the mechanical behavior under oxidation. In addition to the laminates that were discussed in the previous section, 4-ply and 6-ply laminates were analyzed for both Set 1 and Set 2 material properties. First, a damage progression analysis (i.e. no oxidation) was performed on the laminates to determine the mechanical behavior as the load on the laminate was increased. Figure 9.17 gives a plot of the volume averaged σ_{xx} with the volume averaged ε_{xx} for the different laminates using Set 1 material properties. It shows that the overall behavior is not significantly different, which is not surprising. Figure 9.18 shows the same plot for the laminates with Set 2 material properties. Again, the number of plies does not seem to have an effect on the overall behavior. Looking at the evolution of damage in the laminates revealed generally the same trends as seen in the 2-ply laminates. In the case of the Set 1 laminates, the fill tows had initial damage and continued to accumulate much more damage than the warp tows followed by the matrix, which had very little failure. In the case of Set 2 laminates, as seen in the corresponding 2-ply laminate, the damage initiates in the matrix followed by the fill tow failing considerably while the warp tow has less damage in comparison.

The coupled simulations were performed on these laminates as was done for the 2-ply laminates discussed in the previous section. The laminates were analyzed at different strain levels and overall they showed the same trends as seen in the 2-ply laminates. If the strain levels are too low, for example at 0.1%, the oxidation was not found to have any significant effect of the mechanical behavior. The results from the 0.2% and 0.4% strain level simulations will be discussed here. Since the general trends are the same as compared to the 2-ply laminates, the evolution of damage in each laminate will not be discussed here. Instead, comparisons of the overall behavior will be discussed. Comparing the results from the 2-ply, 4-ply and 6-ply laminates is not easy since they do not follow the same load path as shown in Figure 9.18. It would definitely not make sense to make comparisons at same strain level using the predicted volume average

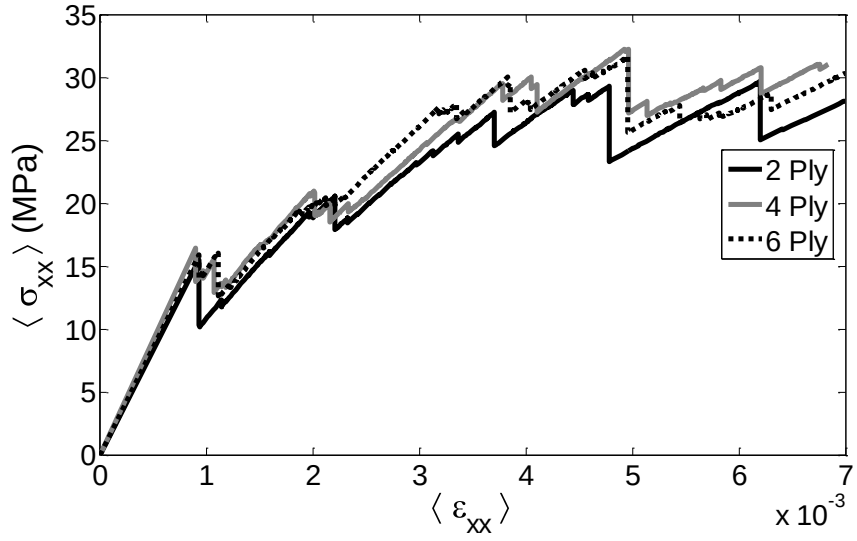

Figure 9.17: Volume averaged stress-volume averaged strain curves for the laminate with Set 1 material properties

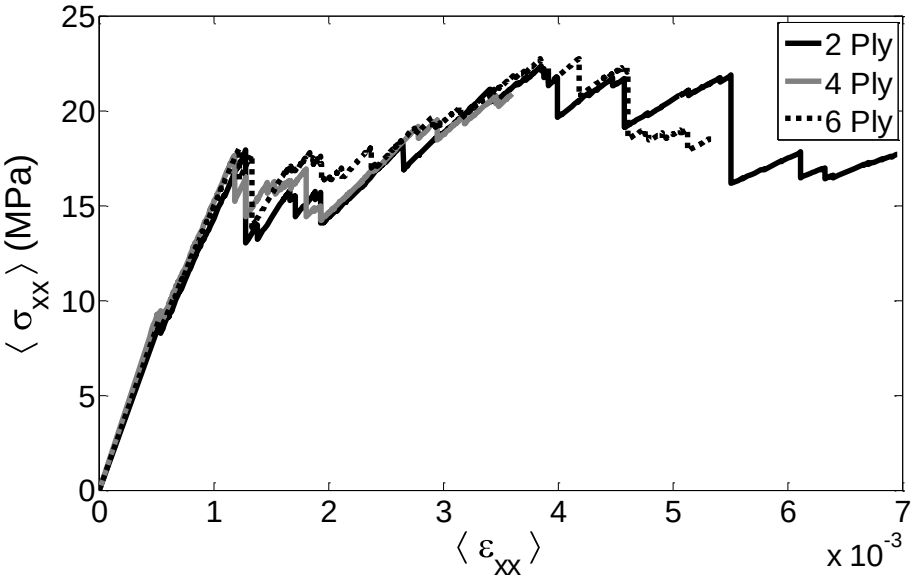

Figure 9.18: Volume averaged stress-volume averaged strain curves for the laminate with Set 2 material properties

stress values because of the same reason. It makes more sense to look at the percentage drop in the volume average stress.

Figure 9.19 shows the variation in normalized volume average stress at 0.2% strain for the 2-ply, 4-ply and 6-ply laminates using Set 1 materials. In the 2-ply laminate, under a 0.2% strain level, the volume average stress drops 15% whereas in the 4-ply model, it

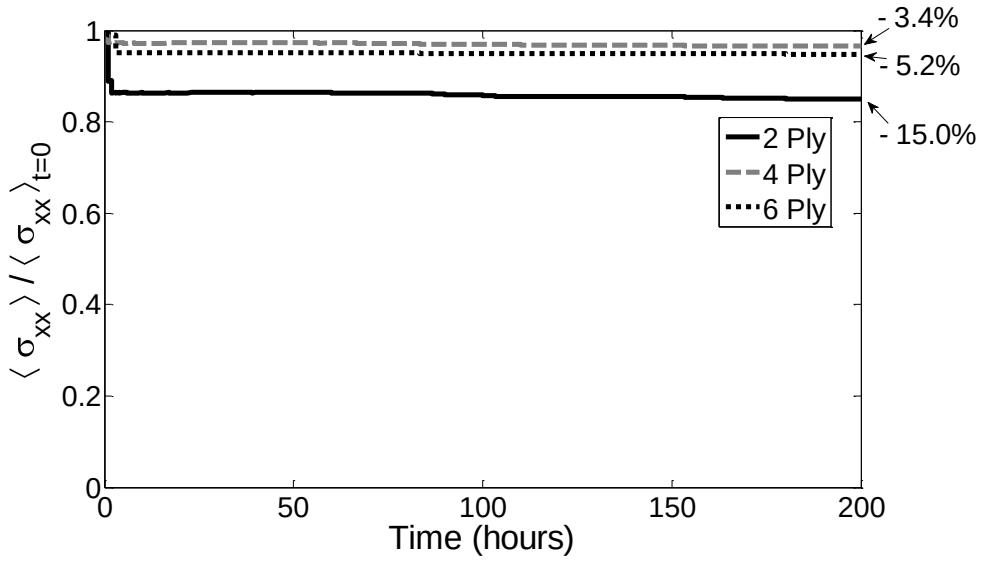

Figure 9.19: Variation in volume averaged stress due to oxidation for the various Set 1 material laminates at 0.2% strain level

drops only 3.4%, which indicates that the damage in the 4-ply laminate was not significant. This is intuitive since a smaller fraction of the laminate is getting oxidized when the number of plies increases from 2 to 4. However when the number of plies is increased from 4 to 6, the stress drop increases slightly from 3.4% to 5.2%. This particular trend could not be explained but as discussed later in this section, this counter-intuitive behavior was not observed for the other material set or for other strain levels. Figure 9.19 also shows that all the Set 1 material laminates experience the significant drop in the volume average stress within 3 hours of oxidation. Figure 9.20 shows the variation of the normalized stress for the 0.4% strain level. It shows the percentage drop in the volume average stress at the end of 200 hours steadily reducing as the number of plies in the laminate increase. Comparison of Figures 9.19 and 9.20 shows that when the strain level was increased, the decrease in percentage load drop was more gradual with

the number of plies. In the case of 0.4% strain, the drop is 22.4% for a 2-ply laminate, 14.8% for a 4-ply laminate and 9.5% for a 6-ply laminate. On the other hand, in the 0.2% strain level, as seen in Figure 9.19, the percentage drop reduces from 15% to less than 6% as the number of plies is increased to 4 and 6. Note that this trend is specific to

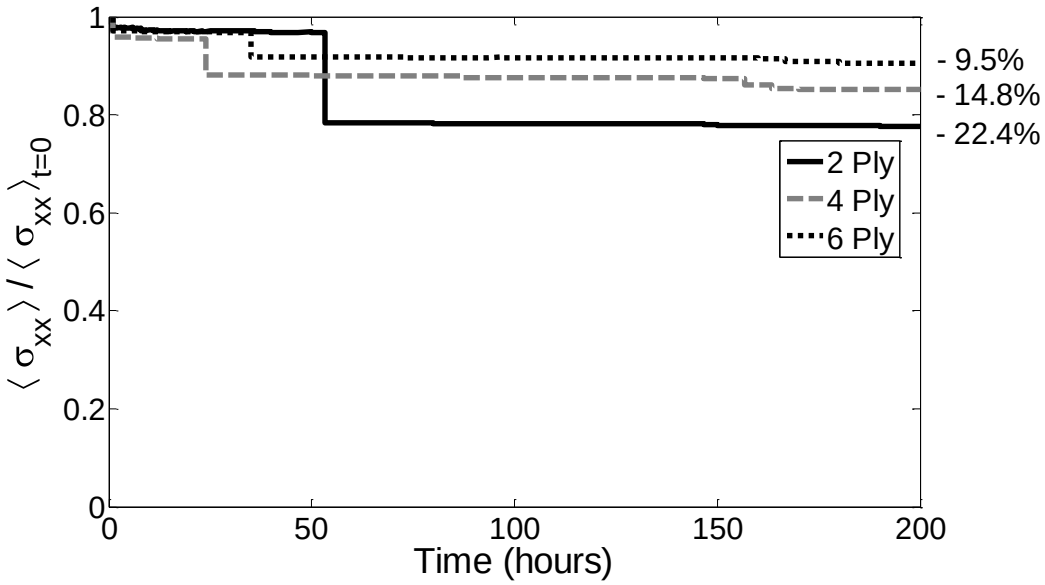

Figure 9.20: Variation in volume averaged stress due to oxidation for the various Set 1 material laminates at 0.4% strain level

the laminates with Set 1 material properties and cannot be generalized. Similar simulations were performed on the corresponding laminates with Set 2 material properties and Figure 9.21 and 9.22 shows the variation in volume average stress for 0.2% and 0.4% strain loading respectively. Again, a similar trend is seen where there is a significant reduction in the percentage drop in volume average stress at the end of 200 hours (from 13% to 4.1%) for a 0.2% loading when the number of plies is increased from 2 to 4. When the number of plies is increased to 6, the drop is only 3.3%, which is a further reduction in the drop compared to the corresponding case in the Set 1 material laminates. Also, the variation in the normalized stress with respect to time is much more gradual in the Set 2 laminates as compared to the Set 1 laminates. When the strain level

is increased to 0.4%, again similar trends are seen where the reduction in the percentage drop is not as drastic as that for 0.2% strain. Figure 9.22 shows that the percentage volume average stress drop at the end of 200 hours of oxidation reduces from 13.3% to 7% when the number of plies go up from 2 to 4 and the drop further reduces to 5.2% when the number of plies is increased to 6. This behavior can be explained based on the fact that the oxidation process oxidizes the same amount of material in all these laminates. In the coupled simulations described in this work, the oxidation analysis does not depend on the stress or damage state in the laminate. Therefore, regardless of the number of plies, the oxidation layer thickness varies in the same manner in all the laminates. This also has to do with the fact that at the end of the 200 hour simulation, the maximum predicted oxidation layer thickness is less than the thickness of a single ply. Increasing the number of plies in the laminate effectively increases the amount of material that can carry load, but the oxidation process only affects the same amount of material regardless the number of plies. Therefore, it would be expected that the percentage drop in volume average stress, or load drop, would decrease as the number of plies increased.

9.5 Summary

The coupled analysis model described in Section 3 is used to predict the mechanical behavior of woven composite laminates that are under mechanical load as well as exposed to oxygen. The configuration that is analyzed and the complete parameters for the material system and the constitutive relations are described in this section. The current implementation of the coupled analysis model makes a number of assumptions when simulating the behavior of the laminate. The effects of thermal expansion and the shrinkage of the matrix due to oxidation are ignored. These are effects that need to be considered in future implementations of the coupled analysis model in order to represent more accurately the behavior of the underlying mechanisms. The effect of the stress and damage state on the oxidation behavior also needs to be considered in future enhancements of the coupled model. However, the analyses described in this work provide a framework for the implementation of a more robust tool to predict the

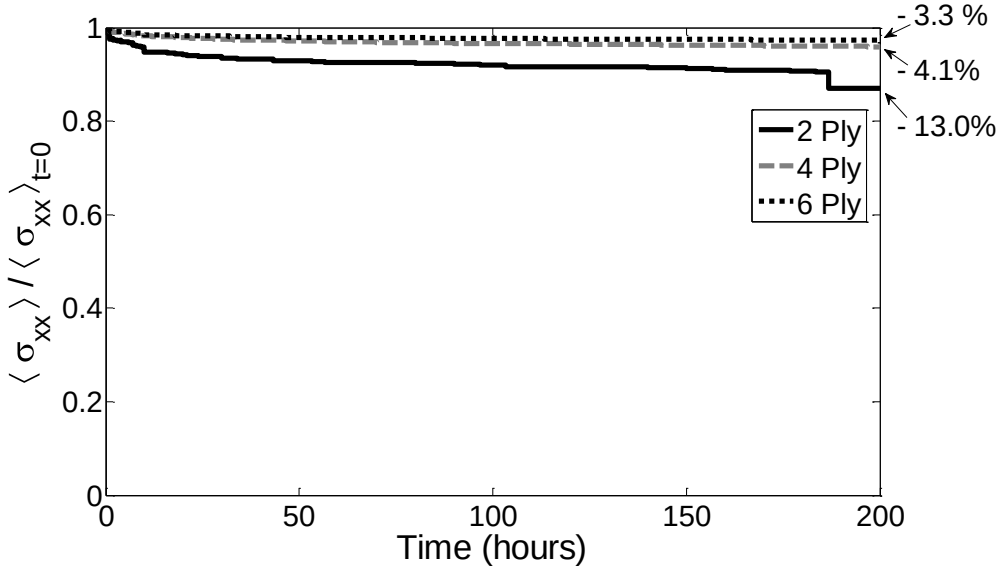

Figure 9.21: Variation in volume averaged stress due to oxidation for the various Set 2 material laminates at 0.2% strain level

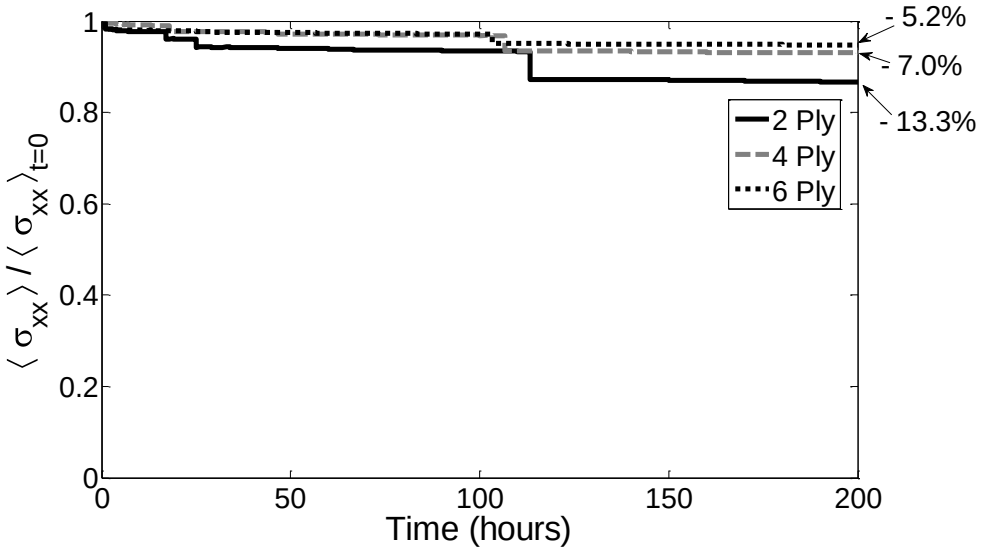

Figure 9.22: Variation in volume averaged stress due to oxidation for the various Set 2 material laminates at 0.4% strain level

behavior of laminates under oxidation. Due to lack of a full set of reliable material properties, two sets of material properties were assumed to the represent the typical behavior of composite materials. Simulations were performed on laminates with both sets of properties. The predicted mechanical behavior due to the effect of oxidation was described. This included illustrating the initiation and progression of damage in the laminate. A parametric study was also performed to determine the effect of the number of plies on the mechanical behavior under oxidation.

10. CONCLUSIONS AND FUTURE WORK

This research work has contributed in various ways to help develop a better understanding of textile composites and materials with complex microstructures in general. An instrumental part of this work was the development of a framework that made it convenient to perform multiscale/multiphysics analyses of advanced materials such as textile composites with complex microstructures. In addition to the studies conducted in this work, this framework lays the groundwork for continued research of these materials. This framework enabled a detailed multiscale stress analysis of a woven DCB specimen that revealed the effect of the complex microstructure on the stress and strain energy release rate distribution along the crack front. In addition to implementing an oxidation model, the framework was also used to implement strategies that expedited the simulation of oxidation in textile composites so that it would take only a few hours. Finally, a coupled diffusion/oxidation and damage progression analysis was implemented that was used to study the mechanical behavior of textile composites under mechanical loading as well as oxidation. The following sections discuss the conclusions drawn from the work performed to achieve the objectives of this research effort. This section concludes by mentioning some suggestions for possible future work.

10.1 Development of Multiscale/Multiphysics Finite Element Framework

A robust finite element framework was developed that is specially geared to perform multiscale/multiphysics analysis of textile composites. The developed framework, called BETA, uses the object-oriented programming paradigm and its design makes it convenient to maintain, enhance and extend the framework. The fact that it is developed in-house gives the advantage of having full access to the core of the software, which can be modified to adapt to any specialized method that a user is interested in implementing. This kind of access is not available when using commercial finite element packages. Having full access to the software also makes it an ideal teaching tool for researchers and students. The framework also allows the user to develop interfaces to other software to take advantage of their advanced features. BETA is portable across Windows and UNIX/LINUX platforms and can take advantage of multiple processors by using parallel

solvers for the finite element analysis. It also allows users to modify the code so that different steps of the finite element analysis can be parallelized to achieve better efficiency. The framework developed as part of this work is used to perform a multiscale analysis of textile composites. It is also used to implement a coupled multiphysics model that is used to predict the mechanical behavior of textile composites under oxidation.

10.2 Multiscale Analysis of Woven DCB Specimen

A detailed stress analysis of a woven composite DCB specimen was performed. Such a configuration contains many microstructural scales such as fiber/matrix, tow architecture and laminate and therefore, a multiscale analysis was required. Such an analysis that took into account the tow architecture of the DCB specimen could not be found in the literature. The finite element framework was used to implement a strategy where the natural hierarchical character of model descriptions and simulation results is exploited to expedite analysis of problems. Hierarchical techniques were used in the development, organization, and management of finite element models, and for the post-processing of the results from the analyses. Models in the hierarchy were 'joined' together by implementing a boundary matching routine that specifies multi-point constraints in order to impose continuity at the interfaces. Using this strategy made it convenient to model the region near the crack front discretely accounting for the tow architecture whereas the regions away from the crack front were modeled using effective properties. In addition to the stresses, the strain energy release rate along the width of the crack front was also calculated. The effect of the complex microstructure on the stress distribution and the G_I distribution was studied. It was seen that the stresses and G_I distribution follow a periodic pattern corresponding to the undulation of the tows in the woven composite, which suggested that the delamination would initiate in certain regions and propagate to the rest of the crack front. The effect of the microstructure on the stresses and G_I as the crack advances was also investigated. The results suggested that there would likely be significant variation in the growth rate as the crack advanced.

10.3 Simulation of Oxidation in Textile Composites

The oxidation behavior of textile composites was simulated using the finite element framework that was developed as part of this work. This involved implementing various strategies because of the multiple scales of microstructure involved in the configuration. An oxidation model was implemented based on the model developed by Pochiraju et al to simulate oxidation in neat PMR-15 resin. Homogenized oxidation material properties for a unidirectional laminate or tow were determined assuming that the fiber was impermeable and un-oxidizable. The homogenized properties were validated using different configurations. It was also determined that the oxidation behavior in heterogeneous configurations is complex and depends on various factors such as the location of the material boundaries. The oxidation model had severe limitation on the element size and time step size based on the finite element formulation. Therefore, a typical oxidation analysis was very computation intensive and it was not feasible to simulate oxidation of a textile composite without strategies to expedite the analysis. Optimal element sizes were determined and the time step size was ramped up to achieve better efficiencies. An adaptive meshing strategy was also developed that exploited certain characteristic of the oxidation behavior to reduce the size of the problem. The adaptive meshing strategy was able to give computational time savings of over 60%. However, these strategies were not enough to make a full 3D oxidation analysis feasible. Therefore, a hybrid modeling strategy was developed that divided up a 3D analysis domain into an array of 1D domains which could then be solved in a matter of hours. The 1D models could also be analyzed independently on different processors in a multi-core machine thereby increasing the efficiency even further. The hybrid model strategy was validated and used in conjunction with the adaptive meshing strategy to simulate oxidation of a plain weave laminate. The analysis revealed that the tow architecture of the textile composite had a significant effect on the oxidation behavior. After 200 hours of oxidation of a 200 micron thick ply, the smallest oxidation layer thickness was found to 84 microns whereas the largest was 110 microns.

10.4 Prediction of Damage Progression in Textile Composites under Oxidation

The multiscale/multiphysics analysis framework was used to implement a coupled diffusion/oxidation and continuum damage analysis to study the mechanical behavior of textile composites in oxidizing environments. The current implementation of the coupled model considers only the effect of oxidation on the mechanical behavior and not vice versa. Since only one-way coupling was assumed, the oxidation simulation could be performed independently before the coupled analysis. The coupled analysis was used to predict progressive damage in a Graphite/PMR-15 plain weave laminate that is uniaxially loaded to a fixed strain level and then exposed to oxidation through the top and bottom surfaces. A constitutive model was developed that degrades the engineering properties depending on the mechanical state and how much the material has oxidized. Due to lack of a full set of reliable material properties, two sets of material properties were assumed to the represent the typical behavior of composite materials. The predicted mechanical behavior due to the effect of oxidation was described and an attempt was made to explain some of the behavior observed. The simulations showed the evolution of damage in the composite as it undergoes oxidation. It was seen that in some cases the effect of oxidation is not localized and that damage also occurs in regions that are not oxidized due to load redistribution. The simulations also showed the variation of the volume averaged stress in the laminate as the laminate oxidizes. It was seen that the strengths of the materials in the laminate had an effect on this behavior. A parametric study was also performed to determine the effect of the number of plies on the mechanical behavior under oxidation. The simulations predicted a significant drop in the load carried by a 2-ply laminate for different strain levels and the load drop reduced, as expected, when the number of plies was increased to 4 and 6. However, the proportion by which the load drop reduces was not very intuitive and indicates that the material properties and the microstructure of the textile laminates have a complicated effect on the behavior under oxidation.

10.5 Future Work

Over the course of this research work, several ideas came up that might have successfully helped in advancing the understanding of these advanced materials. However, not all of them could be pursued due to various reasons. In addition to this, there are some obvious extensions to the research work presented in this dissertation. Many of them are listed below:

1. The BETA framework supports several parallel solvers that can take advantage of the new multi-core machines available in the market today but in many cases, the dominant step is not the solving of the finite element equations. In transient analysis like diffusion/oxidation as well as damage progression analyses, operations that are performed over all the elements such as assembly or updating of state variables are the ones that take the most time. Unfortunately, BETA currently supports parallelization of these operations only for models that do not use multi-point constraints. A generalized parallelizing strategy for these types of operations would make analyses more efficient.
2. For analyzing even smaller length scales, hybrid models directly linking atomistic regions to continuum finite element regions have been developed by several researchers. These include the FEAt model [179], the MAAD approach [180-181], the QuasiContinuum method [182-184] and the coupled atomistic and discrete dislocation plasticity (CADD) approach [185] and the bridging scale method [186]. Currently, the hierarchical strategies explained in this work are implemented only for the continuum mechanics regime. However, it might be worthwhile to explore the possibility of using these strategies in analyzing multiple scale problems involving the atomistic scale.
3. The time integration scheme used for the diffusion/oxidation finite element formulation makes several assumptions to account for the nonlinearity in the governing equations. The Livermore Solver for Ordinary Differential Equations (LSODE)[187] could be an efficient alternative to the scheme that is currently used.

4. The current finite element formulation for the oxidation model assumes that the time step is small enough that the assumptions to account for the nonlinearity hold. Future extensions to the model could look at defining a residual and iterating to drive the residual to zero to account for the nonlinearity at each time step.
5. When trying to replace a heterogeneous material with a homogenized material in an oxidation model, it is reasonable to assume that some or possibly all of these properties might change. In addition to the current homogenization strategy, there is at least one other possible approach for achieving this goal. One is to use a multi-scale analysis that keeps track of the 'local' information such as oxidation state and actual average concentration in the constituent matrix in the homogenized material. Given this information, it would be possible to calculate the reaction rate R at a particular material point in the tow's constituent matrix using eq(3.90). Next, the effective reaction rate for the larger scale homogenized tow is determined by a simple rule of mixtures and plugged into the governing equations. When the equations for a time step are solved, the calculated concentrations are transformed back to the local scale using a rule of mixtures in order to keep track of the oxidation state of the constituent matrix. Thus, a continuous transfer of information between the two scales needs to be maintained throughout the simulation.
6. In this work, the fibers in the tows are idealized to be in a square array and the fibers are assumed to be impermeable and do not oxidize. While there are other factors that can influence the oxidation behavior in composites such as the properties of the fiber/matrix interface or interphase, they are not taken into account for the homogenization model described in this work. Cracks in the matrix or along the fiber/matrix interface can also affect the oxidation behavior by allowing rapid ingress. Depending on the type of damage that is observed in these composites, it might be possible to account for their effects in the homogenized model. For example, if the damage is diffuse, the homogenized

properties can be degraded appropriately or if the damage is confined to certain areas, cracks can be introduced in the homogenized model. These and other such factors should be addressed in a likely extension to the model.

7. The oxidation level information from the hybrid oxidation model is currently approximated as a single linear function to define the active zone. A better approximation could be made using a few more points to define a piecewise linear function for the active zone.
8. A simple constitutive model or property degradation scheme was developed to account for the effect of oxidation on the mechanical behavior. This scheme can be modified and enhanced in the future when the effect of oxidation on the coupled oxidation-mechanical behavior is more accurately determined. This can also include a constitutive model to account for the effect of mechanical damage on the oxidation behavior, which would make the analysis fully coupled.
9. The effects of thermal expansion and the shrinkage of the matrix due to oxidation are ignored in the current implementation of the coupled model. These are effects that should to be considered in future implementations of the coupled analysis model in order to more accurately represent the behavior of the underlying mechanisms.

REFERENCES

1. URL: *http://www.doitpoms.ac.uk/miclib/full_record.php?id=582* [cited 01 June 2009].
2. A & P Technology, Inc. *http://www.braider.com* [cited 01 February 2006].
3. URL: *http://www.gzespace.com/gzenew/index.php?pg=athletic&lang=en* [cited 01 June 2009].
4. URL: *http://www.ptonline.com/articles/200810fa2.html* [cited 01 June 2009].
5. Deepak Goyal, Analysis of Linear Elasticity and Non-Linearity due to Plasticity and Material Damage in Woven and Biaxial Braided Composites, PhD Dissertation, Texas A&M University, 2007.
6. Tang, X., Whitcomb, J. D., Kelkar, A. D., Tate, J. S. (2006). Progressive Failure Analysis of 2x2 Braided Composites Exhibiting Multiscale Heterogeneity. *Composites Science & Technology,* **66**(14): 2580-2590.
7. Tandon G. P., Pochiraju K.V. and Schoeppner G.A. (2006). Modeling of oxidative development in PMR-15 resin, *Polymer Degradation and Stability*, **91:** 1861-1869.
8. Pochiraju, K and Tandon, G. (2007). Modeling Thermo-Oxidative Layer Growth in High-Temperature Resin, *Journal of Engineering Materials and Technology*, **128**(1): 107-116.
9. Schoeppner, G.A., Tandon, G.P., and Pochiraju, K.V. (2008). Predicting Thermo-oxidative Degradation and Performance of High-Temperature Polymer Matrix Composites, In: Kwon, Young W. Allen, David H. and Talreja, Ramesh R. (eds.), *Multiscale Modeling And Simulation Of Composite Materials And Structures*, **1st edn**, p. 359, Springer, New York.
10. Courant, R. L. (1943). Variational Methods for the Solution of Problems of Equilibrium and Vibration, *Bulletin of the American Mathematical Society*, **49:**1-23.
11. Argyris, J.H., Kelsey, S. (1960), *Energy Theorems and Structural Analysis*, Butterworths, London.

12. Turner, M. J., Clough, R.W., Martin, H.C. and Topp, L.C. (1956). Stiffness and Deflection Analysis of Complex Structures, *Journal of Aerospace Science*, **23**: 805-823.

13. Allegretto, W., Lin, Y. and Yang, H. (2001). Finite Element Methods for Pricing American Options on Stocks Source, In: Minev, P. and Lin, Y. (eds.), *Advances In Computation: Theory And Practice, Scientific Computing and Applications*: pp. 287 – 294, Nova Science Publishers, Inc. Commack, New York.
14. URL: *http://www.mscsoftware.com/about/history.cfm* [cited 01 June 2009].
15. URL: *http://www.fea-optimization.com/ans_macro/ANS-history.txt* [cited 01 June 2009].
16. URL: *http://www.asme.org/Communities/History/Resources/Interactive_Timeline.cfm* [cited 01 June 2009].
17. URL: *http://www.simulia.com* [cited 01 June 2009].
18. Barrett, P. R. and Fridline, D., User Implemented Nitinol Material Model in ANSYS, *http://www.caeai.com/papers/ansys_nitinol_paper.pdf* [cited 01 June 2009].
19. Liu, B., Huang, Y., Jiang, H., Qu, S. and Hwang, K.C. (2004). The Atomic-Scale Finite Element Method, *Comput. Methods Appl. Mech. Engrg*. **193**:1849–1864.
20. Lu, J., White, D., Chen, W. (1993). Applying Object-Oriented Design to Finite Element Programming, In: *Proceedings of the 1993 ACM/SIGAPP symposium on Applied computing: states of the art and practice*, Indianapolis, IN: 424 – 429.
21. URL: *http://www.z88.org/* [cited 01 June 2009].
22. URL: *http://homepage.usask.ca/~ijm451/finite/fe_resources/node140.html* [cited 01 June 2009].
23. URL: *http://www.dealii.org/* [cited 01 June 2009].

24. URL: *http://home.gna.org/getfem/getfem_intro.html* [cited 01 June 2009].
25. URL: *http://www.nwnumerics.com/Zebulon/Zebulon.html* [cited 01 June 2009].
26. Besson, J. and Foerch, R. (1997). Large scale object-oriented finite element code design, *Computer Methods in Applied Mechanics and Engineering*, **142**(1-2): 165-18.
27. Stroustrup, B. (2007), Evolving a language in and for the real world: C++ 1991-2006, In: *History of Programming Languages Conference*, College Station, TX, 23 May.
28. URL: *http://www.ctcms.nist.gov/oof/* [cited 01 June 2009].
29. URL: *http://www.comsol.com/* [cited 01 June 2009].
30. URL: *http://en.wikipedia.org/wiki/Shared_memory* [cited 01 June 2009].
31. URL: *http://en.wikipedia.org/wiki/Symmetric_multiprocessing* [cited 01 June 2009].
32. URL: *http://en.wikipedia.org/wiki/Computer_cluster* [cited 01 June 2009].
33. URL: *http://www.llnl.gov/computing/tutorials/pthreads/* [cited 01 June 2009].
34. URL: *http://www.openmp.org* [cited 01 June 2009].
35. URL: *http://www.mpi-forum.org/docs/* [cited 01 June 2009].
36. Schenk, O., Gärtner, K., Fichtner, W. and Stricker, A. (2001). PARDISO: A High-Performance Serial and Parallel Sparse Linear Solver in Semiconductor Device Simulation, *Journal of Future Generation Computers Systems*, **18**: 69-78.
37. Schenk, O. and Gärtner, K. (2004). Solving Unsymmetric Sparse Systems of Linear Equations with PARDISO, *Journal of Future Generation Computer Systems*, 20(3):475—487.
38. Schenk, O. and Gärtner, K. (2006). On fast factorization pivoting methods for symmetric indefinite systems, *Elec. Trans. Numer. Anal.*, **23**:158--179.
39. URL: *http://www.pardiso-project.org/* [cited 01 June 2009].

40. URL: *http://www.intel.com/cd/software/products/asmo-na/eng/307757.htm* [cited 01 June 2009].
41. URL: *http://www.intel.com/cd/software/products/asmo-na/eng/266853.htm* [cited 01 June 2009].
42. URL: *http://glaros.dtc.umn.edu/gkhome/metis/metis/overview* [cited 01 June 2009].
43. URL: *http://glaros.dtc.umn.edu/gkhome/metis/parmetis/overview* [cited 01 June 2009].
44. Karypis, G. and Kumar, V. (1998). A Parallel Algorithm for Multilevel Graph Partitioning and Sparse Matrix Ordering, *Journal of Parallel and Distributed Computing*, **48**: 71 - 85.
45. Balay, S., Buschelman, K., Gropp, W. D., Kaushik, D., Knepley, M. G., McInnes, L. C., Smith, B. F. and Zhang, H. (2001). PETSc, URL: *http://www.mcs.anl.gov/petsc*.
46. Balay, S., Buschelman, K., Eijkhout, V., Gropp, W. D., Kaushik, D., Knepley, M. G., McInnes, L. C., Smith B. F. and Zhang, H. (2004) PETSc Users Manual, ANL-95/11 - Revision 2.1.5, Argonne National Laboratory.
47. Balay, S., Gropp, W. D., McInnes, L. C. and Smith, B. F. (1997). Efficient Management of Parallelism in Object Oriented Numerical Software Libraries, In: E. Arge and A. M. Bruaset and H. P. Langtangen, (eds), *Modern Software Tools in Scientific Computing*, **1st edn**, pp 163-202, Birkhäuser, Boston.
48. Amestoy, P. R., Duff, I. S. and L'Excellent, J.-Y. (2000), Multifrontal Parallel Distributed Symmetric and Unsymmetric Solvers, *Comput. Methods in Appl. Mech. Eng.*, **184**: 501-520.
49. Amestoy, P. R., Duff, I. S., Koster, J. and L'Excellent, J.-Y. (2001). A Fully Asynchronous Multifrontal Solver Using Distributed Dynamic Scheduling, *SIAM Journal of Matrix Analysis and Applications*, **23**(1): 15-41.

50. Amestoy, P. R., Guermouche, A., L'Excellent, J.-Y. and Pralet, S. (2006). Hybrid Scheduling for the Parallel Solution of Linear Systems, *Parallel Computing*, **32**(2): 136-156.

51. Amestoy, P. R., Davis, T. A. and Duff, I. S. (1996). An Approximate Minimum Degree Ordering Algorithm. *SIAM Journal on Matrix Analysis and Applications*, **17**:886–905.

52. Schulze, J. (2001). Towards a Tighter Coupling of Bottom-Up and Top-Down Sparse Matrix Ordering Methods, *BIT*, **41**(4): 800–841.

53. Gould, N.I.M., Hu, Y. and Scott, J. A. (2005). Complete Results From a Numerical Evaluation of Sparse Direct Solvers for the Solution of Large, Sparse, Symmetric Linear Systems of Equations. Technical Report RAL-2005-1, Rutherford Appleton Laboratory.

54. Gould, N.I.M., Hu, Y. and Scott, J. A. (2005). A Numerical Evaluation of Sparse Direct Solvers for the Solution of Large Sparse, Symmetric Linear Systems of Equations. Technical Report RALTR- 2005-005, Rutherford Appleton Laboratory.

55. Gould, N.I.M. and Scott, J. A. (2003). A Numerical Evaluation of HSL Packages for the Direct Solution of Large Sparse, Symmetric Linear Systems of Equations. Technical Report RAL-2003-019, RAL.

56. Tang, X., Whitcomb, J. D., Kelkar, A., and Tate, J. (2005). Progressive Failure Analysis of 2x2 Braided Composites Exhibiting Multiscale Heterogeneity, *Journal of Composites Science & Technology*. **66**: 2580–2590.

57. Koca, O. and Buchholz, F. -G. (1994). Analytical- and Computational Stress Analysis of Fiber/Matrix Composite Models, *Computational Materials Science*, **3**(2): 135-145.

58. Hatta, H., Goto, K., Ikegaki, S., Kawahara, I., Aly-Hassan, M. S. and Hamada, H. (2005). Tensile Strength and Fiber/Matrix Interfacial Properties of 2D and 3D-Carbon/Carbon Composites, *Journal of the European Ceramic Society*, **25**(4): 535-542.

59. Zhifei, S., Yanhua, C. and Limin, Z., (2005). Micromechanical Damage Modeling of Fiber/Matrix Interface Under Cyclic Loading, *Composites Science and Technology*, **65**(7-8): 1203-1210.

60. Whitcomb, J. D. and Noh, J. (2005). Concise Derivation of Formulas for 3D Sublaminate Homogenization, *Journal of Composite Materials*, **34**(6): 522-535.

61. Kim, J-S. (2007). Development of a User-Friendly Expert System for Composite Laminate Design, *Composite Structures*, **79**(1): 76-83.

62. Mayes, J. S. and Hansen, A. C. (2004). Composite Laminate Failure Analysis Using Multicontinuum Theory, *Composites Science and Technology*, **64**(3-4): 379-394.

63. Lee, S.J., Reddy, J.N. and Rostam-Abadi, F. (2006). Nonlinear Finite Element Analysis of Laminated Composite Shells with Actuating Layers, *Finite Elements in Analysis and Design*, **43**(1): 1-21.

64. Zhang, Y., Zhu, P. and Lai, X. (2006). Finite Element Analysis of Low-Velocity Impact Damage in Composite Laminated Plates, *Materials & Design*, **27**(6): 513-519.

65. Yang, Q. D., Rugg, W. K. L., Cox, B. N. and Marshall D. B. (2005). Evaluation of Macroscopic and Local Strains in a Three-Dimensional Woven C/SiC Composite, *Journal of American Ceramic Society,* **88**(3): 719–725.

66. Whitcomb, J., Noh, J. and Chapman, C. (1999). Evaluation of Various Approximate Analyses for Plain Weave Composites, *Journal of Composite Materials*, **33**(21): 1958-1981.

67. Ishikawa, T., and Chou, T. W. (1982). Elastic Behavior of Woven Hybrid Composites, *Journal of Composite Materials*, **16**: 2–19.

68. Ishikawa, T. and Chou, T. W. (1982). Stiffness and strength behavior of woven fabric composites, *Journal of Material Science*, **17**: 3211-3220.

69. Ishikawa, T., Matsushima M. and Hayashi Y. (1985). Experimental Confirmation of the Theory of Elastic Moduli of Fabric Composites, *Journal of Composite Materials*, **19**: 443-458.

70. Naik, N. K. and Shembekar, P. S. (1992). Elastic Behavior of Woven Fabric Composites: I - Lamina Analysis, *Journal of Composite Materials*, **26**: 2196-2225.

71. Naik, N. K. and Ganesh, V. K. (1993). Prediction of Thermal Expansion Coefficients of Plain Weave Fabric Composites, *Composite Structures*, **26**: 139-154.

72. Hahn, H. T. and Pandey, R. (1994). A Micromechanics Model for Thermoelastic Properties of Plain Weave Fabric Composites, *Journal of Engineering Material Technology*, **116**: 517-523.

73. Vandeurzen, P., Ivens, J. and Verpoest, I. (1998). Micro-Stress Analysis of Woven Fabric Composites by Multilevel Decomposition, *Journal of Composite Materials*, **32**(7): 623-651.

74. Whitcomb, J. D. and Tang, X. (2001). Effective Moduli of Woven Composite, *Journal of Composite Materials*, **35**(23): 2127-2144.

75. Paumelle, P., Hassim, A. and Léné, F. (1990). Composites with Woven Reinforcements: Calculation and Parametric Analysis of the Properties of Homogeneous Equivalent, *La Recherche Aérospatiale*, **1**: 1-12.

76. Paumelle, P., Hassim, A. and Léné, F., (1991). Microstress Analysis in Woven Composite Structures, *La Recherche Aérospatiale*, **6**: 47-62.

77. Whitcomb, J. D. and Tang, X. (1999). Effect of Tow Architecture on Stresses in Woven Composites, In: *40th AIAA/ ASME/ ASCE/ AHS/ASC Structures, Structural Dynamics and Materials Conference*, St. Louis, MO, AIAA-99-1479: 1-10.

78. Whitcomb, J. D. (1991). Three Dimensional Stress Analysis of Plain Weave Composites, NASA TM 101672. In: T.K. O'Brien, (ed), *Composite Materials:*

Fatigue and Fracture, (Third Volume), ASTM STP 1110, pp. 417-438, American Society for Testing and Materials, Philadelphia.

79. Kuhn, J. L. and Charalambides, P. G. (1999). Modeling of Plain Weave Fabric Composite Geometry, *Journal of Composite Materials*, **33**(3): 188-220.
80. Kuhn, J. L., Haan, S. I. and Charalambides, P. G (2000). Stress Induced Matrix Microcracking in Brittle Matrix Plain Weave Fabric Composites under Uniaxial Tension, *Journal of Composite Materials*, **34**(19): 1640-1664.
81. Ji, K. H. and Kim, S. J. (2007). Dynamic Direct Numerical Simulation of Woven Composites For Low-velocity Impact, *Journal of Composite Materials*, **41**(2): 175-200.
82. Blackketter, D. M., Walrath, D. E. and Hansen, A. C. (1993). Modeling damage in a plain weave fabric-reinforced composite material, *Journal of Composites Technology & Research*, **15**(2): 136-142.
83. Tang, X. and Whitcomb, J. D. (2003). Progressive Failure Behaviors of 2D Woven Composites, *Journal of Composite Materials*, **37**(14): 1239-1259.
84. Kollegal, M. G. and Sridharan, S. (2000). Strength Prediction of Plain Woven Fabrics, *Journal of Composite Materials*, **34**(3): 240-257.
85. Guan, H. and Gibson, R. F. (2001). Micromechanical Models for Damping in Woven Fabric-Reinforced Polymer Matrix Composites, *Journal of Composite Materials*, **35**(16): 1417-1434.
86. Goyal, D., Tang, X. and Whitcomb, J. D. (2005). Effect of Various Parameters on Effective Engineering Properties of 2x2 Braided Composites, *Journal for Mechanics of Advanced Materials and Structures*, **12**(2): 113–128.
87. D'Amato, E. (2001). Finite Element Modeling of Textile Composites, *Composite Structure*, **54**: 467-475.
88. Naik, R. A. (1996). Analysis of 2-D Traixial and 3-D Multi-Interlock Braided Textile Composites, *AIAA*-96-1530-CP: 1804-1811.

89. Whitcomb, J. D., Chapman, C. D. and Tang, X. (2000). Derivation of Boundary Conditions for Micromechanics Analyses of Plain and Satin Weave Composites, *Journal of Composite Materials*, **34**(9): 724-747.

90. Tang, X. and Whitcomb, J. D. (2003). General Techniques for Exploiting Periodicity and Symmetries in Micromechanics Analysis of Textile Composites, *Journal of Composite Materials*, **37**: 1167 - 1189.

91. Goyal, D. and Whitcomb, J. D. (2006). Analysis of Stress Concentrations in 2 x 2 Braided Composites, *Journal of Composite Materials*, **40**(6): 533-546.

92. Tang, X., Whitcomb, J. D., Kelkar, A., and Tate, J (2006). Progressive Failure Analysis of 2x2 Braided Composites Exhibiting Multiscale Heterogeneity, *Composites Science & Technology*, **66**: 2580-2590.

93. Aggarwal, A., Ramakrishna, S. and Ganesh, V. K. (2001). Predicting the In-Plane Elastic Constants of Diamond Braided Composites, *Journal of Composite Materials*, **35**(8): 665-688.

94. Lee, C. S., Chung, S. W., Shin, H. and Kim, S. J. (2005). Virtual Material Characterization of 3D Orthogonal Woven Composite Materials by Large-scale Computing, *Journal of Composite Materials*, **39**(10): 851-863.

95. Bednarcyk, B. A. and Pindera, M.-J. (2000). Inelastic Response of a Woven Carbon/Copper Composite- Part II: Micromechanics Model, *Journal of Composite Materials*, **34**(4): 299-331.

96. Saff, C.R. (2004). A Potential Path Forward for Hybrid Composite Structures", In: *Innovative Intelligent Design of Hybrid Composite Architectures (IDA) Workshop*, Hampton, VA.

97. Pierron, F., Cerisier, F. and Grediac, M. (2000). A Numerical and Experimental Study of Woven Composite Pin-Joints, *Journal of Composite Materials*, **34**(12): 1028-1054.

98. Jaksic, N., Simon-Weidner, J. (1999). Nonlinear Global-Local Finite Element Analysis of a Future Plasma Fusion Experiment, *Computers and Structures*, **72**: 209-231.

99. Whitcomb, J. D. and Woo, K. (1993). Application of Iterative Global/Local Finite Element Analysis, Part 1: Linear Analysis, *Communications in Numerical Methods in Engineering*, **9**: 745-756.

100. Whitcomb, J. D. and Woo, K. (1993). Application of Iterative Global/Local Finite Element Analysis, Part 2: Geometrically Nonlinear Analysis, *Communications in Numerical Methods in Engineering*, **9**: 757-766.

101. Woo, K. and Whitcomb, J. D. (1993). Macro Finite Element Using Subdomain Integration, *Communications in Applied Numerical Methods*, **9**(12): 937-949.

102. Whitcomb, J. D. and Woo, K. (1994). Enhanced Direct Stiffness Method for Finite Element Analysis of Textile Composites, *Composite Structures*, **28**(4): 385-390.

103. Whitcomb, J. D., Tang, X. and Varghese, J. (2004), Hierarchical Strategy for Rapid Finite Element Analysis, *45th AIAA/ASME/ASCE/AHS Structural Dynamics, and Materials Conference (SDM)*, Palm Springs, California.

104. Dohrmann, C. R. and Key, S. W. (1999). A Transition Element for Uniform Strain Tetrahedral and Hexahedral Finite Elements, *Int. J. Num. Meth. Eng.*, **44**: 1933–1950.

105. Dohrmann, C. R., Key, S. W. and Heinstein, M. W. (2000). Methods for Connecting Dissimilar Finite Element Meshes in Three Dimensions, *Int. J. Num. Meth. Eng.*, **47**: 1057–1080.

106. Dohrmann, C. R., Key, S. W. and Heinstein, M. W. (2000). A Method for Connecting Dissimilar Finite Element Meshes in Two Dimensions, *Int. J. Num. Meth. Eng.*, **48**: 655–678.

107. Ransom, J. B. (1989), Global/Local Stress Analysis of Composite Structures, M.S. Thesis, Department of Mechanical Engineering and Mechanics, Old Dominion University, Norfolk, VA.

108. Knight, N. F. Jr., Ransom, J. B., Griffin, O. H. Jr. and Thompson, D. M. (1991), Global/Local Methods Research Using a Common Structural Analysis Framework, *Finite Elements in Analysis and Design*, **9**: 91-112.

109. Housner, J. M. and Aminpour, M. A. (1991), Multiple Methods Integration for Structural Mechanics Analysis and Design, Ist NASA Advanced Composites Technology Conference, NASA CP 3104, Part 2: 875-889.

110. Aminpour, M. A., Ransom, J. B., and McCleary, S. L. (1995). A Coupled Analysis for Structures with Independently Modeled Finite Element Subdomains, *International Journal for Numerical Methods in Engineering*, **38**: 3695-3718.

111. Ransom, J. B., McCleary, S. L., and Aminpour, M. A. (1993). A New Interface Element for Connecting Independently Modeled Substructures, *34th AIAA/ASME/ASCE/AHS/ASC Structures, Structural Dynamics, and Materials Conference*, La Jola, CA, AIAA Paper No. 93-1503: 1693-1703.

112. Schiermeier, J. E., Housner, J. M., Ransom, J. B., Aminpour, M. A., and Stroud, W. J (1996). The Application of Interface Elements to Dissimilar Meshes in Global/Local Analysis, *Proceedings of the 1996 World MSC User's Conference*, Newport Beach, California.

113. Davilá, C. G., Ransom, J. B., and Aminpour, M. A. (1994). Cross-Surface Interface Element for Coupling Built-up Structural Subdomains, NASA technical memorandum – 109125, National Aeronautics and Space Administration, Langley Research Center, National Technical Information Service, Langley, VA.

114. ANSYS, Inc., 1999, "DesignSpace User Manual for Release 5.x", July 1999.

115. URL: *http://www.simulia.com/products/unified_fea.html* [cited 01 June 2009].

116. Nielan, P., 2002, Sandia Lab News, **54**, URL: *http://www.sandia.gov/LabNews/LN02-22-02/LA2002/la02/compute_story.htm*

117. Noor, A. K., and Malone, J. B. (1997). Computational Tools and Facilities for the Next-Generation Analysis and Design Environment, NASA Conference Publication 3346.

118. Srirengan, K. and Whitcomb, J. D. (1998). Finite Element Based Degradation Model for Composites with Transverse Matrix Cracks, *Journal of Thermoplastic Composites*, **11**: 113-123.

119. Nicoletto, G. and Riva, E. (2004). Failure Mechanisms in Twill-Weave Laminates: FEM Predictions vs. Experiments, *Composites: Part A*, **35**: 787–795.

120. Guagliano, M. and Riva, E. (2001). Mechanical behaviour prediction in plain weave composites, *Journal of Strain Analysis*, **36**(2): 153-162.

121. Chapman, C.D. and Whitcomb, J.D., (2000). Thermally Induced Damage Initiation and Growth in Plain and Satin Weave Carbon-Carbon Composites, *Mechanics of Composite Materials and* Structures, **7**: 177-194.

122. Stanton, E. L. and Kipp, T. E. (1985). Nonlinear Mechanics of Two-Dimensional Carbon-Carbon Composite Structures and Materials, *AIAA Journal*, **23**(8): 1278-1284.

123. Zako, M., Uetsujib, Y., Kurashikia, T. (2003). Finite Element Analysis of Damaged Woven Fabric Composite Materials, *Composites Science and Technology*, **63**: 507–516.

124. Choiy, J and Tamma, K. K. (2001). Woven Fabric Composites Part I: Predictions of Homogenized Elastic Properties and Micromechanical Damage Analysis, *Int. J. Numer. Meth. Engng*, **50**:2285-2298.

125. Karkkainen, R. L. and Sankar, B. V. (2006). A Direct Micromechanics Method for Analysis of Failure Initiation of Plain Weave Textile Composites, *Composites Science and Technology*, **66**: 137–150.

126. Luan, X. G., Cheng, L. and Zhang, L. (2005). Life Prediction of 3D Woven C-SiC Composites at High Temperatures with Low-frequency Cyclic Stresses, *Journal of Composite Materials*, **39**(13): 1195-1202.

127. Hale, J. M. and Gibson, A. G. (1998). Coupon Tests of Fibre Reinforced Plastics at Elevated Temperatures in Offshore Processing Environments, *Journal of Composite Materials*, **32**(6): 526-543.

128. Haque, A. and Rahman, M. (2000). Durability and Damage Development in Woven Ceramic Matrix Composites Under Tensile and Fatigue Loading at Room and Elevated Temperatures, *Journal of Engineering Materials and Technology*, **122**(4): 394-401.

129. Peddiraju, P., Noh, J., Whitcomb, J. and Lagoudas, D. C. (2007). Prediction of Cryogen Leak Rate Through Damaged Composite Laminates, *Journal of Composite Materials*, **41**(1): 41-71.

130. Shen, C. H., Springer, G. S. (1981). Effects of Moisture and Temperature on the Tensile Strength of Composite Materials. In: GS Springer (ed), *Environmental Effects on Composite Materials*. pp. 79–93, Technomic Publishing, Lancaster, PA.

131. Roy, S., Reddy, J. N. (1988). A Finite Element Analysis of Adhesively Bonded Composite Joints with Moisture Diffusion and Delayed Failure. *Comput. Struct*, **29**: 1011–31.

132. Weitsman, Y. (1990). Moisture in Composites: Sorption and Damage. In: Reifsnider, K. L., (ed), *Composite Materials Series – 4: fatigue of composites*. pp. 385–429, Elsevier, New York.

133. Dasgupta, A., Agarwal, R. K. (1992). Orthotropic Thermal Conductivity of Plain-Weave Fabric Composites using Homogenization Technique. *J Compos Mater*, **26**: 2736–58.

134. Roy, S., Dharani, L. R., Gupta, V., Xu, W. (2000). Modeling of Hygrothermal and Aging Effects in Textile Composites. *41st AIAA/ASME/ASCE/AHS/ASC Structures, Structural Dynamics, and Materials Conference and Exhibit*, Atlanta, GA, Apr. 3-6, AIAA-2000-1682.

135. Li, Y., Tang, X., Miranda, J., Sue, H. J., Whitcomb, J. D. and Bradley, W. (1999). Study of Moisture Diffusion Behavior in Hybrid IM7/BMI

Composites. In: *Proceedings of the 57th Annual Technical Conference*. New York: Society of Plastics Engineering.

136. Tang, X., Whitcomb, J. D., Li, Y. and Sue, H. J. (2005). Micromechanics Modeling of Moisture Diffusion in Woven Composites, *Composites Science and Technology*, **65**: 817–826.
137. Whitcomb, J. D. and Tang, X. (2001). Micromechanics of Moisture Diffusion in Composites with Impermeable Fibers, *Journal of Composite Materials*, **36**(9): 1093–102.
138. Tang X., (2001). Micromechanics of 2D Woven Composites, PhD Dissertation, Department of Aerospace Engineering, Texas A&M University, College Station, TX.
139. Yin, X., Cheng, L., Zhang, L., Xu, Y. and Luan, X. (2001). Oxidation Behavior of Three-Dimensional Woven C-SiC Composites, *Mater. Sci. Tech.*, **17**(4): 727-730.
140. Strife, J. R. and Sheehan, J. E. (1988). Ceramic Coatings for Carbon-Carbon Composites, *American Ceramic Society Bulletin*, **67**(2): 369.
141. Courtois, C., Desmaison, J., Tawil, H., (1991). Protection Against Oxidation of C/SiC Composites by Chemical Vapour Deposition of Titanium Diboride : Deposition Kinetics and Oxidation Behaviour of Films Prepared from TiCl4/BCl3/H2 Mixtures, *Journal de Physique IV (Colloque)*, **1**(C2): 657-664.
142. Halbig, M. C., Eckel, A. J., Cawley, J. D. and Brewer, D. N. (1997). Stressed Oxidation of C/SiC Composites, *Proceedings of the 21st Annual Conference on Composites, Advanced Ceramics Materials and Structures*, Cocoa Beach, Florida, January 12-16.
143. Luan, X. G., Cheng, L. and Zhang, L. (2005). Life Prediction of 3D Woven C-SiC Composites at High Temperatures with Low-frequency Cyclic Stresses, *Journal of Composite Materials*, **39**(13): 1195-1202.
144. Halbig, M. C., Eckel, A. J. and Cawley, J. D. (1999). Oxygen Diffusion and Reaction Kinetics in Continuous Fiber Ceramic Matrix Composites,

NASA/TM—1999-208911, National Aeronautics and Space Administration Lewis Research Center ARL–TR–1692

145. McKee, D. W. (1988). Oxidation Behavior of Matrix-Inhibited Carbon/Carbon Composites, *Carbon*, **26**:659-665.
146. Ochoa, O. O. and Elliott, C. H. (1998). Inhibited Carbon-Carbon Composites: Isothermal and Fatigue Exposure, *Journal of Composite Materials*, **32**(12): 1157-1177.
147. Luo, R., Zheng, Y. and Li, L. (2000). Effect of Additives on Mechanical Properties of Oxidation-Resistant Carbon/Carbon Composite Fabricated by Rapid CVD Method, *Carbon*, **38**(15): 2109-2115.
148. Mazany, A. M., Bianco, R. and Stover, E. R. (2005). Oxidation Inhibition of Carbon-Carbon Composites, Patent publication number: WO/2005/047213, latest accessed online *http://www.wipo.int/pctdb/en/wo.jsp?KEY=05/47213.050623* on June 1, 2009.
149. Odegard, G., Kumosa, M., (2000). Elastic-Plastic and Failure Properties of a Unidirectional Carbon/PMR-15 Composite at Room and Elevated Temperatures, *Composites Science and Technology*, **60**: 2979-2988.
150. Rupnowski, P., Gentz, M., Kumosa, M., (2006). Mechanical Response of a Unidirectional Graphite Fiber/Polyimide Composite as a Function of Temperature, *Composites Science and Technology*, **66**: 1045–1055.
151. Rupnowski, P., Gentz, M., Sutter, J., Kumosa, M., (2004). Mechanical Response of a Woven Graphite/Polyimide Composite to In-Plane Shear Dominated Loads at Room and Elevated Temperatures, *Acta Materialia*, **52**: 5603–5613.
152. Odegard, G., Kumosa, M., (2000). Determination of Shear Strength of Unidirectional Composite Materials with the Iosipescu and 10^{o}-Axis Shear Tests, *Composites Science and Technology*, **60**: 2917-2943.
153. Pochiraju, K., Tandon, G., Schoeppner, G., (2008). Evolution of Stress and Deformations in High-Temperature Polymer Matrix Composites during

Thermo-Oxidative Aging, *Mechanics of Time-Dependent Materials*, **12**: 45–68.

154. Roy, S., Singh, S., Schoeppner, G., (2008). Modeling of Evolving Damage in High Temperature Polymer Matrix Composites Subjected to Thermal Oxidation, *Journal of Material Science*, **43**: 6651–6660.

155. Wang, S., Chen, X., (2006). Computational Micromechanics for High-Temperature Constitutive Equations of Polymer-Matrix Composites With Oxidation Reaction, Damage, and Degradation, *Journal of Engineering Materials and Technology*, **128**(1): 81.

156. Varghese, J. (2003). Hierarchical Strategy for Rapid Finite Element Analysis, MS Thesis, Texas A&M University.

157. Colin, X., Verdu, J., (2003). Thermal Aging and Lifetime Prediction for Organic Matrix Composites, *Plastics Rubber and Composites*, **32**: 349–3562.

158. Colin, X., Marais, C., Verdu, J., (2001). A New Method for Predicting the Thermal Oxidation of Thermoset Matrices: Application to an Amine Cross-Linked Epoxy, *Polymer Testing*, **20**: pp.795–803.

159. Pochiraju, K. V., Tandon. G. P., (2004). Time dependent Composite Material Behavior Under Thermo-Oxidative Environmental Conditions. In: *Proceedings of IMECE*, Anaheim, CA.

160. Bowles, K. J., Jayne, D., Leonhardt, T. A. and Bors, D., (1993). Thermal Stability Relationships Between PMR-15 resin and Its Composites. NASA Technical Memorandum 106285.

161. Bowles, K. J., Papadopoulos, D. S., Inghram, L. L., McCorkle, L. S. and Klan, O. V. (2001). Longtime Durability of PMR-15 Matrix Polymer at 204, 260, 288 and 316°C, NASA/TM-2001-210602.

162. Tsuji, L. C., McManus, H. L. and Bowles, K. J. (1998). Mechanical Properties of Degraded PMR-15 Resin. NASA Technical Report, 1998-208487: 1–18.

163. Abdeljaoued, K. (1999). Thermal Oxidation of PMR-15 Polymer Used as a Matrix in Composite Materials Reinforced with Carbon Fibers, MS Thesis, Ecole Nationale Superieure des Arts et Metiers, Paris.

164. Johnson, T. F. and Gates, T. S., (2001). High Temperature Polyimide Materials in Extreme Temperature Environments, In: AIAA Paper 2001-1214, *42nd AIAA/ASME/ASCE/AHS/ASC Structures, Structural Dynamics and Materials Conference and Exhibition*, Seattle, WA.

165. Schoeppner, G. A., Tandon, G. P. and Ripberger, E. R. (2007). Anisotropic Oxidation and Weight Loss in PMR-15 Composites. *Composites Part A: Applied Science and Manufacturing*, **38**: 890–904.

166. Reddy, J. N., (1993). *An Introduction to the Finite Element Method*, 2nd ed., McGraw-Hill, Inc., New York.

167. Colin, X., Marais, C., Verdu, J., (2001). Thermal Oxidation Kinetics for a Poly(bismaleimide). *Journal of Applied Polymer Science*, **82**: 3418–3430.

168. Colin, X., Marais, C., Verdu, J. (2002). Kinetic Modeling and Simulation of Gravimetric Curves: Application to the Oxidation of Bismaleimide and Epoxy Resins. *Polymer Degradation and Stability,* **78**: 545–553.

169. Stroustrup, B. (1986). *The C++ Programming Language*: Special Edition (3rd Edition),Addison-Wesley Professional, New Jersey.

170. URL: *http://software.intel.com/en-us/intel-mkl/* [cited 01 June 2009].

171. URL: *http://www-users.cs.umn.edu/~agupta/wsmp.html* [cited 01 June 2009].

172. Brian Owens, (2009). Implementation of B-Splines in a Conventional Finite Element Framework, MS Thesis, Texas A&M University.

173. Shindo, Y., Horiguchi, K., Wang, R. and Kudo, H. (2001). Double Cantilever Beam Measurement and Finite Element Analysis of Cryogenic Mode I Interlaminar Fracture Toughness of Glass- Cloth/Epoxy Laminates, *ASME J. Eng. Mater. Technol.*, **123**:191–197.

174. NextGrade (Next Generation Rapid Analysis and Design Environment), URL: *http://www.ara.com/nextgrade.htm* [cited 27 March 2004].

175. Varghese, J. and Whitcomb, J. (2006). Effective Properties of Composites Whose Reinforcement has Microstructure, *Journal for Mechanics of Advanced Materials and Structures*, **13**(3): 227-235.

176. Rybicki, E. F. and Kanninen, M. F., (1987). A Finite Element Calculation of Stress-intensity Factors by a Modified Crack Closure Integral, *Engineering Fracture Mechanics*, **9**:931-938.

177. Quaresimin, M., (2002). Fatigue of Woven Composite Laminates Under Tensile and Compressive Loading, *10th European Conference on Composite Materials (ECCM-10)*, Brugge, Belgium.

178. Hull, D. and Clyne, T. (1996). *An Introduction to Composite Materials*, 2nd Ed, Cambridge University Press, New York.

179. Gumbsch, P. (1995). An Atomistic Study of Brittle Fracture: Toward Explicit Failure Criteria from Atomistic Modeling, *J. Mater. Res.*, **10**(11):2897-2907.

180. Abraham, F.F., Broughton, J.Q., Bernstein, N. and Kaxiras, E. (1998). Spanning the Length Scales in Dynamic Simulation, *Computers in Physics*, **12**(6): 538.

181. Abraham, F.F., Bernstein, N., Broughton, J. Q. and Hess, D. (2000). Dynamic Fracture of Silicon: Concurrent Simulation of Quantum Electrons, Classical Atoms, and the Continuum Solid, *MRS Bulletin*, **25**(5):27-32.

182. Tadmor, E.B., Ortiz, M. and Phillips, R. (1996). Quasicontinuum Analysis of Defects in Solids, *Philosophical Magazine A*, **73**(6):1529.

183. Shenoy, V., Miller, R., Tadmor, E. B., Rodney, D., Phillips, R. and Ortiz, M. (1999). An Adaptive Methodology for Atomic Scale Mechanics - The Quasicontinuum Method, *J. Mech. Phys. Sol.*, **47**:611-642.

184. Shenoy, V., Miller, R., Tadmor, E. B., Phillips, R. and Ortiz, M. (1998). Quasicontinuum Models of Interfacial Structure and Deformation, *Phys. Rev. Lett.*, **80**(4):742.

185. Shilkrot, L. E., Miller, R. E. and Curtin, W. A., (2002). Coupled Atomistic and Discrete Dislocation Plasticity, *Phys. Rev. Lett.*, **89**:025501-1–025501-4.

186. Park, H.S., Karpov, E.G., Klein, P.A. and Liu, W.K. (2005). The Bridging Scale for Two-Dimensional Atomistic/Continuum Coupling, *Philosophical Magazine*, **85**(1):79-113.

187. Radhakrishnan, K. and Hindmarsh, A. C. (1993). Description and Use of LSODE, the Livermore Solver for Ordinary Differential Equations, NASA Reference Publication 1327, Lawrence Livermore National Laboratory Report UCRL-ID-113855.

VITA

Name:	Julian Varghese
Address:	Department of Aerospace Engineering, Mailstop 3141, Texas A&M University, College Station, TX 77843
Email Address:	julvar@gmail.com
Education:	B.Tech., Mechanical Engineering, University of Kerala, India, 2000 M.S., Aerospace Engineering, Texas A&M University, 2003